UAB
Universitat Autònoma de Barcelona

Biomimetic Nanophotonic Sensors for Immunotherapy Evaluation

Razia Batool

Doctorat en Ciència de Materials

Departament de Física - Facultat de Ciències

Biomimetic Nanophotonic Sensors for Immunotherapy Evaluation

Doctoral Thesis – 2024

Razia Batool

Author

Dr. Maria Soler Aznar

Prof. Laura M. Lechuga

Directors

Prof. Eva Maria Pellicer Vilà

Tutor

Abstract

This PhD thesis focuses on the development of new nanophotonic biosensors for the screening and evaluation of immunotherapies for cancer and infectious diseases. In particular, the objective is to simplify and accelerate the selection and assessment of monoclonal antibodies (mAb) either as immune checkpoint inhibitors or anti-viral therapy.

Conventional techniques for studying mAb interactions with immune cells or pathogens are laborious and time-consuming, including cell culture and fluorescence or colorimetric assays. These processes ultimately delay the production of effective therapies and increase their cost, challenging their timely and widespread administration. As an alternative, this work introduces pioneering nanophotonic biosensor technologies specially designed and functionalized to offer label-free, real-time, and reliable analysis of biomolecular and cell interactions in a biomimetic format and point-of-care implementation.

The research initially explores the design and large-scale fabrication of short-ordered arrays of plasmonic nanostructures, using gold and silver metals, as well as novel dielectric nanoresonators, made of silicon, to develop label-free refractometric sensors with high sensitivity and resolution. These nanosensors are integrated in compact and user-friendly devices for simple operation and straightforward application in biomedical analysis. In addition, we propose and establish an innovative sensor biofunctionalization protocol for creating on-chip artificial cell membranes. The formation of functional lipid membranes on the sensor surface and subsequent anchoring of specific ligands and cell receptors provides a nature-inspired microenvironment that enhances the efficiency of biomolecular interactions, further increasing the reliability of the therapy evaluation assay. Finally, to demonstrate the utility and benefits of our biomimetic nanophotonic sensors, we present two relevant applications: the screening of mAb candidates as anti-viral therapy for COVID-19, and the evaluation of immune checkpoint inhibitors targeting the programmed cell death 1 (PD1) pathway.

The work carried out in this PhD thesis paves the way for the implementation of nanophotonic biosensors into the emerging area of immunotherapies, contributing to the study and assessment of novel candidates in a simpler, faster, and convenient manner. Furthermore, the technological and biochemical advancements accomplished here offer a promising potential for diverse applications in biomedical research, including precision diagnostics, therapeutic formulation, and personalized medicine.

Resum

Aquesta tesi doctoral se centra en el desenvolupament de nous biosensors nanofotònics per a la selecció i l'avaluació d'immunoteràpies contra el càncer i les malalties infeccioses. En particular, l'objectiu és simplificar i accelerar la selecció i avaluació d'anticossos monoclonals (mAb), ja sigui com a inhibidors de punts de control immunitari o com a teràpia antiviral.

Les tècniques convencionals per a l'estudi de les interaccions dels mAb amb cèl·lules immunitàries o patògens són laborioses i requereixen molt de temps, incloent-hi cultius cel·lulars i assajos fluorescents o colorimètrics. Aquests processos finalment retarden la producció de teràpies eficaces i n'augmenten el cost, fet que en dificulta l'administració oportuna i generalitzada. Com a alternativa, aquest treball introdueix tecnologies pioneres de biosensors nanofotònics, especialment dissenyades i funcionalitzades per oferir anàlisis fiables, en temps real i sense etiquetatge de les interaccions biomoleculars i cel·lulars, en un format biomimètic i d'implementació en el punt d'atenció.

La investigació explora inicialment el disseny i la fabricació a gran escala d'arranjaments de nanostructures plasmòniques, utilitzant metalls com l'or i la plata, així com nous nanoresonadors dielèctrics de silici, per desenvolupar sensors refractomètrics sense marcatge, amb elevada sensibilitat i bona resolució. Aquests nanosensors s'integren en dispositius compactes i fàcils d'usar per a una operació senzilla i aplicació directa en l'anàlisi biomèdica. A més, proposem i establim un protocol innovador de biofuncionalització del sensor per a la creació de membranes cel·lulars artificials sobre xip. La formació de membranes lipídiques funcionals a la superfície del sensor i l'ancoratge posterior de lligands específics i receptors cel·lulars proporcionen un microambient inspirat en la natura que millora l'eficiència de les interaccions biomoleculars, augmentant així la fiabilitat de l'assaig d'avaluació terapèutica. Finalment, per demostrar la utilitat i els beneficis dels nostres sensors nanofotònics biomimètics, presentem dues aplicacions rellevants: la selecció de candidats de mAb com a teràpia antiviral per a la COVID-19 i l'avaluació d'inhibidors de punts de control immunitari dirigits al receptor de la proteïna de mort cel·lular programada 1 (PD1).

El treball realitzat en aquesta tesi doctoral obre el camí per a la implementació de biosensors nanofotònics en l'àrea emergent de les immunoteràpies, contribuint a l'estudi i l'avaluació de nous candidats de manera més senzilla, ràpida i convenient. A més, els avenços tecnològics i bioquímics assolits ofereixen un potencial prometedor per a diverses aplicacions en la recerca biomèdica, incloent-hi el diagnòstic de precisió, la formulació terapèutica i la medicina personalitzada.

Acknowledgements

As I reach the conclusion of this significant journey, I want to express my deepest gratitude to all those who have contributed to making this achievement possible.

First and foremost, I would like to thank my director, Professor Laura M. Lechuga, for the opportunity to pursue my PhD in her esteemed research group. Her expert guidance, trust, and steadfast support have been vital throughout this journey, greatly contributed to my growth and success in the field of biosensors.

I would like to extend my deepest gratitude to my co-director Dr Maria Soler Aznar, whose support, kindness, and unwavering guidance have been instrumental throughout this journey. She has not only been an outstanding mentor but also a source of immense inspiration. Her unique ability to understand exactly how to guide and support me through various challenges has been remarkable. Whether it was offering critical professional advice or providing encouragement at crucial moments, Maria always knew how to offer the perfect balance of insight and reassurance. Her kindness, humility, and deep understanding have shaped my professional growth in more ways than I can express. I have learned so much from her, both as a researcher and as a person, and I feel incredibly fortunate to have had her as my supervisor. I am truly overwhelmed with gratitude and could not have asked for a better mentor. I would also like to thank the Spanish Ministry of Science and innovation and ICN2 for providing me with the opportunity to develop my thesis in such an ideal place.

To all my colleagues at NanoB2A, past and present, who have made the lab a vibrant and enjoyable place, I am deeply grateful to Barbara, Daniel, Cristina, Jessica, Rukmani, Pablo, Juliana, Patricia, Andrés, Pioter, Celia, Victor, Martalu, Medhi, M. Cruz, Mireia, Layre, Alejandro, Sara, and Mariona. Spacial thanks to Beatriz your camaraderie and support have been a source of daily joy. I also wish to acknowledge my ICN2 friends Sharin, Ashita, Noor, Tapas, Qurat-ul-Ain, and Zaheer for their friendship and encouragement.

I would like to thank Dr. Giulia Matusali, Francesca Colavita and Lavinia Fabeni from The National Institute of Infectious Diseases Lazzaro Spallanzani (INMI, Rome, Italy) for collaborating and providing us the clinical samples.

I am profoundly grateful to Professor Christoph Langhammer for the opportunity to conduct research at Chalmers University of Technology, Sweden. The international research stay was a great experience, and I am particularly thankful to Bohdan and Leyla for their collaboration and engaging discussions. A

special mention goes to Sushree, Yashna, Lova, Bjorn, Thanos, Jordi, Carl, and Joachim for fostering a warm and friendly environment.

To my friends in Barcelona from Pakistan Arzoo, Rahima, Masab, and Annie, thank you for the laughter, hanging out, parties and support. I am also grateful to Sundas and her family for making me feel at home away from home. A heartfelt thanks to my housemates Betty, Rosa, and Ganyoun, and to all my friends from Pakistan for their unwavering support.

Lastly, I dedicate this thesis to my beloved family—my siblings, sisters-in-law, brothers-in-law, and nieces, but especially to my Mom and Dad. Your endless support, encouragement, and love have been my greatest strength. I am eternally grateful for everything you have done for me.

Motivations and Objectives

A primary goal in modern biomedical research is advancing the design and implementation of immunotherapies, which hold immense promise for treating a wide range of diseases, including cancer, infections, and autoimmune disorders. Immunotherapies offer a targeted approach by harnessing the body's immune system to fight the disease, representing a transformative shift in treatment strategies. However, significant challenges remain in their development, such as designing therapies that are both highly specific and broadly effective, ensuring scalable and cost-effective production, and overcoming regulatory and logistical barriers for widespread implementation. To address these limitations, next-generation bioanalytical tools and innovative approaches for biomolecular engineering are essential. These will enable more precise immune system modulation, streamline production processes, and improve the accessibility of these therapies, ensuring they reach their full potential in clinical applications.

This PhD thesis aims at introducing novel multifunctional nanophotonic biosensors for rapid and reliable analysis of biomolecular and cell interactions with direct application in the design and study of immunotherapies. The biosensor technology is intended to streamline pre-clinical therapy screening and evaluation processes by integrating advanced photonics engineering with innovative biomimetic sensor functionalization, all within compact and user-friendly devices for straightforward implementation in biomedical research. In particular, the scientific objectives of this thesis include:

- Design and fabrication of nanophotonic biosensors based on plasmonic metals as well as dielectric materials to provide high-quality spectral resonances. A large-scale nanofabrication protocol for cost-effective production of sensor chips.
- Characterization of the nanophotonic technologies for label-free refractometric biosensing. Determination of analytical parameters: sensitivity, resolution, and reproducibility and robustness.
- Integration of the nanophotonic sensors in a compact optical set-up for easy and semi-automated operation, data acquisition and processing through a customized software interface, providing real-time signal readouts.
- Design and optimization of surface biofunctionalization strategies to generate pn-chip artificial cell membranes as biomimetic scaffolds for the study of cell-cell interactions.
- Demonstration of the biomimetic nanophotonic sensors for the screening and evaluation of relevant immunotherapies for cancer and infectious diseases.

Table of Contents

Chapter 1

Introduction

This chapter provides a comprehensive overview of immunotherapy, discussing its promises, challenges, and evolution, while considering future advancements. It highlights the role of optical biosensors as essential tools in biomedical research. The focus then shifts to nanophotonic sensors, particularly nanoplasmonic technologies like SPR and LSPR, covering their merits and current applications. It also introduces dielectric materials as advanced nanophotonic resonators. Finally, the chapter addresses biofunctionalization strategies, emphasizing the use of chemical matrices and lipid membranes to improve biosensor performance in biomedical applications.

1. Introduction

1.1. Immunotherapy: promises and challenges

1.1.1. Definition and classification

Our immune system is our best asset to combat diseases. The immune response against pathogens or malignant disorders in our cells can effectively prevent from serious infections or the spread of cancer. Millions of immune cells patrol our body to search and find foreign organisms and anomalous behaviors that can endanger our health; and when they do so, a comprehensive network of mechanisms is triggered to reduce and eliminate them. But the immune system may fail and, either cannot be sufficient to eradicate the hostile or become ineffective in front of smart immunosuppressive mechanisms developed by tumors. Herein, immunotherapies have emerged as a way to reinforce, improve, and boost our immune system to fight diseases.[1]

Immunotherapy is defined as a biological therapy that stimulates or changes the immune system of the patient to treat a disease. There are different types of immunotherapies, including cytokines, monoclonal antibodies, or cell therapies, among others.

- **Cytokines** are a type of proteins expressed and released by immune cells as signaling mechanisms or for killing other malignant cells (Figure 1.1a). Some cytokine therapies are based on interleukins, like interleukin 2 (IL-2), which has been used to treat kidney cancer and melanoma by stimulating the growth and activity of immune cells. Also interferons, like interferon alpha (INF), are employed to inhibit cell multiplication and treat certain tumors, such as cutaneous lymphoma, or infections, like chronic hepatitis C.[2]

- **Monoclonal antibodies (mAb)** are laboratory-produced molecules engineered to serve as substitute of natural antibodies that can restore, enhance, or mimic the immune system's attack on cancer cells or pathogens. These antibodies are targeted to specifically bind certain antigens (proteins) of cells to either block growing and replication, to facilitate the immune cells to recognize tumor cells, or to inhibit the immunosuppressive mechanisms developed by cancers (Figure 1.1b). The latter is commonly known as immune checkpoint inhibitors (ICIs). ICIs are molecular receptors expressed in either immune or tumor cells that act as brakes for the immune system response; therefore, mAb inhibiting the effect of these checkpoints can effectively reverse the immune cell actuation to terminate malignant cells.[3] Most popular mAb therapies

include rituximab for lymphoma, trastuzumab for breast cancer,[4] and pembrolizumab and nivolumab, which target the programmed cell death 1 (PD-1) checkpoint pathway.[5,6]

- **Cell immunotherapies** generally consist in the selection and biological engineering of immune cells from the patient so that they can recognize and attack the tumor cells (Figure 1.1c). The most popular and advanced approach is the CAR-T cell therapy (i.e., chimeric antigen receptor T cell therapy), with several treatments approved and in use for blood cancers. Cell immunotherapies are one of the most promising personalized medicines for tumors in advanced or metastatic stages, especially for those not responding to conventional treatments.[7]

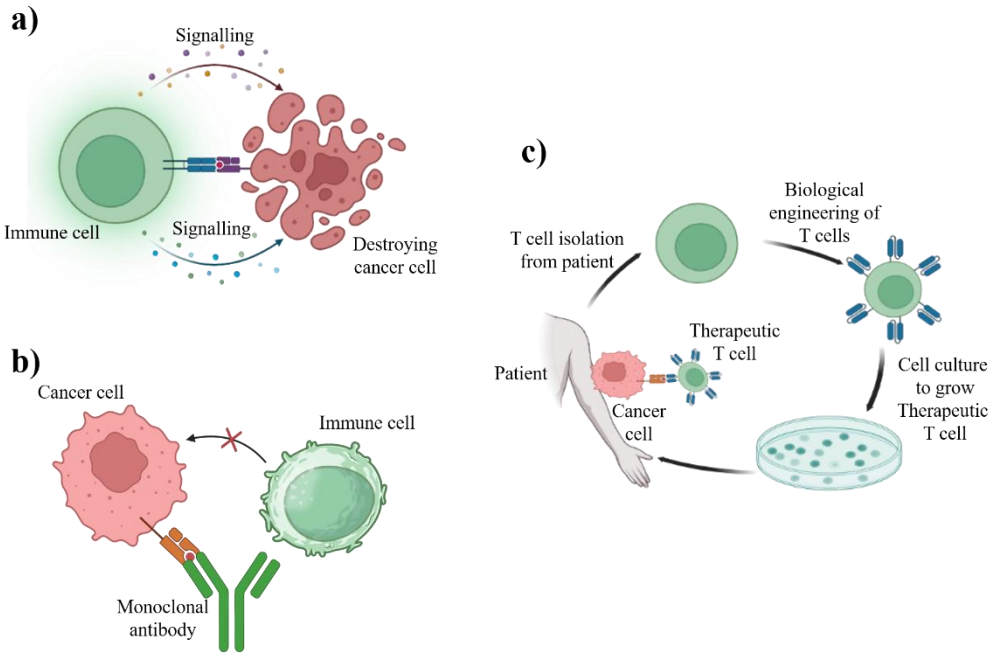

Fig 1. 1. Schematic illustration of immunotherapies: a) Cytokine-based immunotherapy, b) Monoclonal antibody and checkpoint inhibitor immunotherapies, and c) Cell immunotherapy.

In general, immunotherapies offer a powerful tool to treat diseases with outstanding results and efficacies. Since they can be designed to specifically target tumor cells or pathogens while sparing healthy cells, the side effects are often less severe and more manageable than those associated with traditional drugs. Moreover, the immune system has a memory component, which means that immunotherapy can provide long-term protection against disease recurrence. And, due to the high versatility and combination potential, these therapies can be tailored to each individual patient according to their disease profile to enhance the effectivity, minimize the collateral damage, and improve the overall quality of life of patients.

1.1.2. Past, present, and future of immunotherapy

The concept of using the immune system to fight diseases dates back to the late 19th century when Dr. William Coley, known as the "father of immunotherapy," observed that some cancer patients who developed infections after surgery experienced cancer regression.[8,9] He developed the Coley's toxins, a mixture of bacterial toxins, to treat cancer patients by inducing an immune response. In the mid-20th century, advancements in immunology laid the groundwork for modern immunotherapy. The discovery of cytokines and the development of monoclonal antibody technology in the 1970s and 1980s were pivotal. The first monoclonal antibody, muromonab-CD3, was approved in 1986 to prevent kidney transplant rejection,[10] heralding a new era in immunotherapy. The late 20th and early 21st centuries saw significant breakthroughs with the development of immune checkpoint inhibitors and CAR T-cell therapies, leading to remarkable successes in treating previously untreatable cancers.[11] The approval of ipilimumab in 2011 for metastatic melanoma marked the first checkpoint inhibitor to show a survival benefit, followed by approvals for other checkpoint inhibitors targeting the PD-1 pathway.[12]

Today, immunotherapy is a rapidly evolving field with ongoing research focused on improving existing therapies, discovering new targets, and expanding the use of immunotherapy to a broader range of cancers and other diseases. In particular, immunotherapies based on mAbs, hold great potential by offering highly specific targeting of disease-associated antigens, comprising infectious diseases, cancer and autoimmune disorders, etc. However, the assessment and development of mAbs faces many important challenges, especially in terms of the analytical techniques used to ensure efficacy and excellency. For the evaluation of mAbs there are two main analytical process, including binding and affinity analysis, and functional and biological assays. Binding and affinity analysis techniques are essential tools for characterizing mAbs and their interactions with target antigens. These methods include Enzyme-Linked Immunosorbent Assay (ELISA), Biolayer Interferometry (BLI), Isothermal Titration Calorimetry (ITC), and Surface Plasmon Resonance (SPR), each offering unique advantages and facing specific challenges. ELISA, widely used for its high sensitivity and specificity, allows for quantitative results and high-throughput screening but may suffer from false positives due to cross-reactivity and has limitations in detecting low-affinity interactions.[13] BLI enables real-time, label-free analysis of binding kinetics with minimal sample consumption, though it may have lower sensitivity compared to other techniques and potential for non-specific binding.[14] ITC provides direct measurements of binding thermodynamics without the need for labeling, offering valuable insights into mAb-antigen interactions, but requires larger sample amounts and has lower throughput.[15] SPR, known for its high sensitivity and real-time, label-free measurements with less sample consumption, is crucial for understanding therapeutic efficacy but may be affected by mass transport limitations.[16]

Functional and biological assays for evaluating the efficacy and specificity of mAbs involve a range of techniques, including cell-based cytotoxicity assays, flow cytometry, and in-vitro neutralization assays, each designed to assess different aspects of mAb functionality. Cell-based cytotoxicity assays, such as antibody-dependent cell-mediated cytotoxicity (ADCC) and complement-dependent cytotoxicity (CDC) assays, evaluate the ability of mAbs to mediate cell-killing mechanisms. However, these assays face challenges in standardization and may not fully reflect in-vivo activity.[17] Flow cytometry allows for the analysis of mAb binding specificity and functionality on cell surfaces, offering insights into multiple parameters simultaneously, but careful controls are needed to account for non-specific binding, and low-affinity interactions may be difficult to detect reliably.[18] Neutralization assays test the ability of mAbs to neutralize their target antigens, particularly useful for mAbs targeting viruses or toxins, but have limitations in representing in-vivo dynamics due to simplified environments and absence of full immune system components.[19] All these techniques necessitate complex laboratory protocols, rely on large and relatively expensive instrumentation, and are time-consuming, which limits their accessibility for routine or point-of-care applications.

Considering these challenges, there is a need of new analytical techniques in order to improve and accelerate the design, screening, and evaluation of mAb therapies in biomedical research. In particular, techniques that are affordable and scalable for high-throughput applications are needed in order to enable real-time, high-sensitivity monitoring of mAb interactions with the targeted cell receptors together with the associated cell-cell interactions.

Nanophotonic biosensors can be a promising solution to these limitations. These biosensors utilize the exceptional optical properties of the nanomaterials in order to detect, monitor, and quantify biological interactions with excellent sensitivities in a label-free format. By detecting changes in the refractive index near the sensor surface, they provide real-time analysis without the need for colorimetric or fluorescent tags. This approach simplifies the biological analysis to a one-step assay, reducing sample preparation complexity and opening up opportunities for miniaturization. The elimination of complex optics and external labels allows for the design of smaller, more portable devices. Integration with microfluidic systems enables automated sample handling, leading to efficient, accessible tools for multiplexed screening in both clinical and research setting. Nanophotonic biosensor technologies could improve the screening and evaluation of mAb immunotherapies by offering accurate and reliable information of the process with a minimal sample and reagent consumption in less time and more user-friendly environment.

1.1.3. Optical biosensors as tools for biomedical research

A biosensor is defined as an integrated analytical tool that employs a biomimetic or biological receptor directly in contact with a transducer to provide qualitative or semi-quantitative measurement of certain analytes in a sample.[20] Biosensors are mainly composed of a biorecognition element and a transducer (Figure 1.2). The bioreceptors, typically antibodies, nucleic acids, or enzymes, provide selectivity and specificity in recognizing and detecting the target analytes. When the biorecognition interaction takes place, a series of physicochemical changes (i.e., electrochemical, optical, or mechanical) occur close to the sensor surface, which are detected by the transducer and transformed into discrete or continuous measurable signals.

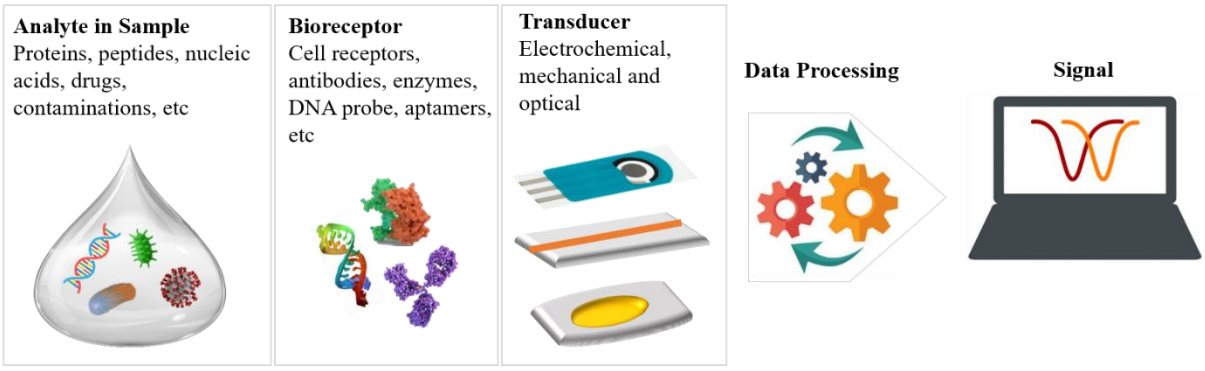

Fig 1. 2. Schematic illustration of biosensor that shows the heterogeneous sample, bioreceptor, transducer, and data processing for signal display.

Among the different types of biosensors, optical technologies have been positioned as powerful tools for facilitating biomedical and clinical research. In particular, surface plasmon resonance (SPR) systems are nowadays considered a mature technology for the analysis of biomolecular interactions, providing real-time and label-free measurements. SPR biosensors are commercially available worldwide, with companies like GE Healthcare, Horiba, Nicoya Lifesciences, Reichert Technologies or Bionavis, among many others (Figure 1.3), offering high-performance instruments with automation and multiplexing capabilities. Such devices are commonly employed in pharmaceutical and biomedical research laboratories for the study, screening, and evaluation of drugs and molecular therapeutics. For example, SPR biosensors can help in identifying and validating biological targets (e.g., proteins, DNA, cell receptors) that interact with potential drugs, enabling the screening of large libraries of compounds for the selection of initial or lead candidates and characterizing the binding properties to the target molecule, such as affinity, kinetics, and specificity.[21–24] This optimization is essential for profiling the efficacy and safety of potential therapies. Furthermore, these biosensors can also be used in mechanistic

studies, investigating how a drug interacts with its target, identifying the binding sites, and understanding the molecular mechanism of action. And finally, SPR instruments can also aid in quality control and bioprocessing, by detecting contaminants or aggregates during purity assessment or monitoring the stability of the drug candidates under various conditions to control their efficacy over time.[25]

Fig 1. 3. Commercially available worldwide surface plasmon biosensors: a) Biacore T200, Ge Healthcare - USA, b) XelPlex, Horiba Scientific - France, and c) Reichert4SPR, Reichert Technologies - USA.

In this regard, SPR biosensors outperform traditional analytical techniques like ELISA or fluorescence-based assays by providing real-time visualization of biomolecular interaction events without the need of incorporating molecular tags and labels, which could interfere with the binding conditions. Furthermore, typical SPR biosensor assays are finalized in about 10 - 15 min, greatly accelerating the evaluation and characterization process. In terms of costs, mid-range SPR instruments can be acquired within a range of $150.000 - $400.000, depending on their multiplexing and automation features. These prices are slightly higher than advanced fluorescence or automated ELISA equipments ($10.000 – $200.000), but they are cost-effective and accessible for the majority of medium and large pharmaceutical companies and established laboratories.

Nonetheless, with the emergence of complex biological therapies, like immunotherapies, the current capabilities and operation characteristics of conventional SPR biosensors might have remained limited. The screening and assessment of novel immunotherapies requires the study of complex cell-cell interactions, involving multiple molecular interactions with certain mobility restrictions, together with a high sensitivity and specificity. New developments in optical biosensor design and fabrication are needed to further expand their application in modern biomedical and pharmaceutical research, conferring them with the ability to perform more reliable and accurate biological studies, and serving

as an alternative or complementary technique to the sophisticated, labor-intensive and time-consuming cell culture procedures and cell analysis techniques.

As response to this endeavor, this PhD Thesis addresses the study and optimization of new optical biosensor technologies and their application in immunotherapy evaluation. The integration of nanostructured materials, such as metals and dielectrics, is a main subject of this research. Novel nanophotonic arrays and biorecognition interfaces are investigated to improve the biosensors' overall performance, sensitivity, and selectivity. In particular, biomimetic functionalization strategies are proposed in this work, mimicking biological processes as closely as possible is the goal of developing nanophotonic sensors which provide more precise and reliable data for evaluating immunotherapy. The need for advanced biosensor technologies that can more accurately measure and track therapy responses is what motivates this study, which will ultimately lead to more individualized and successful therapy design, development, and implementation.

1.2. Nanophotonic sensors: principles and technologies

Nanophotonic sensors working in label-free configuration are generally based on the evanescent wave (EW) sensing principle, which measures changes of the refractive index (RI) of the medium in the vicinity of the sensor surface. An EW is an electromagnetic field generated from a propagating or resonant light wave at the interface of two media with different refractive indices, for example between a metal layer (high RI) and air or an aqueous solution (lower RI).

The propagation of light in EW sensors is essentially due to the total internal reflection (TIR) phenomenon, which is described by the Snell´s Law (Equation 1.1):

$$n_1 \sin\theta_1 = n_2 \sin\theta_2 \qquad (1.1)$$

Where,
θ_1 = Angle of incidence
θ_2 = Angle of refraction
n_1 = Refractive index of dielectric medium (top)
n_2 = Refractive index of dielectric/metallic medium (bottom)

According to Snell´s Law, light will only undergo TIR, if $n_2 > n_1$ and angle of incidence (θ_1) reaches at a critical angle (θ_c). At this point the refraction angle (θ_2) becomes equal to 90°. So the critical angle can be stated as (Equation 1.2):

$$\theta_c = \sin^{-1}\left[\frac{n_2}{n_1}\right] \qquad (1.2)$$

When light undergoes TIR at a dielectric-metallic interface with different RIs, an EW is produced in the interface. The EW does not propagate into the dielectric medium but shows an exponential decay away from the interface. This non-propagating EW intensity decreases with distance from the interface, as described by (Equation 1.3):

$$I_z = I_0 e^{-z/d} \qquad (1.3)$$

Where,

I_z = Intensity of EW at z position from the interface

I_0 = Maximum intensity of EW at the dielectric-metallic interface, where z = 0

d = Decay length of EW intensity

z = Distance from the interface into the dielectric medium

$e^{-z/d}$ = Exponential decay in intensity of EW with increase in distance from the interface

This intensity equation demonstrates that the EW intensity is maximum at the interface, where z = 0 and decaying exponentially with distance (z) which is characterized by the decay length (d). This EW field is confined at a region close to the surface, and its intensity decreases exponentially with distance, limiting its interaction typically in the range of a few hundred nanometers (Figure 1.4). The EW is extremely sensitive to variations of the RI occurring in the local environment near the interface, such as those caused by biomolecules or analytes binding to the sensor surface. These changes affect the characteristics of the EW and the propagating or resonant light, and can be detected, measured, and correlated with the concentration of analytes in the sample.[26,27]

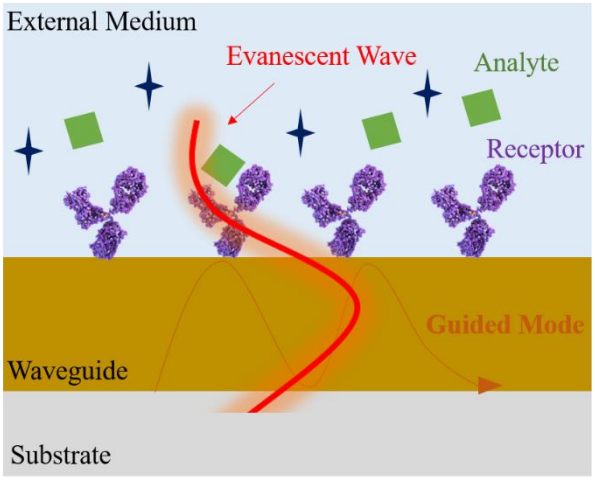

Fig 1. 4. Schematic representation to illustrate the sensing principle of an evanescent wave biosensor. Most common EW biosensors are based on plasmonic, photonics crystal, fiber-optics and silicon photonics technologies:

- **Plasmonic biosensors** can be based on either propagating SPR or localized SPR (LSPR), in which incoming light excites free electron oscillations at a metal-dielectric interface and excites the surface plasmon that generating evanescent field. Common plasmonic materials used in these biosensors include noble metals like gold (Au) and silver (Ag), as well as alternative materials such as aluminium (Al) and copper (Cu).[28] The changes in the refractive index close to the sensor surface are due to molecules binding and changes resonance conditions. These RI changes are measured by monitoring certain properties of the incident or reflected or transmitted light, such as intensity, wavelength, or angle. Plasmonic biosensors offer label-free detection with high sensitivity in real-time, although they require accurate control over the characteristics of metal layer and are restricted to detect relatively large molecules (e.g., proteins and nucleic acids, but no metabolites or small drugs).[29]

- **Photonic crystal biosensors** utilize periodic structures of materials with varying dielectric constants to create a photonic bandgap, which controls light confinement and propagation. This design enables the detection of biomolecule binding through shifts in the resonance wavelength caused by changes in local RI. These shifts are measured by analysing changes in reflected or transmitted light, allowing for label-free and real-time monitoring. Common materials used in these structures include dielectric materials like silicon and silicon nitride, noble metals such as gold and silver for plasmonic effects, and semiconductors like indium tin oxide. These biosensors are potential candidates for multiplexed detection. However, they involve complicated fabrication procedures and potential challenges in achieving a wide range of sensing because of their limited sensitivity and high temperature dependancy.[30,31]

- **Fiber-optic biosensors** utilize optical fibers, typically made of silica or plastic, as the sensing platform, relying on total internal reflection to generate an evanescent field at the core-cladding interface. This allows for interaction with analytes close to the fiber surface while enabling light propagation over long distances for remote sensing. Detection methods commonly involve measuring changes in fluorescence intensity, refractive index, or absorption, with the fiber acting as both the light delivery and collection system. These features make fiber optic biosensors particularly advantageous for in-vivo analysis and challenging sensing environments compared to other evanescent field biosensor technologies. However, it has some limitation such as delicate nature of optical fibers, the potential for signal loss over long distances, and the difficulties in achieving uniform surface functionalization.[32]

- **Silicon photonics biosensors** utilize silicon-on-insulator platforms, typically consisting of silicon-based waveguides on a silicon dioxide substrate. They rely on the interaction between the evanescent field of guided light and analytes near the waveguide surface. Various waveguide geometries are employed, including ring resonators or interferometric systems, like Mach-Zehnder or Bimodal Waveguide interferometers. These structures confine light through TIR in high-index-contrast waveguides. Detection methods commonly involve measuring changes in resonant wavelength, phase, or intensity of the guided light when biomolecules bind to the functionalized sensor surface. Key advantages include ccomplementary metal-oxide-semiconductor (CMOS)-compatible fabrication, enabling high-density integration, miniaturization, and potential for mass production. These are particularly suitable for lab-on-a-chip system applications due to their high sensitivity and multiplexing capabilities. However, they are limited by temperature sensitivity, and relatively complex optical coupling and readout systems.[33]

In this PhD Thesis, our initial focus will be on plasmonic technologies, given their proven high sensitivity and real-time detection capabilities for multiple biomedical applications. Additionally, we will explore the use of new dielectric nanomaterials with photonic resonances as an alternative to plasmonic metals, aiming to overcome some of the inherent limitations of plasmonic sensors while offering similar or better performance.

1.2.1. Nanoplasmonic sensors

Plasmonic systems are based on an optical phenomenon first observed by the American physicist Robert W. Wood in 1902.[34] While studying light diffraction through a metal grating, Wood noticed unexpected variations in the intensity of diffracted light that classical diffraction theory could not explain. He observed sharp decreases or spikes in light intensity at specific wavelengths or angles. These anomalies, known as Wood's anomalies, were later recognized as the result of complex interactions between the grating's surface electromagnetic waves and incident light, marking the beginning of the plasmonic field.[35] In 1907, Lord Rayleigh provided the first theoretical explanation for Wood's anomalies by developing a dynamical theory of gratings, which linked the appearance or disappearance of diffraction patterns to these anomalies. Then, in 1941, Ugo Fano further advanced the understanding of this phenomenon by theorizing that the effects of Wood's anomalies were due to surface plasmons — i.e., waves propagating along the surface of a metal grating.[36] In the 1950s, Pines and Bohm introduced plasmons as quantized plasma oscillations to explain energy losses in metals.[37] In 1957, Rufus Ritchie provided the first theoretical description of surface plasmons. Ritchie explained that the energy loss observed in thin metal films was due to the excitation of surface plasma oscillations. However, the

explicit description of evanescent waves associated with surface plasmons was not part of Ritchie's 1957 work, as this understanding evolved over time.[37]

A significant advancement in plasmonics occurred in 1968 with the development of the attenuated total reflection (ATR) method for exciting surface plasmons on metal films. This breakthrough is attributed to both Erich Kretschmann and Andreas Otto,[37] who independently developed ATR configurations in the same year. Their work made it easier for researchers to study surface plasmons. In 1970, Uwe Kreibig and Peter Zacharias made another important contribution to the field.[38] They modified existing theories to account for the nanoscale size of particles and explained the electronic and optical response of silver and gold nanoparticles in terms of localized surface plasmon excitations. Their work demonstrated that factors such as size, shape, arrangement, medium, and temperature all play crucial roles in controlling the intensity and frequency of plasmonic resonances.[39]

In recent years, the field of plasmonics has grown rapidly, finding applications in biosensing, spectroscopy, nanophotonics, and photovoltaics.[39,40] Researchers have expanded their exploration beyond traditional metallic materials, investigating surface plasmons or similar resonances in alternative materials such as graphene and high-refractive index dielectrics.[41,42] Graphene, with its unique electronic properties, allows for tunable plasmons that can be actively controlled, while dielectric materials like silicon and germanium offer lower loss alternatives, enabling efficient light manipulation at the nanoscale. These advancements highlight the growing interest in non-metallic plasmonic and resonant structures, which provide a broader spectrum of functionalities beyond traditional metallic systems. Today, plasmonic remains a vibrant area of research, with scientists continually working to create new materials, structures, and applications that take advantage of the unique properties of surface plasmons. The journey from Wood's initial discoveries to cutting-edge technologies illustrates how fundamental scientific insights can evolve into transformative innovations.

In the following sections, we will discuss the physical principles underlying nanoplasmonic sensor technologies, focusing on the instrumentation and fabrication processes, along with the state-of-the-art applications of these sensors.

1.2.1.1. Surface Plasmon Resonance (SPR) biosensor

1.2.1.1.1. Physical principles and phenomenon

When light interacts with a metal surface under certain conditions (wavelength, polarization, angle of incidence, etc.), it induces collective oscillations of free electrons known as surface plasmon polaritons (SPPs). SPPs are confined electromagnetic excitations that propagate along the metal-dielectric

interface for a limited distance, with propagation lengths ranging from micrometers (μm) to millimetres (mm). Their propagation length depends on factors like the wavelength of light, the dielectric functions of both metal and dielectric medium, and metal absorption losses (Equation 1.4):[29,43]

$$L_{SPP} \propto \frac{\lambda^2}{Im(\varepsilon_m)} \qquad (1.4)$$

Where,

L_{SPP} = Length of propagation or wave vector along x-axis

λ = Electromagnetic Light wavelength

$Im(\varepsilon_m)$ = Imaginary part of dielectric function of metal

By increasing the wavelength, the SPP modes become less restricted to the surface and reduces the Ohmic losses in metal, resulting in increase in propagation length. Ohmic losses in metals occur due to electron scattering in response to the electromagnetic field. This scattering causes electrons to lose energy, which is converted into heat, resulting in overall energy loss in the metal. For example, in gold or silver, the SPP propagation length is typically a few microns in the visible spectrum. However, by increasing the wavelength to the near-infrared spectrum, this length can be extended to hundreds of microns.[44]

When surface plasmons propagate at a metal-dielectric interface (Figure 1.5a), they create an electromagnetic field near this interface. This field gives rise to evanescent waves that extend into both the metal and the adjacent dielectric medium (Figure 1.5b). These EWs exhibit an exponential decay, typically within a range of 100 nm to 500 nm from the metal surface into the surrounding medium. The SPP is indeed a transverse magnetic (TM) mode, where the magnetic field vector is parallel to the interface and perpendicular to the direction of propagation. The electric field has components both parallel and perpendicular to the interface.

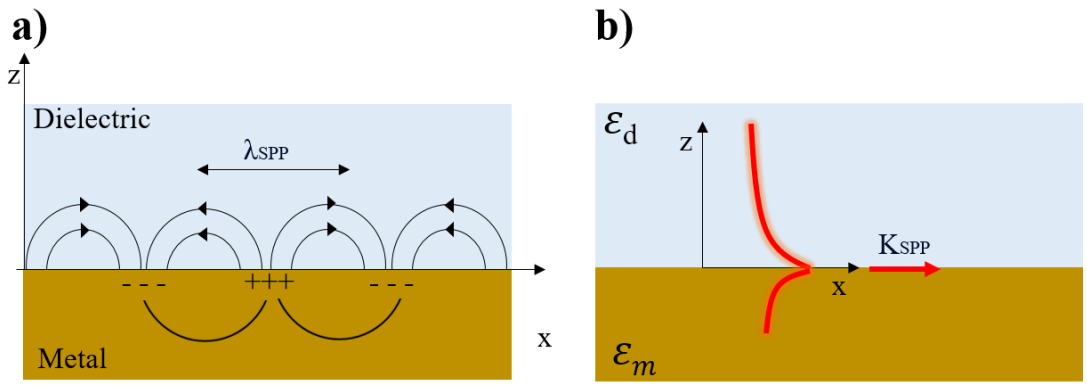

Fig 1. 5. Schematics of a SPP at the interface of a metal and a dielectric showing: (a) the collective charge oscillation at the surface and (b) the transversal evanescent field distribution.

These conditions can be characterized by the EW distribution and its propagation vector, which are described by Maxwell's equations (Equation 1.5):

$$k_X^{SPP} = \frac{\omega}{c}\sqrt{\frac{\varepsilon_m \varepsilon_d}{\varepsilon_d + \varepsilon_m}} \qquad (1.5)$$

Where,

k_X^{SPP} = Wave vector of SPP

c = vacuum light speed

ω = angular frequency

ε_m = dielectric constant of metal

ε_d = dielectric constant of the dielectric medium

The wave vector of SPP indeed depends on the dielectric functions of both the metal and the adjacent dielectric medium. The plasmonic characteristics of metals originate from their distinct optical response and electronic structure upon interaction with electromagnetic radiation. This optical response is primarily determined by the behavior of conduction electrons within the metal, which can be described through the Drude model (Equation 1.6):[45]

$$\varepsilon = \varepsilon_r + \varepsilon_{i,} \qquad (1.6)$$

The dielectric constant (ε) of a material can be expressed as the sum of its real and imaginary components, where ε_r is the real part and ε_i is the imaginary part of dielectric constant. The real part influences the material's capacity to store energy when subjected to an electric field and is related to the material's refractive index. A higher real part of the dielectric function generally corresponds to a higher refractive index, resulting in light propagating more slowly through the material compared to its speed in vacuum. The imaginary component, is associated with energy loss mechanisms within the material, primarily due to absorption and dispersion. As the imaginary part of the dielectric function increases, the material absorbs more energy, resulting in higher losses in terms of heat and leading to a shorter propagation length for electromagnetic waves. Dispersion, which occurs when different wavelengths of light travel at different speeds through the material, is also related to the frequency dependence of the real part of the dielectric function. While dispersion itself does not directly cause energy loss, it can

influence the distribution of light energy and impact the efficiency of energy transfer in various applications, such as optics and photonics.[46]

For SPPs to be excited and propagate at a metal-dielectric interface, the real part of the metal's dielectric function (ε_m) must be negative ($Re[\varepsilon m] < 0$), and its magnitude must be greater than the dielectric constant of the adjacent medium (ε_d), i.e., $|Re[\varepsilon_m]| > \varepsilon_d$. Metals like gold, silver, copper, platinum, chromium, and aluminum meet these requirements in the visible wavelength range (400 nm to 800 nm), with gold and silver being the most extensively used. The main reason for the preference of gold and silver can be attributed to their lower imaginary component of the dielectric function compared to other plasmonic materials,[46] which minimizes energy losses and favors the propagation of plasmonic resonances over longer distances.

The thickness of the metal layer also influences by different parameters of SPPs, including EW penetration depth, dispersion relation, propagation length, and coupling efficiency. In very thin metal films (typically less than 50 nm), SPP modes on both sides can interact, forming coupled long-range and short-range SPPs.[45] As thickness increases, these modes become more independent. Thinner films cause greater deviation from bulk SPP dispersion curves, allowing for more tunability of SPP properties.[47] Propagation length generally increases with metal thickness due to reduced Ohmic losses, but at the cost of decreased electromagnetic field confinement. Coupling efficiency is optimized at specific thicknesses related to the metal's skin depth at the operating wavelength, typically 45-50 nm for gold and 50-55 nm for silver in the visible spectrum.[43] Additionally, thinner metal films often provide higher sensitivity in SPR sensors, but it may reduce signal-to-noise ratio and shorten SPP propagation lengths. Balancing these factors is important for optimizing SPR devices and sensors, with the choice of metal thickness involving trade-offs between field confinement, propagation length, coupling efficiency, and sensitivity, depending on specific application requirements.

1.2.1.1.2. Instrumentation for SPR biosensors

SPPs cannot generally be excited by direct illumination because their propagation vector (k_x^{SPP}) is substantially larger than the wave number of light in the dielectric medium. Specific coupling techniques are therefore required to match the SPP's propagation vector with the parallel component of the light's wave number (k_x^{Light}) at the metal-dielectric interface (Equation 1.7).

$$k_x^{SSP} = \frac{2\pi}{\lambda}\sqrt{\varepsilon}\ Sin\theta = k_x^{Light} \qquad (1.7)$$

Various methods can be employed to couple the light to the metal surface, including prisms, waveguides or gratings,[48] (Figure 1.6).

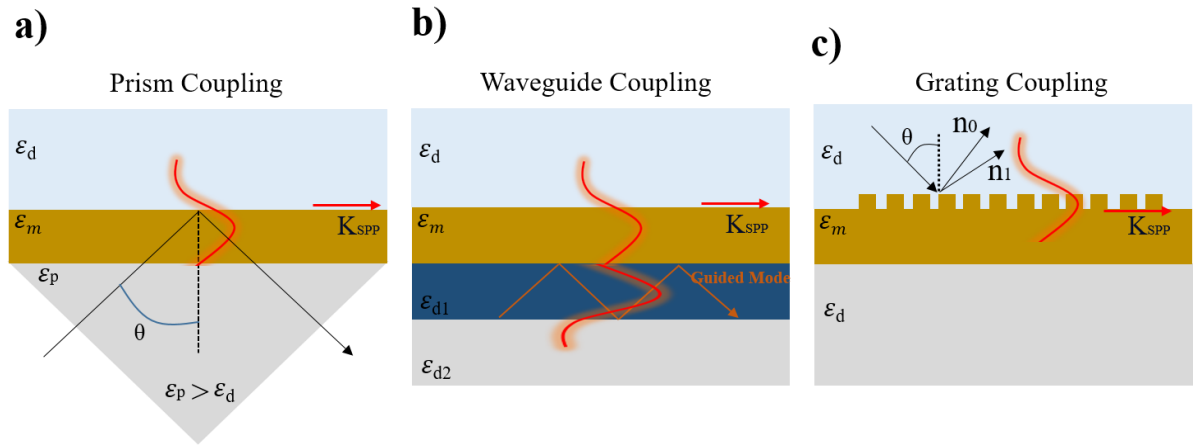

Fig 1. 6. SPR coupling techniques including: a) Prism-coupled Kretschmann configuration, b) Waveguide coupling, and c) grating coupling.

The prism-coupling method, also known as Kretschmann configuration, is the most utilized technique for optical excitation in SPR sensing (Figure 1.6a). In this configuration, light passes through a high RI prism to reach the interface between the prism and the thin plasmonic metal layer. At this interface, TIR occurs, generating EW that excites the plasmonic resonance at the outer metal-dielectric interface.[49] This EW propagates along the interface with a specific propagation vector. By modifying the angle of incidence or the wavelength of the light at a fixed angle, the properties of this wave can be adjusted to match the SPP vector, allowing for precise control of the resonance condition. In Kretschmann configuration, the optimal metal thickness is typically around 50 nm for gold films in the visible spectrum,[50] though this can vary depending on the specific metal used and the wavelength of light employed.

SPPs can also be excited through optical waveguides (Figure 1.6b). In this approach, light is guided through an optical waveguide via total internal reflection. As the guided light reaches the metal layer, it penetrates evanescently through the metal, exciting plasmons on the outer surface.[43] This method can offer advantages in terms of device compactness and integration potential. Another technique for exciting SPPs utilizes grating couplers (Figure 1.6c). Here, light is directed onto a metal grating with a periodic structure that diffracts the incident beam into various orders. By carefully designing the grating period, the wave vector of a diffracted order can be matched to the SPP wave vector, thereby exciting the plasmonic resonance at the metal surface.[51] Grating coupling allows for normal incidence excitation, which can simplify the optical setup in certain applications.

For the SPR visualization and monitoring, the reflected light spectra are acquired. The plasmonic resonance is identified by a dip in spectrum. When the resonance condition is met, photon´s energy is efficiently transferred to the surface plasmons, causing strong light absorption at a specific angle and wavelength. This results in a sharp drop in the intensity of reflected light, creating a noticeable dip in the resonance SPR peak. The characteristics of the SPR peak are key to understand the sensor's performance.

The peak is identified by the specific angle or wavelength where the strongest interaction occurs between the incident light and the surface plasmons, and it is affected by many factors, such as the refractive index of the surrounding medium, the characteristics of the metal film (thickness and composition), and wavelength of incidence light. For example, aluminum exhibits a broader SPR peak that spans the ultraviolet to visible spectrum, typically within the 200 – 400 nm range,[52] in contrast, gold shows a narrower SPR peak in the visible to near-infrared spectrum, around 600 – 800 nm.[53] On the other hand, silver has an even narrower SPR peak compared to gold, typically occurring in visible range between 400–500 nm,[47] (Figure 1.7).

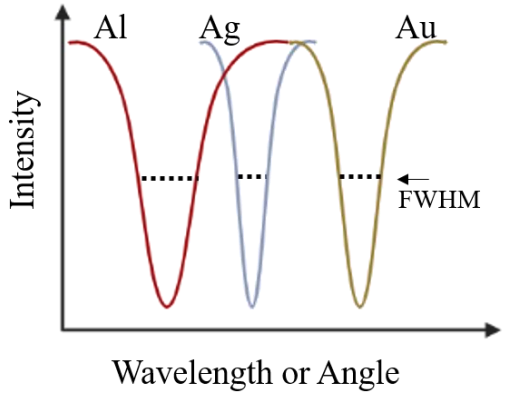

Fig 1. 7. Extinction spectra of aluminium, gold, and silver.

The bandwidth of the SPR is relevant for determining the precision of a sensor, and it is often indicated by the full width at half maximum (FWHM) value. This represents the width of the peak where the curve reaches half of its maximum value. A sharp, narrow peak (smaller FWHM) enables more precise identification of peak shifts, allowing for detection of smaller changes. In contrast, a broader peak complicates the detection of subtle changes.

The FWHM of the SPR peak is influenced by factors like damping effects, metal film thickness, quality, and surface roughness. Damping effects, such as energy loss from electron scattering or electron-phonon interactions, broaden the peak and reduce its sharpness, lowering sensor precision. Metal film

thickness is also critical due to radiation damping, especially ocurring in thicker films.[54,55] Surface roughness adds complexity by increasing light scattering, broadening the peak, and affecting the refractive index at the metal-dielectric interface, thus impacting overall sensitivity.

1.2.1.2. Localized Surface Plasmon Resonance (LSPR) biosensor

1.2.1.2.1. Physical principles and phenomena

With the objective of improving the performance and sensitivity of SPR sensors, last decade's research has focused on incorporating nanostructures that exhibit non-propagating surface plasmon resonances. When an electromagnetic wave interacts with small metallic nanoparticles, it induces non-propagating collective oscillations of the conduction electrons within the nanoparticles. These oscillations occur in the confined region of the nanoparticles, leading to a phenomenon known as Localized Surface Plasmon Resonance (LSPR). For nanoparticles much smaller than the wavelength of the incoming electromagnetic wave, these electron oscillations generate a dipole field, where one side of the nanoparticle becomes negatively charged, and the opposite side becomes positively charged, at any moment (Figure 1.8).

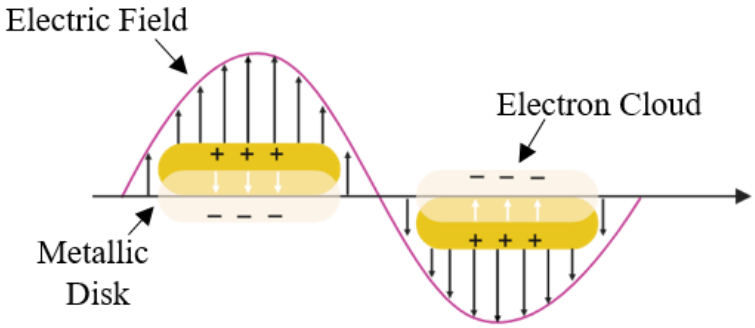

Fig 1. 8 . Illustration of the excitation of localized surface plasmon resonance in metallic disk.

The dipole field influences the resonance effect and the optical properties of nanoparticles by affecting absorption, light scattering, and electromagnetic field strength near the nanoparticle surface.[48] The LSPR phenomenon is directly related to the polarizability of the nanodisk, which can be expressed by (Equation 1.8):

$$a = 4\pi d^3 \frac{\varepsilon_{m\,(\omega)} - \varepsilon_d}{\varepsilon_{m\,(\omega)} + 2\varepsilon_d} \qquad (1.8)$$

Where,

α = polarizability of the metallic disks

d = size of the metallic disk

$\varepsilon_m(\omega)$ = dielectric constant of metallic disk

ε_d = dielectric constant of dielectric media

The strength of the LSPR effect is determined by the polarizability of the nanoparticles, which is influenced by the size of the metallic particle and the dielectric properties of both the metal and the surrounding medium. Polarizability reaches its maximum, resulting in strong resonance enhancement, when the Fröhlich condition is met (Equation 1.9). This occurs when the real part of the metallic dielectric constant Re[ε_m], becomes equal to -2ε_d. Noble metals like gold and silver satisfy this condition within the visible spectrum.

$$\mathrm{Re}[\varepsilon_m(\omega)] = -2\varepsilon_d \qquad (1.9)$$

The Fröhlich condition highlights the impact of a metal nanoparticles resonance frequency depends on their environment. As the dielectric constant of the surrounding medium increases, the resonance frequency moves towards higher wavelengths (red shift).[56,57] Therefore, when molecules bind to the surface of metallic nanoparticles, they alter the local refractive index, causing a shift in the extinction peak wavelength (λ_{max}). The following equation 1.10 represents the shift in λ_{max}:

$$\Delta\lambda_{max} \cong S\Delta n\left[1 - e^{-\frac{2d}{I_d}}\right] \qquad (1.10)$$

Where,

S = sensitivity

Δn = change in RI

d = thickness of effective adsorbate

I_d = decay length of EM field

In addition to that, the extinction wavelength of LSPR can be tuned by choosing different materials, owing to their unique optical properties of metals and their interaction with the light. Metals vary in electron density and mobility, which affect electron oscillation when illuminated. The speed of this oscillation determines the resonance peak displacement, with the frequency of localized surface plasmons influenced by factors such as electron density,[58] effective electron mass,[59] and the surrounding dielectric environment.[60] Higher electron density leads to faster oscillations, while lighter effective electron mass results in higher frequencies. Similarly, to propagating SPR, most common materials used for LSPR sensing are gold and silver, which show strong responses to light in the visible to near-infrared range. Aluminium and gallium are also used, especially for applications in the ultraviolet range.

The ability to tune the LSPR position is influenced not only by the material but also by the size and shape of the nanoparticles.[58] As the nanoparticle size increases, the electrons have more space to move, which typically lowers their natural oscillation frequency, shifting the LSPR peak to longer wavelengths (a red shift). Conversely, a blue shift occurs when electron density increases or the effective mass of the electrons decreases, both of which raise the natural oscillation frequency, shifting the peak to shorter wavelengths. Additionally, changes in nanoparticle shape, particularly changing their aspect ratio (length to width), can also tune the LSPR position. Different shapes, such as triangles, spheres, disks, or rods, create varying distributions of electron density, which affect the oscillation modes of the electrons. In nanorods, for example, the aspect ratio plays a critical role. Longer rods, with a higher aspect ratio, slow the electron oscillations along the length, shifting the LSPR peak to longer wavelengths. In contrast, oscillation across the width occurs more rapidly, resulting in a shift to shorter wavelengths.[61]

Changing the RI of the medium also alters the polarizability of the nanoparticles, resulting in a shift in the LSPR peak. A higher RI slows down the electron oscillation frequency, causing a red shift, while a lower refractive index leads to a blue shift. Unlike propagating SPR, the LSPR's evanescent field is confined to the particle's surface and decays rapidly in the surrounding medium, with a penetration depth of only a few tens of nanometers (nm). This short penetration depth allows LSPR sensors to achieve high-resolution detection, even at the level of individual particles,[62,63,64] (Figure 1.9). By carefully selecting and adjusting factors such as material, shape, and the surrounding medium's refractive index, the LSPR can be tuned to specific wavelengths, making plasmonic nanoparticles highly valuable for applications in sensing, imaging, and photothermal therapy.

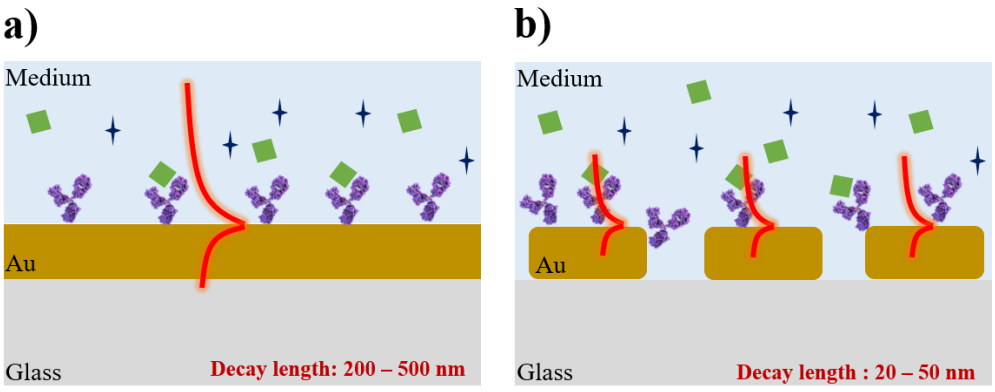

Fig 1. 9. Representation of the differences in the evanescent decay length between: a) conventional SPR biosensor, and b) LSPR biosensor.

1.2.1.2.2. Instrumentation and fabrication

LSPR sensing is simpler than conventional SPR systems, as it does not require bulky coupling mechanisms. The resonance effect is an intrinsic property of metallic nanoparticles, triggered naturally when light interacts with them at the right wavelength.[58] Furthermore, the spectral tunability of LSPR sensors facilitate the combination of different light sources and detectors, based on the needs of the application. For example, light emitting diodes (LEDs) are often used for their affordability and long lifespan, making them suitable for cost-effective and portable systems, while lasers provide high brightness and precision, ideal for sensitive measurements where precise control of the light source is required. Broadband light sources, like deuterium-halogen lamps, offer a wide spectral range, making them useful for full spectral analysis in systems that require multi-wavelength interrogation. On the detection side, spectrometers are commonly used to measure light intensity across wavelengths, tracking LSPR peak shifts with high accuracy. Alternatively, complementary metal oxide semiconductor (CMOS) sensors are employed for imaging-based LSPR systems, where capturing spatial data is essential. These detectors allow real-time monitoring of changes in the refractive index on the sensor surface.[28,41,65–68]

However, one of the main challenges of LSPR sensors compared to conventional SPR is the often complex, laborious, and expensive fabrication of nanostructured sensor chips, which hampers their scalability for industrial production. Plasmonic nanostructures can be fabricated using either top-down or bottom-up approaches (Figure 1.10), both showing advantages and limitations in terms of resolution, costs, and scalability.

Top-down nanofabrication techniques begin with bulk materials and gradually remove or define sections. This approach is useful in large-scale manufacturing because they can yield patterns with high accuracy over relatively big areas. However, top-down methods can be time-consuming, particularly when creating extremely small features, high prices, and considerable material waste.[69] Photolithography, electron beam lithography (EBL), focused ion beam (FIB) lithography and nanoimprint lithography (NIL) are categorized as top-down nanofabrication methods. Photolithography is the most common top-down technique utilized in the fabrication of plasmonic materials (Figure 1.10a). The procedure involves coating a substrate with a photoresist that is sensitive to light, and then exposing it to a light source with a pattern. After that, the exposed or unexposed regions are etched away to create the required nanostructures. More sophisticated methods like ultraviolet (UV) lithography may provide precision of around 50 nm,[70] while extreme ultraviolet (EUV) lithography can reach resolutions below 15 nm.[71] Photolithography techniques have been mostly used to make large-area plasmonic nanohole arrays,[72] and it is also being used for the creation of micro or nanodisks arrays made of multilayer materials such as $Au/SiO_2/Au$.[73]

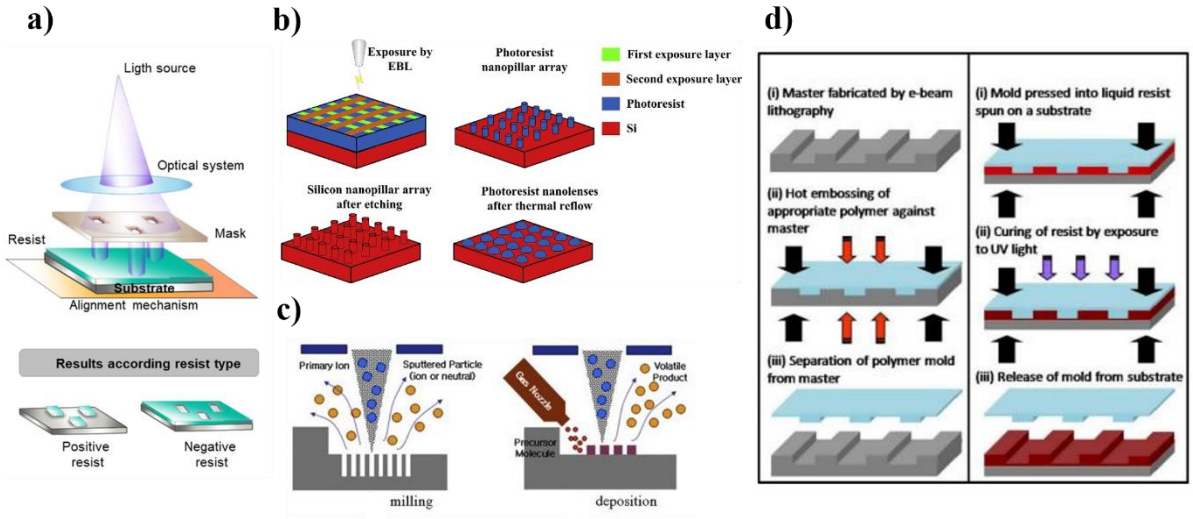

Fig 1. 10. Top-down nanofabrication techniques: a) Photolithography, adapted from reference 75,[74] b) Electron beam lithography, adapted from reference 76,[75] c) Focused ion beam milling and deposition, adapted from reference 77,[76] and d) Nanoimprint lithography, adapted from reference 78.[77]

The EBL process starts with substrate preparation (Figure 1.10b), where the substrate is cleaned and coated with an electron-sensitive resist. Next, a pattern is designed using specialized software. During exposure, a focused electron beam scans the resist according to the pattern. The development stage involves removing the exposed or unexposed areas of the resist using a developer solution. In pattern transfer, the material is either etched away or deposited on the exposed areas of the substrate. Finally, any remaining resist is removed, completing the process.

EBL achieves resolutions of less than 10 nm by writing patterns directly into a resist material using a focused electron beam.[78] EBL is commonly used to create precise nanostructures for plasmonic sensing, nanogap sensors, and quantum dot positioning.[79] On the other hand, FIB procedure (Figure 1.10c), similar to EBL in terms of precision, differs in its direct approach. FIB uses gallium ions instead of electrons to scan the substrate, directly milling or depositing material without needing a resist layer or post-processing, and an integrated electron microscope allows real-time inspection during fabrication. While EBL requires a resist and post-exposure development, FIB offers immediate material modification, making it ideal for tasks like localized milling or deposition.[79] For example, Lin et al. fabricated gold nanodisk arrays on optical fiber tips using EBL for biochemical sensing applications.[80] A comparative study by Konečná et al. examined plasmonic antennas fabricated by both EBL and FIB lithography. They found EBL antennas had more intense and confined LSPR peaks compared to FIB antennas.[81] Despite the great precision, EBL and FIB lithography are not viable for large-scale

production due to their high cost, lengthy procedures, and restriction to small nanostructured regions.[82,83]

NIL is a more modern technique used to create very small patterns on a surface by pressing a patterned mold into a thin layer of material on a substrate (Figure 1.10d). The process begins with creating a mold using precise techniques like EBL. A thin layer of imprint material, such as a thermoplastic polymer or a UV-curable resin, is then applied to the substrate. The mold is pressed into this layer under controlled conditions. For thermal NIL, the material is heated and then cooled while under pressure, whereas for UV-NIL, the resist is cured with UV light. After the resist is solidified, the mold is removed, leaving the pattern on the substrate, which can then be transferred using etching or other methods. The NIL process enables fast and cost-effective production of high-quality optical gratings with features smaller than 100 nm, improving the performance of devices that need precise light control, like spectroscopic tools. Although NIL offers higher throughput and larger patterning areas compared to traditional methods, it faces challenges in resolution due to mold quality and material flow. Additionally, it requires specialized equipment, molds, and often post-processing.[84,85]

On the other hand, bottom-up nanofabrication techniques such as chemical synthesis and self-assembly lithography, construct nanostructures starting at the molecular or atomic level, providing benefits in terms of material efficiency and atomic accuracy. Chemical synthesis involves seed-mediated growth (Figure 1.11a), which is a technique used to synthesize plasmonic nanoparticles, such as gold and silver. The process starts with the creation of small seed nanoparticles (3-5 nm), which are then added to a growth solution containing metal salts and shape-directing agents to control the growth of larger nanoparticles with sizes ranging from ~10 nm to several hundred nm. This method is used to produce structures like gold nanorods, nanostars, and nanoplates. It allows precise control over nanoparticle size, shape, and complexity, with the added benefit of surface functionalization and cost-effectiveness. However, it faces challenges with uniformity, seed stability, reaction complexity, and substrate deposition. This technique is used in applications like LSPR sensing with colloidal gold nanorods and developing tunable plasmonic properties in core-shell particles.[86]

In-situ growth is also a chemical synthesis technique with sub-100 nm resolution, used for directly growing gold nanoparticles on substrates. In this process, metallic ions are chemically reduced directly on the substrate, forming nanoparticles without the need for initial colloidal synthesis (Figure 1.11b). This method enables the integration of plasmonic nanoparticles into devices without requiring additional assembly steps, improving scalability and reducing complexity in the manufacturing process.[87] This method faces limitations in controlling particle size, shape, and distribution, as well as challenges with substrate compatibility, contamination risks, and difficulties in creating complex or multi-material nanostructures compared to other fabrication techniques.

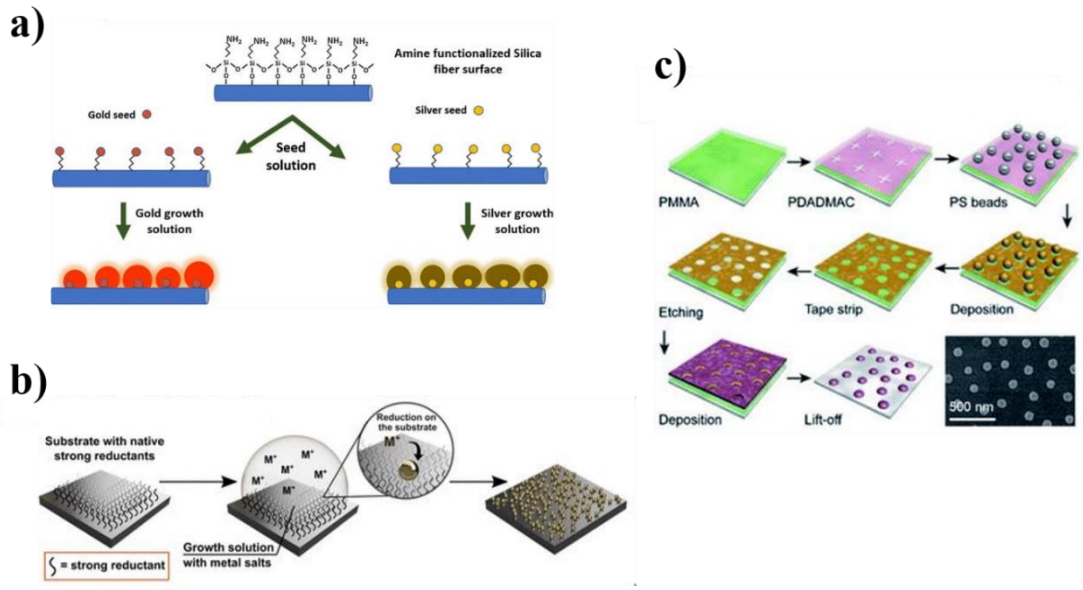

Fig 1. 11. Bottom-up nanofabrication techniques: For chemical synthesis, a) Seed-mediated growth process, adapted from reference 91,[88] b) In-situ growth of metallic nanostructures, adapted from reference 90.[87] c) Hole-mask colloidal lithography, adapted from reference 92.[89]

NSL is another widely used bottom-up approach with potential benefits for substrate nanostructuring. It uses a monolayer of self-assembled nanospheres as a mask to create nanopatterns on a substrate. Typically, a colloidal solution of nanospheres is deposited on the substrate, forming a closely packed array. The metal is then deposited through the gaps between the spheres, and the nanospheres are removed, leaving behind the patterned nanostructures. A specific variation, the Hole-Mask Colloidal Lithography (HCL), introduces an additional resist layer. The nanospheres are deposited on top of the resist, and plasma etching is used to shrink the nanospheres, creating well-defined holes in the resist layer. Material is then deposited through these holes, and after removing the resist and nanospheres, precise nanostructures are left on the substrate (Figure 1.11c). HCL allows for more control over the size and spacing of nanostructures, making it ideal for applications like LSPR sensors. Compared to other methods, HCL is more affordable, simpler, and scalable, with resolutions typically between 20 and 200 nm.[122,123] While it has lower resolution and accuracy than EBL or FIB, HCL is a flexible method that can create large-area nanopatterns.

Ultimately, the choice of nanofabrication method depends on the specific needs of the plasmonic application, and often a combination of different techniques is used to maximize benefits.

1.2.2. Figure of merits for of nanoplasmonic biosensors

The performance of both SPR and LSPR sensors is mainly evaluated by their capacity to detect variations in the RI at the interface. In both sensor technologies, the variations can be monitored by interrogating the shift of the reflectivity dip in the spectrum (Figure 1.12a). SPR sensors typically operate based on either angle (θ) or wavelength (λ) interrogation, where a peak shift is observed in response to RI changes.[68] For LSPR sensors, the shift is typically observed as a wavelength displacement. The shift in peak position upon dielectric changes in the environment can be defined as Δn (Figure 1.12b).

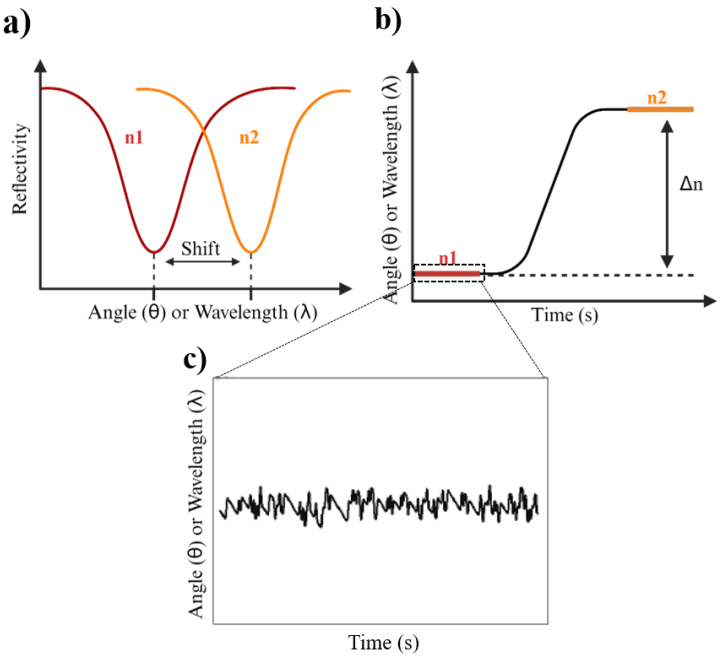

Fig 1. 12. a) Illustration of spectral shift in surface plasmon resonance peak interrogated with angle (θ) or wavelength (λ), b) Real-time sensogram changes in environment (Δn), and c) Background noise level of a sensorgram monitored over the time.

In both cases, the sensitivity (S) of the sensor is defined as the change in the SPR angle or LSPR wavelength per refractive index unit (RIU) change (Equation 1.11):

$$S = \frac{\Delta\,(\theta,\lambda)\mathrm{SPR/LSPR}}{\Delta\,\mathrm{n}} \qquad (1.11)$$

The resolution, on the other hand, refers to the smallest change in the measured parameter that can be accurately detected, also known as Limit of Detection (LOD). This is influenced by the bandwidth of the plasmonic peak (determined by the FWHM) and the level of noise present in the system (Figure

1.12c). A commonly used metric to evaluate overall sensor performance is the Figure of Merit (FOM), which is the ratio of sensitivity to the FWHM (Equation 1.12):

$$FOM = \frac{S}{FWHM} \qquad (1.12)$$

This equation applies to both SPR and LSPR sensor and illustrates that a higher sensitivity and narrower peak lead to a higher FOM, meaning better sensor performance. Additionally, the relationship between noise and LOD can be expressed as (Equation 1.13):

$$LOD = \frac{3\sigma}{S} \qquad (1.13)$$

Where,
σ = standard deviation of the background noise
S = sensitivity (the slope of the calibration curve).

This equation illustrates that as the noise level increases, the LOD rises, reducing the system's sensitivity to low analyte concentrations.

Several factors influence the noise level, including the quality of the plasmonic peak, which is reflected in its FWHM and high-quality instrumentation. A narrower FWHM indicates a better quality peak with lower noise. Additionally, precise temperature control, and effective data processing techniques can also contribute to reducing noise levels.

1.2.3. State of the art and applications of nanoplasmonic biosensors

Along the last two decades, the research in nanoplasmonic biosensors has been directed, on one hand, to enhance their analytical performance and sensitivity, through the design and fabrication of sophisticated nanostructured sensors, and on the other hand, to their integration in compact devices and application in the clinics, especially as point-of-care diagnostic systems.

Within the first segment, advances in the design of new nanostructured devices have focused on achieving superior performance, particularly in terms of sensitivity, for applications such as single-molecule sensing or specialized uses, like chirality detection. Advances in nanofabrication techniques, including the use of Fano resonances and metasurfaces, have improved optical properties. Fano resonances, with their sharp and asymmetric spectral features, are used in nanostructures like metal-insulator-metal waveguides and nanoparticle arrays, enabling highly sensitive detection of

biomolecules.[92,93] For example, Fano resonance-based sensors have been shown to achieve sensitivities up to ten times greater than traditional sensors, making them effective for detecting trace amounts of biomolecules or gases.[92]

Additionally, metasurfaces are emerging platform for biosensing, offering significant advantages over traditional methods. Recent advancements include bound states in the continuum (BIC) metasurfaces,[94] and versatile designs that integrate multiple sensing modalities into a single device.[95] Portable metasurfaces sensors are being developed for point-of-care diagnostics, while machine learning is improving data analysis. Dielectric metasurfaces enable hyperspectral imaging from single images, and graphene-based metasurfaces show potential for terahertz sensing with refractive index sensitivities over 3000 nm/RIU and detection limits reaching the nanomolar range.[96,97,98,99,100] These innovations are paving the way for highly sensitive, compact biosensors in a wide range of applications. However, several challenges hinder their widespread adoption in real-world settings. One major issue is scalability and cost. Traditional fabrication methods, such as EBL and FIB lithography, are unsuitable for large-scale production due to their low throughput, high cost, and limited patterning areas.[101,102] While newer techniques like deep-ultraviolet lithography and nanoimprint lithography offer greater scalability, but they still face difficulties in achieving the precision required for high-performance metasurfaces.[103]

Another barrier for nanoplasmonic biosensors is the reliance on expensive equipment and large instruments, such as advanced spectrometers or microscopes, which restrict their practicality in field settings. In this regard, our group has made strides in this area by developing a compact setup for both surface plasmon resonance SPR and LSPR sensing (Figure 1.13). Our device combines nanoplasmonic sensors with microfluidics and a custom-designed software, resulting in a miniaturized platform less than 20 x 20 cm. This setup features a white light source, a small spectrophotometer, and automated open-source software for user-friendly operation and data analysis. By enabling real-time detection in small sample volumes, our integrated system demonstrates great potential for practical applications in point-of-care implementation, addressing many barriers to the real-world use of nanoplasmonic biosensors.[48]

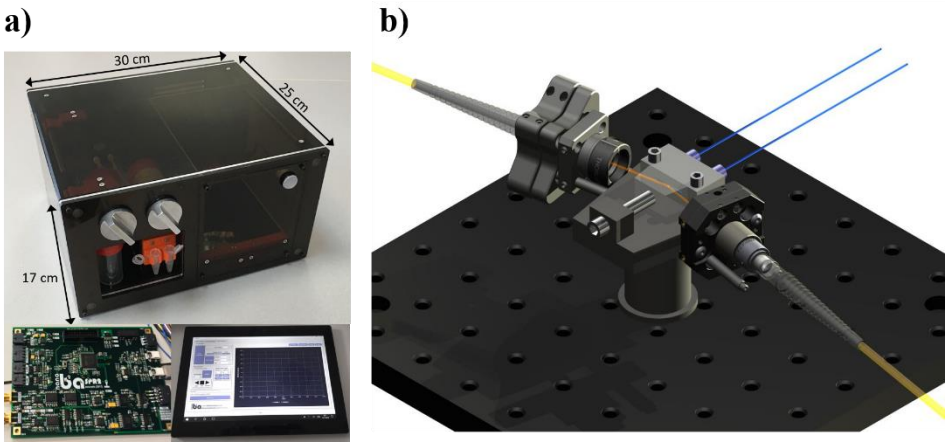

Fig 1. 13. Compact set-up developed in our group for: a) Surface plasmon resonance, and b) Localized surface plasmon resonance.

Finally, in terms of applications, nanoplasmonic biosensors have shown great potential for a variety of diagnostic applications, demonstrating high sensitivity and specificity in detecting clinical biomarkers such as proteins, nucleic acids, and pathogens in human body fluids. Their ability to identify low-abundance biomarkers and differentiate between closely related molecular entities makes them particularly valuable for early detection and disease monitoring.[48,104] Besides, nanoplasmonic biosensors offer rapid and reliable analysis, with applications extending to early cancer diagnostics, infectious disease detection, food safety, and environmental monitoring.[105,106] In our group, we account with an extensive experience in developing and validating clinical applications for nanoplasmonic sensors. For instance, a nanoplasmonic biosensor was demonstrated for tumor-associated antibody detection in early colorectal cancer diagnosis, achieving detection limits around 1 nM in blood plasma samples without complex sample processing.[107] Another breakthrough includes a biosensor for drug allergy diagnosis using gold nanodisks functionalized with dendrimer-based conjugates. This platform detects specific antibodies with a detection limit of 0.6 ng/mL with no sample pretreatment, making it ideal for rapid testing and confirmation.[108] Additionally, a nanoplasmonic biosensor device has been developed for monitoring the anticoagulant drug acenocoumarol in blood plasma. Utilizing gold nanodisks, this device offers real-time quantification with high sensitivity and low sample volume requirements, showing great potential for point-of-care, personalized dosage management.[109]

These recent developments highlight the versatility and clinical potential of nanoplasmonic biosensors across diverse diagnostic needs. Nonetheless, limitations arise when addressing the application of these technologies to more complex biomedical studies, like immunotherapy evaluation, which require the monitoring of cell interactions and accurate detection of biomolecules at low concentrations in small sample volumes. In this PhD thesis, we propose different complementary solutions for this challenge:

(i) the design and development of novel nanophotonic sensors with improved sensitivity and resolution together with biocompatible properties for on-chip cell-based assays, and (ii) the implementation of innovative biofunctionalization methods that enable reliable and nature-mimicking assays in a label-free and real-time format. In the following sections, an overview on these two topics is provided.

1.2.4. Dielectric materials as nanophotonic resonators

An important advancement in nanophotonics has been the recent discovery of EM resonances in high-refractive index dielectric nanostructures. Historically, research on light-matter interactions focused primarily on plasmonic (metallic) materials due to their powerful surface plasmon resonances. However, the high Ohmic losses of metals, particularly in the visible spectrum, prompted an exploratory shift toward other high refractive index materials, such as titanium dioxide (TiO_2), germanium (Ge), and silicon (Si). Between 2010 and 2012, studies by Evlyukhin and colleagues demonstrated that high-refractive-index dielectric nanoparticles could support both electric and magnetic resonances in the visible spectrum, a groundbreaking discovery showing that dielectric particles can mimic the electromagnetic responses of plasmonic nanostructures.[110,111]

Around the same period, García-Etxarri and his team published a pivotal study showing that silicon nanospheres could simultaneously support electric and magnetic resonances, leading to directional scattering effects. This work emphasized the potential of high-index dielectrics for manipulating light at the nanoscale.[112] In 2013, Kuznetsov and colleagues provided experimental evidence of magnetic dipole resonances in silicon nanoparticles using dark-field optical spectroscopy, confirming earlier theoretical predictions and opening up new avenues for all-dielectric nanophotonics.[113] Simultaneously, Gómez-Medina and his team developed a theoretical framework to describe the electric and magnetic dipolar response of high refractive index nanospheres, providing a solid analytical foundation for understanding the electromagnetic behaviour of these particles.[114] Building on these foundational discoveries, about a decade ago, researchers began exploring the applications and extensions of high-index nanoparticles. In particular, Fu and colleagues demonstrated in 2013 that silicon nanoparticles could be utilized for low-loss electric and magnetic field-enhanced spectroscopy, further expanding the possibilities of this technology.[42]

The EM resonances in high-RI dielectric nanoparticles can be understood using Mie theory, which describes the scattering of electromagnetic waves by spherical particles. According to Mie theory, the scattering efficiency of a dielectric particle is determined by the size parameter (ratio of particle size to the wavelength) and the refractive index contrast between the particle and its surrounding medium. Based on this theory, all-dielectric nanostructures exhibit optical responses comparable to the

nanoplasmonic phenomenon, generating dipolar resonances (electric and magnetic) that display less heat losses.[115]

Light interacts with silicon nanostructures in complex ways that involve both propagation and generate resonant modes. The electric mode is caused by the charge polarization within the nanostructure, generated by the electric field of incident light (Figure 1.14a). This mode varies with the diameter (d) of the nanostructure, which affects the electric field distribution and charge oscillations. These charge oscillations create a magnetic current loop within the nanostructure, helping to minimize heat losses in the surrounding environment. The magnetic mode arises from the displacement of current inside the nanostructure, inducing a magnetic dipole moment perpendicular to the electric mode (Figure 1.14b). To generate a magnetic dipole mode in a dielectric nanoresonator, the height (h) of the nanoresonator must be sufficient to allow enough retardation in the electric field at the top and bottom surfaces. It has been demonstrated that a height larger than 100 nm is necessary for dielectric silicon nanoresonators to support these magnetic dipole modes.[116] The induced electric and magnetic fields are perpendicular to each other and align with the direction of wave propagation, generating an electromagnetic wave (Figure 1.14c).

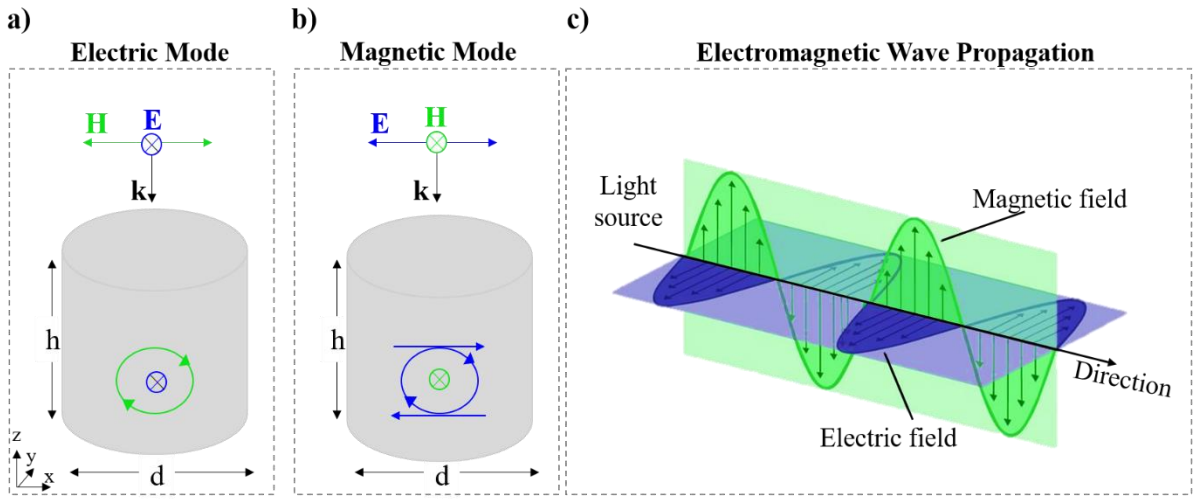

Fig 1. 14. Schematic illustration of electric and magnetic modes in all-dielectric nanoresonator:
a) Electric mode induces the magnetic current loop (green circle) in a result of collective charge polarization in nanoresonator. b) The magnetic mode as a result of electrical displacement current loop (blue circle). Above the structures, the polarizations of the matching incident plane-wave are illustrated. c) Illustrates electric and magnetic field in an electromagnetic wave.

Maxwell's equations are fundamental to understanding light scattering interactions in Mie theory, which describes how spherical particles scatter light.[117] Mie theory uses two main scattering coefficients, a_n for electric mode coefficient (Equation 1.14) and b_n for magnetic mode coefficient (Equation 1.15) to quantify how light interacts with these particles. These coefficients are determined by the particle's size, its refractive index, and the refractive index of the surrounding medium. They indicate the strength and type of resonances that occur when light interacts with the particle, which can be described by the following equations (Equations 1.13 and 1.14):

$$a_n = \frac{m\varphi_n(mka)\varphi_n'(ka) - \varphi_n(ka)\varphi_n'(mka)}{m\varphi_n(mka)\varepsilon_n'(ka) - \varepsilon_n(ka)\varphi_n'(mka)} \qquad (1.13)$$

$$b_n = \frac{\varphi_n(mka)\varphi_n'(ka) - m\varphi_n(ka)\varphi_n'(mka)}{\varphi_n(mka)\varepsilon_n'(ka) - m\varepsilon_n(ka)\varphi_n'(mka)} \qquad (1.14)$$

Where,

m = relative refractive index of the particle

k = 2 π / λ (wavenumber of surrounding medium)

a = radius of the round-shaped particle

φ_n, ε_n and φ_n', ε_n' are Riccati-Bessel functions and their derivatives, respectively, which describe the scattering of electromagnetic waves. These complex coefficients, a_n and b_n, are responsible for expressing the amplitude of the scattered light in both electric and magnetic fields, respectively.

The first-order coefficients (a_1 and b_1) represent dipole resonances, with a_1 corresponding to the electric dipole and b_1 to the magnetic dipole. Higher-order terms, such as a_2 and b_2, describe quadrupole resonances, and this pattern continues for higher multipoles. Large values of these coefficients indicate strong resonances, meaning the particle scatters or absorbs light effectively at certain wavelengths These resonances are highly sensitive to changes in the particle's size, shape, and the material's refractive index. Larger particles tend to exhibit higher-order multipolar resonances, which shift to longer wavelengths as particle size increases. Similarly, a higher refractive index contrast between the particle and the surrounding medium enhances light confinement, leading to stronger, sharper resonances.[115] As the refractive index of the particle increases, the resonance wavelengths also shift to longer wavelengths. Non-spherical particles introduce additional complexity, supporting multiple resonances and exhibiting anisotropic scattering, where the direction of light scattering depends on the particle's orientation.[118]

Resonances are highly sensitive to changes in the refractive index of the surrounding medium because the resonance condition depends on the size parameter, x = (2 π m a) / λ. As the refractive index ´m´

changes, the size parameter shifts, altering the resonance conditions. Variations in the refractive index contrast between the particle and its medium affect electromagnetic field confinement, influencing the distribution of fields both inside and outside the particle. Additionally, changes in the medium's refractive index shift the effective wavelength, modifying the phase accumulation within the particle and further influencing resonance behavior.[113,119]

Resonance sensitivity is typically higher for higher-order modes (larger n in a_n and b_n) and for resonances where a larger portion of the electromagnetic field extends outside the particle.[119] This is particularly true for particles with sizes comparable to the wavelength of light, making them highly responsive to environmental changes. The ability to predict and control resonance behavior, and how it responds to environmental changes, makes these coefficients invaluable for applications such as sensing, imaging, and photonic devices.[120,121] By carefully analyzing and manipulating Mie coefficients, we can fine-tune the optical properties of nanoparticles for a variety of technological applications, particularly in areas requiring precise light manipulation.

The refractometeric sensitivity of all-dielectric nanoresonators shares similarities with metallic plasmonic resonances, but with distinct underlying mechanisms. In metallic nanostructures, LSPR is driven by the collective oscillation of free electrons, resulting in strong localization of electromagnetic fields near the particle surface. In contrast, all-dielectric nanoresonators exhibit Mie resonances, where the interaction of light with the dielectric material induces electric and magnetic multipole modes.[122] These modes confine electromagnetic fields in and around the nanostructures, particularly near the boundaries where the refractive index contrast between the dielectric material and the surrounding medium is greatest.[123] The strength of the field enhancement in the near-field makes both types of resonances highly sensitive to changes in the local refractive index.

All-dielectric nanoresonators offer key advantages for refractometeric sensing, including sharper resonance peaks due to lower losses compared to metals, which enhances sensitivity to small refractive index changes. Additionally, they support higher-order multipolar resonances, enabling a wider range of resonant modes and more complex light-matter interactions, unlike the primarily dipolar nature of LSPR.[121,124] The ability of all-dielectric nanoresonators to exploit both dipoles, while minimizing heat losses, makes them promising alternatives to metallic counterparts.[125] Silicon, in particular, is widely used in nanophotonic due to its high refractive index, availability, compatibility with microelectronics, and cost-effective production methods.[111,126,127,128] Both theoretical and experimental studies have demonstrated that the optical response of silicon nanostructures is highly sensitive to environmental changes, making them a potential candidate for low-loss photonic technologies and sensing applications.[125]

However, despite their potential, the development of dielectric nanostructures for sensing remains mostly at the proof-of-concept stage, with many experiments relying on expensive fabrication techniques such as EBL and high-end instrumentation. Most of these efforts have focused on the near-infrared (NIR) and infrared (IR) regions. Early demonstrations, like laser-ablated silicon nanosphere dimers,[129] and more recent work on silicon nanodisk arrays by Bontempi et al.,[130] have highlighted the sensitivity of these structures to refractive index changes. Silicon nanostructures have even been integrated into lab-on-chip (LOC) devices for proof-of-concept biomarker detection.[116] Despite these promising results, the reliance on costly equipment and focus on NIR-IR wavelengths limit the broader scalability and accessibility of these technologies. Nevertheless, the low optical losses, high sensitivity, and biocompatibility of all-dielectric nanostructures make them attractive for developing next-generation label-free nanophotonic biosensing systems.[116]

Given these challenges, our aim is to explore the use of silicon nanostructures in the visible range, aiming to integrate these structures into portable and affordable sensing devices, harnessing the advantages of dielectric nanostructures (low optical losses and high sensitivity) for more practical and commercially viable applications. Also, we will attemp fabrication of sensors using large-scale, cost-effective techniques, which will help reduce production costs, expand the range of potential applications, and facilitate the deployment of these sensors in real-world scenarios.

1.3. The biorecognition interface

Beyond the design of the nanosensor transducer, the biorecoginition interface is a key parameter in biosensors development, determining the accuracy and reliability of the device for biomedical applications. The interface consists of a specific biological receptor that selectively detect and capture the target analyte, typically immobilized on the sensor surface through chemical procedures. The most commonly used biological receptors in nanophotonic biosensors include antibodies for the detecting proteins, peptides, or small molecules, and single-stranded DNA probes for nucleic acid targets. Although other molecules can also be used, such as cell receptors, aptamers or molecularly imprinted polymers (MIPs).[131] The selection of the biorecognition element depends on the nature of the target analyte, the affinity and specificity required for the detection, and the robustness needed for the biosensor to function reliably in various environments (e.g., laboratory conditions or remote locations). This bioreceptor layer plays an important role in determining the sensor's sensitivity, especially when detecting low concentrations of the target biomolecule.[132–134]

Together with the selection of the optimum bioreceptor, the surface biofunctionalization strategy is crucial to ensure maximum sensitivity, selectivity, and reproducibility of the biosensor. Three main factors must be considered: the stability and robustness of the bioreceptor immobilization, the density

and orientation of biorecognition molecules, and the prevention of non-specific adsorptions on sensor surface.

The stability and robustness of bioreceptor immobilization are essential for maintaining functionality and ensuring long-term sensor performance. A reliable immobilization method secures the bioreceptors in place, preventing their loss during use and preserving their activity. This directly impacts several key factors: sensor longevity, stable immobilization extends the sensor´s operational life; reproducibility, consistent immobilization allows more reliable and repeatable results; and sensitivity, properly immobilized bioreceptors retain their binding capabilities, enhancing overall sensor sensitivity.[105] The bioreceptor interface plays a crucial role in ensuring the biosensor's reliability and reproducibility over time and across varying conditions (e.g., pH, concentrations). The stability of the biorecognition layer ensures the sensor functions effectively during each use and through the regeneration process. Regeneration, which involves removing the target molecule post-detection without affecting the immobilized bioreceptor layer, requires the biorecognition layer to remain functional and stable after multiple uses.[135]

Equally important is the density and orientation of biorecognition molecules on the sensor surface. A higher surface density of bioreceptors increases the number of available binding sites, potentially improving sensitivity However, this must be carefully regulated to avoid steric hindrance, especially with larger analytes, which could impede efficient binding. Proper orientation ensures that the active sites of the bioreceptors are accessible to the target analytes, allowing for optimal interaction. By optimizing both the density and orientation, binding efficiency is maximized, leading to improve the signal-to-noise ratio, and increased overall sensitivity of the biosensor.[136,137]

Also, the prevention of non-specific adsorption is critical for ensuring accurate and specific detection. In biosensors, especially those operating in a label-free format, non-specific adsorption of molecules on the sensor surface can lead to false-positive signals, compromising the reliability of the results. To maintain specificity, the bioreceptor layer must effectively differentiate target biomolecules from other components in the sample. Hydrophilic surface coatings are often used to reduce non-specific binding, preventing the unwanted adsorption of non-target biomolecules and ensuring that only the target analyte is detected.[138]

Designing the biorecognition layer requires selecting suitable recognition elements tailored to the target analyte, optimizing the surface to maximize binding efficiency while minimizing non-specific interactions, and ensuring biocompatibility and stability under operational conditions. Additionally, integrating effective signal transduction mechanisms is essential for biosensor performance. In the following sections, we will briefly review the state of the art in nanophotonic sensor

biofunctionalization strategies and introduce the development of innovative approaches with significant potential for applications in immunotherapy evaluation.

1.3.1. Biofunctionalization through chemical matrices

Traditional functionalization strategies for attaching bioreceptors to sensor surfaces typically involve methods such as physical adsorption and covalent binding. Physical adsorption, while simple and effective, often suffers from limitations like low stability and uncontrolled orientation of the bioreceptors, which can hinder their ability to bind analytes.[139] To improve stability, bioreceptors can also be embedded within polymer matrices, which help preserve their activity but may introduce challenges related to analyte diffusion and mass transport.[134,135] Another common approach widely used in gold-based sensors is direct chemisorption of thiol (SH)-functional bioreceptors, such as thiolated DNA probes, thiol-modified aptamers, or antibody fragments with exposed thiols. This method can provide better control over the orientation of bioreceptors, potentially improving their binding capacity, although they require an in-depth optimization of the probe density by including lateral spacers.

To address some of the limitations described above, self-assembled monolayers (SAMs) offer an attractive method for the covalent immobilization of biomolecules on various sensor surfaces. This biofunctionalization strategy relies on thiolated organic molecules (R-SH) that self-organize onto sensor surfaces, forming a tightly packed and ordered matrix.[140,142] These molecules typically consist of three components: a head group, which interacts with the surface; an alkyl chain that provides structural support; and a tail or external group that offers functionality to the SAM, such as facilitating biomolecule attachment (Figure 1.15). SAMs provide exceptional versatility in sensor biofunctionalization, allowing modification of a wide range of materials beyond gold surfaces. The adaptability of SAMs stems from the diverse functionalization strategies they support. For example, SAMs of alkanethiols on gold and alkoxysilanes on silicon-based sensors create well-organized scaffolds for immobilizing biomolecules.[143,144] These chemical matrices can be easily tailored to adjust grafting density, incorporate affinity tags or linkers, and enhance resistance to fouling.[145–147] Additionally, the versatility of SAMs extends to other materials through salinization, enabling the functionalization of surfaces like glass, metal oxides, and polymers. This broadens their applicability across various sensor platforms, making SAMs a powerful tool for biofunctionalization in numerous sensing technologies.[148]

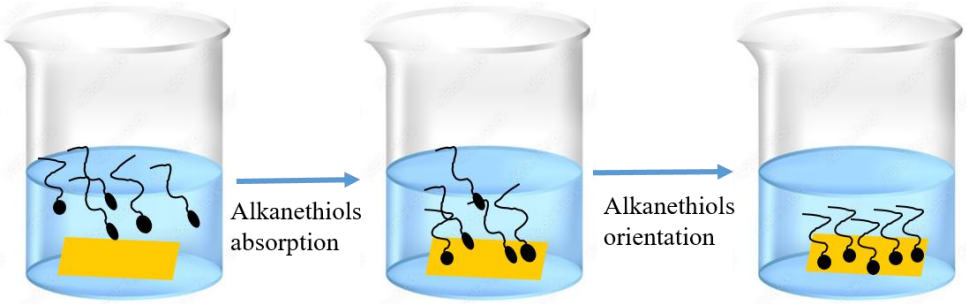

Fig 1. 15. SAM formation on an immersed gold-coated substrate.

One key challenge in biosensor applications, especially for point-of-care testing, is reducing non-specific protein adsorption, which can interfere with sensor accuracy. To address this, hydrophilic moieties, such as polyethylene glycol (PEG), are commonly incorporated, as they create a hydration layer that minimizes non-specific adsorption. Additionally, zwitterionic compounds are used to modify the sensor surface's net charge, preventing unwanted electrostatic interactions that could attract non-target molecules. While these modifications significantly improve the sensor's antifouling properties, completely eliminating the need for sample pre-treatment in undiluted media remains difficult.[149] To further enhance sensor performance, chemical matrices can be fine-tuned by blending compounds with reactive and unreactive functional groups. This enables precise control over the density of active sites for bioreceptor immobilization and the distribution of functional groups on the sensor surface. Such control allows for optimal bioreceptor orientation, spacing, and accessibility, which in turn improves the sensor's specificity and overall performance for targeted biosensing applications.[143]

To immobilize protein bioreceptors, such as antibodies or cell receptors, on SAM-functionalized sensor surfaces, the most common approach is amine coupling (Figure 1.16). In this method, carboxyl groups in the SAM's chemical matrix are cross-linked to the primary amine groups on the proteins.[150] This technique has several advantages, including the formation of stable covalent bonds, high reaction yields, versatility across a wide range of proteins, simplicity, and compatibility with various SAMs and sensor surfaces. However, amine coupling has limitations, particularly in controlling the orientation of immobilized proteins. Since amine groups are randomly distributed on the protein surface, this can lead to non-oriented attachment through critical sites, potentially reducing protein activity.

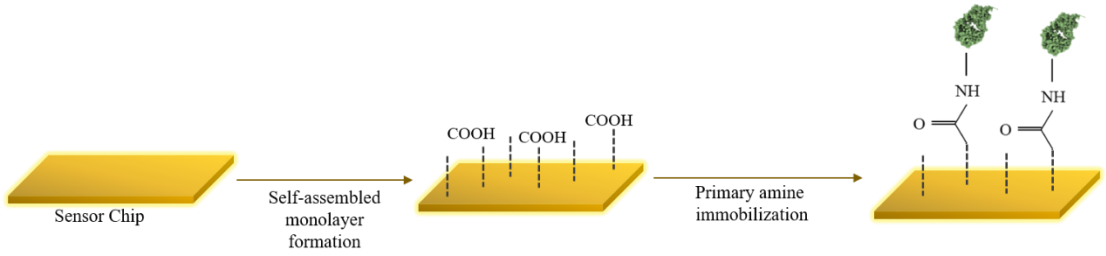

Fig 1. 16. Illustration of covalent binding procedure.

Another widely used method for immobilizing bioreceptors is biotin-avidin affinity-based immobilization (Figure 1.17). This approach offers advantages such as strong and controlled bioreceptor orientation, versatility across various bioreceptor types, preservation of bioactivity, and the potential for multiplexing. Despite these benefits, biotin-avidin immobilization introduces complexities, including multiple preparation steps, increased surface thickness, and higher costs.[151] While the biotin-avidin bond is strong, the system's overall stability is dependent on the underlying SAM and the method of avidin attachment. Compared to direct covalent immobilization, biotin-avidin can provide better orientation control, but the added complexity makes the choice of method dependent on the specific needs of the biosensor application. Nevertheless, for both strategies it is necessary to optimize many factors that influence the efficiency of surface attachment (e.g., pH, concentration, ionic strength, among others).[133]

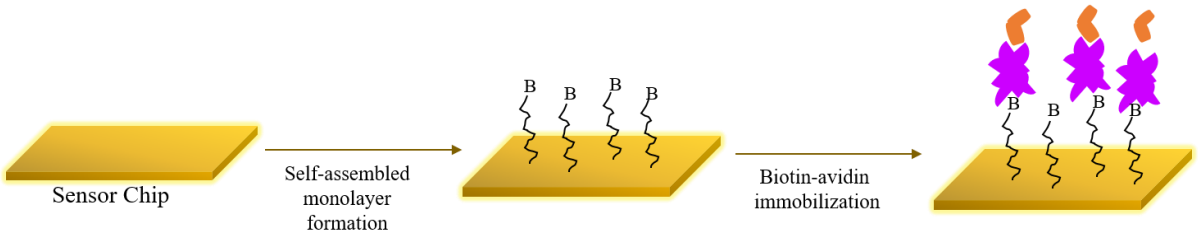

Fig 1. 17. Illustration of biotin-avidin binding procedure.

While chemical matrices are widely used in biosensor functionalization due to their versatility and ease of use, one notable limitation is the lack of lateral mobility for immobilized bioreceptors, which can hinder the formation of clusters necessary for effective biological interactions. This limitation is particularly important in applications involving cell-cell interactions, where the dynamic reorganization of surface molecules plays an important role in facilitating proper function.[143] To that, novel strategies can be investigated such as the use of functional lipid bilayers as artificial cell membranes. These lipid

bilayers offer several advantages, including lateral mobility of incorporated biomolecules, the ability to form dynamic clusters, tuneable composition, and the integration of native membrane proteins.

1.3.2. Biofunctionalization through lipid membranes

Lipid membranes are utilized in various biomedical applications, such as drug delivery systems,[152] biosensing technologies,[131] and artificial cell development.[153] These synthetic or semisynthetic membranes mimic the natural cell membranes while offering the capability to tailor their functionality and interface for the objective of the study. The lipid membrane structure is composed of phospholipid molecules, which are hydrophilic at the heads and hydrophobic at the tails. These molecules arrange themselves into a bilayer, with the hydrophobic tails positioned towards each other and the hydrophilic heads facing either the bulk water or the inside of the closed structure (Figure 1.18).

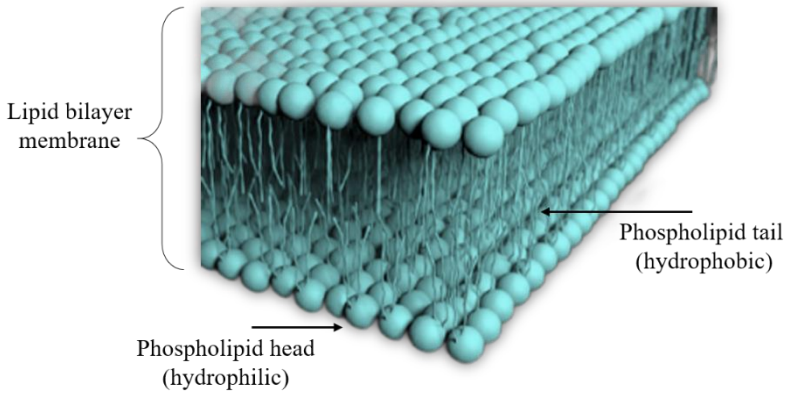

Fig 1. 18. Representation of phospholipid bilayer membrane.

The use of model lipid membranes deposited on solid supports has gained significant popularity in biosensing applications, particularly for studying the fundamental mechanisms of cell membranes, protein and ion transport, and cell-cell interactions. Several lipid membrane models have been developed, including supported lipid bilayers (SLBs),[154] hybrid bilayers,[155] suspended lipid bilayer membranes,[156] polymer-cushioned lipid bilayers,[157,158] and tethered lipid membranes,[159] (Figure 1.19).

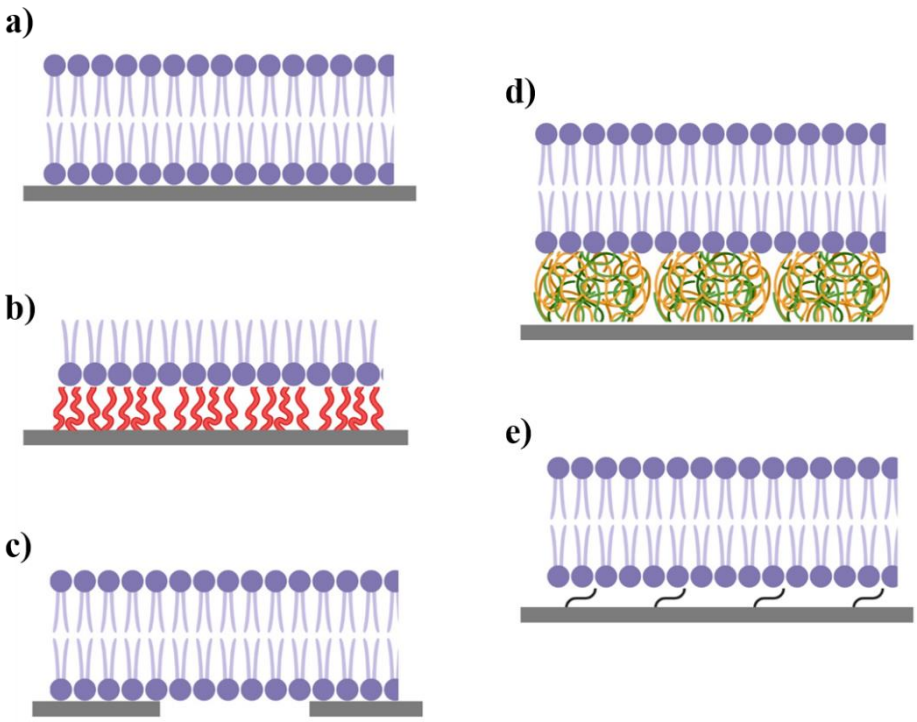

Fig 1. 19. Planar lipids bilayer models: a) Supported lipids bilayer membrane, b) Hybrid lipid bilayer membrane, c) Suspended lipid bilayer membrane, d) Polymer-cushioned lipid bilayer membrane, and e) Tethered lipid bilayer membrane.

SLBs are directly formed onto a hydrophilic solid substrate, becoming a planar and stable membrane with high fluidity (Figure 1.18a).[160] Hybrid lipid bilayers (Figure 1.18b), which consist of a self-assembled monolayer as the lower leaflet and a lipid monolayer as the upper leaflet, have gained popularity for their improved stability and ease of preparation, though they are somewhat limited by reduced fluidity in the lower leaflet.[161,162] Suspended bilayers (Figure 1.18c), offer reduced substrate interference and allow access to both sides of the membrane, but are more challenging to prepare.[156] The polymer-cushioned bilayers (Figure 1.18d), which improve membrane fluidity and reduce substrate effects, involve more complex preparation processes.[163] Tethered bilayer lipid membranes (Figure 1.18e) are also increasingly used in biosensing with improved stability as compared to other lipid model, particularly for studying membrane-protein interactions, but has less reproducibility and mobility due to tethering molecules.[159]

Our focus will be on the formation of SLBs due to their ease of formation, lateral fluidity, and ability to integrate with microfluidic systems. Also, SLBs can be customized with various lipid compositions carrying functional reactive groups, like COOH or biotin, among others. This allows the subsequent immobilization of specific ligands and cell receptors through conventional surface chemistry strategies like covalent binding or biotin/avidin strategy. Thanks to the lipid membrane fluidity, the immobilized

bioreceptors will have lateral mobility, enabling the formation of clusters that might enhance binding efficiency and mimic real biological interactions.

SLBs have been successfully applied in biosensing and cell biology studies, including investigations into protein-membrane interactions,[164] drug discovery,[165] and the evaluation of cell immunotherapies for cancer.[166] For example, Jonsson et al.,[157] demonstrated the formation of SLBs on nanoplasmonic sensors, highlighting the lateral mobility of bioreceptors immobilized on the lipid membrane and the enhanced protein binding to cell membrane mimics, compared to conventional surface immobilization methods. More recently, Yoon et al.,[167] utilized a nanoplasmonic sensor for real-time visualization of morphological changes in SLBs, with applications in designing antimicrobial surfaces. Plasmonic sensors combined with SLBs have also been demonstrated for evaluating T-cell immunotherapies for cancer.[166] In this study, the sensor utilized a biomimetic scaffold created with planar lipid bilayers, effectively mimicking the natural cellular environment. This design enabled efficient capture of intact tumor-specific T cells and real-time monitoring of their interactions. The use of planar lipid bilayers was crucial, as it provided a more physiologically relevant environment compared to traditional sensing methods. The system provided high accuracy and selectivity in analyzing CD8+ T cells engineered with varying T-cell receptor (TCR) affinities. The results of this study were the first demonstration of the potential application of label-free plasmonic biosensors for accelerating and improving immunotherapy evaluation studies, serving as inspiration and motivation for the work presented in this thesis.

Chapter 2

Design, fabrication and characterization of nanoplasmonic sensors

In this chapter, we design and fabricate nanoplasmonic structures made of gold and silver, optimize their performance through computational studies, and evaluate their sensitivity and resolution for refractometeric label-free sensing

2. Design, fabrication and characterization of nanoplasmonic sensors

2.1. Context and motivation

Localized surface plasmon resonance (LSPR) sensors are highly effective for detecting and analyzing biomolecular interactions due to their exceptional sensitivity, label-free analysis, and real-time performance. Among these, gold nanodisks (AuNDs) sensors have been one of the main focuses of our research group. In previous work, we successfully fabricated short-ordered arrays of AuNDs sensors (height 20 nm, diameter 100 nm) at low cost and integrated them into compact device for real-time biomolecular analysis. These sensors were fabricated using a bottom-up approach based on hole-mask colloidal lithography (HCL). The nanostructured array was designed to optimize the plasmonic field enhancement while positioning the spectral peak in the visible spectrum range. The resulting nanoplasmonic sensor exhibited an LSPR peak at 778 nm, with a full width at half maximum (FWHM) of 86 nm, and a refractometeric bulk sensitivity of approximately 100 nm/RIU. These AuNDs sensors have demonstrated excellent performance in diagnostic applications, including detection and quantification of clinical protein biomarkers for early diagnosis of colorectal cancer,[107] rapid identification of antibiotic allergy,[108] or for therapeutic drug monitoring.[168] However, to broaden the use of nanoplasmonic sensors in more complex biomedical studies, such as immunotherapy evaluation - where monitoring cell-cell interactions and highly sensitive biomolecular analysis are essential - we address the design and evaluation of novel nanostructured arrays with enhanced sensitivity and resolution.

The resolution of our nanoplasmonic sensors is dictated by the ability to detect and monitor minute LSPR peak displacements, which primarily depend on the LSPR position and bandwidth. In general, a narrower LSPR bandwidth (lower FWHM) allows for more precise shift measurements, resulting in higher resolution of the device. To improve our sensor performance, we propose two strategies: (1) reducing the diameter of AuNDs and (2) using a different plasmonic material, such as silver (Ag).

By reducing the diameter of the AuNDs, we can shift the plasmon resonance peak to shorter wavelengths, which will be directly accompanied by a narrowing of the peak bandwidth. In smaller nanodisks, the electron cloud is highly confined, producing a stronger restoring force which leads to spatial confinement of the electrons and the quantitation of their energy levels.[169,170] As a result, the energy gaps between these quantized levels increase. Since resonance energy is inversely proportional to the wavelength of the incidence light, the resonance occurs at shorter wavelengths.[171] This

confinement also reduces the electron´s degree of freedom, leading to fewer pathways for energy loss.[172] The larger energy gaps between quantized levels allow only few electrons to occupy intermediate energy levels, reducing the damping process.[46] In smaller nanodisks, higher-energy photons are less likely to be absorbed by the material, further confining the resonance to the nanodisks surface and reducing damping losses.[173] Collectively, these factor contribute in damping reduction and narrowing LSPR peak bandwidth. Studies have shown that reducing the diameter of gold nanostructures can significantly improve the LSPR quality. For instance, Farooq et al. demonstrated that gold nanodisks with radius of 30 nm exhibited narrower plasmon resonance peaks (FWHM 44 nm) compared to their 100 nm counterparts.[174] On the contrary, increasing the size of gold nanodisk size shifts the LSPR spectra toward higher wavelengths, which is associated with an enhanced surface scattering and broadening of the LSPR bandwidth (Figure 2.1).[175]

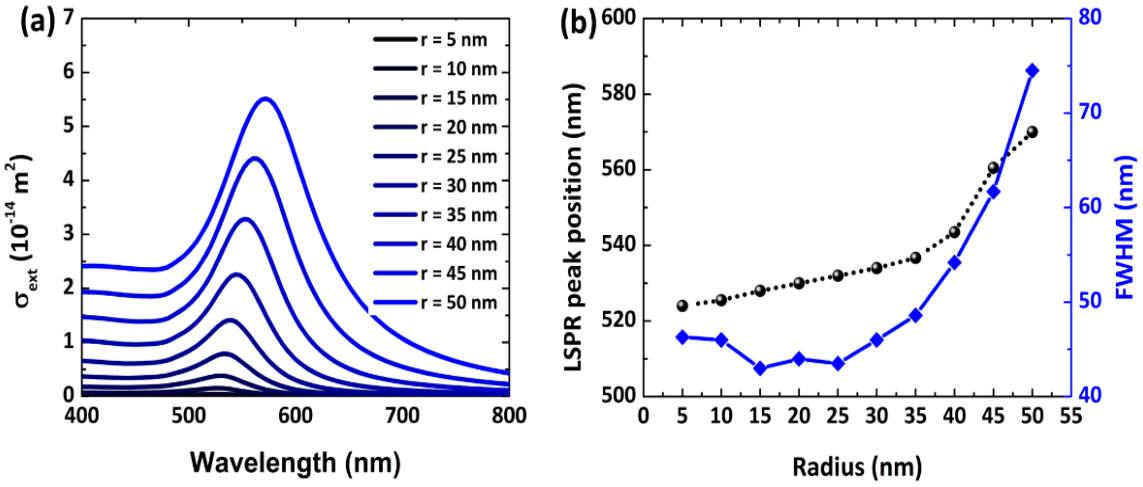

Fig 2. 1. a) LSPR spectral plasmonic resonance, and b) LSPR peak position (black dots) along with FWHM (blue squares) as a function of particle radius. Adapted from reference 180.[175]

For our second strategy, silver is proposed as plasmonic material due to the expected sharper LSPR peak compared to gold. This difference arises from several interconnected parameters related to electromagnetic characteristics of the metals, such as the refractive index and extinction coefficient, scattering properties, the inter-band transitions, and the imaginary part of the dielectric function.[176,177,178]

First, silver has a higher refractive index and extinction coefficient than gold, showing resonances in the broad UV-VIS range.[179,180,181] The high frequency of silver resonances directly positions the LSPR peak at shorter wavelengths with reduced bandwidths. Additionally, the conduction electrons in silver experience less scattering, particularly phonon-electron scattering.[182] This reduced scattering allows the electrons to resonate more freely, resulting in sharper and narrower resonance peaks due to lower intrinsic damping.[183] Moreover, the differences in the electronic structures and optical properties of

silver and gold also influence the shape and width of the resonance peak. Silver has highest electrical conductivity of all metals, which reduces resistance during electron resonance and minimizes energy dissipation, further contributing to a sharper resonance peak.[184] Another key factor is that silver experiences fewer inter-band transitions in the visible spectrum compared to gold.[185] These transitions in silver mainly occur in the ultraviolet region, which prevents overlapping in the visible spectrum and results in a more distinct resonance peak. Finally, silver has a higher quality factor for plasmonic resonance due to its lower imaginary part of the dielectric function, which also leads to less energy dissipation and narrower resonance peaks. These factors collectively make silver an excellent choice for achieving sharper LSPR peaks with improved sensor performance.

Hence, the main scientific objectives of this chapter are to design and fabricate a novel nanoplasmonic sensor with enhanced performance in terms of sensitivity and resolution for applications in complex biomedical studies. It begins with a computational study to optimize nanostructure design, followed by fabrication using hole-mask colloidal lithography method. The fabricated arrays will then be characterized to assess their performance as refractometeric sensors, measuring sensitivity to changes in refractive index and evaluating resolution. By addressing these issues, the goal is to optimize and advance the technology to a stage where it can be widely adopted for more complex biological studies, such as immunotherapy evaluation, which requires a high sensitivity for the detection and analysis of cells and biomolecules at low concentrations.

2.2. Computational modelling of plasmonic nanostructures

An initial computational study was performed for the design of nanoplasmonic arrays based on short-ordered gold nanodisks (AuNDs) and silver nanodisks (AgNDs). We used the finite element method (FEM) within COMSOL Multiphysics software. A three-dimensional (3D) unit cell model was employed, featuring a single nanodisk on a silicon dioxide (SiO_2) substrate with a cladding layer of water (RI 1.33) (Figure 2.2). To include LSPR interactions between close by nanostructures, we set periodic boundaries in both lateral directions of the nanodisk. We used the physics control mesh offered by COMSOL and selected an extra fine meshing (3 – 100 nm) for precise calculations. The wavelength-dependent RI of the SiO_2 substrate was calculated using the Sellmeier formula.[186] For the calculation of the wavelength-dependent RI of gold and silver, we employed an interpolation function based on existing literature.[187]

To analyze the LSPR characteristics, a TM-polarized light with wavelengths ranging from 400 nm to 900 nm was set to illuminate the nanodisks from the bottom of the SiO_2 substrate and it was collected after passing through the water cladding layer. The incidence angle determined for gold was 70°, based on our previously optimized studies,[107] and for silver it was selected at 46°, based on the reported study

by R.K. Bommali et al.[188] The generated near-fields around the nanodisks were examined using frequency domain analysis and the transmitted light spectra were obtained for different geometries over the determined wavelength range.

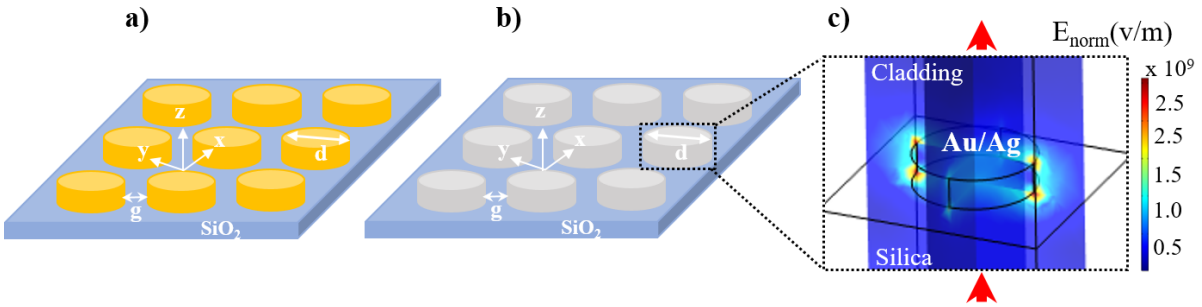

Fig 2. 2. Schematic illustration of short-ordered nanoplasmonic arrays on glass substrate, a) gold nanodisks short-ordered arrays, b) Silver nanodisks short-ordered arrays and, c) Electric field distribution in a 3D unit cell of the short-ordered gold/silver nanodisks, colour scale indicating normalized electric field strength.

Based on previously optimized nanostructures, we first studied the LSPR characteristics of two different AuNDs arrays of 20 nm height (h) with varying diameters (d): 80 nm and 100 nm. The spacing distance between the nanostructures (gap, g) was initially set at 80 nm. Figure 2.3 shows the transmittance spectra obtained for both geometries.

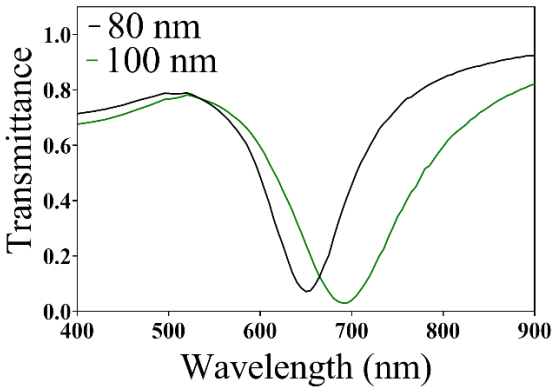

Fig 2. 3. Transmission spectra of AuNDs arrays with different diameters: 80 nm (black) and 100 nm (green). Height and gap were kept equal to 20 nm and 80 nm, respectively.

As can be seen, by making the nanodisks smaller, we could shift the LSPR peak to shorter wavelengths in the visible spectrum, from λ_{LSPR} = 778 nm for 100 nm AuNDs to around λ_{LSPR} = 650 nm for 80 nm AuNDs. The wavelength displacement also results in a narrower peak, with a FWHM = 88 nm for 80 nm AuNDs, compared to the 100 nm AuNDs with FWHM = 130 nm. According to literature, we also

expect more penetration of evanescent field when the nanostructures size reduces.[189] Next, we examined how the distance between two nanodisks (the gap) affects the LSPR (Figure 2.4). We observed that increasing the gap distance from half the diameter (g = 40 nm) to twice the diameter (g = 160 nm) resulted in a sharper and narrower peaks, but it also slightly reduced the intensity. For the best performance, balancing sharpness and intensity, we selected the gap equal to the nanodisk diameter (g = d = 80 nm).

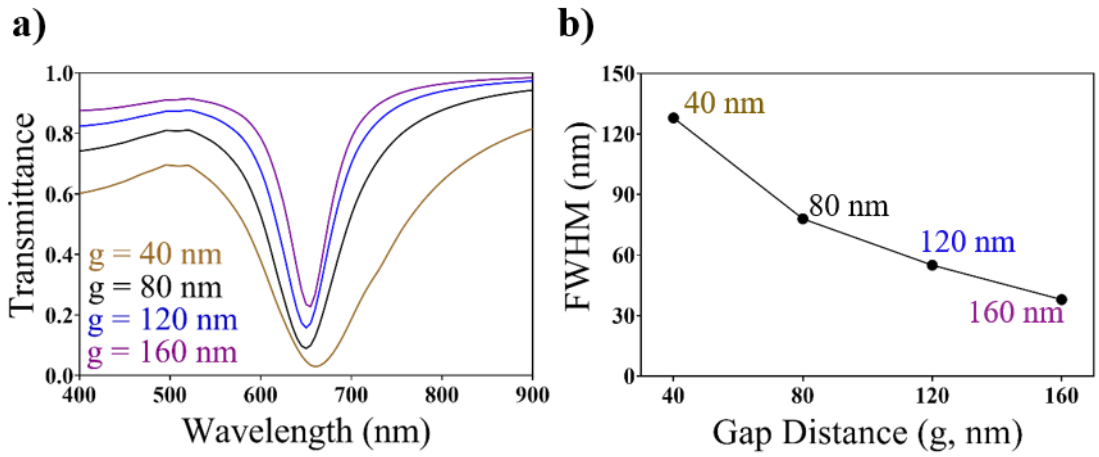

Fig 2. 4. a) Gap distance of AuNDs analysis in range of d/2 to 2d for 80 nm of diameter, and b) FWHM values for different gap distances between AuNDs.

An analogue simulation study was then performed for AgNDs. In this case, in order to adjust the structure geometry for LSPR sensing in the visible range, we first examined the LSPR peak with different heights (20, 30, 50 nm), different diameters (80, 100 nm), and different gap distances (70 - 250 nm). Figure 2.5 shows that the LSPR peak of AgNDs with different heights and diameters, maintaining the gap at 150 nm, falls within the visible range, confirming one of our objective. For the 80 nm diameter, increasing the height we observed a blue shift from 568 nm to 504 nm, but a broader peak from 54 nm to 81 nm (Figure 2.5a). Notably, a blue shift ($\Delta\lambda = 61$ nm) is induced in the resonance peak position with increasing the height. Similarly, by increasing the height same trend was observed in 100 nm diameter, a blue shift ($\Delta\lambda = 83$ nm) from 637 nm to 557 nm, with a broader resonance peak from 58 nm to 63 nm, (Figure 2.5b).

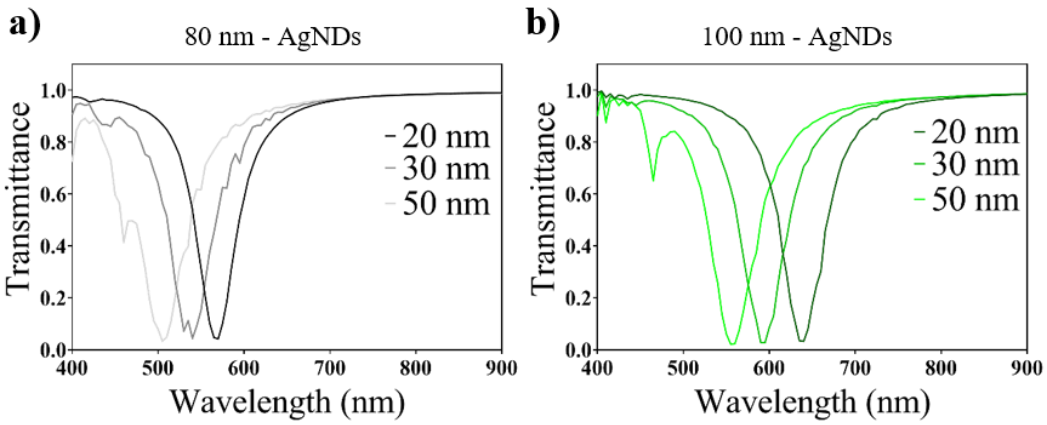

Fig 2. 5. Transmission spectra of AgNDs with different heights (20nm, 30nm, and 50nm) and diameters: a) 80 nm diameter, and b) 100 nm diameter.

For both diameters, we observed a gradual shift to shorter wavelengths and wider resonance peak with increasing height, in visible spectrum (Table 2.1).

Table 2. 1. Summary of measured parameters of silver nanodisks at different heights.

Height (nm)	**Diameter, 80 nm**		**Diameter, 100 nm**	
	FWHM (nm)	λ_{LSPR} (nm)	FWHM (nm)	λ_{LSPR} (nm)
20	54	568	58	637
30	57	540	61	593
50	81	504	63	557

Increasing the height of the nanodisks alters their aspect ratio, enhancing the interaction of light by generating a stronger electromagnetic field along the vertical axis, affecting the electron density distribution. These differences directly influence the restoring force of the electrons. Taller nanodisks result in more confined electron oscillations, which contribute to a higher resonance frequency and a shift toward shorter wavelengths. At the same time, other factors, such as radiation damping and surface scattering, come into play. A greater height increases the surface area, leading to higher radiation damping, which causes the oscillating electrons to lose energy more quickly, resulting in a broader resonance peak. Furthermore, with more surface area available, the electrons have a larger space to oscillate, potentially reducing their coherence and further broadening the peak. Considering these results, the 20 nm appears as the optimal height for both diameters (80 nm and 100 nm). This selection is based on its comparatively narrower spectral width (FWHM = 54 nm and FWHM = 58 nm, respectively), indicating sharper plasmonic resonance characteristics.

Finally, we examined how the LSPR of AgNDs is affected by the nanostructure array gap (Figure 2.6). As we varied the gap from 70 nm to 250 nm for both 80nm and 100 nm diameter nanodisks at a constant height of 20 nm, we observed a shift of the LSPR peak towards the larger wavelengths, accompanied by sharper peaks but reduced intensity. For both diameters, the optimum gap was found at around 200 nm, showing a narrow resonance peak with high intensity and in the visible range. In the case of smaller nanodisks (d = 80 nm), a gap of 200 nm provided the optimal resonance peak position (λ_{LSPR} = 575 nm, Figure 2.6a) with a FWHM of 37 nm (Figure 2.6b). For larger diameter nanodisks (d = 100 nm), the best gap was determined also at 200 nm, with a peak within the visible spectrum (λ_{LSPR} = 638 nm, Figure 2.6c) but a slightly higher bandwidth (FWHM = 63 nm, Figure 2.6d).

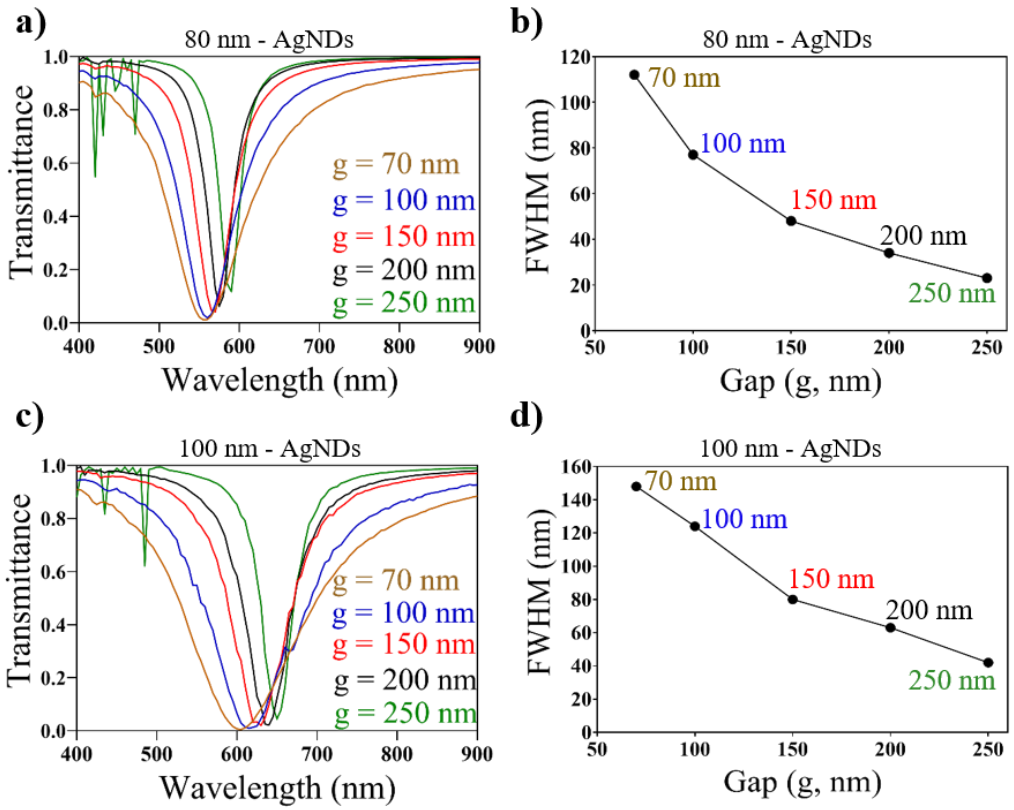

Fig 2. 6. Interspacing distance (g) analysis of silver nanodisks with different diameters: a) 80 nm AgNDs, and c) 100 nm AgNDs. FWHM values for different interspacing distances between AgNDs with diameters: b) 80 nm AgNDs (back), and d) 100 nm AgNDs (green).

To conclude, in this computational study, we have designed gold and silver nanodisks with different geometric characteristics optimized to provide narrower resonance peaks with good intensities, and in visible spectral region. The main parameters obtained for the different geometries are summarized in Table 2.2. Based on these results, the configurations with 80 nm and 100 nm diameters, and 20 nm of

height, were selected for both AuNDs and AgNDs. For AuNDs, an 80 nm gap was selected by balancing the lower FWHM with high peak intensity. For AgNDs, the 200 nm gap provided the narrower and sharper resonance peak in the visible spectrum.

Table 2. 2. Summary of Optimization Parameters for Metallic Nanodisks: Gold and Silver

Nanodisks (NDs)	**Diameter (d, nm)**	**Height (h, nm)**	**Gap (g, nm)**	**FWHM (nm)**	**λ_{LSPR} (nm)**
Gold (Au)	80	20	40	30	660
			80	82	650
			140	58	650
			160	32	653
	100	20	80	130	690
Silver (Ag)	80	**20**	70	112	555
			100	77	560
		30	150	48	570
		50	**200**	**37**	**575**
			250	23	590
	100	**20**	70	148	605
			100	124	620
		30	150	80	629
		50	**200**	**63**	**638**
			250	42	650

2.3. Fabrication and characterization of nanostructured plasmonic arrays

After designing and theoretically optimizing the nanoplasmonic array geometries, we proceeded with their fabrication and experimental characterization. Various nanofabrication techniques have been explored for shaping and patterning the plasmonic materials at nanoscale. Among these, nanosphere lithography, particularly HCL, offers simplicity and scalability, with resolutions typically varying from 20 to 200 nm, depending on the size of the colloidal particles used as masks.[91] Smaller particles enable finer features, but may introduce challenges related to handling and uniformity.

HCL, first introduced by Fredrickson et al,[190] is a simple, versatile, and cost-effective nanolithography technique based on self-assembled colloidal spheres. It is widely used for fabricating short-ordered arrays of nanostructures with various materials (e.g., Au, Ag, Pt, Si) over a large scale with low cost and high reproducibility.[191] While HCL may not offer the same level of resolution and precision as techniques like EBL or FIB, it is highly adaptable, allowing for nano-patterning over wide surfaces with

diverse dimensions, shapes, and inter-nanostructure spacing. Moreover, it requires fewer processing steps and less time, producing nanostructures with homogeneous optical properties and high reproducibility. However, a limitation of HCL method is that each step of the process must be carefully controlled and optimized to render the desired nanostructure arrays. It is important to note that, while our simulation study was performed with regular arrays, we anticipate to not obtaining perfectly regular arrays but short-ordered arrays. Therefore, to confirm the best geometry, it is important to experimentally test different parameters such as density and diameters in order to determine the best geometry.

2.3.1. HCL fabrication of short-ordered arrays of plasmonic nanostructures

In our research group, we previously established an HCL protocol for the fabrication of short-ordered arrays of AuNDs.[107,108,192] The HCL nanofabrication protocol is illustrated in Figure 2.7 and it was carried out as detailed hereafter:

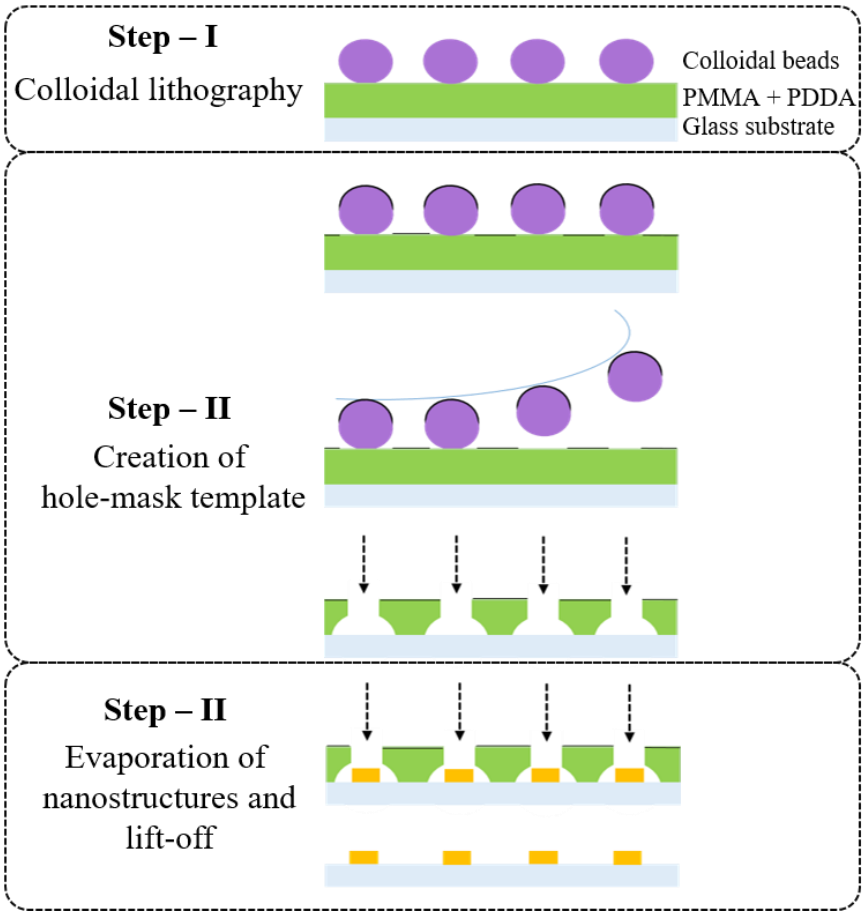

Fig 2. 7. Schematic illustration of the fabrication protocol based on HCL technique.

Prior to start the nanofabrication process, glass substrates (20 x 26 mm) underwent a thorough cleaning process. This involved a sequential cleaning with SSD (0.5 % wt), HCl (0.1 M) and milli-Q water, dry with nitrogen (N_2) stream. Then, the substrates were immersed in a freshly prepared piranha solution (3:1, H_2SO_4:H_2O_2) for 20 minutes. After rinsing and drying with N_2 stream, the HCL fabrication was initiated.

Step I. Colloidal lithography

A high molecular weight polymer, polymethyl methacrylate (PMMA), is commonly used in lithography procedures both as a resist and sacrificial layer. In this work, a 200 nm-thick layer of 950 K PMMA (4% in anisole) was spin-coated (4000 rpm, 3000 $r.s^{-2}$) as a sacrificial layer directly on the glass substrates. Following a 5 min baking process at 155° C, the substrates were exposed to a brief O_2 plasma treatment (18s, 75W, 75 mTorr, 40% O_2-flux) to enhance the hydrophilicity. Then, an oppositely charged polyelectrolyte solution (0.2% poly (diallyldimethylammonium chloride), PDDA) was drop-cast onto the PMMA layer for 1 min to create an adhesive surface. Finally, polystyrene beads with diameters of 80 nm and 100 nm were deposited on the PDDA layer by drop-casting different solutions at various concentrations (0.2 – 0.4%). The electrostatic repulsion between the colloidal beads and the attractive force between the particles and the PDDA layer define short-ordered nanoarrays of polystyrene spheres with different spacing distances correlated with the initial bead concentration.

Step II. Creation of the hole-mask template

Next, for creating the hole-mask template, a 15 nm titanium (Ti) layer was evaporated as a sacrificial layer using e-beam evaporator in cleanroom facility. Then, colloidal spheres were stripped-out by using blue tape, resulting in the removal of the metal-coated spheres while retaining a polymeric sacrificial layer with a perforated Ti layer. The metal layer is resistive to O_2 plasma treatment, therefore a reactive ion etching (RIE) process was applied to remove the polymeric layers underneath the metal holes. The RIE process, set at 75 W, 75 mTorr, and 50% O_2-flux for 5 minutes, utilized its directional etching capability to create well-defined holes on the samples while preserving the integrity of the substrate sidewalls.

Step III. Formation of metal nanodisks structures

Finally, the metal nanodisks were evaporated within the hole-mask template using e-beam evaporation. Initially, a 1.5 nm adhesive layer of titanium (Ti) was deposited, followed by a 19 nm layer of either gold or silver. The remaining mask was removed by sonication in acetone and Milli-Q water for 1 min each at room temperature, followed by rinsing with Milli-Q water and drying with a nitrogen stream. The final result is an array of Au or Ag nanodisks with a height of 20 nm, diameters of 80 nm or 100 nm, and varying spacing distances based on the different colloidal concentrations.

Through this method, we could fabricate a collection of different nanoplasmonic arrays with different materials and geometries at a low cost. In each nanofabrication batch, we obtain up to 16 sensor chips (2 x 1 cm), which can be individually tested and characterized. A photograph of some arrays fabricated in this project is shown in Figure 2.8. The different colours observed in the 80 nm and 100 nm of silver and gold nanodisks are attributed to their plasmonic scattering properties. This variation in colours also indicates that different geometries will produce distinct LSPR characteristics.

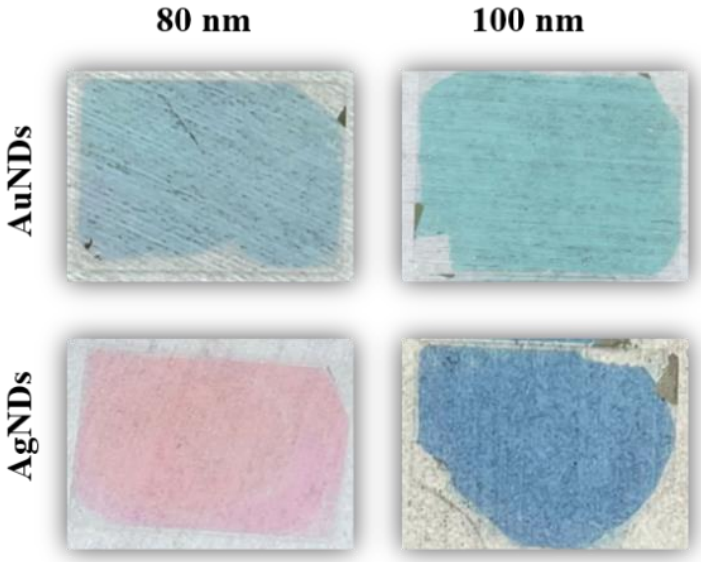

Fig 2. 8. Photographs of the fabricated gold and silver nanoplasmonic chips using the HCL method, with a height of 20 nm and diameters of 80 nm and 100 nm.

2.3.2. Electron microscopy characterization of nanoplasmonic arrays

The geometry and distribution of the fabricated nanoplasmonic sensors were analyzed using scanning electron microscopy (SEM). For both metals (Au and Ag), SEM images shown the expected short-range ordered distribution of nanodisks with a mean diameter of approximately 79.3 ± 2.7 nm and 100.8 ± 5.7 nm (Figure 2.9 and Figure 2.10).

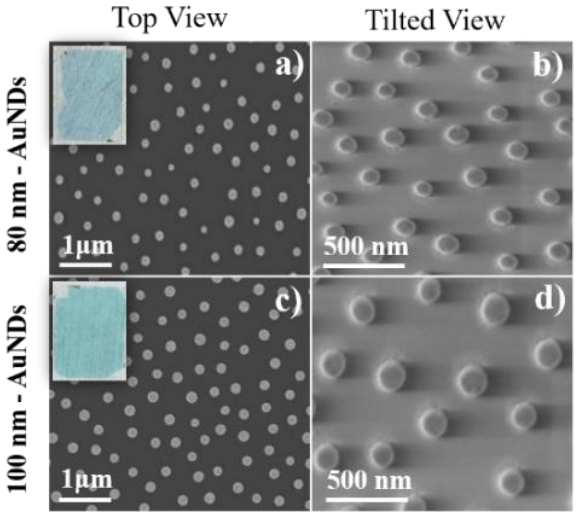

Fig 2. 9. SEM images of AuNDs fabricated using the HCL method, with h = 20 nm, d = 80 nm (left panels) and 100 nm (right panels) and colloidal suspension density of 0.2%. For each geometry, top view and tilted views are displayed.

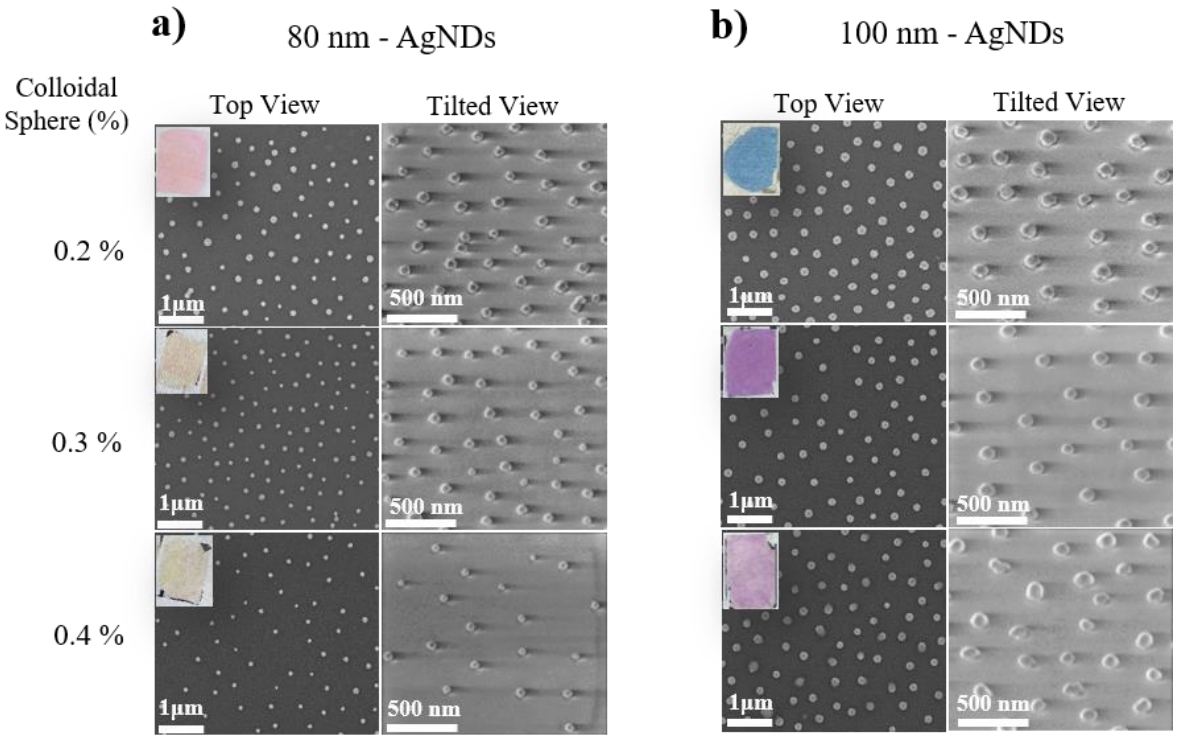

Fig 2. 10. SEM images of AgNDs fabricated using the HCL method, with h = 20 nm, d = 80 nm (left panels) and 100 nm (right panels) and colloidal suspension densities of 0.2% (first line), 0.3% (second line) and 0.4% (third line). For each geometry, top view and tilted views are displayed.

We also determined the mean gap distance of metal nanostructures for each colloidal density, as shown in Table 2.3. The gap difference in colloidal distribution with different densities can be seen in SEM

images (Figure 2.10). It's important to note that the diameters of the nanodisks and their gap distance are entirely dictated by the properties of the colloidal polystyrene bead solution, determined by factors such as concentration and electrostatic interactions. The increase in gap distance between polystyrene beads on a PDDA-coated surface at higher concentrations is primarily due to intensified electrostatic repulsion between the negatively charged beads. At lower concentrations, there are fewer beads per unit area, allowing them to settle closer together where attractive forces from the PDDA layer balance out electrostatic repulsion. However, as bead concentration rises, more beads are deposited within the same area, leading to increased repulsive forces between adjacent beads. This repulsion prevents close packing and causes beads to settle with greater spacing to minimize repulsive interactions, resulting in a less dense and more widely spaced arrangement on the PDDA-coated surface.

Table 2. 3. Summary of calculated parameters of metallic nanostructures at a height of 20 nm.

Diameter (d, nm) (Mean ± SD)	**Colloidal Density (%)**	**Gap (g, nm) (Mean ± SD)**
79.3 ± 2.7	0.2	148. 5 ± 31.6
	0.3	178.9 ± 25.6
	0.4	220.7 ± 35.6
100.8 ± 5.7	0.2	115.7 ± 17.9
	0.3	188.5 ± 30.3
	0.4	198.7 ± 19.3

The reproducibility of the HCL method varies across different dimensions of the nanostructures. Analysis of the percentage of variability between different batches reveals that the method is highly reproducible in controlling the height of the nanostructures, with a low variability of 2.3 ± 1.3%. This suggests that the process parameters for height are well-optimized, ensuring consistent and precise control over this dimension. In contrast, the variability in the diameters of the nanostructures is notably higher. For 80 nm diameter, the variability is around 16.5 ± 6.3%, while for 100 nm diameters, it is 9.3 ± 4.3%. This increased variability in diameter can be largely attributed to the non-uniform size of the colloidal beads used as a mask during the fabrication process. The commercially acquired beads exhibit a distribution in size, leading to inconsistencies in the mask pattern and resulting in variations in the final diameters of the nanostructures.

Additionally, the variability in the gaps between the nanostructures is moderate, with measurements showing 4.2 ± 1.3% and 5.4 ± 2% with respect to the dimeters 80 nm and 100 nm, respectively. While this variability is slightly higher than that of the height, it remains relatively controlled compared to the diameter. Overall, while the HCL method demonstrates strong reproducibility, reliability and high resolution in height and gap control, the diameter variability indicate that the process could be improved.

Addressing the issue of bead size uniformity could enhance diameter consistency and overall reproducibility of the HCL method.

2.3.3. Optical spectroscopy characterization of nanoplasmonic arrays

Once confirmed the precision and reproducibility of the HCL fabrication method, we proceeded to spectroscopically characterize the LSPR of the nanosensors. First, we analyzed the LSPR of AuNDs. To that, we employed an in-house developed optical set-up based on prism-coupling LSPR excitation from a collimated TM-polarized broadband light at a fixed angle of incidence at 70° and wavelength interrogation (Figure 2.11).

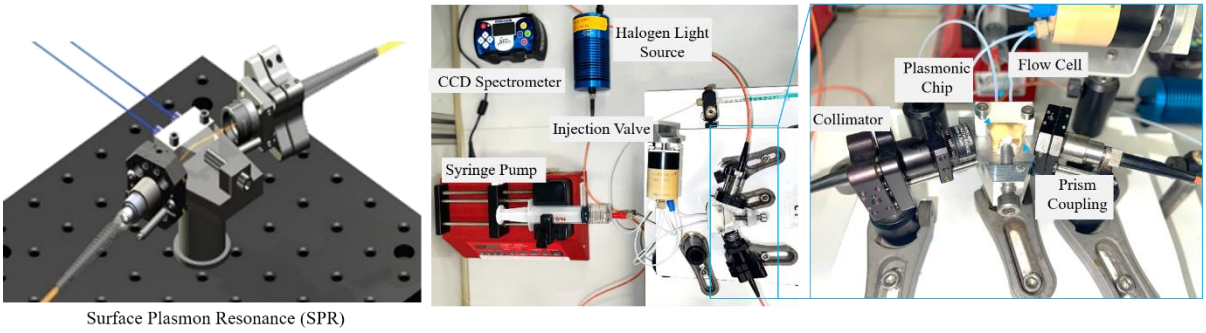

Fig 2. 11. Photographs of the fixed angle (70°) experimental SPR sensor set-up.

The nanodisks sensors were sandwiched between a trapezoidal prism (n:1.52) and RI matching immersion oil (n = 1.51), connected to a customized flow cell and a microfluidic system with an adjustable syringe pump ensuring constant liquid flow. The system also includes a manually operated injection-valve and a 150 - 200 µL loop for sample injection. A collimated halogen light source excites the LSPR, and the reflected response is collected by a fiber-coupled mini spectrometer. A software interface was also developed in Python for signal monitoring and data analysis. The software allows for the visualization of the collected reflected light spectra (Figure 2.12a) and the interrogation of the LSPR minimum vs. time (i.e., real-time sensorgrams, Figure 2.12b). The data is presented in two main types of graphs: reflectance spectra and real-time sensorgrams.

In Figure 2.12a, the reflectance spectrum shows the resonance peak appearing as a sharp dip. When binding events occur, the increase in mass translates to an increase in the RI, causing the peak shifting toward higher wavelengths (rightward). Conversely, when desorption occurs from the sensor surface, the RI decreases, shifting the peak toward lower wavelengths (leftward). Simultaneously, the sensorgrams plot the wavelength displacements ($\Delta\lambda$) over time, allowing for the real-time monitoring of biomolecular interactions.

In Figure 2.12b, an increasing curve indicates a red shift (e.g., binding events), while a decreasing curve indicates blue shift (e.g., desorption). For the precise monitoring of the resonance peak position, the software uses a polynomial fitting algorithm. To optimize the signal-to-noise ratio (S/N), the software constantly acquires reflectivity spectra every 3 milliseconds, averaging 300 consecutive spectra to produce a stable resonant spectrum. This setup allows us to easily examine and evaluate the main features of the LSPR peak, including wavelength position and bandwidth, from different nanoplasmonic sensors.

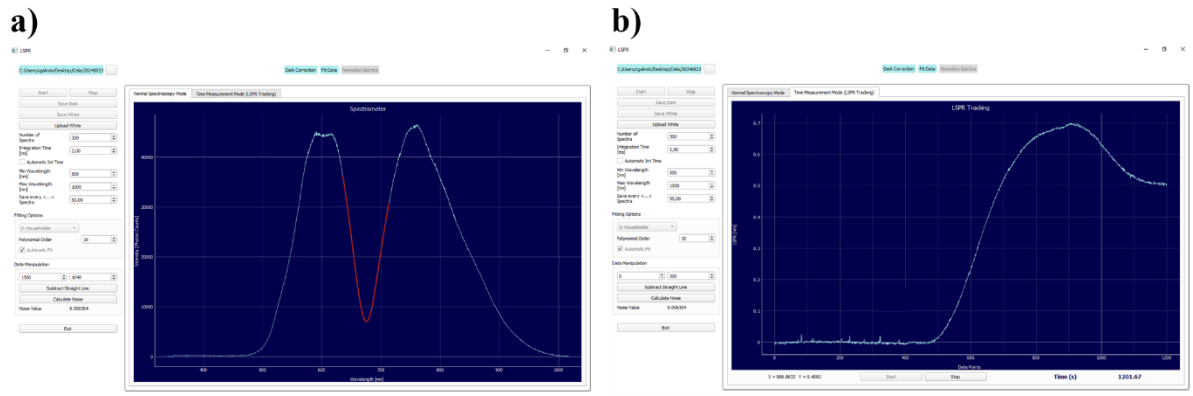

Fig 2. 12. Screenshots of the home-made readout software showing in real-time: a) The wavelength spectra, and b) the sensorgram tracking the SPR signal in nm (Δλ).

Gold nanodisks with 80 and 100 nm diameters were placed in the LSPR set-up and illuminated at 70° angle of incidence. The resonance peaks were observed at λ_{LSPR} = 680 nm for 80 nm AuNDs, and at λ_{LSPR} = 749 nm for 100 nm AuNDs (Figure 2.13). The bandwidths of the peaks were calculated as FWHM = 67 nm for 80 nm AuNDs and FWHM = 82 nm. As expected, both LSPR peaks fall within the visible to near-infrared spectrum range, showing a shift to shorter wavelengths with smaller diameter. Our experimental results are consistent with the simulations, which predicted a sharper and narrower peak for the 80 nm AuNDs positioned around 650 nm.

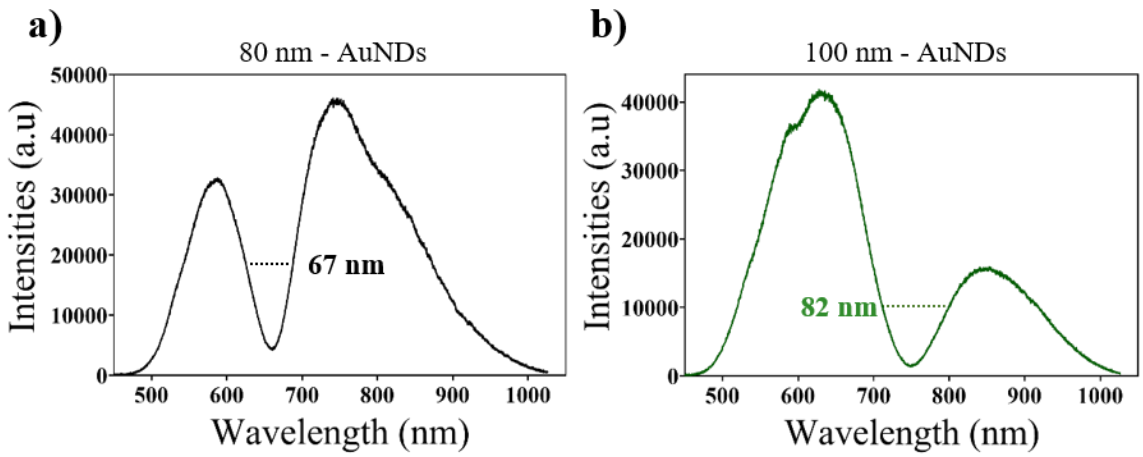

Fig 2. 13. Optical spectrum of reflected light of gold nanoplasmonic sensors at a height of 20 nm with a colloidal sphere density of 0.2%: a) 80 nm diameter of AuNDs (black) showing LSPR peak around 680 nm in the visible region, and b)100 nm diameter of AuNDs (green) showing LSPR peak around 749 nm in near-visible region.

Next, we examined the LSPR characteristics of the AgNDs. Contrary to AuNDs, silver sensors may require a different angle of incidence to achieve the optimal excitation of their plasmonic resonances.[188] In fact, our simulation studies showed optimum resonance achieved with an incident angle of 46°. To meet this requirement, we developed a new customized setup that allows us to adjust the angle of incidence in range from 45° – 90° (Figure 2.14). This device essentially contains the same optical, fluidic, and electronic components than the previously developed, but the sensing module (including sensor, prism and microfluidic chamber) is placed on a micrometric rotating platform. This new configuration gives the flexibility needed to thoroughly study the LSPR properties of AgNDs across a variety of incidence angles, allowing the selection of the best angle for maximum resonance excitation.

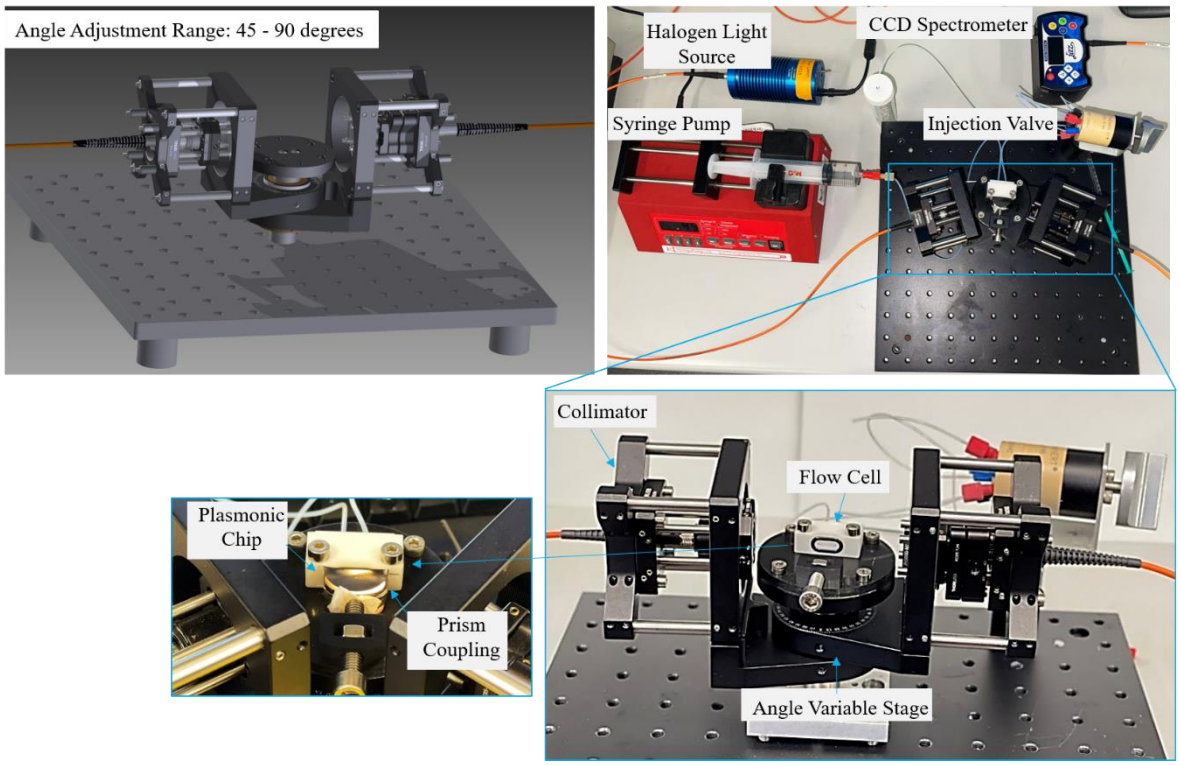

Fig 2. 14. Photographs of the angle variable (45° – 90°) experimental LSPR sensor set-up.

For the selection of the optimum angle of incidence, preliminary AgNDs sensors fabricated with 0.2% of colloidal density (g = 148 nm) were studied at different angles ranging from 34° to 46° (Figure 2.15). This angle range was chosen based on the literature, suggesting that the highest sensitivity for silver nanoplasmonic sensors has been demonstrated both theoretically and experimentally within this range.[188] For the AgNDs with a diameter of 80 nm (Figure 2.15a), the LSPR peak appeared at wavelengths below 600 nm, which cannot be accurately acquired in our optical setup. In the case of 100 nm AgNDs (Figure 2.15b), an intense LSPR peak was observed within the visible range (λ_{LSPR} between 650 and 700 nm), with the peak positioning shifting to lower energies (red shift) at increasing angle of incidence (Table 2.4).

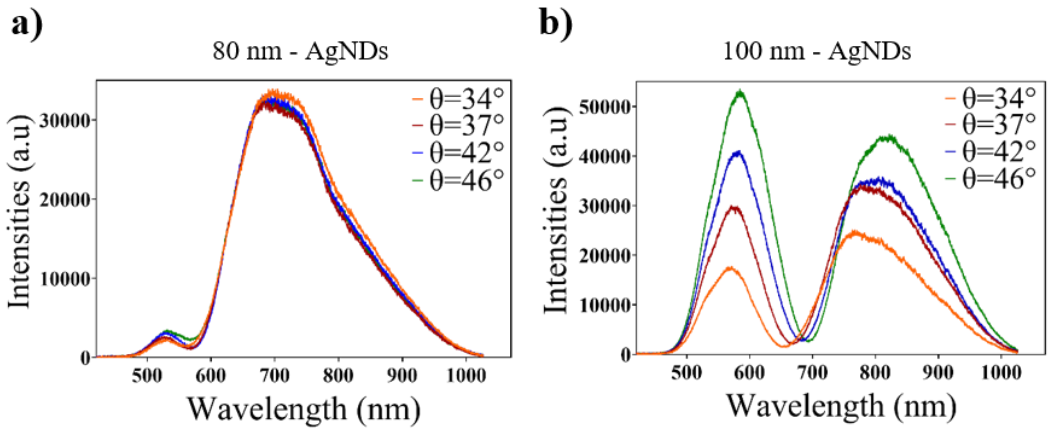

Fig 2. 15. Optical spectra of silver nanodisks (AgNDs) at different angle of incidence in range of 34° - 46° with 0.2 % of colloidal sphere densities and diameters: a) 80 nm – AgNDs, and b) 100 nm – AgNDs.

In terms of LSPR bandwidth, we observed that the FWHM of silver LSPR peaks decreases with increasing wavelength, with the sharpest resonance occurring at 46°. At this angle, perfect coherence of the resonance is achieved, resulting in a narrower and more intense peak. This coherence is due to stronger light-nanodisk interactions, which reduce scattering and damping. The increased optical path length, caused by multiple scattering events among the nanodisks, enhances light absorption and leads to a red shift. Furthermore, the localized surface plasmon also generate strong local fields, further intensifying these interactions. At 46°, the coherence of collective electron oscillations minimizes damping, sharpening the LSPR peak, whereas at other angles, increased damping broadens the resonance. Our experimental results align with simulations, confirming these trends in LSPR behaviour.

Table 2. 4. Summary of LSPR characteristics for 100 nm diameter silver nanodisks (AgNDs) with a height of 20 nm.

Incidence Angle (θ°)	**FWHM (nm)**	**λ_{LSPR} (nm)**
34	117	650
37	109	667
42	108	683
46	98	693

In summary, based on our experiments with silver nanodisks, we determined the optimal angle of incidence for LSPR resonance to be 46°. At this angle, AgNDs with 100 nm diameter showed a strong LSPR peak at λ_{LSPR} = 693 nm, characterized by a FWHM of 98 nm and high intensity. However, this FWHM is broader than those obtained for AuNDs, indicating the need for further optimization. Our

experimental results are not matching with the simulation results, conducted at the same angle of incidence, where AgNDs 100 nm diameter showed a narrower FWHM of 62 nm at λ_{LSPR} = 638 nm in visible spectra, which is more than 50 nm shifted from the experimental peak. This discrepancy indicates the need to explore additional factors affecting the LSPR response such as gap distance between the nanostructures.

We evaluated the peak position and bandwidth of AgNDs with different nanostructure densities, with gaps ranging from 150 - 200 nm for 80 nm AgNDs, and from 110 - 200 nm for 100 nm AgNDs (corresponding to colloidal densities from 0.2% - 0.4%) (Figure 2.10). For both diameters, the plasmonic peaks appeared in the visible spectrum across all applied gaps (Figure 2.16). At higher colloidal densities, the nanostructure´s average gap increases, essentially due to the increasing repulsion forces between the beads. Theoretically, these larger gaps, reduce the plasmonic coupling, result in a broader distribution of resonance energy and broader bandwidth, and therefore inducing an LSPR peak shift to higher wavelengths.

As expected, a red shift was observed for the 80 nm AuNDs with a broader width (FWHM = 73 nm). Accurate calculations for smaller gaps are challenging because the LSPR peak occurs below 600 nm, outside the measurable range of our optical setup. Conversely, for the 100 nm AgNDs, we observed a blue shift of the LSPR peak position and a broader bandwidth (FWHM = 104 nm). This unexpected result, deviating from our simulations, may be attribute to the corrosive nature of silver and potential degradation of the nanostructured. Nonetheless, the overall spectral features observed for 100 nm AgNDs are better than the ones obtained for 80 nm AgNDs, especially in terms of LSPR peak position and bandwidth (Table 2.5). Therefore, we selected the 100 nm AgNDs with a lower gap for further evaluation.

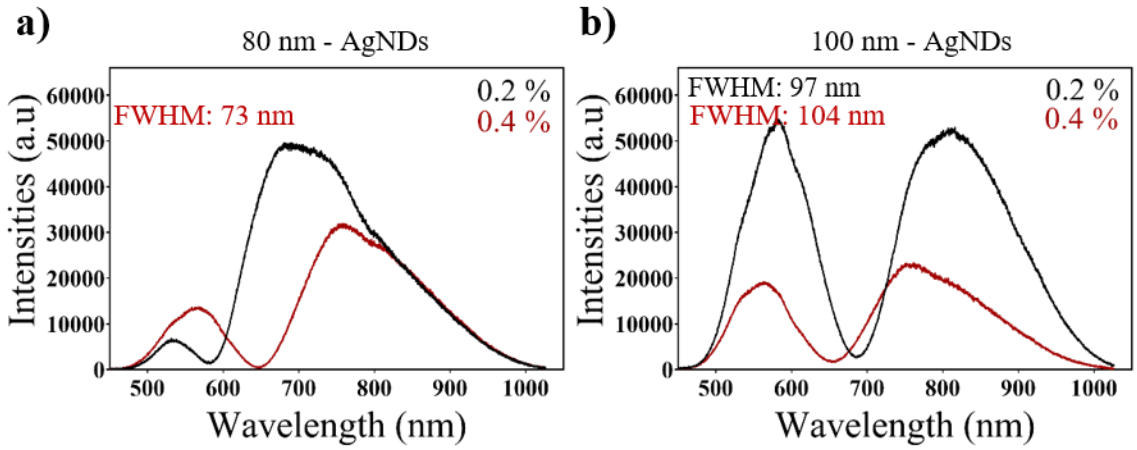

Fig 2. 16. Optical spectra of AgNDs with distance gaps (corresponding to colloidal densities from 0.2% - 0.4%) with diameters: a) 80 nm – AgNDs, b) 100 nm – AgNDs at an incident angle of 46° degrees.

In summary, for AgNDs, we experimentally observed broader resonance peaks than those predicted by our simulations. A potential hypothesis for this discrepancy is that the simulations assume a regular, periodic array of nanodisks, whereas the experimental setup involves a random distribution. Additionally, factors such as the chemical stability of the silver nanodisks, which could influence the plasmonic response, need to be addressed. This aspect will be further discussed in the following sections.

Table 2. 5. Spectral peak positions measurements correspond to colloidal densities of AgNDs corresponds to colloidal densities (%) at a height of 20 nm.

Densities (%)	**80 nm AgNDs**			**100 nm AgNDs**		
	Gap (Mean ± SD) nm	***λ_{LSPR} (nm)***	***FWHM (nm)***	***Gap (Mean ± SD) nm***	***λ_{LSPR} (nm)***	***FWHM (nm)***
0.2	148.5 ± 31.6	580	-	115.7 ± 17.9	685	97
0.4	220.7 ± 35.7	647	73	198.71 ± 19.3	654	104

2.4. Evaluation of nanoplasmonic sensors for biosensing

2.4.1. Refractometeric bulk sensitivity characterization

To assess the refractometeric sensing performance of the selected AuNDs and AgNDs nanoplasmonic sensors, we carried out a bulk sensitivity calibration curve. Serial dilution solutions of HCl (25 mM, 50 mM, 100 mM and 500 mM) of known RI (i.e., determined with a digital refractometer) were flowed through the microfluidic system, employing milli-Q water as running buffer. We measured and plotted the LSPR wavelength shift displacements ($\Delta\lambda_{LSPR}$, nm) as a function of the RI changes (Δn, RIU) (Figure 2.17). The bulk sensitivity ($\eta_B = \Delta\lambda/\Delta n$) is defined as the shift in resonance peak caused by the change in refractive index of dielectric medium surroundings of sensor surface. By fitting our data to a linear regression function we can determine the η_B values for sensors. Besides, we determined the limit of detection (LOD), defined as the minimum RI change measurable and calculated as 3 times the standard deviation of the background signal, LOD = 3 x $SD_{Background\ Signal}$. The LOD will provide an estimation of the resolution of the sensors.

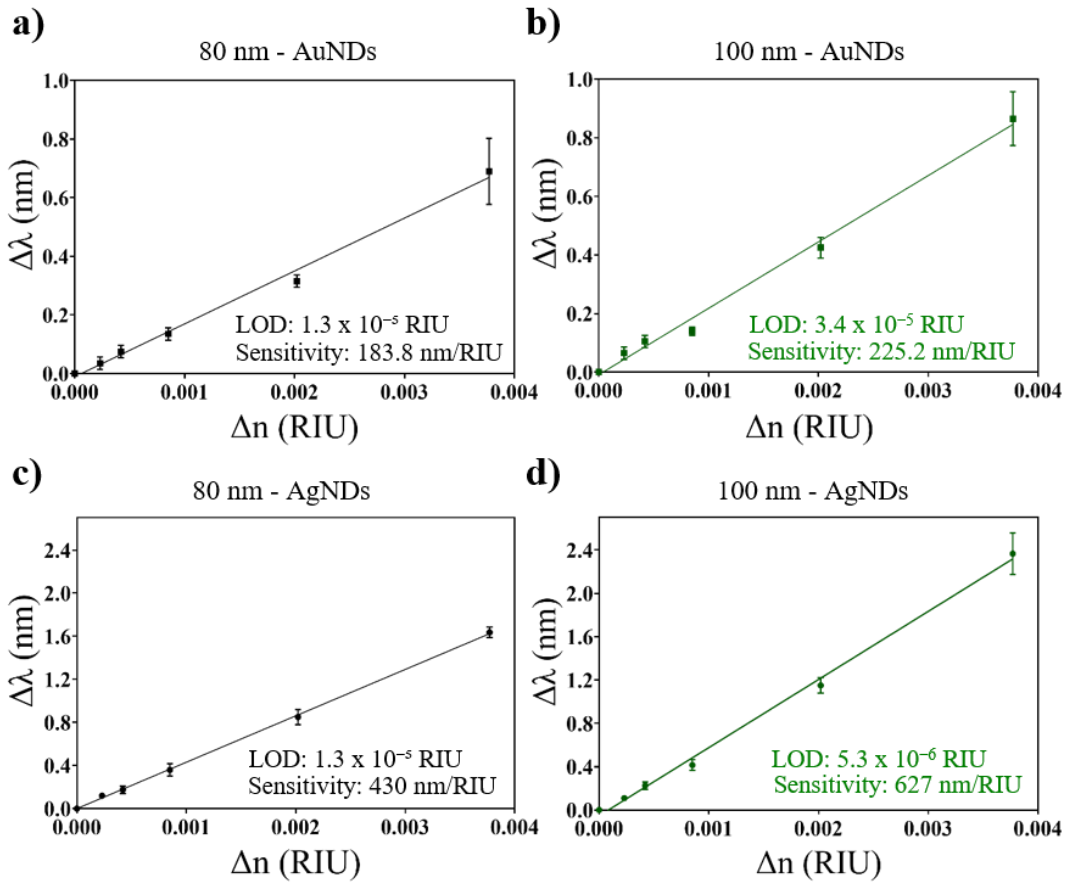

Fig 2. 17. Bulk sensitivity calibration curves of nanoplasmonic sensors (Gold and Silver): a) 80 nm AuNDs, b)100 nm AuNDs, c) 80 nm AgNDs, and d) 100 nm AgNDs, obtained with sequential measurements of different HCl concentrations over a milli-Q water running flow. Each measurement corresponds to the mean ± SD of triplicate measurements.

For 80 nm AuNDs, the sensitivity was determined at 183.8 nm/RIU with a limit of detection of 1.3 x 10^{-5} RIU (Figure 2.17a). For 100 nm AuNDs, the sensitivity was 225.2 nm/RIU with a limit of detection of 3.4 x 10^{-5} RIU (Figure 2.17b). Compared to our previous study using 100 nm AuNDs,[108] this new design with smaller AuND diameters showed a slightly lower sensitivity. However, it offered the same or better resolution therefore an enhanced capability to detect low analyte concentrations, mainly because of the narrower peak bandwidth (FWHM 67 nm). Also, our gold nanodisks' performance in refractometric sensing is similar to other nanoplasmonic sensors reported before, detecting changes between 10^{-4} and 10^{-6} RIU.[56,169,164] We determined the coefficient of variability (CV%) for 80 nm AuND and 100 nm AuND nanodisks, obtaining values 2.4 % and 3.6 %, respectively, over more than 8 nanofabrication processes.

On the other hand, the 80 nm AgNDs demonstrated a significantly higher sensitivity of 430 nm/RIU with a detection limit of 1.3 x 10^{-5} RIU (Figure 2.17c). For 100 nm AgNDs, the sensitivity further

increased to 627 nm/RIU, with an improved detection limit of 5.3 x 10^{-6} RIU (Figure 2.17d). The CV% for the 80 nm and 100 nm AgNDs were 7.3% and 5.2%, respectively, throughout 6 nanofabrication batches. This suggests good reproducibility, similar to that observed with gold nanodisks.

Comparing the performance of the 4 nanoplasmonic sensor designs - silver and gold nanodisks at both 80 nm and 100 nm diameters - a clear distinction emerges. The AgNDs exhibited up to 3 times higher sensitivity compared to their gold counterparts, with the 100 nm silver nanodisks showing the highest sensitivity among all tested samples. These results align with both our simulation studies and existing literature,[46] which suggest that silver's greater electrical conductivity and stronger plasmonic response contribute to its higher sensitivity. However, despite their superior sensing performance, the resolution of AgNDs is comparable to AuNDs, as their LSPR bandwidths are broader than theoretically expected. This discrepancy can be directly attributed to the chemical instability and rapid oxidation of silver under experimental aqueous conditions or even ambient humidity. This trade-off between high sensitivity and material stability is also consistent with previous findings, which emphasize the challenge of maintaining silver's stability in practical sensing applications.[180,193,194]

2.4.2. Chemical stability characterization

While gold is known for its high chemical stability in air and aqueous conditions, silver spontaneously reacts with the environment, especially oxygen, halogens, and sulfur compounds, which can lead to tarnishing (i.e., formation of a thin layer of silver sulfide) and degradation. These reactions can alter the LSPR characteristics of AgNDs, potentially compromising the sensing performance and reproducibility. In this study, we focus on characterizing the chemical stability of the different nanoplasmonic sensors under various laboratory conditions, as well as evaluating the application of different chemical and physical strategies for enhancing its durability and suitability for long-term biological analysis.

The stability of the previously optimized and selected gold and silver sensors were monitored over a two-day period in air atmosphere, at room temperature (25 °C) and at a relative humidity around 70% (Figure 2.18). We measured the LSPR of the gold nanodisks at the beginning of the test and then re-measured it at day 2. The results, presented in Figure 2.18a, showed that the LSPR peak position, bandwidth and intensity of the gold sensors remained unchanged over the two-day period (FWHM = 67 nm and λ_{LSPR} = 680 nm). On the othe hand, the silver nanodisks showed a sharp and well-positioned LSPR peak on Day 1, but by Day 2, the peak had shifted towards higher wavelengths (λ_{LSPR} = 710 nm), broadened significantly (ΔFWHM = 17 nm), and exhibited lower intensity (Figure 2.18b). In addition to these spectral changes, we also observed a considerable color variation in the nanodisk chips that was noticeable to the human eye. Thus, the stability test revealed that the LSPR peak of AgNDs is

indeed susceptible to oxidation and corrosion, resulting in significant changes in their plasmonic properties over a relatively short period at room temperature.

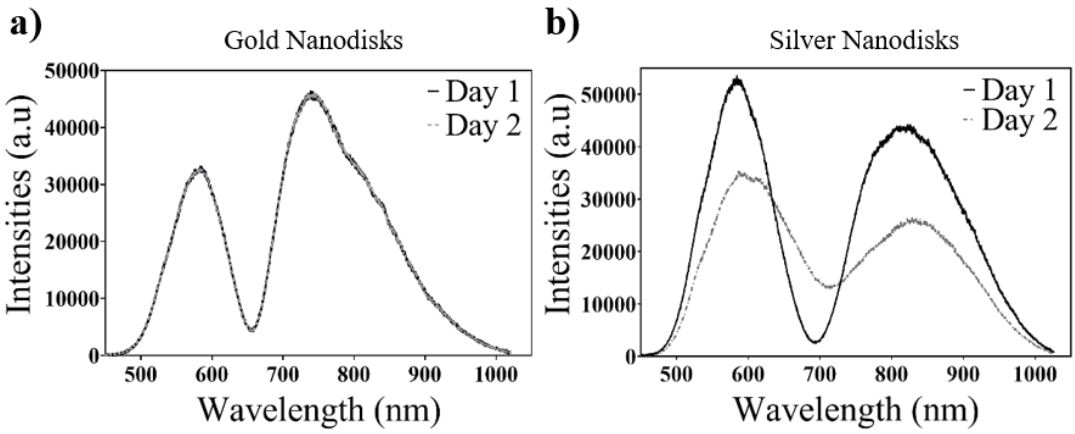

Fig 2. 18. Nanoplasmonic disks stability test at room temperature (Day 1: Solid line and Day 2: dotted line): a) Gold nanodisks, and b) silver nanodisks.

As a primary strategy, in order to protect the AgNDs from environmental sulfur-reactive compounds, responsible for the creation of the tarnish silver sulfide layer, we considered the chemical coating with a functional self-assembled monolayer (SAM). To that, for a good comparison, both the AuNDs and AgNDs sensors were incubated in solution of common alkanethiols (MHDA:MUOH 1:5 molar ratio). To assess the impact of the SAM layer on the plasmonic properties of the nanodisks, the optical spectra were recorded before and after the application of the SAM layer (Figure 2.19). The stability test results for gold nanodisks showed a different outcome compared to silver nanodisks, as expected. The SAM layer significantly retained the stability of the gold nanodisks without compromising their plasmonic properties. The optical spectra recorded before and after the application of the SAM layer demonstrated no changes in the LSPR peak position, peak width and peak intensity (λ_{LSPR} = 680 nm, FWHM = 67 nm) (Figure 2.19a). This indicates that the gold chemical functionalization did not affect the plasmonic properties.

On the contrary, for AgNDs, the optical spectra acquired before and after SAM application revealed considerable changes in the LSPR characteristics, similar to those observed in the previous evaluation. The plasmonic peak shifted to higher wavelengths (λ_{LSPR} = 723 nm), the bandwidth increased (ΔFWHM = 20 nm) and the intensity was reduced. (Figure 2.19b). The use of SAM layer to shield AgNDs against tarnishing caused by ambient sulfur compounds was supposed to prevent the creation of silver sulfides. However, our results suggest that the SAM is not just unable to shield the AgNDs from corrosion, but may have even accelerated their decomposition. This problem is not due to the AgNDs chemical coating

itself or changes in the nanostructures, but rather to the presence of specific chemicals, oxides, and water in the alkanethiol solution used to create the SAM.

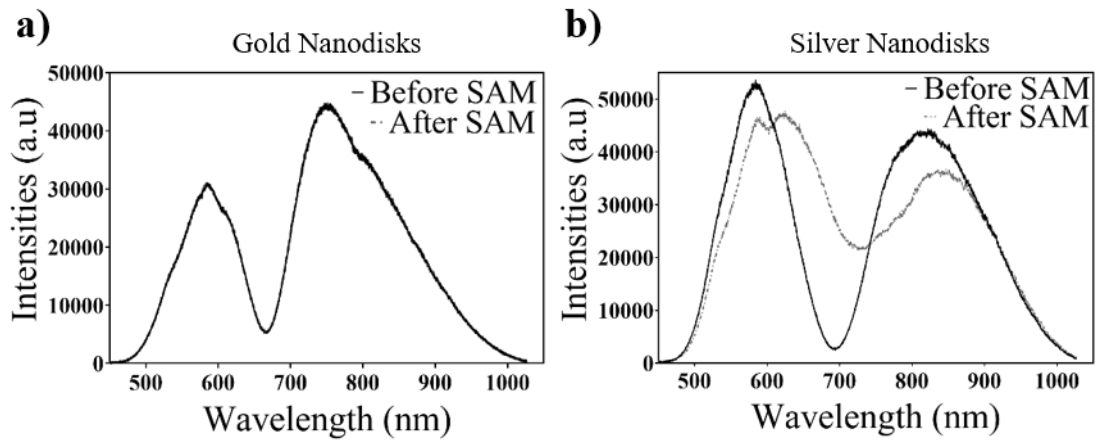

Fig 2. 19. SAM stability test of nanoplasmonic sensors at room temperature before (solid line) and after (dotted line): a) Gold nanodisks, and b) silver nanodisks.

As an alternative strategy for protecting AgNDs, we tested the direct physical coating of the nanostructures with a thin layer of silicon dioxide (SiO_2) at different thicknesses. The SiO_2 evaporation step was incorporated into the nanofabrication protocol immediately after the lift-off procedure in the clean room facility. Initially, two thin layers of SiO_2 (3 nm and 5 nm) were evaporated on two different AgNDs chips. Spectral changes were recorded by mounting the sensors on the LSPR setup and comparing the results with another chip of bare AgNDs, as depicted in Figure 2.20.

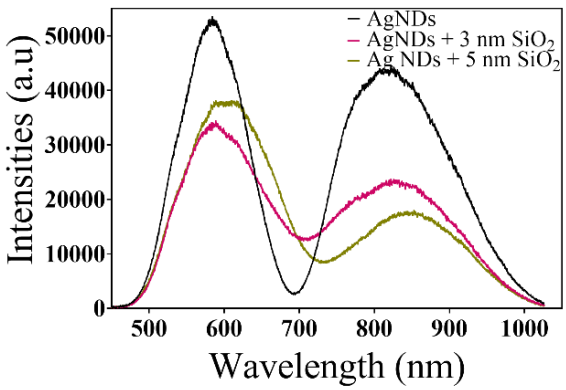

Fig 2. 20. Optical spectra of silver nanodisks: for bare AgNDs (black), AgNDs with a 3 nm SiO_2 layer (pink), and AgNDs with a 5 nm SiO_2 layer (light green).

The resonance peak position λ_{LSPR} shifted from 693 nm to 730 nm, exhibiting a redshift of $\Delta\lambda = 37$ nm as the SiO_2 thickness increased from 3 nm to 5 nm and broader in bandwidth. These results could be attributed to two main causes. First, the SiO_2 coating significantly increases the RI at the interface between the nanostructure and the surrounding medium, causing a substantial shift in the resonance wavelength. Second, the broadening of the resonance peak may be due to the oxidation of the silver nanodisks, which likely occurred when they were exposed to environmental air during the SiO_2 evaporation process immediately after the lift-off procedure.

A potential solution to this issue would be to integrate the SiO_2 coating step within the vacuum evaporation process, before the lift-off, to prevent the silver nanodisks from being exposed to the environment. However, the uncoated edges of the nanodisks would still remain vulnerable to oxidation. As a result, we concluded that silver nanostructures may not be suitable for our future studies, and we will continue using gold nanodisks instead.

2.5. Summary and conclusions

To improve the resolution of our nanoplasmonic sensors for complex biomedical applications, we investigated and characterized various nanostructure sizes, geometries, and materials. We focused on two main strategies: reducing the diameter of the nanodisk structures and switching the plasmonic material from gold to silver.

First, we conducted a computational study to predict the optimal architectures in terms of diameter, height, and gap. This study confirmed our hypothesis that reducing the diameter of AuNDs from 100 nm to 80 nm would shift the LSPR peak to shorter wavelengths and result in a narrower bandwidth. Additionally, we confirmed that using silver nanodisks could significantly enhance both sensitivity and resolution. For experimental validation and further sensor optimization, we implemented a nanofabrication protocol based on hole-mask colloidal lithography. This approach allowed us to fabricate short-ordered arrays of both AuNDs and AgNDs with various geometries. Demonstrating excellent reproducibility for gold nanodisks over 9 fabrication batches. To evaluate their performance as refractometeric sensors, we utilized a customized optical setup based on a prism-coupling configuration integrated with a microfluidic system, controlled through in-house software.

In general, all the fabricated nanoplasmonic sensors exhibited the expected optical properties in terms of LSPR peak position and bandwidth. Among the different sensors tested, the 100 nm AgNDs showed the highest sensitivity. However, the chemical instability of silver, along with the challenges of protecting it from oxidation and corrosion, led us to abandon its use for biomolecular sensing. Despite

this, our newly designed AuNDs demonstrated comparable sensitivity to previous designs, along with improved resolution, making them an ideal choice for further development in biomedical applications.

2.6. Experimental Section

2.6.1. Chemicals

Reagents for cleaning the substrates, including sodium dodecyl sulfate (SDS) 99% and hydrogen peroxide (H_2O_2) 30%, were purchased from Sigma-Aldrich (Steinheim, Germany). Hydrochloric acid (HCl) 37%, sulfuric acid (H_2SO_4) 96%, acetone, and ethanol were provided by Panreac AppliChem (Barcelona, Spain). For hole-mask lithography (HCL) nanofabrication, including poly(diallyldimethylammonium chloride, PDDA), Mw 400000 – 500000, 20 wt% and anisol (99 %) were purchased from Sigma-Aldrich (Steinheim, Germany). E-beam resist polymethyl methacrylate (PMMA) 950 K for nanostructuring was provided by Allresist GmbH (Strausberg, Germany). Sulfate latex beads, 8% w/v, 0.08 μm and 0.1 μm were purchased from Thermofisher Scientific (Paisley, United Kingdom).16-mercaptohexadecanoic acid (MHDA) and 11-marcapto-1-undecanol (MUOH) were provided by Sigma-Aldrich (Steinheim, Germany).

2.6.2. Hole-mask colloidal lithography nanofabrication protocol

First, glass substrates (20 x 26 mm No.4, Menzel-Glaser, Germany) underwent a thorough cleaning process. This involved a sequential cleaning with SSD (0.5 % wt), HCl (0.1 M) and mili-Q water, dry with nitrogen (N_2) stream. Subsequently, the substrates were immersed in a freshly prepared piranha solution (3:1, H_2SO_4:H_2O_2) for 20 minutes. After rinsing and drying with N_2 stream, the HCL fabrication was initiated. Before depositing the colloidal sphere beads, a 200 nm-thick layer of 950 K Polymethyl methacrylate (4% PMMA in 4% anisole) was spin-coated (Laurell Tech. Corporation, WS400BZ-6NPP LITE) (4000 rpm, 3000 $r.s^{-2}$) on piranha-cleaned glass substrates. Following a 5-minute baking process at 155° C temperature, the substrates were subjected to a brief exposure to O_2 plasma (Oxford PlasmaPro 100 Cobra) (18s, 75W, 75 mTorr, 40% O_2-flux) to enhance the hydrophilicity of PMMA-coated substrates. An oppositely charged polyelectrolyte was drop casted onto the PMMA layer to create an adhesive surface. For this purpose, surface was coated with 0.2 wt% PDDA (Sigma-Aldrich, Germany) for 1 min and thoroughly rinsed with mili-Q water and dried with N_2 stream. Following this, colloidal solutions containing 0.2 wt% of 80 nm diameter of polystyrene beads (Invitrogen, USA) were deposited for 1 min, subsequently rinsing with milli-Q water and drying with N_2 stream, respectively. The electrostatic repulsion between the colloidal sphere beads and the attractive force between these spheres' particles and the PDDA layer define a randomly arranged nanoarrays of polystyrene spheres. The hole-mask template was formed by evaporating a 15 nm of

titanium layer as a sacrificial layer using e-beam evaporator (AJA International Inc. ATC-8E Orion) in clean room facility. This sacrificial layer is resistive to O_2 plasma treatment. Then, colloidal spheres were stripped-out by using blue tape, resulting in the removal of the spheres while retaining a PMMA sacrificial layer with a perforated titanium layer, which acts as a mask here, on the top. The sacrificial PMMA layer beneath the holes was removed by O_2 plasma etching treatment (Oxford PlasmaPro 100 Cobra) applied for 300 s at 75 W, 75 mTorr with 50 % O_2-flux. The resulting masks were utilized as a deposition mask for the gold nanodisks. Using electron-beam evaporation, a 1.5 nm thick adhesive layer of Ti was initially deposited, followed by a 19 nm layer of Au evaporation. Finally, the remaining mask was removed through a lift-off process through sonication in acetone and Milli-Q water for 1 minute each at room temperature, followed by rinsing with Milli-Q water and drying using a N_2 stream.

2.6.3. Scanning electron microscopy analysis

The distribution of nanostructures over the glass substrates were characterized by Field Emission Scanning Electron Microscopy Image (FEI Magellan 400L SEM, Oxford instruments) and the gap distances were calculated using ImageJ. Software.

2.6.4. Angle adjustable LSPR biosensor device description

The setup utilized TM-polarized light at different incident angles (45°- 90°) with a collimated polychromatic light beam. The nanodisk substrates were positioned between a trapezoidal prism (n: 1.52) and a refractive index-matching immersion oil (n: 1.51). This assembly was connected to a microfluidic system linked to a syringe pump, which generated a constant sample flow with a manually operated injection (CHEMINERT®, VICI, Texas, USA). Collimated halogen light source (Ocean Optics, USA) was used to illuminate the substrate surface, exciting the localized surface plasmon resonance (LSPR) through the coupled prism. The reflected response was collected by a fiber-coupled spectrometer (Jazz Module, Ocean Optics, USA. To monitor real-time changes in resonance peak position, a polynomial fitting algorithm (National Instruments, Labview, USA) was employed through a custom-made software developed using open-source programming scripts (Python).To optimize signal-to-noise ratio (S/N) and acquisition time, the software acquired 300 reflectivity spectra with an integration time of 3 ms. The plasmonic behaviour of the nanostructures was characterized in water (n: 1.33).

2.6.5. Data analysis

The data from nanoplasmonic sensors were analyzed using Origin 8.0 software (OriginLab, Massachusetts, USA) and Graphpad Prism (Graphpad Software, Inc., California, USA). The mean

sensor response (Δλ) and its standard deviation (SD) were plotted against the change in refractive index (Δη) to generate calibration curves. These curves were fitted using a linear regression model. The experimental limit of detection (LOD) was determined as three times the SD of the sensor signals obtained from the background signal using water as a running buffer. Coefficients of variation (CV%) were calculated as the ratio of the standard deviation to the mean of multiple measurements taken on the same or different sensor chips, expressed as a percentage.

2.6.6. Bulk sensitivity

To evaluate the bulk sensitivity of the nanoplasmonic sensors, various concentrations of hydrochloric acid (HCl) solutions were injected. The concentrations ranged from 25 mM to 500 mM. The injections were performed at a controlled flow rate of 30 μL/min, using a total injection volume of 150 μL for each concentration. This procedure allowed for the assessment of the sensor's response to different HCl concentrations, which is essential for determining its sensitivity and dynamic range.

2.6.7. Stability test

Two different stability tests were conducted on nanoplasmonic sensors. Firstly, the cleaned nanoplasmonic sensor chips were coated with various thicknesses (3 nm and 5 nm) of SiO_2 material. Secondly, the nanoplasmonic sensor chips were immersed in a solution of MHDA (1:5 ratio) at a final thiol concentration of 1 mM, dissolved in absolute ethanol. This immersion was done overnight at room temperature (RT) to ensure proper surface coverage. After the overnight immersion, the sensor chips were thoroughly rinsed with absolute ethanol and dried using a gentle stream of nitrogen gas. Subsequently, all prepared chips were mounted on LSPR instruments. The instrument was used to monitor the nanoplasmonic resonance peak positions and bandwidth, providing critical data on the stability and performance of the sensor chips.

Chapter 3

Design, fabrication, and characterization of all-dielectric nanophotonic sensors

In this chapter, we explore the potential of all-dielectric nanostructures for biosensing applications in the visible range. We optimize dielectric resonances based on Si for sharper spectral features, develop scalable fabrication techniques, and integrate these sensors into compact, user-friendly devices. Finally, we evaluate their performance for refractometeric sensing, comparing them to traditional nanoplasmonic sensors.

3. Design, fabrication, and characterization of all-dielectric nanophotonic sensors

3.1. Context and motivation

The optimization study of nanoplasmonic sensors using different geometries and materials (Chapter 2), suggests that transitioning to high-refractive-index dielectric material can further improve sensing resolution. Introducing dielectric materials, such as silicon (Si), is primarily motivated by the expectation of narrower resonances, resulting from lower energy dissipation, which directly enhances sensing precision. Furthermore, silicon's high refractive index enhances light confinement, increasing the interaction with the surrounding environment and potentially boosting sensor's sensitivity.

A few works have already reported the use of silicon nanostructured substrates for biosensing;[129,130,195–197] however, these technologies are often designed to operate in the NIR, mid-IR, or infrared range, which is not optimal for biological sensing. Moreover, the fabrication of these structures typically relies on expensive and time-consuming techniques like EBL, which limits their scalability and affordability for widespread use. Furthermore, these systems often require large, bulky instruments such as microscopes and spectrometers for operation, making them unsuitable for compact and portable biomedical tools. Therefore, there is a need to develop more cost-effective fabrication methods, extend the operational wavelength into the visible range, and miniaturize the equipment to enable practical applications in biosensing.

The main objective of this chapter is therefore to explore the potential and capabilities of all-dielectric nanostructures for biosensing applications, focusing specifically on their operation in the visible range. First, we aim to identify and optimize all-dielectric resonances that can offer sharper spectral features and improved sensitivity compared to traditional plasmonic structures. Second, the fabrication of these sensors will be addressed using large-scale, cost-effective technique, moving beyond expensive methods to more scalable alternatives. Another important objective is to integrate these dielectric sensors into compact, user-friendly devices, overcoming the challenges of bulky and complex equipment often associated with such systems. Finally, the performance of these sensors will be assessed, with an emphasis on their ability for label-free biomolecular sensing applications as analogues to existing nanoplasmonic sensors.

3.2. Design and computational modelling of silicon nanostructures

Our primary idea is to design a nanophotonic sensor, building on our previous work with gold nanodisk arrays in Chapter 2, but replacing them with silicon nanostructures on a silicon dioxide (SiO_2) substrate. To design and optimize this sensor, we utilized the computational tool COMSOL Multiphysics for simulation analysis considering a unit cell of silicon nanodisks (SiNDs) for analysis of electromagnetic properties of the device. Our focus was on factors such as near-field distributions and resonance wavelengths, crucial for achieving the resonance in the visible range with refractometeric sensitivity and narrow FWHM. The model was set up in a three dimensional environment, where a single unit cell of the nanodisk was created and periodic boundary conditions were applied. The nanodisk was placed on a glass substrate with water as the cladding layer (RI 1.33). The dimensions of the silicon nanodisk were varied both in terms of height (h) and dimeter (d). For the glass substrate, the refractive index was calculated using the Sellmeier formula,[186] a well-established equation that relates the refractive index to the wavelength of light, taking into account the dispersion characteristics of material. For the silicon nanodisks, the refractive index was calculated using an interpolation function based on reported data,[187] ensuring accurate modelling of the silicon's optical characteristics across the relevant wavelength range.

A polarized light source with a wavelength range of 400 nm to 900 nm was introduced from the bottom of the glass substrate at an incident angle of $\theta = 70°$ with both TM and TE polarizer modes. These configurations are corroborated by a previously reported study that employed 300 nm diameter with the average height of 185 nm of silicon nanopillers, obtaining the resonance peak position within a range from 400 nm to 900 nm.[198,199] The system's response was collected from the top of the cladding layer. To ensure precise and accuracy of the results, a fine mesh ranging from 3 nm to 100 nm was used throughout the simulation analysis, accurately capturing the interaction of light with the nanostructure. We analyzed the multi-slice polarization in terms of the electromagnetic field distribution around the silicon nanodisk's single unit model (as demonstrated in Figure 3.1).

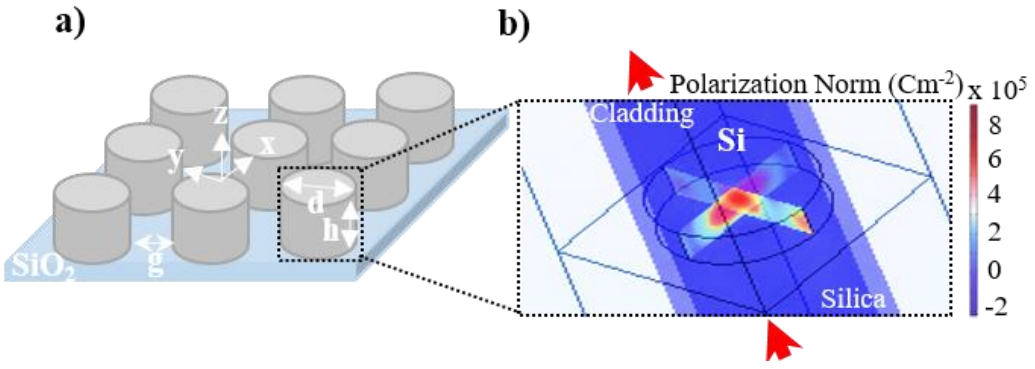

Fig 3. 1. a) Schematic illustration of SiNDs arrays on a glass substrate, indicating the three-dimensional orientation (x, y, z) and dimensions of the nanodisks (height and diameter), and b) Distribution of electric and magnetic fields within a single 3D unit cell of the silicon nanodisk array. The colour scale represents the polarization norm in C/m², showing the intensity of the fields.

First, we investigated the effect of TE and TM polarizations on the resonance modes to understand light interactions with silicon nanodisks, using determined geometry parameters: diameter = 300 nm, height = 130 nm, and gap = 150 nm. A detailed explanation of the optimization process will be provided in the following sections. The silicon nanodisk transmission spectra showed the optical response and resonant features under both polarizations in visible range (Figure 3.2).

Under TM polarization, we observed the appearance of 2 major resonance peaks within the visible range. This phenomenon is due to the ability of the perpendicular electric field component to excite various resonant modes inside the nanodisks, including higher-order modes.[200] The first resonance peak was recorded at position λ = 655 nm, with narrower bandwidth (FWHM = 8nm) but a slightly lower intensity than the second peak, found at λ = 688 nm, with a broader bandwidth (FWHM = 22 nm). The first and narrower peak is presumably produced by a more coherent and sharp resonance, potentially indicating a higher quality factor.

Under TE polarization, only one resonance peak was recorded at λ = 680 nm with FWHM of 22 nm. In TE polarization, where the electric field is parallel to the surface of the nanodisks, more complex and higher-order modes are excited. These modes result in broader and less confined resonance peaks.[201] Additionally, in TE mode, the electromagnetic field is less confined to the nanodisks and interacts more with the external medium, which also leads to wider resonances. Based on these analysis, the TM polarization mode would likely be considered the best polarization mode for the silicon nanodisks for further optimization studies.

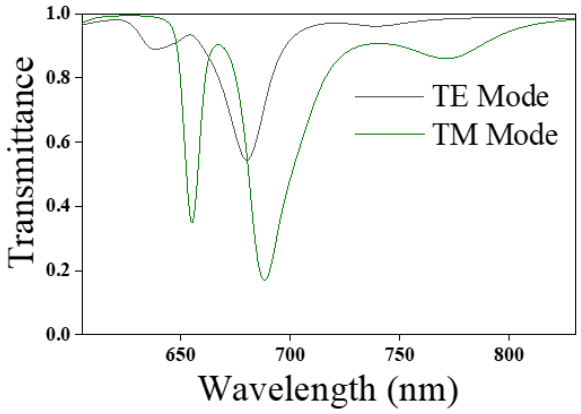

Fig 3. 2. Displays the transmission spectra of the silicon nanodisks with diameter = 300 nm, height = 130 nm and gap = 150 nm for transverse electric (black) mode and transverse magnetic (green) mode.

Next, we tested the diameter of SiNDs within range from 100 nm to 300 nm considering height of 100 nm while maintaining the gap distance, g = 150 nm (Figure 3.3). The spectral analysis showed that larger diameter 300 nm exhibit optimal performance with strong, well-defined resonant modes and sharp, narrow peaks, indicating substantial electromagnetic confinement. These larger nanodisks also show better separation of different resonance modes,[202] and support higher-order modes, resulting in a narrower bandwidth.[203]

As the diameter decreases, the resonance features become irregular and broader, reflecting weaker electromagnetic interactions and reduced confinement. This size also potentially exhibits multimode behavior due to the emergence of higher-order resonances. The smallest diameter (100 nm) shows poor resonance quality. It is worth mentioning that extremely large diameters may lead to a wider resonance peak due to scattering enhancements. Therefore, an optimal geometry is suggested to achieve narrower and sharper resonance behavior in silicon nanodisks. Based on these results, we selected 300 nm diameter for further studies.

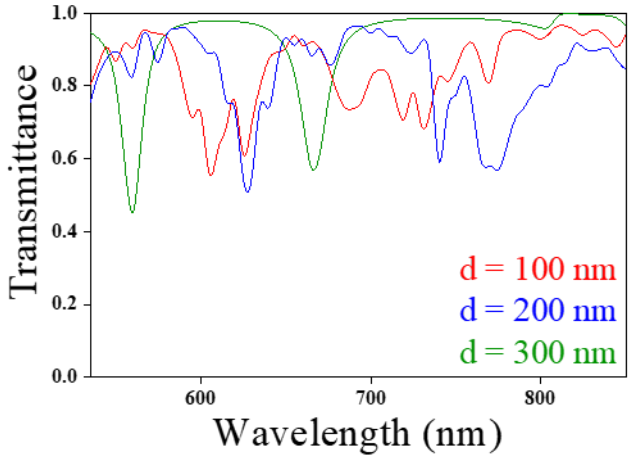

Fig 3. 3. Transmission spectra of silicon nanodisks with diameters 100 nm (red), 200 nm (blue) and 300 nm (green) at a height of 100 nm while maintaining the gap of 150 nm. The spectra show electromagnetic resonance peaks in visible spectrum range at an angle of $\theta = 70°$.

The height of the nanodisk plays essential role in tailoring their electromagnetic resonance characteristics such as filed confinement and mode support.[198,202] Herein, we explored the impact of varying the height of SiNDs from 90 nm to 150 nm, using an optimized diameter (d = 300 nm) and maintaining a gap (g = 150 nm). The obtained spectra, displayed in Figure 3.4, revealed multiple

resonance peaks across both visible and near-visible spectra and the optical resonance properties for each height are calculated in Table 3.1. By increasing the height from 90 nm to 150 nm, it resulted in progressively narrower and better resolved peaks. The SiNDs with 150 nm height showed the narrowest peaks λ = 624 nm (FWHM = 12 nm) at) and at λ = 783 nm (FWHM = 8 nm). This improvement is due to larger volume available for light interaction within nanodisks which allows for enhanced field confinement and support higher-order resonant modes, resulting into narrower resonance peak.[199] Nevertheless, the SiNDs with 110 nm height (green) showed a more intense and sharp resonance peak, making it an optimal choice for biosensing applications.

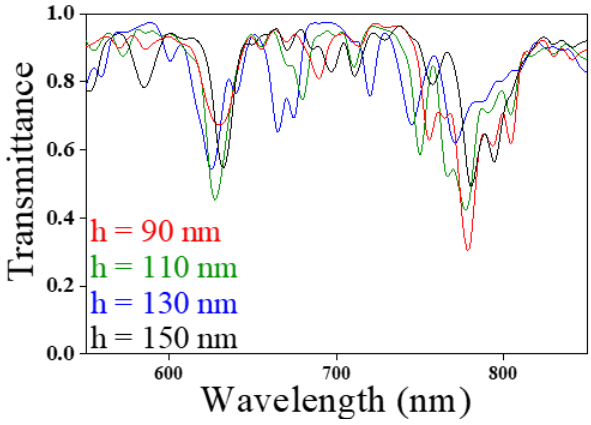

Fig 3. 4. Transmission spectra of silicon nanodisks with varying heights of 90 nm (red), 110 nm (green), 130 nm (blue) and 150 nm (black) at an optimized diameter of 300 nm, while maintaining the gap distance of 150 nm. The spectra show electromagnetic resonance peaks in visible and near-visible spectrum range at an angle of θ = 70° degrees.

Table 3. 1. Optical resonance characteristics of silicon nanodisks at different heights.

Height (nm)	**Visible Spectrum**		**Nera-Visible Spectrum**	
	Wavelength (λ, nm)	*FWHM (nm)*	*Wavelength (λ, nm)*	*FWHM (nm)*
90	623	18	780	15
110	622	14	750	9
130	630	16	747	10
150	624	12	783	8

Later, we systematically examined the gap distance ranging from half of the diameter (g = d/2 = 150 nm) to twice of the diameter (g = 2d = 600 nm) (Figure 3.5). As the gap increases, we observed a red shift in the resonance peaks along with an increase of the resonance bandwidth, which can be attributed to the reduced near-field coupling between the SiNDs (Table 3.2). At smaller gaps (150 nm, green), multiple peaks indicate strong electromagnetic interactions between neighboring nanodisks, resulting

in near-field coupling and the splitting of resonance energies into lower and higher modes. Additionally, smaller gaps increase the electromagnetic field intensities in the gap regions, which can affect the overall resonance properties of the system. In contrast, larger gaps of 300 nm (blue) and 600 nm (red) reduced near-field coupling, causing shifts and broadening of resonance peaks and altering field distribution.

These effects are important for optimizing the design and performance of SiND-based devices in various photonic and sensing applications. Based on these results, we chose the smaller gap of g = d/2 = 150 nm for further sensitivity studies, as it demonstrated optimal resonance characteristics with narrow peaks.

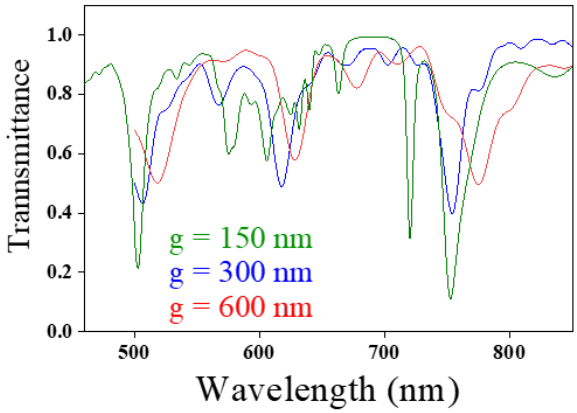

Fig 3. 5. a) Transmission spectra analysis of silicon nanodisks gap distances ranging from 150 nm to 600 nm, d = 300 nm and h = 110 nm of SiNDs.

Table 3. 2. Optical resonance characteristics of silicon nanodisks at different gap distances.

Gap (nm)	***Wavelength (λ, nm)***	***FWHM (nm)***
150	502	11
	720	5
	752	19
300	617	17
	752	18
600	628	18
	755	33

Once geometric parameters of SiNDs were assigned, we evaluated the potential sensitivity of the resonances to changes in the RI of the medium. As the RI of cladding layer was varied from 1.331 to 1.334, a shift in some of the resonance peaks was observed (Figure 3.6a). By focusing on our targeted resonance peak around 700 nm, a significant displacement of the peak minimum's wavelength position

can be seen (Figure 3.6b). The resonance shift in SiNDs occurs due to changes in the surrounding medium's refractive index, similar to plasmonic systems.[204]

The refractometeric sensitivity analysis was performed by measuring the change in resonant wavelength ($\Delta\lambda$) as a function of the change in refractive index (Δn, RIU) (Figure 3.6c). By fitting the plot to a linear regression model, we could calculate the bulk sensitivity (S_B) of the designed device at 200 nm/RIU, which is comparable with conventional nanoplasmonic sensors (as described in Chapter 2).

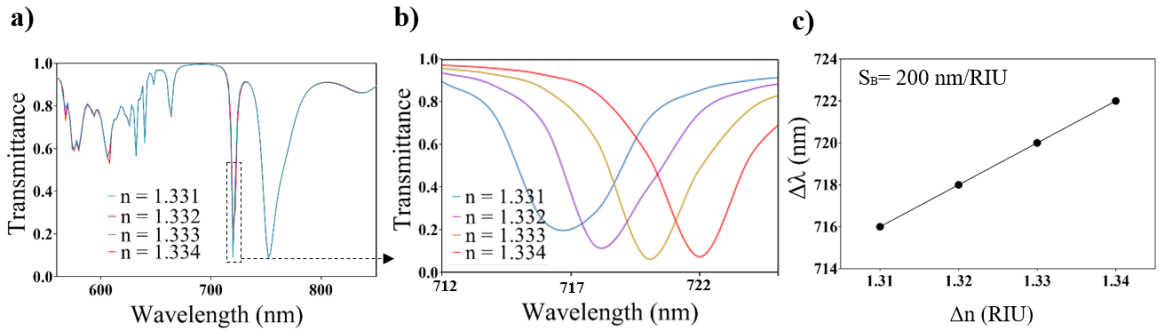

Fig 3. 6. Bulk sensitivity of silicon nanodisk with optimized parameters with diameter, d = 300 nm, height, h = 110nm and interspacing gap, g = 150 nm: a & b) Transmission spectra of refractive index changes in range from 1.331 to 1.334 (water cladding), and c) Bulk sensitivity calibration curve of silicon nanodisks.

In summary, we designed a SiNDs sensor with optimized dimensions (d = 300 nm, h = 110 nm, and g = 150 nm), exhibiting a sharp and narrow resonance peak in the visible range (λ = 720 nm, FWHM = 5 nm). The refractometeric sensitivity of our targeted SiNDs resonance peak has been determined at around 200 nm/RIU, predicting a comparable bulk sensitivity to conventional LSPR sensors (e.g., AuNDs).

3.3. Nanofabrication and characterization of SiNDs nanophotonic sensors

For the fabrication of our silicon nanophotonic arrays, we opted for applying and optimizing a protocol based on HCL technique. As demonstrated in the previous chapter, HCL allows for a large-scale and cost-effective production of short-ordered arrays of nanostructures with good reproducibility and precision. Although the short-ordered arrays could slightly differ from our simulated regular arrays in terms of peak positioning and bandwidths, this fabrication technique will enable the easy fine-tuning of the dimensions and geometry of the sensors, greatly accelerating the optimization process compared to other commonly employed techniques, like EBL. Moreover, recent studies have been shown that short-

ordered arrays of SiNDs can effectively support the desired Mie resonances in the visible and near-infrared spectral range.[198,205]

3.3.1. Nanofabrication protocol optimization

As substrates, we commercially acquired glass wafers with one-side coating of a polycrystalline Silicon (polySi) layer of 130 nm. PolySi was selected, instead of amorphous Si, due to its much lower optical absorption and scattering losses in the visible to NIR range, making it better suited for applications where low-loss optical performance and high quality resonances are required. Besides, polySi has a higher refractive index, it is more stable under optical illumination, and it is widely used in semiconductor and photonic industries, especially in CMOS-compatible fabrication environments. Prior to start the nanofabrication process, the polySi substrates (25 x 25 mm^2) were cleaned thoroughly by rinsing with 0.5% wt SDS, followed by 0.1 M HCl, and milli-Q water. Subsequently, the cleaned substrates underwent a 5-min sonication process in acetone, isopropanol and milli-Q water at 65 °C, rinsed again with milli-Q water and dried using a stream of N_2. Following these preparatory steps, the HCL fabrication process was initiated. Each step of the fabrication was optimized by following the nanofabrication protocol depicted in Figure 3.7 as described as follows:

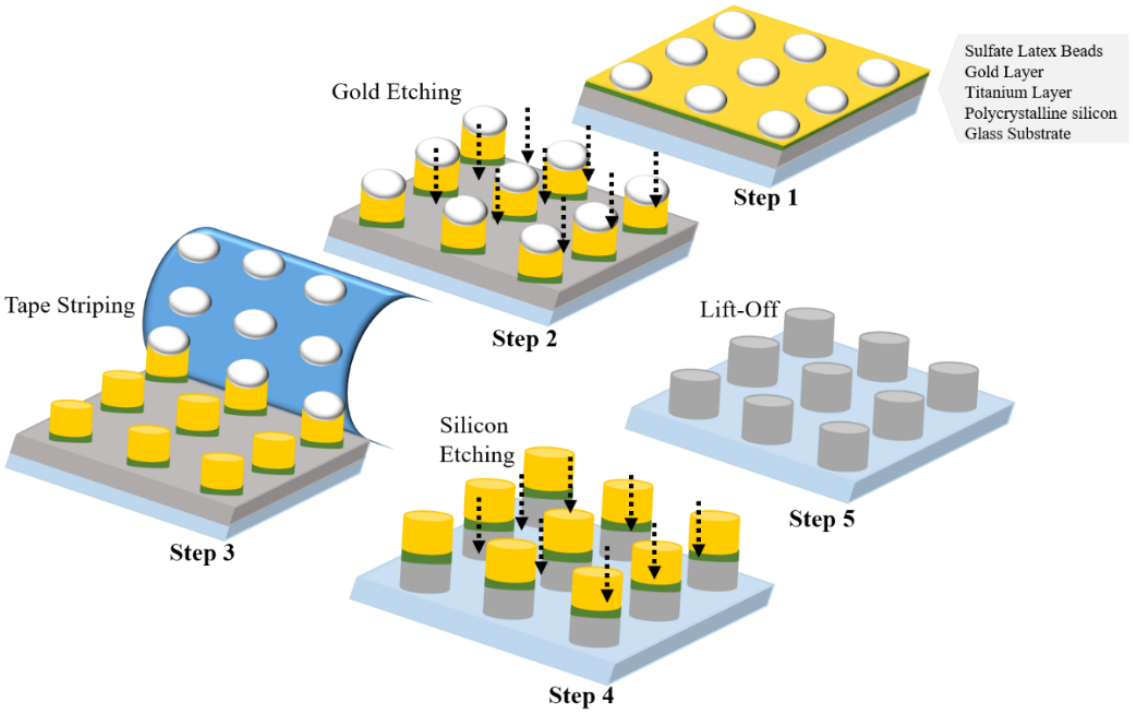

Fig 3. 7. Schematic illustration of SiNDs hole-mask colloidal lithography nanofabrication protocol steps.

Step 1: Evaporation of sacrificial layer and colloidal lithography

The polySi substrates were first coated with 2 nm of Ti and 50 nm of Au as a sacrificial layer using e-beam evaporator in clean room facility. To enhance the surface hydrophilicity, the substrates were subjected to a brief exposure oxygen plasma (18 s, 75 W, 75 mTorr, 40 % O_2-flux). Then, the colloidal lithography procedure was performed by coating the substrates with PDDA and sulphate latex beads. Various diameters ranging from (60 nm - 300 nm) and different concentrations (0.2% to 0.6%) of colloidal beads were drop-casted on the PDDA-coated substrates, covering the entire surface.

Step 2 & 3: Gold etching and removal of beads

Subsequently, the gold layer was vertically etched using argon (Ar) gas in a reactive ion etching (RIE) process. The parameters were selected at pressure 6 mTorr, power HF/ICP 40/250, Ar-flux 50%, and time 2 min 30 s. The beads acted as masks during the gold etching process and after, they were removed by gentle tape stripping.

Step 4: Silicon etching

Next, to completely etch the polySi layer a C_4H_8/SF_6 RIE process was optimized.[198] Different etching rates from 60 nm/min to 190 nm/min with different time intervals from 75 s to 250 s were evaluated. This range allowed us to observe how different rates affected the precision and uniformity of the etching process, to achieve the desired nanodisk height without over-etching or under-etching. Both the pressure (ranging from 15 to 20 mmTorr) and power settings (inductively couple plasms (ICP) and radio frequency (RF)) were adjusted and optimized during the etching process. These adjustments helped in controlling the etching environment and achieving consistent results. These optimizations were crucial to ensure that the Si nanodisks met our specifications in terms of height and uniformity. All the optimization details and settings used during the etching process are provided in Table 3.3.

Step 5: Lift-Off

For the final lift-off of the gold layer from top of the polySi nanodisks, two approaches were tested based on piranha and gold etchant solutions. At first, the chips were immersed in piranha solution for 1 to 3 min. However, this method was not successful in completely removing the gold layer. We then used a potassium iodide (KI) mixture, and immersed the chips for different durations, ranging from 2 min to 30 min at room temperature. Additionally, we applied sonication for 2 to 30 min at temperature between 25°C to 65°C. All the optimization parameters for lift-off are detailed in Table 3.3

Table 3. 3. Key parameters for optimizing the nanofabrication protocol of SiNDs using the HCL-based technique.

Parameters	Range	Optimized Parameters
Diameter (d, nm)	60 – 300	300
Height (h, nm)	130	130
Density (%)	0.2 – 0.6	0.4
Si Layer Etching		
Etching Rate (nm/min)	150	150
C_4F_8 (sccm)	25-30	30
SF_6 (sccm)	10	10
ICP (W)	0-1200	1000
RF (W)	30-300	50
Time (s)	75 - 250	200
Lift - Off		
Gold Lift-Off : Potassium Iodide (KI) Solvent		
KI - Incubation Time (min)	2 - 30	20
KI – Sonication (°C)	25 - 65	45
KI – Sonication (min)	2 - 20	10
Angle (degree)	61 – 70	70

Through this method, we could achieve the desired silicon nanostructures with dimensions, d = 300 nm and h = 130 nm. We fabricated multiple batches (6 chips) of SiNDs (25 x 25 mm^2 chips) with different diameters and using different colloidal concentrations (%), which can be individually tested and characterized. At least 4 different batches were fabricated to confirm the reproducibility of the method.

3.3.2. SEM characterization of SiNDs arrays

During the optimization of the HCL protocol, the fabricated arrays were characterized through SEM to analyze the geometry and distribution of the nanodisks. Figure 3.8 shows the SEM images obtained for different SiNDs diameters, employing colloidal beads of 60, 80, 100, 200, and 300 nm. A 0.4% of colloidal density was employed in this preliminary experiments. A random distribution of nanostructures was obtained for all cases, as expected, with a significant variability in the diameters (see Table 3.4).

It was difficult to calculate the mean diameter and colloidal density of 60 nm nanostructures because no clear nanostructures were visible in the SEM images (Figure 3.8, 60 nm). This might be due to the resolution limits of the SEM or insufficient contrast at this small scale. The SiNDs with diameters of 80 nm, 100 nm and 200 nm appeared non-uniform in size with random distribution along a high percentage of variability between different batches. The high variability observed in the SiNDs fabrication process, which was not seen in the production of nanoplasmonic sensors (AuNDs and AgNDs), can be attributed to two main factors. First, the absence of a PMMA coating in the SiNDs

protocol, which was not implemented due to difficulties in lifting off this polymer on Au substrates, may have contributed to the variability. Second, the different etching and lift-off processes utilized in the SiNDs protocol, compared to the HCL protocol used for nanoplasmonic sensors, may have played a role. The SiNDs fabrication involves harsh RIE treatments and lift-offs, which could affect both the uniformity of the structures array and their diameter.

In contrast with 300 nm of diameter, the nanodisks were quite regular in size and showed a short-ordered distribution. At this larger size, the fabrication process seems to be more stable and controllable, leading to more consistent and uniform nanodisk formation. The coefficient of variability calculated for the 300 nm nanodisks was around 8.5%. Besides, 300 nm diameter is the optimal value predicted by our simulations for SiNDs sensors.

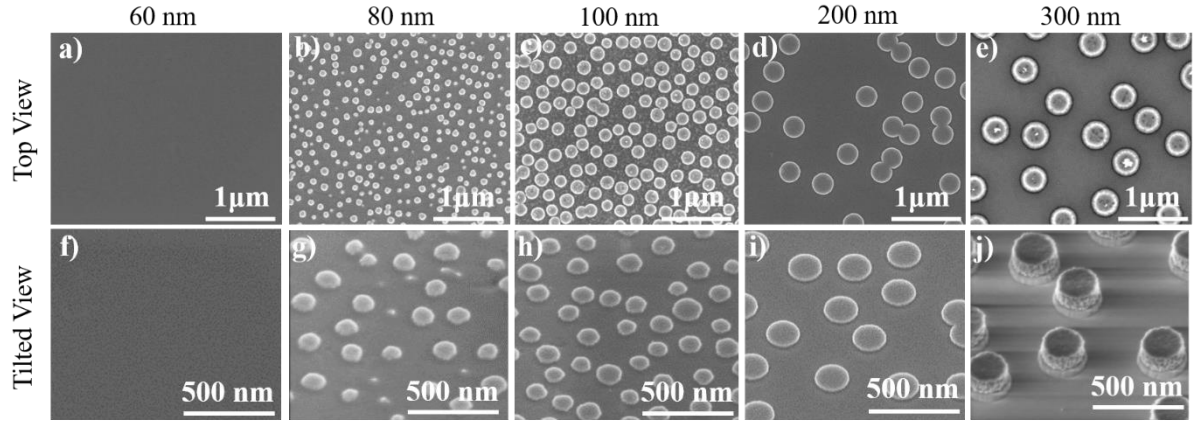

Fig 3. 8. Scanning electron microscopy images of SiNDs fabricated in diameter (60 nm to 300 nm).

Table 3. 4. Summary of diameters and coefficient of variability (%) of SiNDs fabrication.

Targeted Diameter (d, nm)	**Calculated Diameter (d, nm) (Mean ± SD)**	**Variability Percentage (%)**
80	69.8 ± 30	45
100	89.7 ± 20	29
200	210.9 ± 12.7	19
300	313 ± 15	8.5

Next, we evaluated the density of 300 nm colloidal spheres in a range from 0.2% to 0.6%. SEM images showed the nanodisk distribution with increasing gaps for increasing colloidal density (Figure 3.9, Table 3.5). According to our simulations, the optimum gap for SiNDs sensors should be around 150 nm, which corresponds to a 0.4% colloidal density. Therefore, it was selected for subsequent optimization.

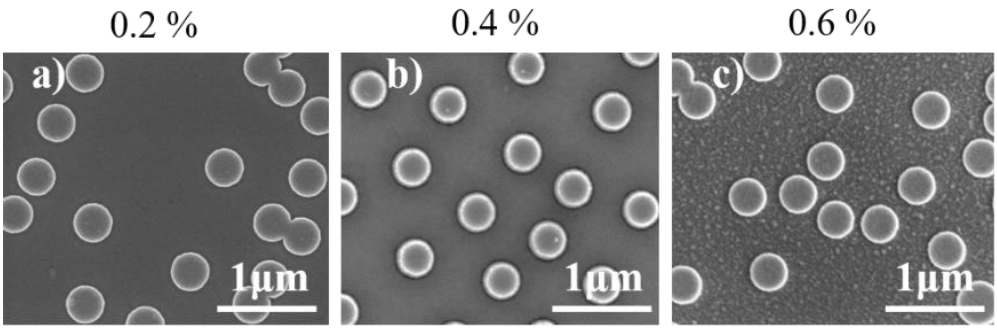

Fig 3. 9. SEM images of silicon nanodisks fabricated with the diameter of 300 nm at 150 nm/min etching rate for 75 seconds, with colloidal sphere densities (0.2 % to 0.6 %).

Table 3. 5. Summary of colloidal concentrations and gaps of SiNDs fabrication.

Colloidal Concentrations (%)	**Gap (nm) (Mean ± SD)**
0.2	132 ± 14.8
0.4	156 ± 8.5
0.6	180 ± 11.7

As can be observed in previous SEM images, the height of the nanostructures obtained so far was highly variable and not reaching the desired 110 nm. To optimize the pSi layer etching, we first tested different etching rates, ranging from 60 nm/min to 190 nm/min, over a fixed duration of 75 s (Figure 3.10). At the lower etching rate (Figure 3.10a), the resulting nanostructures had a height of approximately 10 nm. This minimal height likely corresponds to the residual gold layer on top of the nanodisks, indicating that the lower etching rate was insufficient to penetrate the silicon layer coating the substrate.

Conversely, at the highest etching rate, the nanostructures appeared almost eroded (Figure 3.10c). The moderate etching rate (150 nm/min, Figure 3.10b) produced the most consistent results, yielding an average height of 41 nm with a smooth etch. It is worth noting that these SEM images were taken before the lift-off process, which is why the gold coating is visible on top of the silicon nanodisks in Figure 3.10b. Based on these findings, we selected the 150 nm/min etching rate for further optimization.

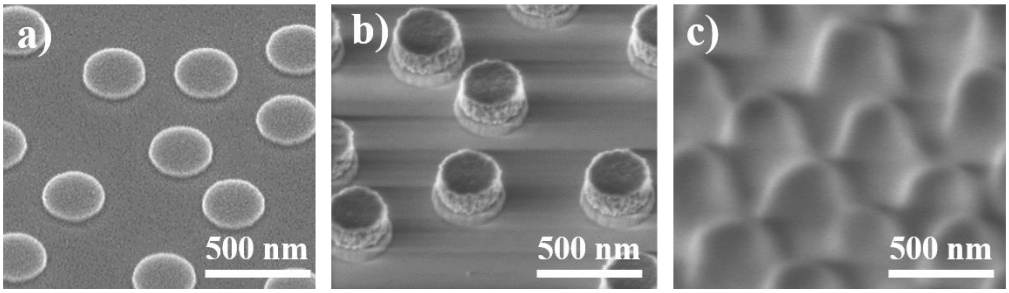

Fig 3. 10. SEM images of SiNDs at different etching rates for 75 seconds. a) At a lower etching rate of 60 nm/min, b) A moderate etching rate of 150 nm/min, and c) At a higher etching rate of 190 nm/min.

Next, with the fixed etching rate, we varied the etching times from 75 s to 250 s. Figure 3.11 shows the SEM images of the different sensors fabricated, with the determined heights and gaps specified in Table 3.6. The most suitable nanostructures were obtained with 200 s etching time, with a mean height of 128.5 nm ± 2.5 nm and a mean gap of 156.2 nm ± 8.5 nm. Taking into account that our initial substrates were coated with a 130 nm layer of polySi, we could not expect to obtain nanostructures shorter than that. Moreover, it can be observed that at etching times longer than 200 s, the top edges of the Si nanodisks began to show damage.

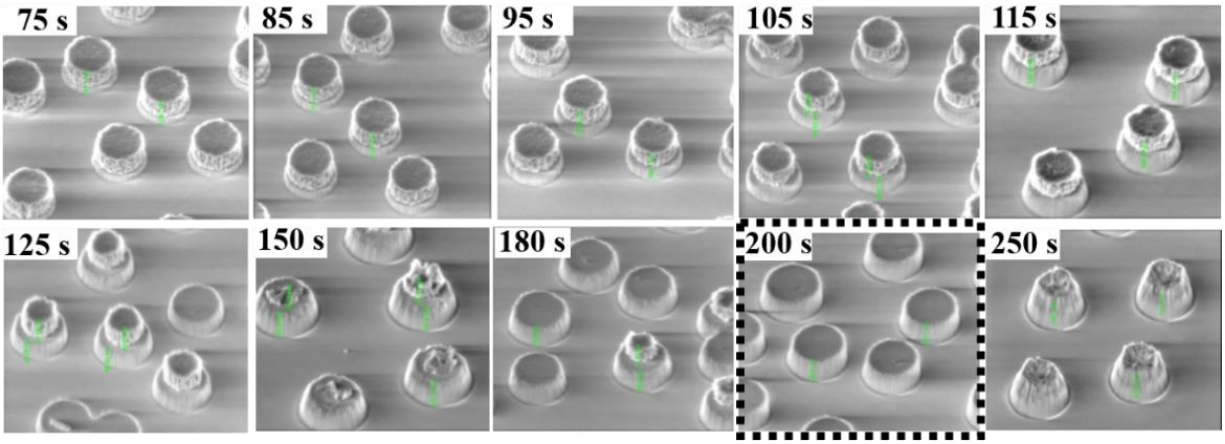

Fig 3. 11. SEM images of SiNDs fabricated at different etching time (75 – 250 seconds) at 130 nm of higher and 300 nm of diameter – 150 nm/min etching rate and 0.4% colloidal sphere density. The scale bar of all SEM images is 500 nm.

Table 3. 6. Summary of height and gap of SiNDs at various etching times.

Si Etching Time (s)	**Colloidal Sphere Density (0.4%), Expected diameter: 300 nm and height: 130 nm**	
	Calculated Height (h, nm) (Mean ± SD)	*Gap (g, nm)* (Mean ± SD)
75	37.5 ± 5.2	139.6 ± 11.6
85	51.82 ± 4.9	142.8 ± ±12.8
95	63.16 ± 4.5	140.4 ± 11
105	64.8 ± 3.5	146.5 ± 11.5
115	65.5 ± 3.8	145.6 ± 9.8
125	83.7 ± 4.2	135.8 ± 9.5
150	121.6 ± 3.9	141.3 ± 8.9
180	137.3 ± 3.8	140 ± 8.6
200	128.5 ± 2.5	156.2 ± 8.5
250	145.3 ± 3.5	167.6 ± 9.5

In addition, we optimized the final lift-off process of the chips, in which the sacrificial Au layer covering the SiNDs is removed. For that, we tested both piranha solution and a KI solution. For the KI etching, we optimized the incubation time, further including a sonication step for different durations (2 – 30 min) and at different temperatures (25°C – 65°C). Figure 3.11 shows SEM images of SiNDs after each lift-off procedure. As can be seen, that unsuccessful etching leaves gold residues on top of the nanostructures. Clean structures were achieved by incubating in KI solvent for 20 min, followed by 10 min of sonication at 45°C, and a final 3-5 min of sonication in milli-Q water, which successfully removed the gold material from the SiNDs.

Interestingly, the successful etching and lift-off could also be observed at bare eye. Figure 3.12 shows the SiNDs chips fabricated with different etching times, before and after Au lift-off. The transparent color corresponding to Si nanostructures on a glass substrate was only achieved at 200 s, confirming the removal of both gold residues on top of the nanodisks and the polySi coating.

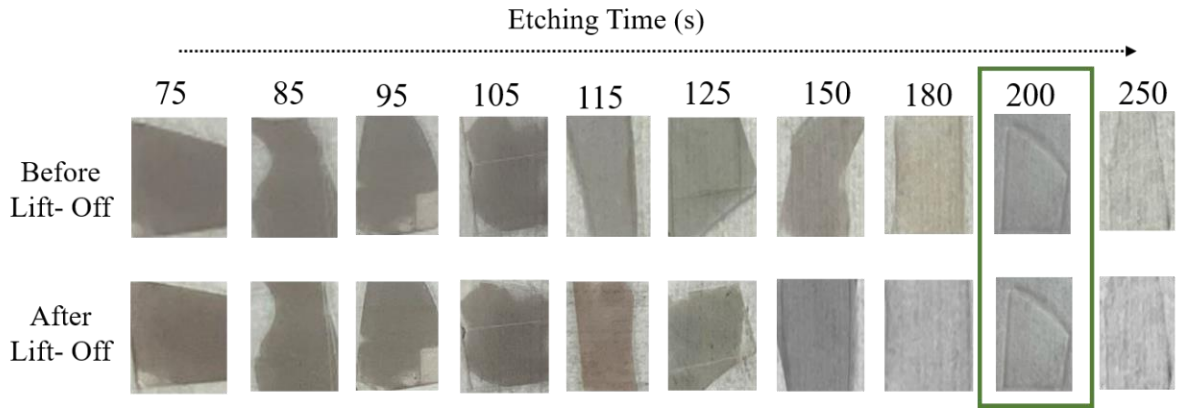

Fig 3. 12. Photographs of SiNDs fabricated using varying etching times (75 – 250 s). The top row shows the nanodisks before the lift-off process, while the bottom row shows the nanodisks after the lift-off process. The green box highlighted the SiNDs with optimized parameters, demonstrated completely removal of gold and polySi coating layers.

With this comprehensive optimization, we successfully refined the nanofabrication protocol to produce SiNDs with an average height of approximately 128.5 ± 2.5 nm, a diameter of 313 ± 15 nm, and a gap distance of 156.2 ± 8.5 nm, exhibiting a low variability of 8.5 %. These dimensions closely match our simulation design, mainly differing in the array regularity and the slightly higher height of the structures. The fabrication method proved to be highly reproducible, offering precise control over the diameter, height, and gap distance of the nanodisks, and importantly, it allowed us to experimentally adjust all parameters to obtain the desired arrays in a facile and cost-effective method.

3.3.3. Optical spectroscopy characterization of silicon nanophotonic sensors

We proceeded to assess the optical response and refractometeric sensing capability of the SiNDs sensors. After a standard cleaning, SiNDs chips were mounted on our custom-built, angle-variable optical set-up employed for the characterization of AgNDs in Chapter 2 (section 2.3.3). The sensors were illuminated at angle of incidences in the range of θ = 63° to θ = 70° using both TE and TM polarization modes. The reason for angle optimization was based on the fact that different nanodisks heights can excite multiple resonance peaks at different wavelengths, as predicted in our simulation study. Since the SiNDs were fabricated with 130 nm of height and simulation optimized height was 110 nm, there is a possibility that with increased height, the resonance spectrum changes. Figure 3.13 shows the spectra obtained for the SiNDs with different polarizations and at different angle of incidence.

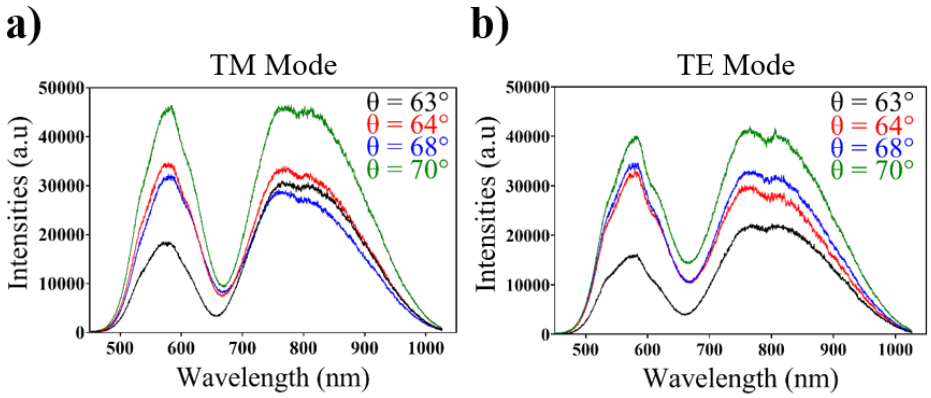

Fig 3. 13. Shows the optical spectra of SiNDs at incidence angles ranging from 63 ° to 70 ° in two different polarization modes: a) TM and b) TE.

In both cases, a resonance peak was obtained in the visible range (Table 3.7). As predicted by simulations, TM polarization yielded a narrower and more intense resonance band (FWHM = 84 nm) at λ = 668 nm when illuminated at 70°. In contrast, TE polarization produced a broader and less intense resonance peak at the same wavelength, due to weaker coupling from the electric field orientation parallel to the silicon nanodisk plane.[206] The critical angle (70°) maximizes light-nanodisk coupling, optimizing resonance conditions and producing the sharpest.[207,208]

The discrepancy between the simulated FWHM of 5 nm and the experimental value of 84 nm arises from idealized simulations versus practical fabrication limitations. Actual nanodisk arrays have random distribution, leading to broader resonance peaks. While taller nanodisks theoretically enhance resonance, practical factors like optimal height limits and random distribution may limit this

enhancement. Overall, we achieved fabrication of SiNDs sensors with electromagnetic resonances in the visible spectrum.

Table 3. 7. Resonance characteristics of silicon nanodisks under TM and TE polarization modes at various angles of incidence.

Angle (θ)	**TM-polarizer**		**TE-polarizer**	
	Wavelength (λ, nm)	*FWHM (nm)*	*Wavelength (λ, nm)*	*FWHM (nm)*
63°	656	102	661	110
64°	668	94	667	96
68°	668	91	667	97
70°	668	84	666	92

3.3.4. Evaluation of SiNDs sensors for refractometeric sensing

To ultimately evaluate the refractometeric sensing capability of our new SiNDs sensor, we performed a bulk sensitivity calibration curve. Using milli-Q water as a running buffer, serial dilution solutions of HCl (25 mM, 50 mM, 100 mM, and 500 mM) with known RI were passed through the microfluidic system. The resonance wavelength shifts displacements (Δλ, nm) were recorded and plotted as function of the RI changes (Δn, RIU) (Figure 3.14).

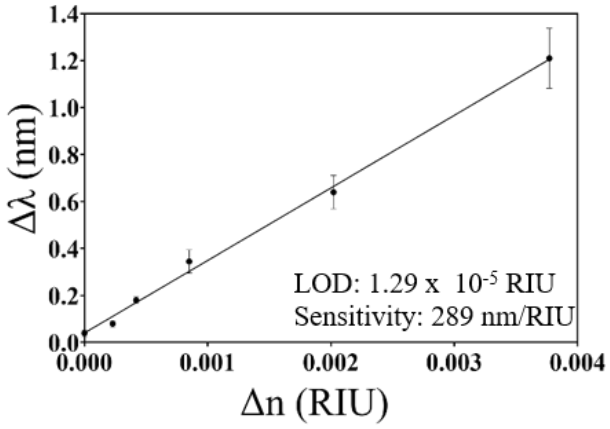

Fig 3. 14. Bulk sensitivity calibration curves of silicon nanophotonic sensors obtained with sequential measurements of different HCl concentrations over a milli-Q water running flow. Each measurement corresponds to the mean ± SD of triplicate measurements.

The bulk sensitivity was determined at 289 nm nm/RIU with a limit of detection of 1.29 x 10^{-5} RIU (Figure 3.14). Notably, this SiNDs sensor demonstrated a higher bulk sensitivity compared to the plasmonic AuNDs sensor (183 nm/RIU, Chapter 2, Figure 2.17) but a similar LOD (1.3 x 10^{-5} RIU). This can be attributed to the fact that the resonance peak for SiNDs was broader (84 nm) than those of AuNDs (67 nm), which was unexpected. This difference may result from the distinct interactions of silicon and gold with light or variations in nanodisk size and arrangement and the fact that our fabricated Si nanodisks were taller than those in the simulations but with random distribution, likely contributed to this broader resonance.

Compared to previously reported studies using dielectric nanoresonators, our SiNDs sensors could show a superior performance (bulk sensitivity 289nm/RIU). The most similar system in literature, random arrays of SiNDs of 130 nm in height and 280 nm diameter, only achieved a bulk sensitivity of 89 nm/RIU.[198] Another study utilizing 50 nm height SiNDs in periodic arrays reported a bulk sensitivity of 227 nm/RIU.[116] Our fabricated silicon sensor shows a comparable performance in detecting RI changes, falling within the reported range of sensitivities spanning from 86.7 to 657 nm per RIU.[209,210,211] But, these systems are commonly operated in the near-infrared range, have been fabricated using electron beam lithography, and they are characterized with a super continuum laser and NIR spectrometer.

In contrast, our SiND sensors are designed to operate in the visible spectrum and can be used with a compact and portable device available in the laboratory, which includes a microfluidic system and real-time monitoring software**.** This eliminates the complexity associated with NIR systems and provides a potential for more scalable and cost-effective production compared to EBL-based methods. These advantages make our SiND sensors particularly suitable for biological analysis applications, combining high performance with practical simplicity.

3.4. Summary and conclusions

To improve the resolution and performance of biosensing devices, we focused on investigating all-dielectric nanostructures, specifically silicon nanodisks, for use in the visible range. Our aim was to optimize the dimensions of these structures to achieve sharper resonance features and higher resolution compared to traditional plasmonic materials. First, we conducted computational studies and predicted the optimal SiND architectures with a diameter of 300 nm, height of 110 nm, and gap of 150 nm, which were expected to exhibit sharp resonance peaks and enhanced sensitivity, achieved sensitivity comparable to conventional plasmonic sensor.

For experimental validation, we implemented and optimized a cost-effective, large-scale nanofabrication protocol based on hole-mask colloidal lithography, which allowed us to fabricate

SiNDs with a reproducible geometry closely matched the predictions from our simulations, except height (130 nm). The fabricated SiND arrays displayed a low variability, demonstrating the precision of our method. To evaluate their performance as refractometeric sensors, we utilized a customized angle-variable optical setup based on a prism-coupling configuration integrated with a microfluidic system, controlled through in-house software.

In general, the fabricated SiNDs exhibited optical properties in visible range with higher refractometeric sensitivity, as compared to conventional nanoplasmonic sensors. We also integrated these SiND sensors into a compact, user-friendly device that includes a microfluidic system and real-time monitoring software, overcoming the limitations of bulky and expensive equipment typically required for all-dielectric sensor technologies. Despite some discrepancies between simulations and experiments, the SiND sensors offered comparable resolution to plasmonic alternatives, with the added advantage of compact, portable operation, making them a potential candidate for biomolecular sensing applications.

Future work will focus on evaluating the biosensing capabilities of the optimized SiNDs through biofunctionalization and biomolecular sensing. While the resolution of SiNDs did not outperform AuNDs, their unique properties make them well-suited for applications in complex biomedical sensing where heat dissipation is critical. Additionally, SiNDs sensor could facilitate biomimetic functionalization strategies, such as the incorporation of lipid membranes, positioning them as promising candidates for advanced biomedical sensing technologies.

3.6. Experimental Section

3.6.1. Chemicals

Reagents for cleaning the substrates sodium dodecyl sulfate (SDS) 99% was purchased from Sigma-Aldrich (Steinheim, Germany). For hole-mask lithography (HCL) nanofabrication, including poly (diallyldimethylammonium chloride, PDDA) was purchased from Sigma-Aldrich (Steinheim, Germany). Sulfate latex beads, 8% w/v, 0.06 μm, 0.08 μm, 0.1 μm, 0.2 μm and 0.3 μm were purchased from Thermofisher Scientific (Paisley, United Kingdom). Standard gold etchant potassium monoiodide solvent was provided by Sigma-Aldrich (Steinheim, Germany).

3.6.2. Hole-mask colloidal lithography nanofabrication protocol

We fabricated silicon nanodisks (SiNDs) on a glass wafer (25 x 25 mm^2) coated with 130 nm of polycrystalline silicon on the front side by using the hole mask colloidal lithography technique. Initially, the residues from Si-substrates were rinsed with solutions (0.5 %wt SDS, 0.1 M HCL, and mili-Q water) followed by 1-minute sonication (acetone, isopropanol, miliQ water) at 65^o C temperature. Metals

(Ti/Au, 2 nm/50 nm) were evaporated as a mask on cleaned Si-substrates by an e-beam evaporator (AJA International Inc. ATC-8E Orion) in clean room facility. To enhance the surface hydrophilicity, chips were incubated in O_2 plasma (Oxford PlasmaPro 100 Cobra) (18s, 75W, 75 mTorr, 40% O_2-flux) and 0.2 wt% of PDDA (Sigma-Aldrich, Germany) was coated for 1 min and thoroughly rinsed with mili-Q water and dried with N_2 stream. Following this, the various diameters ranging from 60 nm to 300 nm of colloidal solutions (Invitrogen, USA) were dispersed in different concentrations ranges (0.1% to 0.6%) for 1 min over the charged surface, separately. Subsequently, the gold layer was vertically etched (beads acted as masks) employing reactive ion etching (Oxford PlasmaPro 100 Cobra) for 2:30 min in presence of argon gas (Ar: 40 sscm) at power (ICP/RF 250/40) and pressure of 6 mTorr, beads were removed by gentle tape striping. The exposed silicon layer was etched in presence of fluorine gasses mixture (C_4H_8/SF_6, 30/10 sccm). We tested silicon etching at different etching rates in range of (60 nm/min - 195 nm/min) and at different time intervals (75 s to 250 s) to achieve precise silicon nanostructures on the substrate. Finally, various strategies for gold lift-off were tested, involving both piranha and potassium Iodide (KI) solvent, over different time intervals (2 min – 20 min). Additionally, sonication was performed within a temperature range 0 – 65^o C, varying in time duration from 2 min to 20 min.

3.6.3. Scanning electron microscopy analysis

ImageJ software was used to determine the gap lengths and Field Emission Scanning Electron Microscopy Image (FEI Magellan 400L SEM, Oxford Instruments) was used to describe the distribution of nanostructures over the glass substrates.

3.6.4. Angle adjustable optical biosensor device description

Si nanodisks were fabricated using the hole-mask colloidal lithography technique and mounted on our in-house built angle variable optical setup for analysis. The setup utilized TM-polarized light at different incident angles (45°- 90°) with a collimated polychromatic light beam. The nanodisk substrates were positioned between a trapezoidal prism (n: 1.52) and a refractive index-matching immersion oil (n: 1.51). This assembly was connected to a microfluidic system linked to a syringe pump, which generated a constant sample flow with a manually operated injection (CHEMINERT®, VICI, Texas, USA). Collimated halogen light source (Ocean Optics, USA) was used to illuminate the silicon sensor substrate through the coupled prism. The reflected response was collected by a fiber-coupled spectrometer (Jazz Module, Ocean Optics, USA. To monitor real-time changes in resonance peak position, a polynomial fitting algorithm (National Instruments, Labview,USA) was employed through a custom-made software developed using open-source programming scripts (Python).To optimize signal-to-noise ratio (S/N) and

acquisition time, the software acquired 300 reflectivity spectra with an integration time of 3 ms. The resonance behaviour of the nanostructures was characterized in water (n: 1.33).

3.6.5. Data analysis

The data from nanophotonic sensors were analyzed using Origin 8.0 software (OriginLab, Massachusetts, USA) and Graphpad Prism (Graphpad Software, Inc., California, USA). The mean sensor response ($\Delta\lambda$) and its standard deviation (SD) were plotted against the change in refractive index ($\Delta\eta$) to generate calibration curves. These curves were fitted using a linear regression model. The experimental limit of detection (LOD) was determined as three times the SD of the sensor signals obtained from the background signal using water as a running buffer. Coefficients of variation (CV%) were calculated as the ratio of the standard deviation to the mean of multiple measurements taken on the same or different sensor chips, expressed as a percentage.

3.6.6. Bulk sensitivity

To evaluate the bulk sensitivity of the Si nanophotonic sensors, various concentrations of hydrochloric acid solutions were injected. The concentrations ranged from 25 mM to 500 mM. The injections were performed at a controlled flow rate of 30 µL/min, using a total injection volume of 150 µL for each concentration. This procedure allowed for the assessment of the sensor's response to different HCl concentrations, which is essential for determining its sensitivity and dynamic range.

Chapter 4

On-chip formation of artificial cell membranes

In this chapter, we design and develop a protocol for forming supported lipid bilayers (SLBs) on nanoplasmonic sensors. We also optimize a strategy to functionalize these SLBs to mimic real cell membranes in order to allow reliable monitoring of cell interactions in biomedical applications.

4. On-chip formation of artificial cell membranes

4.1. Context and motivation

Supported lipids bilayers (SLBs) have been widely used as in-vitro model systems for mimicking the cell membrane and studying biological mechanisms, such as cell-cell interactions or intracellular molecular transport. In sensing applications, SLBs have been mostly applied in SPR-based sensors for analyzing and studying molecular interactions with cell membranes. Although not the first work in the area, in 2007, Jonsson et al.[157] thoroughly described the formation of SLB on nanoplasmonic sensors and demonstrated that bioreceptors attached to these lipid membranes can move laterally, similar to how they do in natural cell membranes. This lateral mobility improves protein binding compared to traditional methods of immobilizing proteins directly onto a surface, enhancing the sensors' effectiveness in studying biological interactions. As a typical application example, G-protein coupled receptors have been reconstituted using SLBs on SPR sensors, enabling research on the real-time binding affinities and kinetics of these proteins, peptides, and small molecules with ligands.[212,213] Other works employed lipid bilayers that resembled bacterial membranes in order to investigate the interaction of the antimicrobial peptides.[214] The study showed that antimicrobial peptides bind to cell membranes and the level of impact they cause, which is crucial for understanding their mechanisms and developing novel anti-infective therapies. And more recently, Yoon et al.[167] used a nanoplasmonic sensor to visualize changes in the shape of SLBs in real-time, also with potential applications in designing antimicrobial surfaces.

Planar and functional SLBs can be formed onto the sensor surfaces through a well-established methodology based on spontaneous disruption of small unilamellar vesicles (SUV) upon contact with hydrophilic surfaces, like SiO_2 (Figure 4.1).[215–218] The resulting SLB membrane is composed of phospholipid molecules, with the hydrophilic head groups facing both the surface and the external medium, while the hydrophobic tails are oriented inward, forming a bilayer which is separated a few nanometers from the surface.[219]

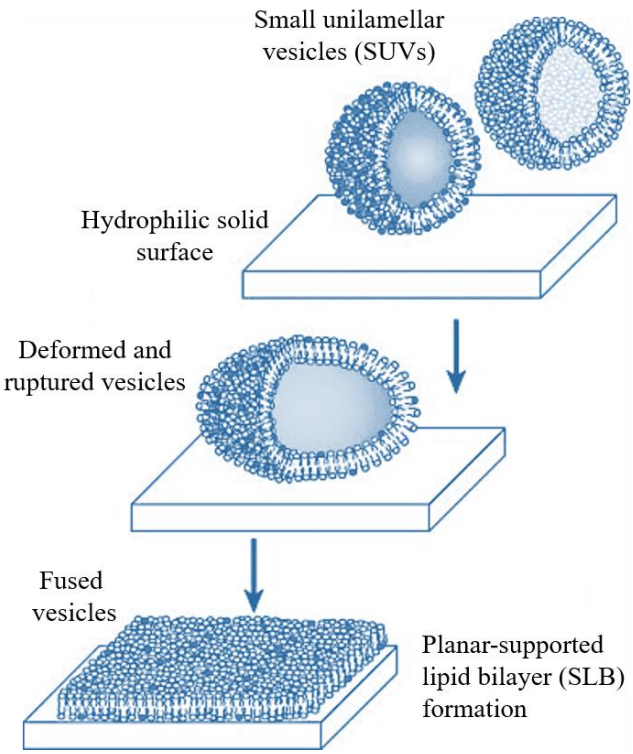

Fig 4. 1. Schematic illustration of planar-supported lipid bilayer formation via vesicle fusion method.

The main objective of this chapter is to develop and optimize a protocol for the formation of functional SLBs on nanoplasmonic sensor surfaces that will act as artificial cell membranes for biomedical analysis applications. This involves the design of the lipid vesicle composition to ensure the exposure of reactive groups for bioreceptor anchoring, establishing robust and reproducible methods to form uniform and stable SLBs on planar and nanostructured surfaces, and demonstrating the efficient immobilization of cell receptors onto the SLB. This approach is known for its simplicity and effectiveness in developing high-quality SLBs that can be tailored to display different functionalities according to the chemical structure and composition of the phospholipids forming the vesicles.

However, it has to be accurately optimized by controlling the lipid composition and concentration,[220] the buffer pH and additives,[221,222] and the substrate surface, which must be sufficiently hydrophilic to trigger vesicle disruption and regular planar bilayer assembly.[223] The latter can be controlled achieved through plasma treatment, silanization, or polymer coating.[220] Plasma treatment is a simple and widely used method for making surfaces hydrophilic. However, a limitation of this technique is that the surface must be used immediately for SLB formation, as the hydrophilicity degrades quickly over time. In contrast, methods like silanization and polymer coatings offer more lasting hydrophilicity. Silanization forms a covalent bond between functional silane molecules and the surface, maintaining hydrophilicity for an extended period; but it can introduce impurities that may interfere with the functionality of the

SLB. Similarly, polymer coatings provide long-term hydrophilicity but involve complex preparation steps, which can contaminate the surface and negatively affect SLB stability.

For SLB application in plasmonic sensors, usually a SiO_2 coating added to the gold surface to facilitate the stable formation of SLB. This is necessary because gold inherently lacks the hydrophilicity required for successful SLB assembly.[164] Besides, gold surfaces tend to lose hydrophilicity quickly when exposed to air.[224] Other methods for forming SLBs have also been explored, such as hybrid bilayers. In this approach, the gold surface is modified with a hydrophobic SAM that mimics the phospholipid tails. Vesicles then rupture to form a single lipid layer on top of the SAM. However, this method may offer less reproducibility compared to pure lipid bilayers due to its more complex formation process.[166]

In the composition and preparation of lipid suspensions, the length of phospholipid tails and electrostatic interactions play crucial roles in vesicle assembly and stability, since non-uniform vesicles may cause irregularities in bilayer formation. Phospholipids with longer tails promote stronger intermolecular electrostatic interactions, leading to more tightly packed and stable large vesicles. However, this stability reduces vesicle flexibility and decreases the likelihood of spontaneous rupturing. In contrast, shorter phospholipids form vesicles with weaker electrostatic interactions, resulting in looser packing, higher fluidity, and increased spontaneous rupturing of smaller vesicles.[225] Therefore, small, homogeneous vesicles are generally more effective at fusing to form a stable, uniform bilayer.

Additionally, to achieve optimal stability of SLB, pH, ionic strength, and temperature are also important parameters need to be considered. SLBs generally exhibit the highest stability at neutral to slightly alkaline pH levels, with an ideal range between pH 7.0 and 8.0.[226] This pH range allows for a balance between surface charges and intermolecular interactions that foster SLB formation and maintain structural stability. In terms of ionic strength, a lower level is typically more favourable. Using either pure water or buffers with low ionic strength (around 10 - 25 mM) is recommended,[227] as high ionic strength can adversely affect SLB solubility and stability, potentially leading to structural disruption. Lower temperatures are generally preferred, as the solubility and overall integrity of SLBs tend to decrease with rising temperatures. A range between 10 °C and 25 °C, is ideal for preserving SLB structure and function.[226] Sut *et al.* used an SPR sensor to demonstrate that variations in these parameters significantly alter the stability of SLBs.[228] While these conditions are typically effective for maintaining SLB stability, specific requirements may vary depending on the lipid composition and the substrate used in the experiment or application.

The main objectives of this chapter are to design and establish a protocol for the formation of SLBs on our nanoplasmonic sensors, as well as to optimize and demonstrate a strategy for functionalizing SLBs

to mimic a real cell membrane. The ultimate goal is to create an on-chip artificial cell membrane that can be used for reliable monitoring of cell interactions in biomedical applications.

4.2. Design and formation of functional supported lipid bilayers

For the formation of an artificial cell membrane, the composition of the SLB-forming phopholipids was designed taking into account the stability and fluidity of the planar bilayer and the presence of functional reactive groups at the lipids head. Phospholipids can be generally classified in four main structures: phosphatidylcholine (PC), a major component of cell membrane that provides a fluid and neutral charge environment, phosphatidylethanolamine (PE), which contributes to membrane curvature and stability, phosphatidylserine (PS), the provides a negatively charged surface useful for interactions with proteins, and phosphatidylglycerol (PG), also negatively charged and commonly employed for studying electrostatic interactions. These molecules are commercially available and can be acquired with specific functionalities. In this work, we selected POPC (1-palmitoyl-2-oleoyl-snglycero-3-phosphocholine) as main phospholipid (Figure 4.2a), because it generates a stable bilayer that mimics natural mobility and dynamic of human cell membrane.[224] The POPC was combined with two different functional lipids: DOPS (1,2-dioleoyl-sn-glycero-3-phospho-L-serine), with a terminal COOH group (Figure 4.2b),[229] and Biotinyl-PE (1,2-dipalmitoyl-sn-glycero-3-phosphoethanolamine-N-(biotinyl)), which enables bioreceptor immobilization through biotin-streptavidin interactions (Figure 4.2c).[230] These phospholipid molecules and mixtures have been previously employed for the formation of SLBs on plasmonic sensors, enabling the subsequent immobilization of bioreceptors.[157,166,167,231]

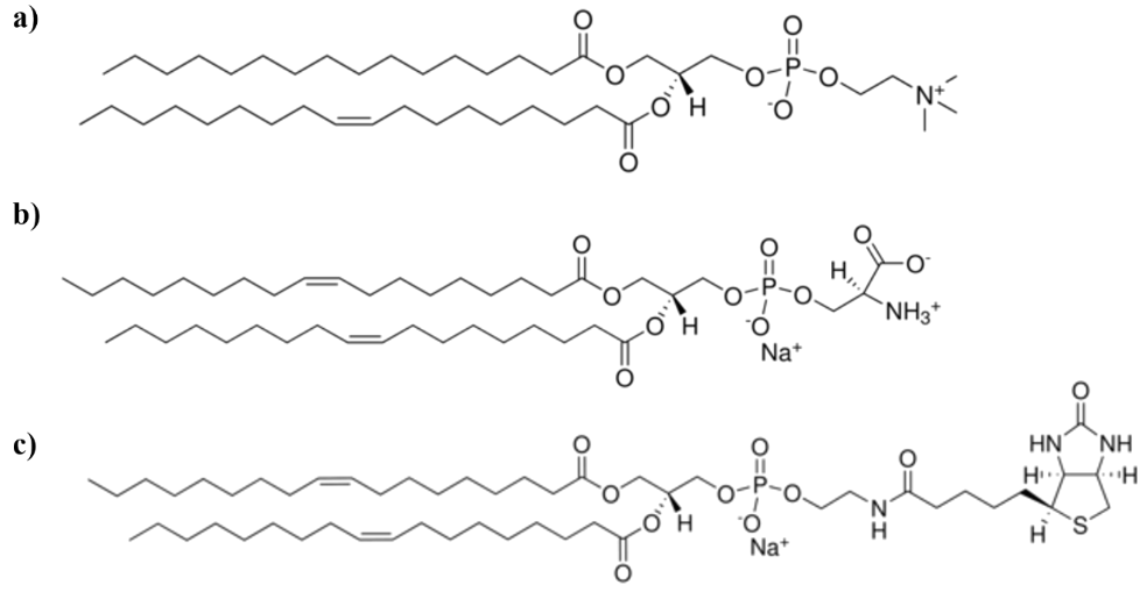

Fig 4. 2. Chemical structures of phospholipids; a) POPC, b) DOPS, and c) Biotinyl-PE

In order to optimize and evaluate the formation of a stable lipid bilayer on our sensors, we first employed a conventional SPR biosensor. The Au thin-film chips were coated with a 10 nm layer of SiO_2 to ensure surface hydrophilicity. Upon SLB formation, SPR follows vesicle binding kinetics and their subsequent fusion into a bilayer, offering information about the bilayer's stability and homogeneity. It has been demonstrated that the accurate detection and the creation of SLBs by SPR, the initial increase in the SPR signal corresponds to vesicle adsorption and spread into a bilayer, resulting in shift in resonance wavelength or angle and these shifts correlate with changes in mass and thickness of bilayer.[232,233]

For preparation of small unilamellar vesicles (SUVs), we initially carried out a simple protocol based lipid suspension sonication. In particular, we employed a mixture of POPC and DOPS at 10:1 for formation of SLB, the higher ratio of POPC is the one which is providing the essential stability to SLB. The lipid suspension was sonicated for different time intervals, ranging from 15 to 60 min, at 30 °C. The resulting SUVs suspensions were quickly injected into the SPR biosensor device and flowed over the hydrophilic SiO_2-coated Au sensor, previously cleaned and treated with a UV/ozone plasma. PBS buffer at pH 7.4 was used as running buffer at a constant flow rate of 20 µL/min. Additionally, a cleaning step using 10 mM NaOH (pH 10) was included to verify the stability of the lipid bilayer formation.

Figure 4 shows the real-time sensograms acquired for the different sonication times tested: 15 min, 30 min, and 60 min. For the first protocol (15 min), no significant signal was obtained, indicating that the vesicles flowed over the sensor surface without attaching to it (Figure 4.3a and 4.3c). Figure 4.3d shows that with longer sonication times (30 min), a few vesicles might get adsorbed onto the surface, resulting in a $\Delta\lambda_{SPR}$ of 0.35 nm from the baseline, which results insufficient for considering formation of a dense lipid bilayer. Finally, for the protocol using 60 min sonication, a more notable sensor signal was obtained ($\Delta\lambda_{SPR}$ = 5 nm, Figure 4e). However, with the NaOH cleaning step, the baseline returned to the initial position, meaning that the vesicles were adsorbed onto the sensor surface but did not disrupt to form the desired stable lipid membrane (Figure 4.3b). These unsuccessful results can be explained due to the limited capacity of sonication for generating and homogeneous solution of nanometer-sized SUVs. The likely presence of large and more stable vesicles in the suspension can result in the binding of these entities over the sensor surface due to hydrophilic and electrostatic interactions, hampering the formation of a planar membrane and being easily desorbed with a change of pH of the medium.

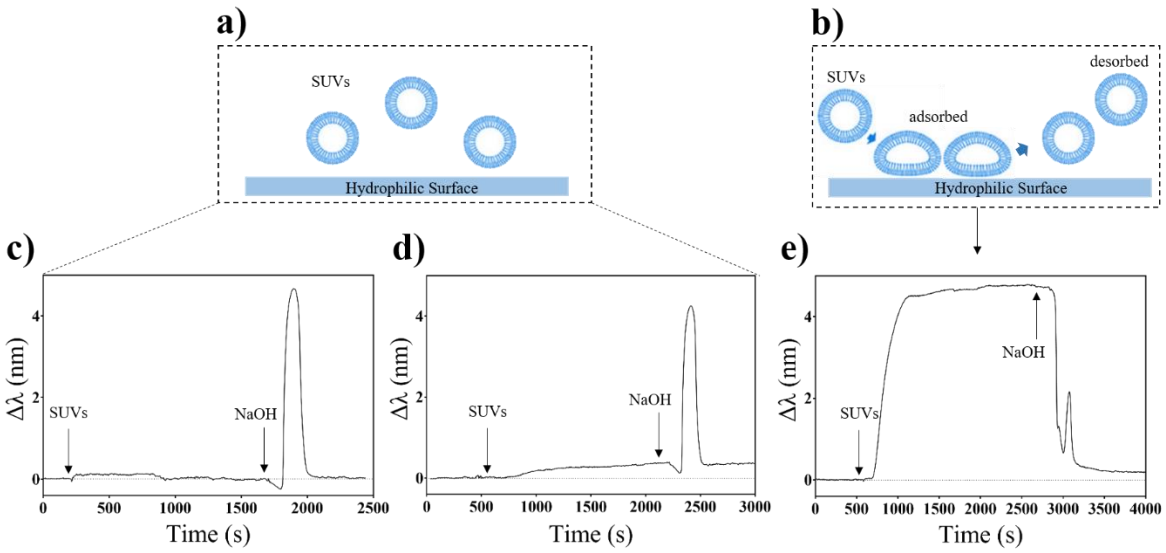

Fig 4. 3. Scamatic representation of: a and b) small unilamellar vesicles interaction onto hydrophilic surface at different sonication times: c) 15 minutes, d) 30 minutes, and e) 60 minutes.

Next, an alternative approach based on the extrusion method was tested (Figure 4.4).[216,217,229,234] Extrusion is a method employed to prepare a suspension of small and uniform vesicles by filtering the large vesicle suspensions through a membrane with a determine porous size. For this, we employed a commercial mini extruder kit with a polycarbonate membrane of 100 nm pore size. The lipid mixture suspension was sonicated at room temperature for one hour and poured into one of the air-tight syringes connected to the extruder and fixed onto heating block (Figure 4.4a and 4.4b). The lipid suspension, containing an irregular mixture of vesicles, was driven across the membrane's nanopores, forming vesicles that are evenly sized. These extrusion cycles were repeated 100-times at constant 55 °C temperature to ensure the vesicles achieved the desired size and uniformity. This was evident from the increased transparency of the extruded vesicles, as shown in Figure 4.4c.

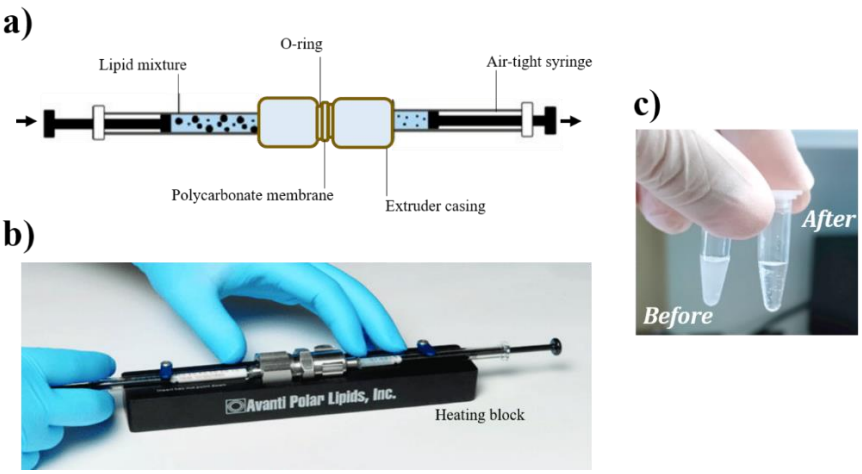

Fig 4. 4. a) Schematic illustration of extrusion method, b) Extrusion kit c) Before and after vesicles extrusion.

After obtaining the SUVs through this extrusion method, they were quickly injected on the SPR biosensor (Figure 4.5). The real-time sensogram showed a sharp increase of the sensor response that reached equilibrium at $\Delta\lambda = 14$ nm. The abrupt increase in the SPR signal is characteristic of cooperative binding dynamics, where SUVs rapidly adsorb and start to disintegrate as soon as they come into contact with the hydrophilic sensor surface. Cooperative binding occurs when SUVs first attach to the surface, increasing the chance that other SUVs will do the same, resulting in a quick and noticeable change in the sensor signal. This sudden rise suggests that the SUVs go through a structural transition rather than just staying adsorbed; they swiftly rupture and spread out to form a uniform supported lipid bilayer. Upon reaching equilibrium, a steady SLB forms throughout the sensor surface, signifying the end of notable association or structural changes which is reflected in the sensogram. The stability of the bilayer was tested by passing a 10 mM NaOH cleaning solution over the surface. The sensor signal remained steady throughout this stage, indicating that the SLB was safely formed and was unaffected by the cleaning solution.

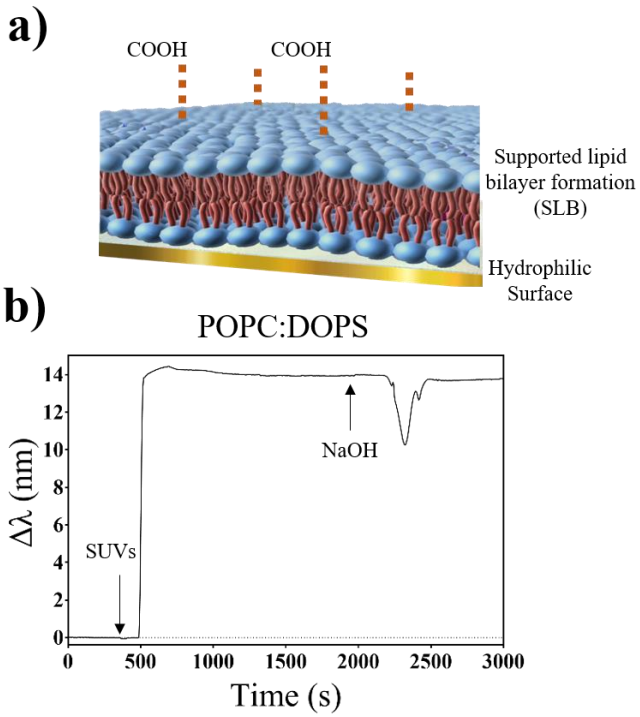

Fig 4. 5. a) Schematic illustration of SLB formation with carboxylic functionalities (POPC:DOPS) through the rapid disruption of SUVs on SiO_2-coated plasmonic surface. b) Real-time sensogram showing stable SLB formation on SiO_2-coated gold thin film, followed by a NaOH cleaning step.

To further evaluate and confirm the reliability of the SUV preparation protocol, we carried out analogue experiments for the formation of biotin-functional SLBs, using a mixture of POPC and Biot-PE at the same 10:1 ratio (Figure 4.6). The real-time sensograms displayed a sharp increase in sensor response, similar to that observed with carboxylic SLBs, indicating successful biotinylated SLB formation. The response reached the equilibrium at $\Delta\lambda$ = 14 nm and remained stable upon introduction of a cleaning solution (NaOH 10 mM) for 2 minutes.

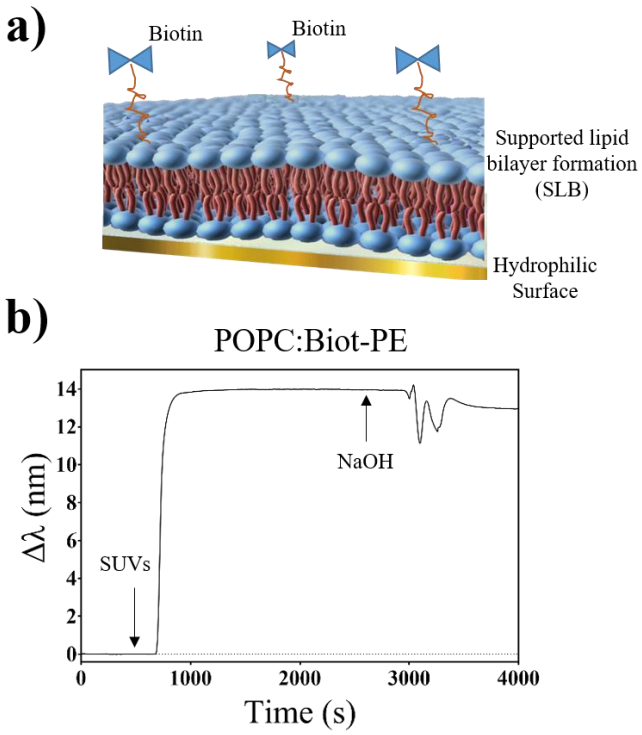

Fig 4. 6. Schematic illustration of SLB formation with biotin functionalities (POPC:Biot-PE) through the rapid disruption of SUVs on SiO_2-coated plasmonic surface. b) Real-time sensogram showing stable SLB formation on SiO_2-coated gold thin film, followed by a NaOH cleaning step.

To assess the robustness and reproducibility of the procedure for bilayer cell membrane formation, we repeated the two different SLB formation processes over more than 25 different sensor chips, obtaining a coefficient of variation (CV) around 7 % for both, carboxyl and biotin functional scaffolds.

4.3. Functionalization of supported lipid bilayers

Following the successful formation of two different SLBs on SiO_2-coated SPR sensors, the next critical step was to use the COOH and biotin functional groups to immobilize specific biomolecules. In this study, we employ model recombinant cell receptors as biorecognition elements to be immobilized. This

type of biomolecules are commercially available and contain the specific peptide or protein domain, responsible for the interaction with the complementary ligand, conjugated to the Fc region of a generic antibody, which allows for easy and oriented immobilization (Figure 4.7).

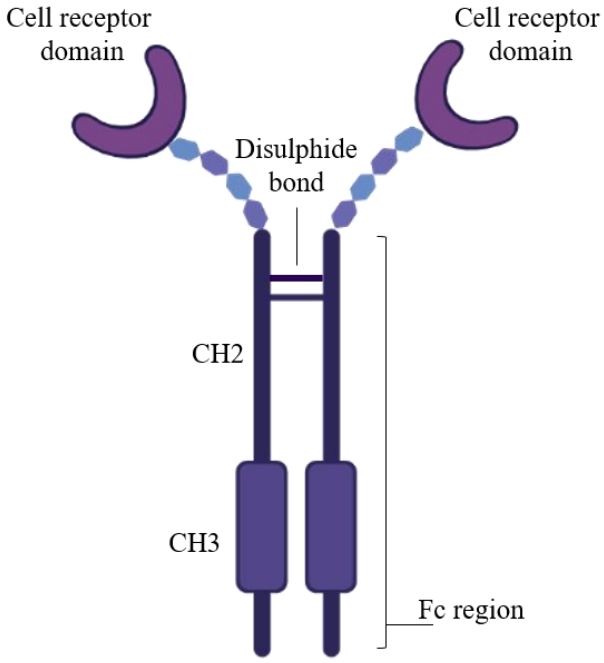

Fig 4. 7. Schematic illustration of the model cell receptor.

For the biofunctionalization of the COOH-functional SLB, we selected the EDC/NHS chemistry protocol, which enables the formation of covalent bonds between COOH groups and the terminal amines present in native proteins and antibodies.[235] On the other hand, biotin groups can be employed for the immobilization of previously biotinylated receptors through the high affinity interaction with avidin proteins (i.e., neutravidin, streptavidin).[236] Although both strategies are popular and well established, they require the particular optimization of pH and buffer conditions for the immobilization of different molecules to enhance and maximize their interaction with the functional groups and minimize non-specific adsorptions on the surface.[237,238]

As a preliminary study, we performed pH and buffer optimizations for both carboxylic and biotin functionalization using a conventional alkanethiol SAM formed on SPR sensors. In particular, we selected a mixed monolayer of MHDA (16-mercaptohexadecanoic acid and MUOH (11-marcapto-1-undecanol) in molar ratio 1:5. This SAM mixture has been optimized in our group for protein and antibody.[239,240] The SAM contains carboxylic acid (COOH) functionalities, which will be used on one hand for direct covalent binding of bioreceptors via amine-reactive (EDC/NHS) chemistry (Figure 4.8a), and on the other hand, to immobilize of neutravidin proteins, making an affinity layer for direct immobilization of biotinylated cell receptors (Figure 4.8b).

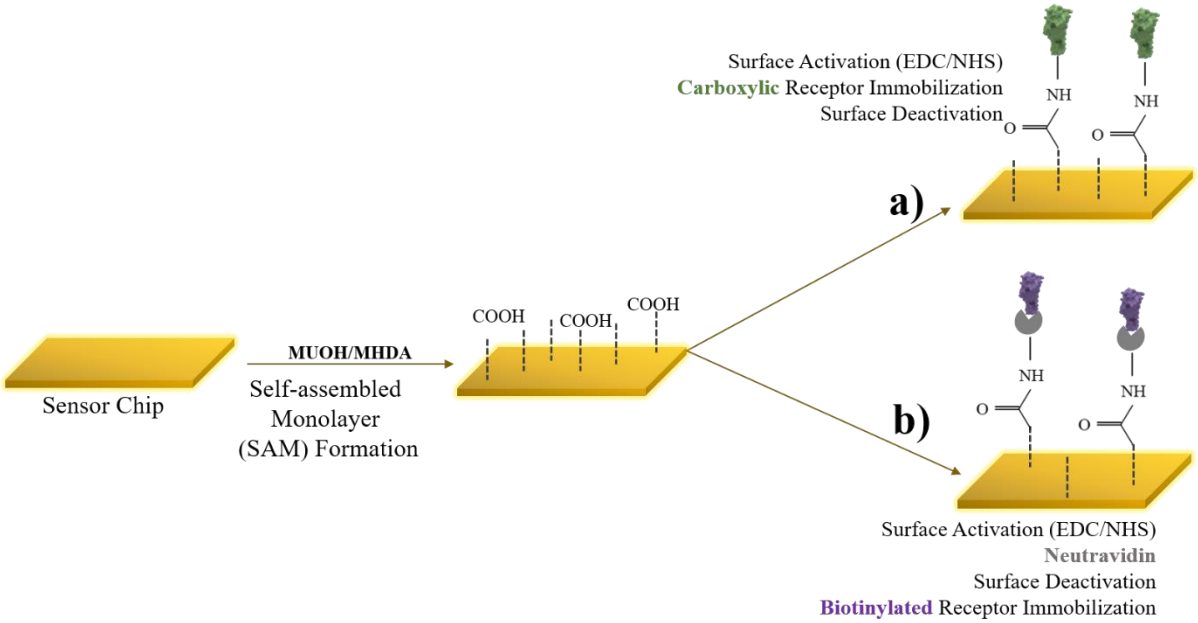

Fig 4. 8. Schematic illustrations of different immobilization strategies on SAM layer on plasmonic sensor surface: a) Carboxylic immobilization of cell receptors through covalent binding using EDC/NHS chemistry, and b) Biotinylated immobilization of cell receptors thorough binding affinity using neutravidin.

The binding efficiency of the cell receptors to the functionalized sensor was evaluated across different common buffers including PBS, HEPES (4-(2-hydroxyethyl)-1-piperazineethanesulfonic acid) and MES (2-(N-morpholino) ethanesulfonic acid), with pH values ranging from 5 to 7 (Figure 4.9a and 4.9b). The pH is important for favouring immobilization and avoiding nonspecific binding because it influences the electrostatic interactions between bioreceptors and the sensor surface. At optimal pH levels, the charges on both components are balanced, promoting specific binding while minimizing nonspecific interactions. Additionally, pH affects protein conformation and the reactivity of functional groups involved in immobilization. By selecting the appropriate pH and buffer, we enhance specific binding and reduce nonspecific adsorption, leading to more efficient immobilization of bioreceptors on sensor surfaces.

The results indicated that higher amount of COOH-immobilized receptor was achieved when using 50 mM MES buffer at pH 5.5 (Figure 4.9a) and highest biotin-immobilized receptors was measured in 50 mM PBS buffer at pH 6.5 (Figure 4.9b). Additionally, nonspecific bindings were also evaluated over a non-active surface. We used bovine serum albumin (BSA) as a negative control, a protein that is often used in bioapplications to avoid non-specific interactions. The binding effectiveness between this

control and the functionalized sensor was compared in each buffer pH, and all signals were attributed to non-specific interactions against MES buffer pH 5.5 for COOH-cell receptors (Figure 4.9c) and PBS buffer 6.5 pH for biotin-cell receptors (Figure 4.9d). This test allowed us to verify that the bioreceptors were immobilized through the desired strategies: covalent binding to NHS, and the biotin-avidin system with negligible non-specific adsorption.

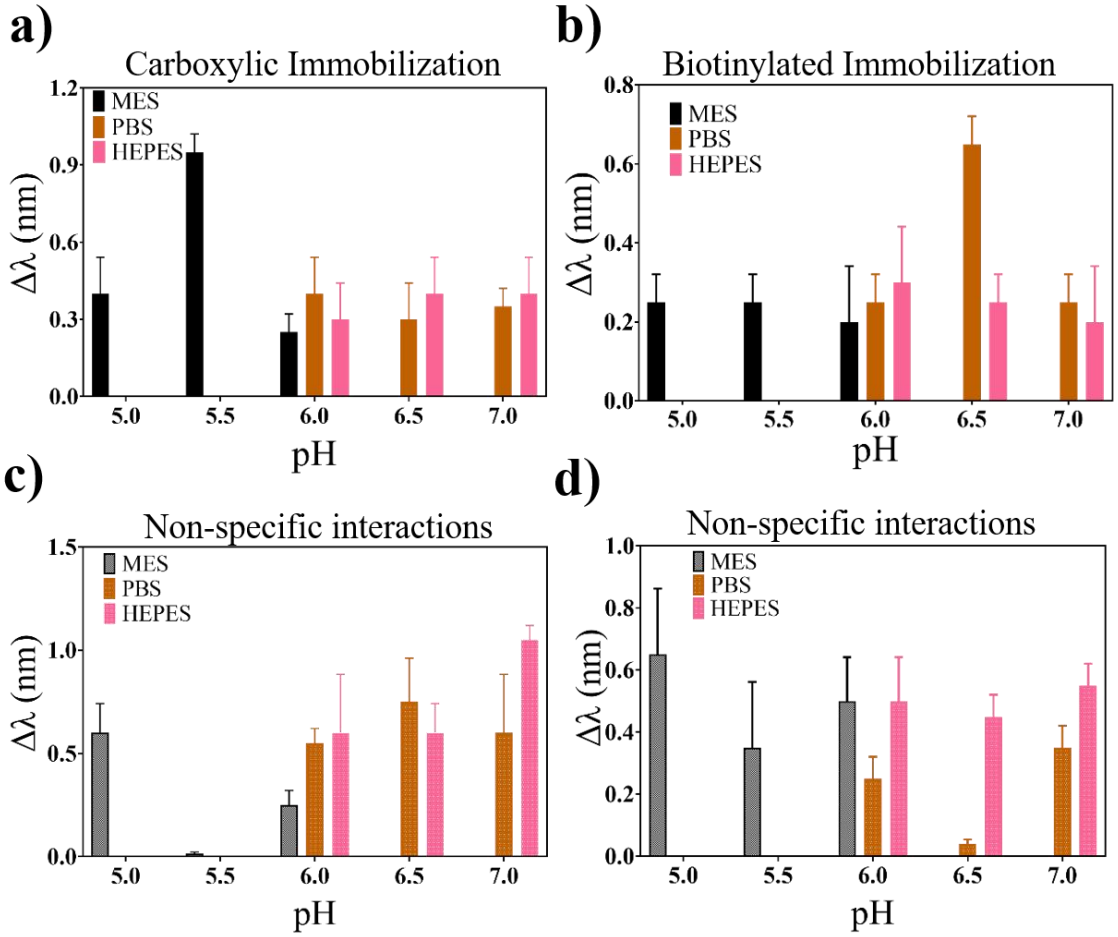

Fig 4. 9. Buffers and pH optimizations with conventional SAM layer on gold sensor chip for different immobilizations: a) Cayboxylic immobilization, b) Biotynilated immobilization, c) Non-specific interactions for carboxylic immobilization, and d) Non-specific interactions for biotynilated immobilization.

After optimizing the pH and buffer conditions, the immobilization protocols were applied to the MHDA:MUOH SAM layer. The carboxylic groups of the SAM were activated using EDC/NHS chemistry. The COOH-cell receptor 50 µg/mL was then covalently immobilized, resulting in a signal ($\Delta\lambda$ = 13 nm), which remained stable after ethanolamine deactivation (Figure 4.10c). In a similar approach, the surface was activated using the same EDC/NHS chemistry. The amino groups of

neutravidin were then bound to the COOH groups, and to prevent non-specific adsorption, the surface was deactivated using ethanolamine (Figure 4.10d). The biotin-cell receptor 30 µg/mL was subsequently immobilized on the neutravidin-activated surface, driven by high biotin-neutravidin affinity, which produced a sensor signal (Δλ = 8 nm) as shown in Figure 4.10e. The immobilized bioreceptor's stability was tested by introducing a 10 mM NaOH cleaning step, demonstrating that the receptors remained attached to the sensor surface, as they were not removed during this process. Both immobilization methods were stable and effective on conventional SAM, with the receptors staying attached even after cleaning.

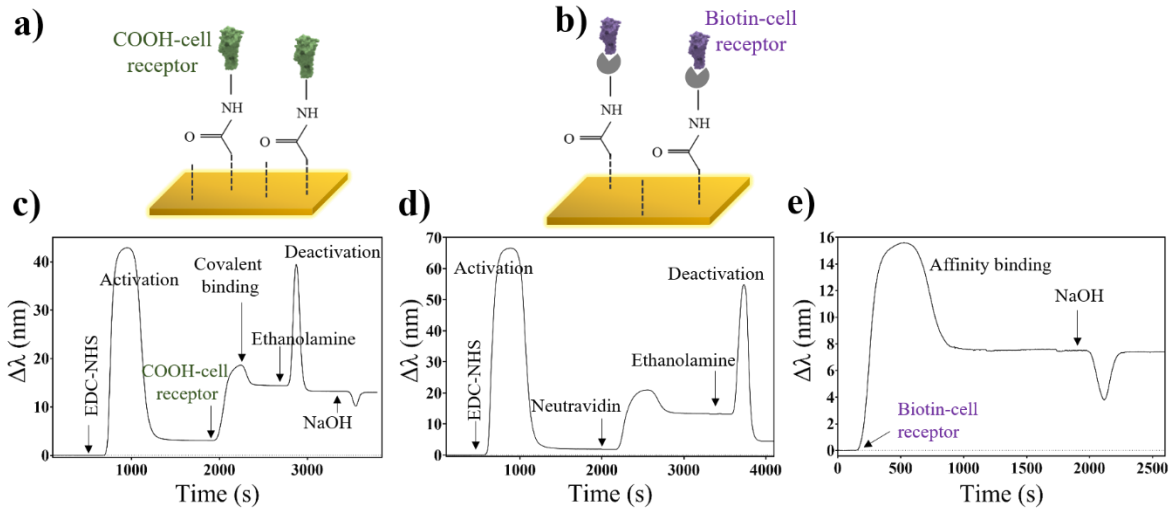

Fig 4. 10. Schematic illustrations of different immobilization strategies on conventional SPR sensor surface: a) Carboxylic immobilization of cell receptors, b) Biotinylated immobilization of cell receptors. SPR sensorgrams showing two different immobilizations: c) The covalent immobilization of COOH-cell receptors through EDC/NHS chemistry, and d and e) Biotinylated immobilization of cell receptors thorough binding affinity using neutravidin immobilized on activated surface through EDC/NHS chemistry.

We proceeded to optimize the bioreceptor concentration by testing a range of concentrations from 10 to 70 µg/mL on conventional sensor (Figure 4.11). For the carboxylic strategy, the highest immobilization signal (Δλ = 13 nm) was observed at a bioreceptor concentration of 50 µg/mL (Figure 4.11a), while for the biotin strategy, the maximum signal (Δλ = 8 nm) was obtained with 30 µg/mL (Figure 4.11b). Overall, COOH-functionalized surfaces resulted in higher immobilization signals than biotin-functionalized surfaces, possibly due to the lower availability of binding sites on neutravidin surface compared to COOH groups.

It is worth noting that the maximum immobilization signal is not achieved at the highest concentration, likely due to steric hindrance effects. It is also important to mention that the concentrations initially optimized may need to be re-evaluated for analyte detection, especially when transferring this method to an SLB with a different functionality ratio than the 1:5 SAM used in this study. Based on these results, the receptor immobilization strategies established and confirmed with the optimized buffer and pH conditions together with a concentration of 50 µg/mL for carboxylic bioreceptor (50 mM MES buffer at pH 5.5), and 30 µg/mL for biotinylated bioreceptors (50 mM PBS buffer at pH 6.5).

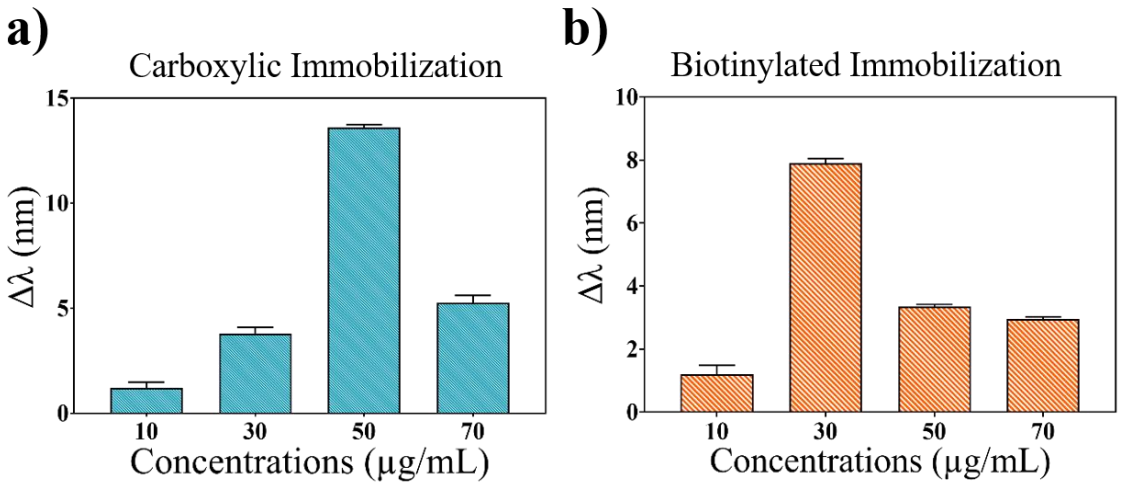

Fig 4. 11. Bioreceptor concentration optimization ranging from 10 to 70 µg/mL for different immobilization strategies: (a) Carboxylic immobilization using MES buffer at pH 5.5, and (b) Biotinylated immobilization using PBS buffer at pH 6.5, using a conventional self-assembled monolayer on a gold sensor.

Once the immobilization conditions were established on the conventional SAM, we transferred both immobilization strategies onto the functional supported lipid membranes (Figure 4.12). The COOH-functionalized SLB was activated following the EDC/NHS chemistry procedure, using a bioreceptor concentration of 50 µg/mL, resulting in a sensor signal of $\Delta\lambda$ = 8.5 nm (Figure 4.12c). After receptor attachment, ethanolamine was introduced in order to deactivate the unreacted functional groups. For the biotin immobilization strategy, the first step was creating a neutravidin layer (50 µg/mL in PBS buffer) over the biotin-functional SLB, which is resulted in an increase of $\Delta\lambda$ = 7.6 nm, followed by a cleaning step with NaOH for 1 min to confirm the stability of the layer (Figure 4.12d). It should be noted that in this case, the neutravidin was directly immobilized on biotinylated lipids instead of covalently bond to COOH molecules.

Upon introducing the 30 µg/mL bioreceptor to the sensor surface, it causes a further increase in $\Delta\lambda$ = 3.4 nm, which is nearly half of the signal obtained for the covalent binding approach. Besides, the final

cleaning step (NaOH) results in a sligth decrease in $\Delta\lambda$ = - 0.9 nm, showing the removal of some bioreceptors that were non-specifically adsorbed onto the surface. This lower immobilization signal may be attributed to the lower availability of binding sites in the neutravidin layer compared to the COOH scaffold. Overall, both the biotin receptor system and carboxylic receptor system demonstrated an efficient immobilization with good stability. To confirm the robustness and reproducibility of the SLB biofunctionalization procedures, we determined the coefficient of variability for both immobilization strategies over more than 25 biofunctionalization experiments performed in different sensor chips and different days. The CV% for the carboxylic immobilization was determined at 14%, while for biotinylated immobilization it resulted 21%.

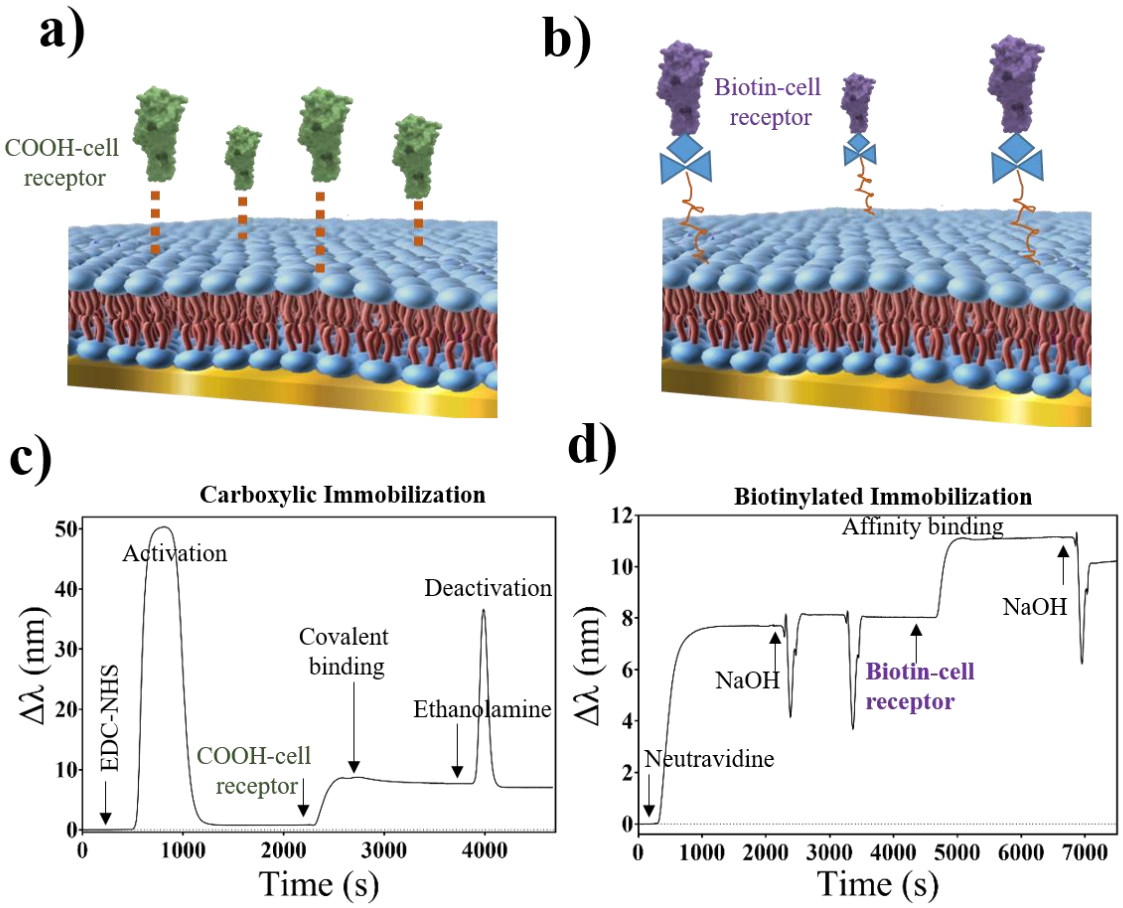

Fig 4. 12. Schematic illustrations of different functionalities SLB formation on SiO_2-coated plasmonic sensor surface: a) Carboxylic immobilization of cell receptors, b) Biotinylated immobilization of cell receptors. SPR sensorgrams showing two different immobilizations: c) The covalent immobilization of COOH-cell receptors on the SLB via EDC/NHS chemistry, and d) Biotinylated immobilization of biotin-cell receptors though binding affinity.

In conclusion, we have established a protocol for SLB functionalization using two different strategies: carboxylic and biotinylated, achieving excellent immobilization efficiency, stability, and reproducibility. Interestingly, the immobilization of bioreceptors on a fluid SLB is hypothesized to provide additional lateral mobility of the bioreceptors, which could enhance the subsequent detection of receptors with higher efficiency.

4.4. Multi-targeted immobilizations onto complex supported lipids bilayer

Next, we addressed the immobilization of two different bioreceptors onto the same sensor as strategy to provide a multi-targeted scaffold. Our main objective was to develop artificial cell membranes containing multiple types of receptors and ligands, rather than just one. To achieve this, we focused on creating SLBs with diverse functionalities for the co-immobilization of various receptors. This strategy involves developing a complex bilayer using a mixture of lipids containing both carboxylic and biotin functional groups. By integrating these two types of lipids, the sensor surface can be selectively functionalized with different receptors at the desired ratio.

We prepared a mixture of both lipid compositions (POPC:DOPS:Biot-PE, 10:1:1) in PBS buffer and obtained homogeneous complex SUVs by extrusion method. The SUVs were quickly injected into the sensor surfaces and spontaneously disrupted to form a stable multifunctional SLB. The sensorgram, shown in Figure 4.13a, shows a signal increase of $\Delta\lambda = 14$ nm, which is similar to the results we obtained with both lipids separately (Figure 4.5 and Figure 4.6). This is a good result since it indicates that the mixed SLB can also form effectively on the surface in the same way as the individual lipids.

The sequential immobilization strategy involved two key steps (Figure 4.13b). First, we immobilized biotinylated cell receptors on the SLB surface through the high-affinity biotin-neutravidin interaction, and obtained a sensor response similar to the previous individual biotin functionalization approach ($\Delta\lambda = 3.4$ nm, Figure 4.12d). After stabilizing the biotinylated receptors, we proceeded to immobilize carboxylic cell receptors on the same sensor surface, again with a signal similar to the previous individual COOH-functionalization ($\Delta\lambda = 8$ nm, Figure 4.12c). This proof-of-concept result demonstrate the effectiveness of our sequential immobilization approach to integrate two receptors onto a single sensor surface in a site-selective manner and without sacrificing efficacy in bioreceptor immobilization. Our method could be applied for the study of complex biological interactions where co-immobilization of ligands is required, such as in mimicking cell-cell interactions.

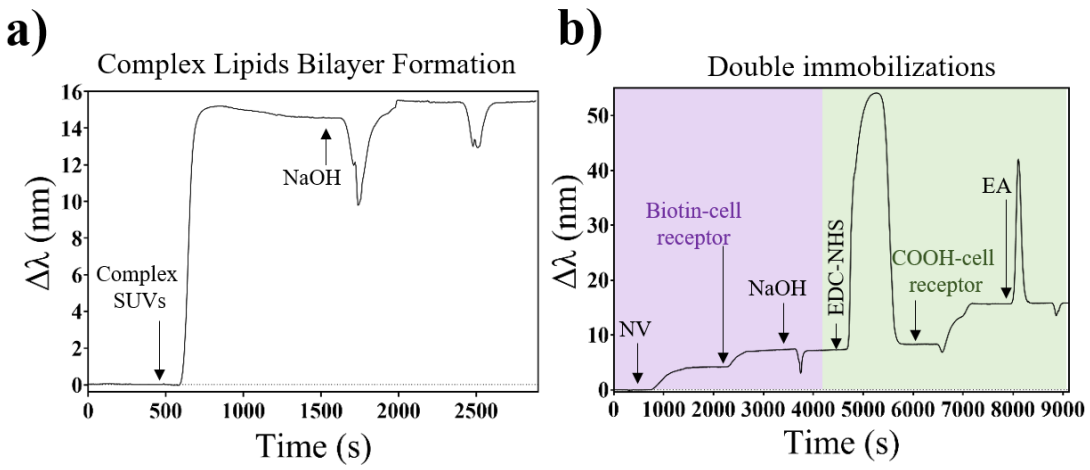

Fig 4. 13. a) SPR sensogram showing the complex SLB formation on SiO_2-coated plasmonic sensor by disruption of small unilamellar vesicles (SUV), followed by a NaOH cleaning step, and b) SPR sensorgram showing the multiple bioreceptor immobilizations on the complex-functional SLB.

4.5. Formation of SLB on nanoplasmonic sensors

So far in this chapter, SLBs have been formed on conventional SiO_2-coated SPR sensors. However, our aim is to use the plasmonic nanostructured sensors developed in Chapter 2 for biomedical applications, requiring the evaluation and optimizing of the formation of SLB on these LSPR nanoplasmonic substrates.

In this regard, the standard SiO_2 coating strategy that works well for SPR sensors may not be suitable for LSPR sensors. This is due to the more localized resonances and confined evanescent fields in LSPR, with an approximate penetration depth reaching up to 50 nm.[187] Covering the nanostructured sensor surface with a thin layer of SiO_2 and forming an SLB (5-10 nm thick),[166] would space the recognition event out from the sensor's sensitive area, substantially lowering the detection sensitivity. Indeed, the scarce studies reporting the formation of SLBs on nanoplasmonic sensors utilize nanohole arrays (NHA), where the sensing mechanism combines both LSPR and propagating SPR, therefore exhibiting larger evanescent fields and allowing for a SiO_2 coating of the nanostructured sensor.[169,36,37,38]

Herein, our hypothesis considers that the gold nanodisks (AuNDs) sensors fabricated and optimized in Chapter 2 might behave similar to a glass substrate for direct SLB formation. Thanks to the quasi-planar structure of the surface (only 20 nm height) and the apparent low density of metal over the substrate, our nanoplasmonic sensors may enable the direct formation of SLBs without the need of specific coatings or functionalization. To evaluate that, we carefully assessed the hydrophilic behavior of the nanoplasmonic sensor and test the SLB formation following the previously established procedure.

4.5.1. Surface preparation and hydrophilicity

First, we examined the 80 nm AuNDs sensors through SEM to determine the actual density of metal nanostructures (Figure 4.14). The total metal density was determined by calculating the surface of the nanostructures, based on their diameter and distribution (gap), and dividing by the total surface of the substrate, which was found to approximately 6 - 7%.

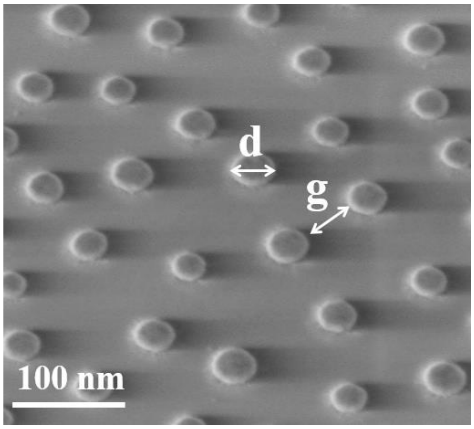

Fig 4. 14. Scanning electron microscopy image of 80-nm AuNDs fabricated using the HCL method.

Then, we analyzed the hydrophilicity of the AuNDs sensors through contact angle measurements, comparing them to glass substrates and Au thin-film sensors. The analysis was performed over a time frame from 0 hour to 3 hours after conventional cleaning (Figure 4.15). The cleaning procedure consisted in sequential rinsing with acetone, ethanol, and milli-Q water, followed by 1-minute sonication at room temperature and drying with N_2 stream.

At the first hour, the LSPR sensor showed a contact angle of 42.3°, which indicates a surface wettability and hydrophilicity comparable to the glass substrate (40.5°) and significantly better than gold thin film (54.6°) (Table 4.1), as expected.

We assessed this study over three hours because stability of the hydrophilicity is important for ensuring reproducibility and reliability of the SLB formation. During this period, the LSPR sensor only showed a slight increase of the contact angle (+2 degrees), whereas the contact angles of gold and glass increased up to 4 degrees each. This implies that, in contrast to the other substrates, the LSPR sensor holds its hydrophilicity over time with better consistency and can be advantageous for our stable SLB formation. A more stable hydrophilic surface minimizes the probability of changes during the formation of stable SLB, improved the reproducibility and overall sensor reliability.

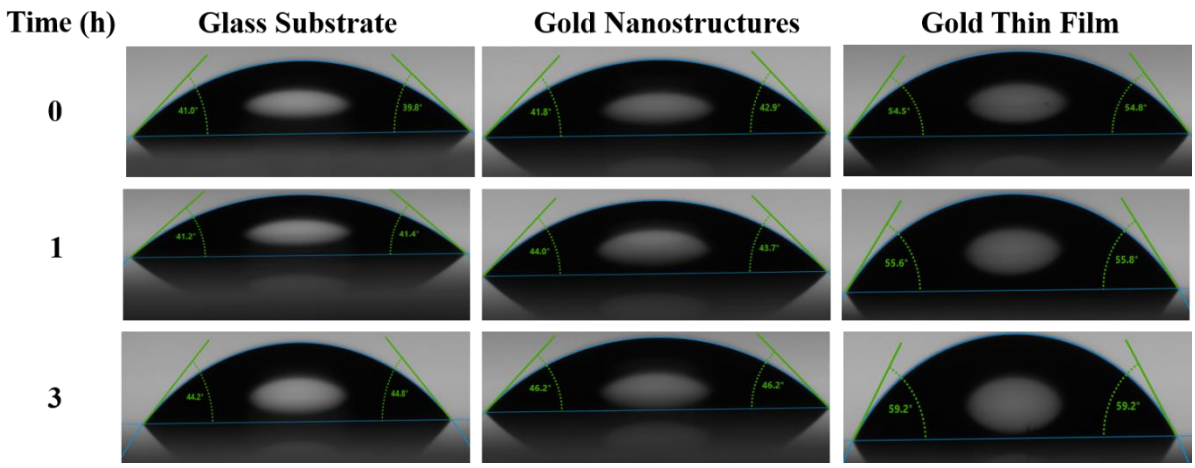

Fig 4. 15. Contact angle measurement over different time periods from 0 to 3 hours: a) Glass substrate, b) Gold nanostructures, and c) Gold thin film.

Table 4. 1. Summary of contact angle measurements of different substrates in different time periods.

Time (h)	Glass Substrate (θ)	Gold Nanostructures (θ)	Gold Thin Film (θ)
0	40.5 ± 2.1	42.3 ± 2.0	54.6 ± 2.4
1	41.4 ± 2.0	43.8 ± 1.7	55.7 ± 2.0
3	44.3 ± 1.9	44.2 ± 1.5	59.2 ± 3.2

This experiment confirmed our hypothesis that a low-density nanoplasmonic sensor can exhibit the same hydrophilic behavior than bare glass substrates, being significantly higher than plasmonic gold thin film surfaces. Therefore, since the formation of SLB on glass substrates has been previously demonstrated, we could expect the successful formation of SLB on our AuNDs sensors with an analogue hydrophilic behavior. Nonetheless, the presence of nanostructures on the substrate increases to roughness of the surface, which might also affect the SLB formation efficiency and stability,[220] hence it needed to be confirmed.

4.5.2. Formation and functionalization of supported lipid bilayers

Colloidal solutions of different functional SUVs (carboxylic and biotinylated) were prepared through the previously optimized extrusion method. Once ready, the SUV solutions were quickly injected into the LSPR biosensor, and the vesicle disruptions and planar bilayer formations were monitored (Figure 4.16). Figure 4.16c displays the sensorgram for the COOH-functional lipid bilayer formation, showing a signal increase up to 4 nm, accompanied by signal stability for 5 minutes. To verify the robustness

and stability of the carboxylic planar lipid bilayer, we injected a NaOH solution, which indicated that it did not remove anything from the sensor surface. In Figure 4.16d, the sensorgram for the biotinylated SLB shows an initial signal increase of around 2.5 nm, which later decreases to 1.8 nm upon NaOH injection. This drop indicates instability and disruption of the bilayer, likely due to the weaker surface attachment of the biotinylated bilayer. However, upon re-introduction of NaOH, the signal stabilizes, suggesting that some level of reorganization or stabilization occurs over time.

When comparing these results to previous experiments using the SPR sensor (Figures 4.5 and 4.6), it is evident that the SLB formation signal was higher, reaching up to 14 nm. In contrast, the current LSPR sensing experiments indicated much smaller signals, around 4 nm. This difference can be attributed to the distinct active sensing area in both sensors. In propagating SPR, the SLB is formed on a continuous sensing surface, while in LSPR, only the lipid bilayer coating the small nanodisks can be detected, that being less than 10% of the surface. Nonetheless, our results with LSPR sensors are consistent with other studies using nanoplasmonic sensing, which reported similar signal magnitudes.[241,242] We have also demonstrated the consistency across 25 measurements, with a coefficient of variation around 6% for both carboxylic and biotinylated SLB formations, which is similar to the SLB formation on conventional SPR (7%).

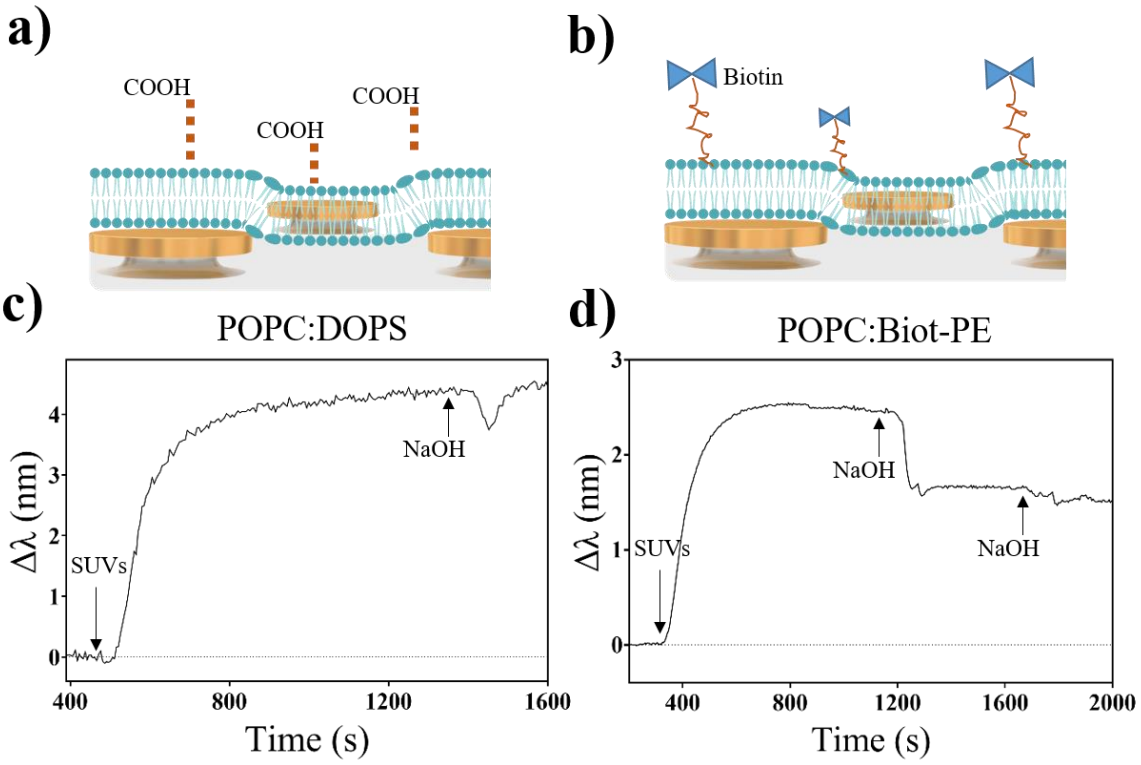

Fig 4. 16. Schematic illustration of supported lipid bilayer formation with, a) Carboxylic (POPC:DOPS), and b) Biotin functionalities (POPC:Biot-PE), through the rapid disruption of small

unilamellar vesicles on nanoplasmonic sensor surface. LSPR sensorgram showing the formation of different functional supported lipid membrane through the disruption of SUVs followed by a NaOH cleaning step: c) POPC:DOPS, carboxylic bilayer, and d) POPC:Biot-PE, biotinylated bilayer.

Once the SLB was formed on the nanoplasmonic sensors, the subsequent biofunctionalization was assessed (Figure 4.17). Cell receptors were immobilized by covalent binding to the carboxylic groups available from DOPS via EDC/NHS chemistry, producing a significant signal increase ($\Delta\lambda = 3$ nm), which was stable after ethanolamine deactivation and a NaOH cleaning step (Figure 4.17c). Also, biotinylated cell-receptors were immobilized by affinity interaction to a neutravidin layer formed on the biotinylated SLB, producing a large signal increase ($\Delta\lambda = 5$ nm) that was stable after NaOH cleaning step (Figure 4.17d). The reproducibility of the entire biofunctionalization process were evaluated on over 15 sensor chips. The coefficients of variability were 12% for COOH immobilization and 19% for biotinylayed immobilization, comparable to the previous SPR experiments (14% and and 21%, respectively) and demonstrating that the protocol is reliable.

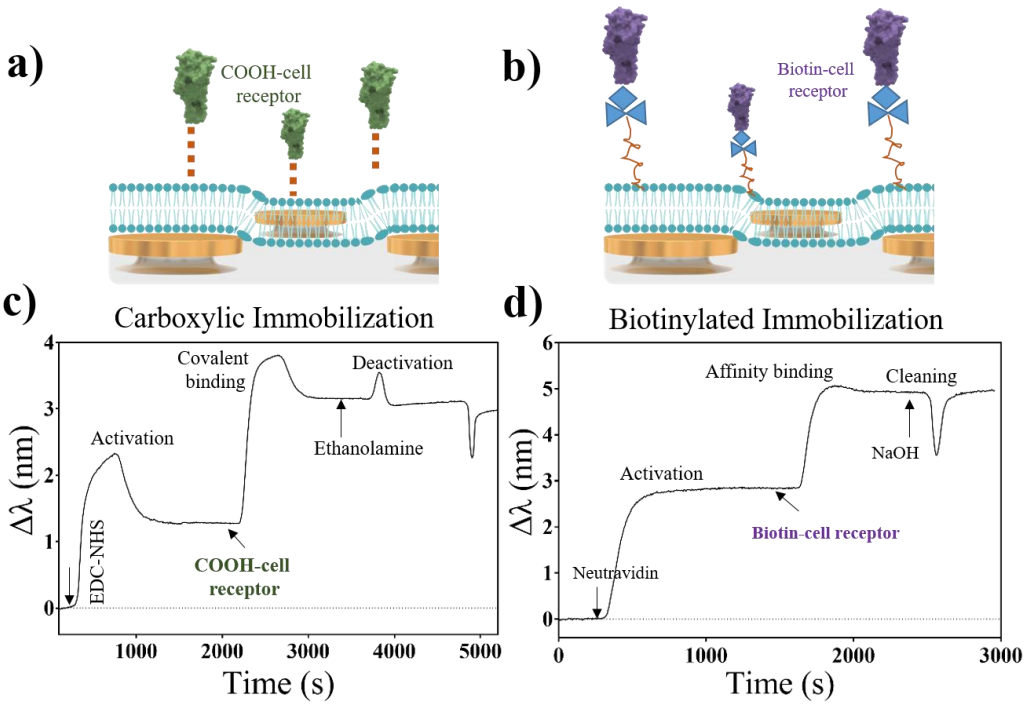

Fig 4. 17. LSPR sensorgram showing two different immobilizations: a) The covalent immobilization of COOH-cell receptors on the SLB via EDC/NHS chemistry, and b) Biotinylated immobilization of biotin-cell receptors though binding affinity.

In this study, we have successfully demonstrated for the first time that SLBs can be formed and functionalized directly on a nanoplasmonic sensor surface. This achievement allows us to fully leverage

the higher resolution potential of LSPR sensors, as discussed in Chapter 2, for complex biomedical applications including cell-cell interaction analysis.

4.6. Summary and conclusions

We have explored the creation of on-chip artificial cell membranes, based on the formation of stable and functional SLBs on different plasmonic sensors: SiO_2-coated SPR sensors and AuNDs LSPR sensors. The SLBs were functionalized with carboxylic and biotin groups, allowing the immobilization of specific cell receptors through covalent and affinity binding approaches, respectively. We also explored the development of a dual-functional SLB that could simultaneously immobilize various types of receptors, enhancing the sensor's versatility for complex biological studies. We further extended these results to nanoplasmonic sensors, hypothesizing that SLBs could be directly formed on these sensors without additional surface coatings, thanks to the low-density of gold nanostructures. The study confirmed that these sensors exhibited hydrophilic properties similar to glass substrates, and sustained over a period of time. The formation and functionalization of SLBs directly on AuNDs sensors resulted comparable to the results obtained with conventional SPR sensors.

By establishing reliable protocols for SLB formation on nanoplasmonic sensors, we open up new opportunities for complex biomedical applications, particularly in immunotherapy field. Our innovative biomimetic sensors, with an on-chip artificial cell membrane biofunctionalization, might facilitate and improve the monitoring and analysis of cell-cell interactions, providing faster and reliable results for therapeutic evaluation, drug screening, or even to contribute to the understanding of immuno-oncology processes.

4.7. Experimental section

4.7.1. Chemicals and bioreagents

Acetone and ethanol were purchased from Panreac Applichem (Barcelona, Spain). Lipids (POPC, 1-palmitoyl-2-oleoyl-snglycero-3-phosphocholine), DOPS (1,2-dioleoyl-sn-glycero-3-phospho-L-serine) and Biot-PE (1-oleoyl-2-(12-biotinyl (aminododecanoyl))-sn-glycero-3- phosphoethanolamine) were provided by Avanti Polar Lipids (Alabaster, Alabama, USA). Reagents for buffer preparation (10 mM PBS (Phosphate buffer saline, pH 7.4), 50 mM HEPES (N-(2-Hydroxyethyl) piperazine-N-(2-ethanesulfonic acid), pH 7.4), MES (2-(N-morpholino) ethane sulfonic acid)) and sodium hydroxide (10 Mm NaOH, pH 10) and reagents for carboxylic groups activation (1-ethyl-3(3-dimethylaminopropyl) carbodiimide hydrochloride (EDC), sulfo-N-hydroxysuccinimide (s-NHS)) and

for deactivation ethanolamine (EA), Potassium monoiodide, 16-mercaptohexadecanoic acid (MHDA) and 11-marcapto-1-undecanol (MUOH) were provided by Sigma-Aldrich (Steinhem, Germany). Neutravidin was provided by Thermofisher Scientific (Madrid, Spain). Carboxylic and biotinylated cell receptors were acquired from GenScript (Leiden, The Netherlands).

4.7.2. Sensor chip preparation

The sensor chips were prepared to mount on SPR sensor set-up by sonication in acetone, ethanol, and Milli-Q water for 1 minute each, then dried with a N_2 stream. The chips were then exposed in a UV/Ozone for 30 minutes to improve surface hydrophilicity. Prior to bioreceptor immobilizations, the cleaned gold chips were immersed overnight in a SAM mixture of MHDA:MUOH (1:5) in absolute ethanol at room temperature, under dark conditions to prevent photo oxidation. After rinsing and drying, the chips were placed on the SPR setup.

4.7.3. Data analysis

Biosensor data were analysed and processed using Origin 8.0 software (OriginLab, Massachusetts, USA). Data and statistical analysis were performed using Graphpad Prism (Graphpad Software, Inc., California, USA). The real-time sensograms responses ($\Delta\lambda$) were plotted as a function of time. The coefficients of variation were obtained as the ratio of the standard deviation and the mean of several measurements on the same or different sensor chips, expressed in percentages (% CV).

4.7.4. Supported lipid bilayer formation and receptor immobilizations

The functional SLB was formed by disrupting small unilamellar vesicles (SUVs) over a hydrophilic sensor surfaces. To prepare the lipid solution, different lipid formulations (POPC: DOPS 10:1, POPS:Biot-PE 10:1 and POPC:DOPS:Biot-PE 10:1:1) were dissolved in chloroform and mixed in a glass vial to yield 1 mg of dry lipids. Each vial was placed in a vacuum desiccator with a continuous flow of N_2 at room temperature overnight to evaporate any remaining solvent and form a dry lipid film. The lipid film was then rehydrated by adding 1 mL of PBS buffer (10 mM, pH 7.4) to achieve a concentration of 1 mg/mL. The solution was vortexed for 2–3 minutes and sonicated at room temperature for 1 hour to produce a heterogeneous vesicle solution. These vesicles were then extruded into SUVs using a polycarbonate membrane with a 100 nm pore size, performing 100 extrusion cycles at 60°C with a mini-extruder (Avanti Polar Lipids, Inc., Alabaster, AL, USA). The resulting SUV solution was quickly injected over the sensor surface to form a lipid bilayer on the hydrophilic sensor surface. A subsequent cleaning step with 10 mM NaOH was performed to ensure the stable formation of a planar lipid layer. After stabilization of the functional SLB layer, 50 μg/mL COOH-cell receptors diluted in 50 mM MES buffer pH 5.5 and 30 μg/mL biotin-cell receptors diluted in 50 mM PBS buffer

pH 6.5, were immobilized onto the functional SLB layer using EDC/NHS (0.4 M/0.1 M) chemistry in MES buffer (50 mM, pH 5.5). The COOH-cell receptors were covalently bound, while the biotin-cell receptors were immobilized through affinity binding. To deactivate any unreacted COOH groups, ethanolamine (EA, 1 M, pH 8) was injected for 1 minute. All measurements were conducted using PBS buffer 10 mM as the running buffer at a flow rate of 20 µL/min.

4.7.5. Contact angle analysis

The hydrophilicity of different substrates including glass substrates, gold nanostructures, and gold thin films were characterized by Contact Angle analysis (Drop Shape Analyzer DSA25S KRÜSS). The sensor chips were first prepared through a cleaning process that involved sonication in acetone, ethanol, and Milli-Q water for 1 minute each, followed by drying with a nitrogen (N_2) stream to ensure clean surfaces. To enhance surface hydrophilicity, the chips were then treated with UV/Ozone for 30 minutes. For the CA measurements, a small water droplet was placed on the surface of each substrate for different time intervals from 0 to 3 hours, and the angle formed between the droplet's baseline and the substrate was measured. This contact angle provided an indication of the surface wettability, with lower angles signifying more hydrophilic surfaces and higher angles indicating more hydrophobic surfaces. Each measurement was performed in triplicate, and the mean values, along with the standard deviations, were calculated to ensure the reliability and consistency of the results.

Chapter 5

Application to COVID-19 immunotherapy evaluation

In this chapter, we demonstrate the application of the biomimetic biosensor platform for the evaluation of monoclonal antibodies as anti-viral immunotherapy for SARS-CoV-2 infection. The work includes optimization of sensor biofunctionalization, monitoring of virus – cell membrane interactions, and assessment of different therapies for different virus variants.

5. Application to COVID-19 immunotherapy evaluation

5.1. Context and motivation

The World Health Organization (WHO) declared COVID-19 a pandemic which is caused by SARS-CoV-2 in early 2020,[243–245] resulting in a rapid global spread with millions of cases and deaths.[246] In addition, a number of healthcare systems have been severely impacted by the COVID-19 pandemic due to a sharp increase in workload and a shortage of resources for quick diagnosis and prognostic information as well as cutting-edge patient care.[247,248] Considerable endeavours were undertaken to develop and distribute quick diagnostic tests,[249–252] and vaccines[253] that effectively enabled effective population screening, slowing down the spread of the virus, and significantly decreasing the medical implications and SARS-CoV-2 infection-related mortality. Nevertheless, the specific treatment of the coronavirus disease with antiviral therapies has proven to be rather challenging.

The SARS-CoV-2 virus infects human cells through specific binding of the receptor binding domain (RBD) of the spike (S) protein to the angiotensin-converting enzyme 2 (ACE-2) receptor, which is found on the surface of many different types of cells, including those found in the intestines, heart, and lungs.[254] Upon interaction, the spike protein undergoes a conformational shift that allows the virus to fuse with the membrane of the host cell. This fusion allows the virus to enter the cell and take control of its machinery, causing it to generate more viral particles. Since these freshly generated viruses are subsequently released to infect more cells, one of the most important targets in the battle against COVID-19 is the RBD of the virus. Targeting the viral RBD allows for more specific intervention against the virus without directly affecting the host cells' ACE-2 receptors, which have important physiological functions.[254]

For COVID-19, early treatments with antivirals are essential for those at high-risk patients with comorbidities, poor immunity, or restricted vaccination availability.[255,256] In addition to being as successful as possible in preventing and controlling SARS-CoV-2 infection with the fewest possible adverse effects, they should be broadly accessible, reasonably priced, and appropriate for patients who are not hospitalized. The most promising options among the several candidates have been immunotherapies using monoclonal antibodies (mAbs),[257] followed by convalescent plasma,[258] antivirals paxlovid and remdesivir.[256,257] Monoclonal antibodies can imitate the ability of the immune system to minimize and eliminate the coronavirus infection by attaching to exterior viral spike proteins (Figure 5.1), blocking the virus's ability to interact and restrict multiplication with the host cell receptor.[256]

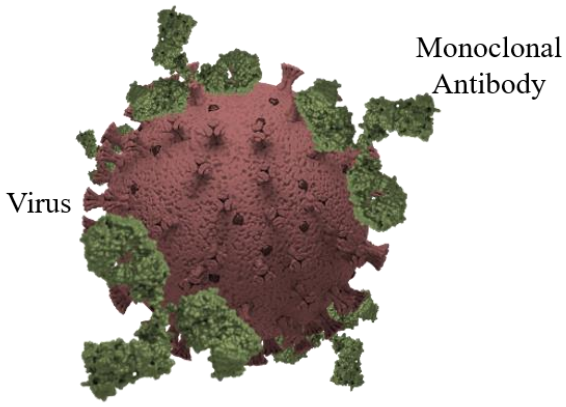

Fig 5. 1. Schematic illustration of mAb blocking the virus´s viral spike proteins.

In order to treat the mild-moderate coronavirus patients, the European Medicine Agency (EMA) and the American Food and Drug Administration (FDA) approved a few monoclonal antibodies between 2021 and 2022. These therapies include bamlanimivab, regdanvimab, sotrovimab, and the cocktails casirivimab/imdevimab and tixagevimab/cilgavimab.[259,260] However, their expensive and delayed approval reflect the challenging, prolonged, and time-consuming processes involved in developing and evaluating antiviral monoclonal antibodies, which may pose a significant obstacle to their widespread use in healthcare systems.[261 262]

The identification and validation of mAb therapies are commonly performed using neutralization assays.[263] In this assay, viral samples (or pseudotyped viruses) are incubated with the mAb at various concentrations, followed by their addition to cultured cells that mimic the host. In the absence of neutralizing antibodies, the virus infects the host cells, leading to plaque formation. The neutralizing capability of the mAb is evaluated by either counting the number of plaques formed or by measuring the inhibition of cytopathic effects (i.e., microneutralization test) across increasing antibody concentrations. Prior to neutralization assays, initial screening of potential mAb candidates is typically performed using faster methods such as enzyme-linked immunosorbent assays (ELISA) or bead-based assays (e.g., Luminex). These techniques assess the binding affinity of mAbs to viral proteins, such as the spike protein or its receptor-binding domain, but they do not directly assess the mAbs' ability to neutralize the virus. Although these initial screening methods are efficient for quickly identifying promising candidates, they must be followed labor-intensive neutralization assays to confirm the actual neutralizing efficacy of the mAbs against the virus.

In recent years, J. Coutu et al. have performed SPR-based pseudo-neutralization assay to evaluate SARS-CoV-2 antibodies, analyzing over 1000 clinical samples. The assay measured inhibition binding

between viral spike protein and ACE-2 receptor. Their results correlated well (r = 0.74) with live virus microneutralization assays, demonstrating that SPR can serve as a rapid, safe, and quantitative alternative for assessing SARS-CoV-2 antibody responses in biosafety laboratories (BSL-2).[264] Additionally, researchers employed this SPR sensing method to investigate cross-reactivity of antibodies with both native and variant SARS-CoV-2 spike proteins, offering a faster, cost-effective, and safer alternative to traditional cell-based neutralization assays.[265] However, these studies have certain limitations. They rely on isolated spike proteins and ACE-2 receptors, which do not fully replicate the complex environment of cell membranes. In living cells, receptors can move, cluster, and influence virus-receptor interactions,[166]factors that are not fully captured in SPR assays using immobilized proteins. These assays also overlook the natural mobility and constraints of receptors within cell membranes, focusing only on isolated biomolecular interactions. While SPR provides useful information, these limitations emphasize the need to use it as a complementary tool alongside cell-based neutralization assays, which provide a more accurate representation of in vivo conditions.

The objective of this chapter is to demonstrate the application of our SPR biosensor functionalized with an artificial cell membrane for COVID-19 immunotherapy evaluation, in particular for the screening of anti-viral mAbs targeting the SARS-CoV-2 virus. To that, a SLB is formed on the plasmonic sensor and functionalized with ACE-2 cell receptors, allowing for direct detection and monitoring of virus-cell interactions (Figure 5.2, left panel). Then we will evaluate therapeutic efficacy of mAbs by performing a competitive assay (Figure 5.2, right panel). The biomimetic sensor will be employed to measure the ability of mAbs to neutralize the virus by blocking its interaction with the ACE2 receptors on the artificial membrane. The platform will provide real-time evaluation on the neutralization process, ensuring an efficient and direct method for assessing the performance of antiviral therapies.

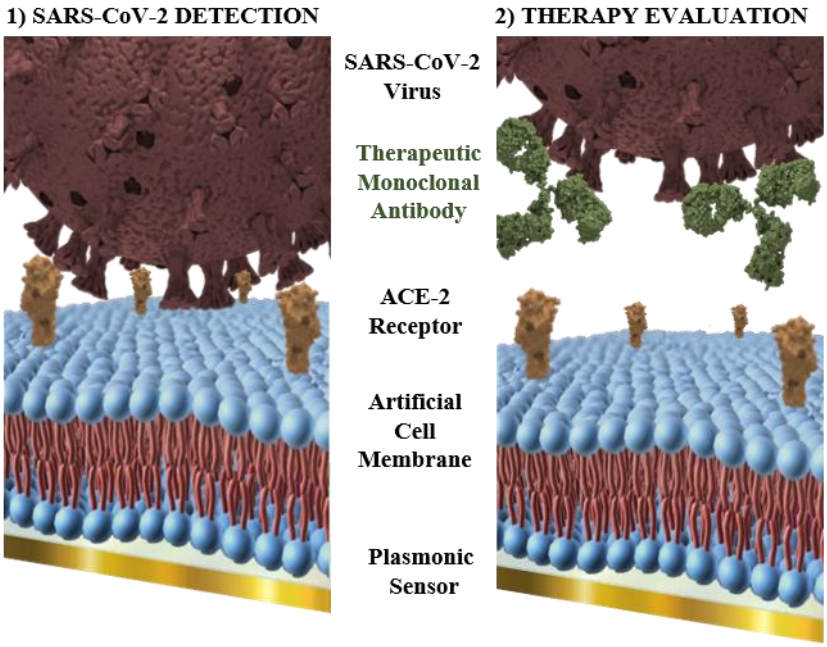

Fig 5. 2. Schematic representation of the biomimetic plasmonic biosensor method for mAb therapy evaluation via neutralization assays. 1) Panel demonstrates the direct detection of SARS-CoV-2 viruses over an artificial cell membrane showing ACE-2 receptors created on the plasmonic sensor. 2) Panel illustrates how therapeutic monoclonal antibodies attach to Spike protein of the SARS-CoV-2 virus, preventing and reducing its interaction with the host cell receptor.

5.2. Formation of ACE-2 functional membranes

In order to create an artificial host cell interface with the ACE-2 receptors, we used our proprietary SPR biosensor, based on prism-coupling excitation and the wavelength interrogation, and coating the sensor chips with a 10 nm SiO_2 layer (Figure 5.3a). For formation of a planar and the functional SLBs, we selected a mixture of POPC and carboxyl (-COOH) functionalized DOPS lipids at 10:1 molar ratio in PBS buffer (10 Mm, pH 7.4). A homogeneous suspension of 100 nm small unilamellar vesicles was prepared using the extrusion method (detailed in Chapter 4) and was rapidly injected over the plasmonic sensor. The formation of the SLB onto sensor surface was observed in real time (Figure 5.3b). The sensor response increased significantly, reaching equilibrium at $\Delta\lambda = 14$ nm, with the typical profile of a cooperative binding.

To ensure SLB stability, a cleaning solution (10 mM NaOH) was applied to the bilayer for two minutes indicating nothing was removed from the surface and sensorgram remained stable. After, the ACE-2 receptors (50 μg/mL) were covalently bond to the COOH-functional SLB by means of well-known EDC/NHS chemistry (Figure 5.3c). We used a recombinant human ACE-2 peptide conjugated to an Fc domain to enable the efficient and oriented anchoring to the lipid surface, ensuring virus accessibility

to the ACE-2 peptide. The entire biofunctionalization process was performed in situ at room temperature and was completed in approximately 2 h. To verify the robustness and reproducibility of the artificial cell membrane formation procedure, we calculated the coefficient of variability for SLB formation and ACE-2 immobilization. The values were 7% and 14%, respectively, across more than 25 biofunctionalization processes.

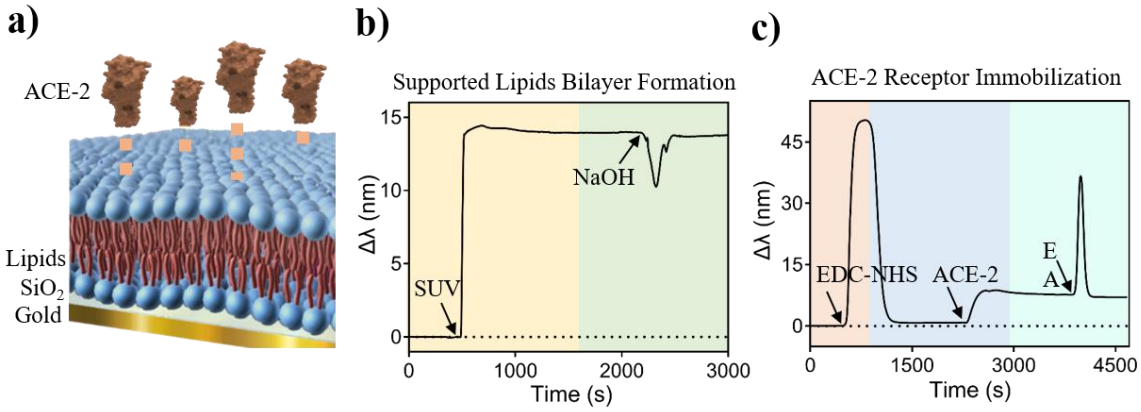

Fig 5. 3. a) Schematic illustration of ACE-2 functional SLB designed on SiO_2-coated plasmonic sensor surface, b) SPR sensorgram showing creation of a SLB from disruption of small unilamellar vesicles, followed by a NaOH cleaning step, and c) SPR sensorgram displaying ACE-2 receptor immobilization on COOH-functional SLB.

5.3. Analysis of virus-cell interactions

As a preliminary study for the evaluation of the affinity and specificity of our ACE-2 biorecognition layer towards the SARS-CoV-2 virus, we used recombinant viral antigens corresponding to the Spike protein of both Delta and Omicron virus variants. SARS-CoV-2 viral antigen samples at various concentration ranging from 15 to 5000 ng/mL diluted in standard HEPES buffer (50 mM, pH 7.4) were flowed over biomimetic scaffold on sensor surface. The recorded sensorgrams show an effective binding of the viral antigens in both cases, with increasing sensor signals corresponding to the increasing protein concentrations (Figure 5.4).

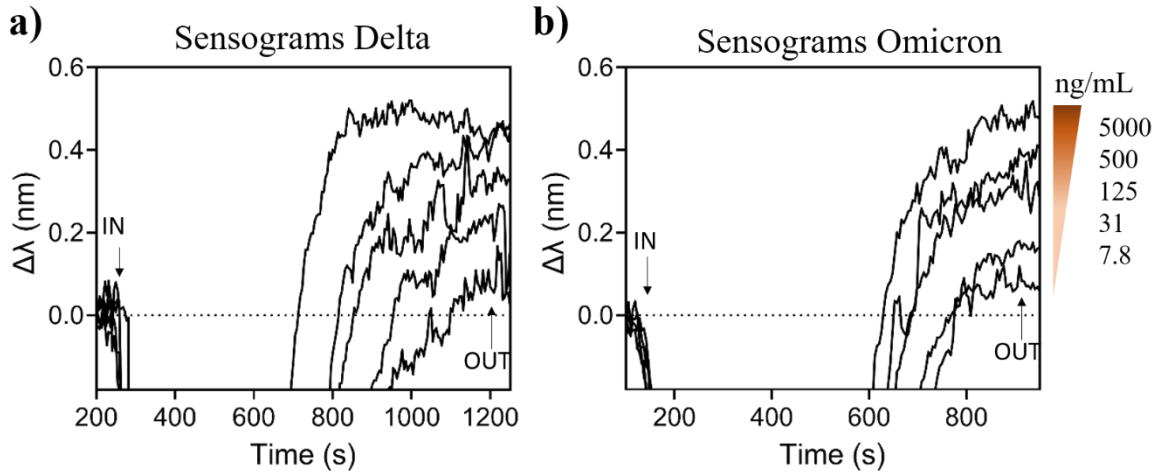

Fig 5. 4. a) Representative SPR sensorgrams obtained for different concentrations of Delta SARS-CoV-2 S antigens, and b) Representative SPR sensorgrams obtained for different concentrations of Omicron SARS-CoV-2 S antigens.

From these assays, we obtained the standard calibration curves by plotting the biosensor signal (Δλ) as a function of the viral antigen concentration and fitting to a one-site specific binding model (Figure 5.5). For the Delta variant, the LOD was determined at 18 ng/mL and the LOQ at 49 ng/mL. For the Omicron variant, the LOD was calculated at 12 ng/mL and the LOQ at 37 ng/mL.

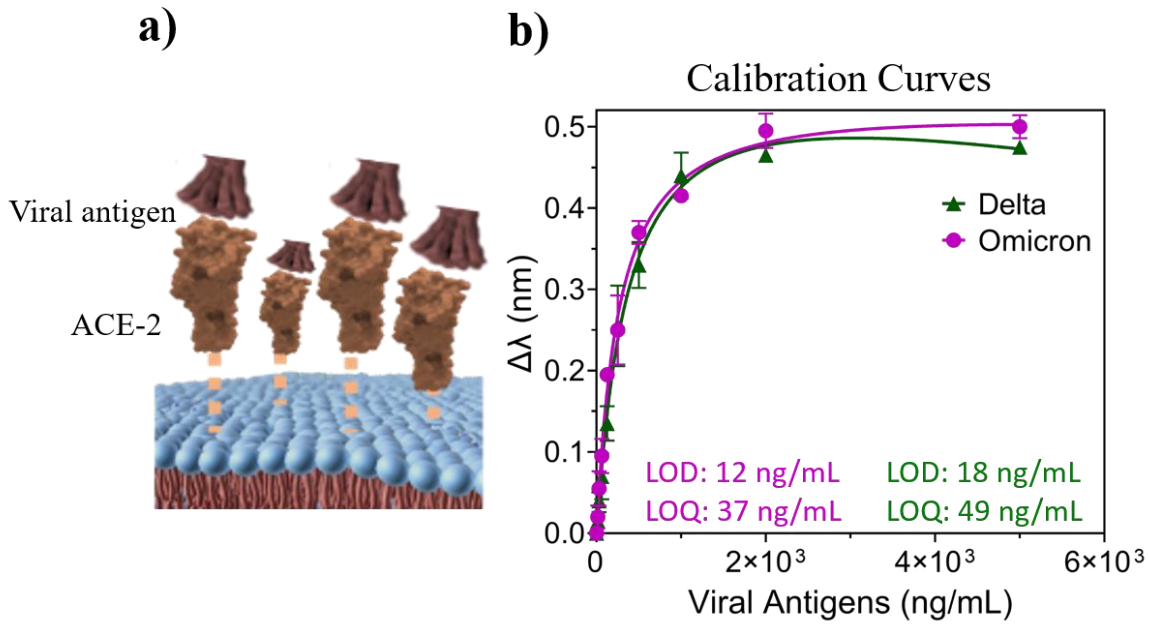

Fig 5. 5. a) Schematic illustration of SARS-CoV-2 viral antigens binding with ACE-2 anchored on biomimetic scaffold. b) Standard calibration curves for the SARS-CoV-2 viral antigens (Delta and

Omicron) were obtained with triplicate measurements of various concentrations over a range between 30 ng/mL to 5000 ng/mL for each specific protein variant.

Next, we proceeded to directly use the whole SARS-CoV-2 viruses as the primary target. We employed inactivated viruses produced and supplied by the National Institute of Infectious Diseases (INMI) in Rome, Italy. The viruses were inactivated through 15 minutes of ultraviolet (UV) irradiation at a wavelength of 254 nm, with successful inactivation confirmed by injecting the viruses into VeroE6 cells, and observing no viral duplication across three repeated passages. UV inactivation process is designed to target only virus genomic material (RNA), leaving external structure of the viral particles intact. To confirm it, we analyzed different samples of inactivated SARS-CoV-2 viruses, through UV and also conventional thermal inactivation, by transmission electron microscopy (TEM) (Figure 5.6).

In the UV inactivation (254 nm) treatment, the viral particle before inactivation appears intact, with a well-defined spherical shape. Thermal inactivation at 56°C causes partial damage and may be loss of spike proteins, while thermal inactivation at 95°C results in complete structural breakdown and fragmentation of the viral particles. Overall, the TEM images demonstrate that UV inactivation preserves the virus structure, while increasing heat progressively damages and ultimately destroys the viral particles. This ensures the virus can be safely handled in BSL-2 without compromising its structural integrity.[266]

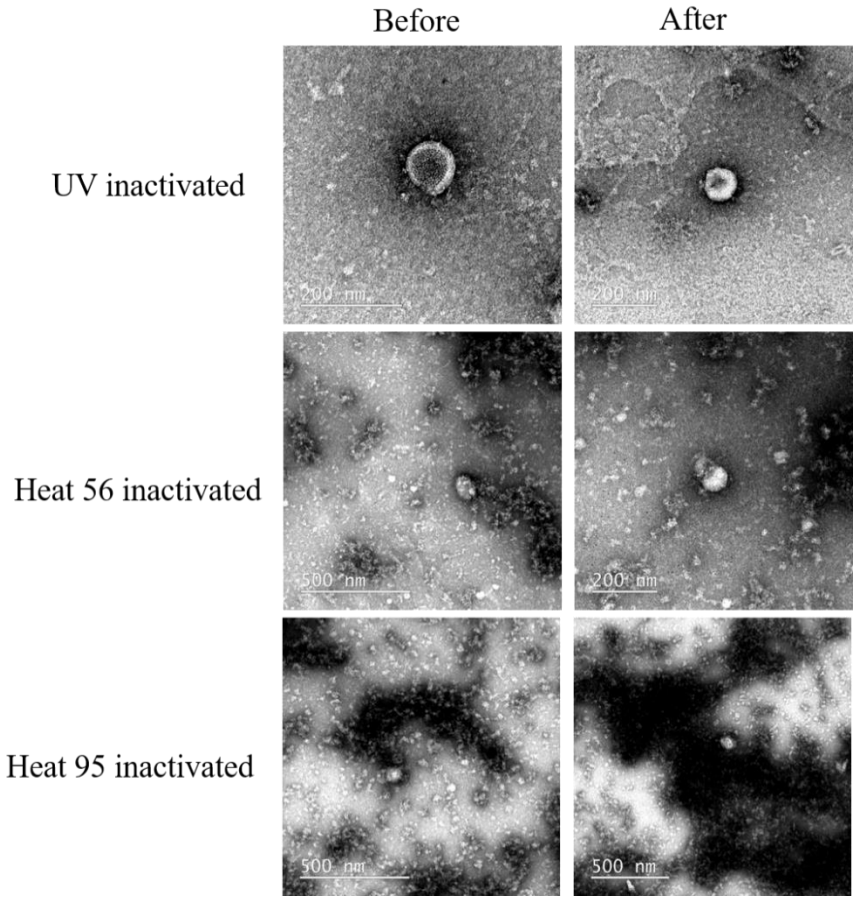

Fig 5. 6. TEM images of SARS-CoV-2 virus before and after inactivation through ultraviolet irradiation at a wavelength of 254 nm, and conventional thermal inactivation at 56 °C and 95 °C.

SARS-CoV-2 virus samples at various titers ranging from 10^3 to 5×10^5 TCID50/mL were prepared by serial dilution in the HEPES buffer and flowed over biomimetic scaffold on sensor surface. The real-time recorded sensorgrams show an effective binding of both Delta (Figure 5.7a) and Omicron (Figure 5.7b) virus variants, with increasing sensor signals corresponding to the increasing the viral load. The bulk changes in sensogram are due to the different composition of the stock virus samples compared to the running flow buffer.

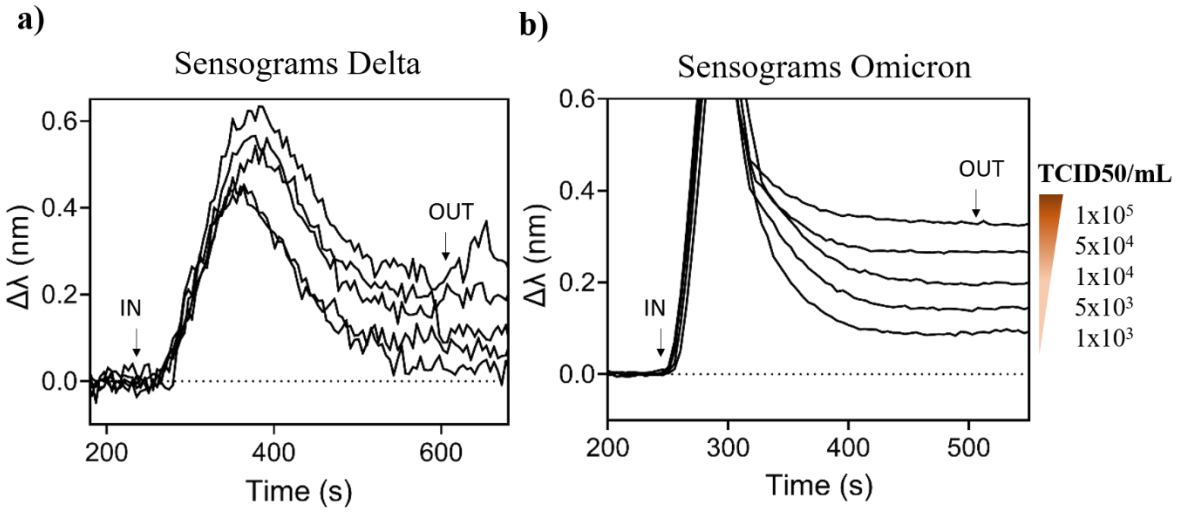

Fig 5. 7. a) Representative SPR sensorgrams obtained for different concentrations of Delta SARS-CoV-2 virus, b) Representative SPR sensorgrams obtained for different concentrations of Omicron SARS-CoV-2 virus.

From these direct assays, standard calibration curves were generated for both the Delta and Omicron variants by plotting the biosensor response (Δλ) against the whole virus concentration and fitting the data to a one-site specific binding model (Figure 5.8). For the Delta and Omicron variants, the LODs found to be 630 TCID50/mL and 200 TCID50/mL, respectively, and the LOQs were calculated to be 4700 TCID50/mL and 1200 TCID50/mL, respectively. Here, we observed that Omicron SARS-CoV-2 viruses attach to the ACE-2 receptor with a better effectiveness (25% higher) than Delta SARS-CoV-2 viruses. This difference could be partially attributed to variations in viral production and purification methodologies. Such differences may have influenced the bulk changes observed in the Omicron assay. Nevertheless, the sensitivity achieved in both direct assays demonstrates that our strategy can be effectively applied to both variants, supporting its robustness across different viral strains.

Besides, non-specific interactions were assessed by using a negative control sample (C-reactive protein, CRP, 2000 ng/mL). The signals produced were minimal, confirming that the sensor's response was primarily due to virus and ACE-2 interactions. Additionally, the lipid membrane effectively covered the entire sensor surface, preventing any significant non-specific adsorption. To evaluate the reproducibility of our detection assay for both variants, we conducted measurements across more than 37 different biomimetic sensor chips. Determined the coefficient of variation of approximately 6.2 % for the Delta variant and 5.8 % for the Omicron variant.

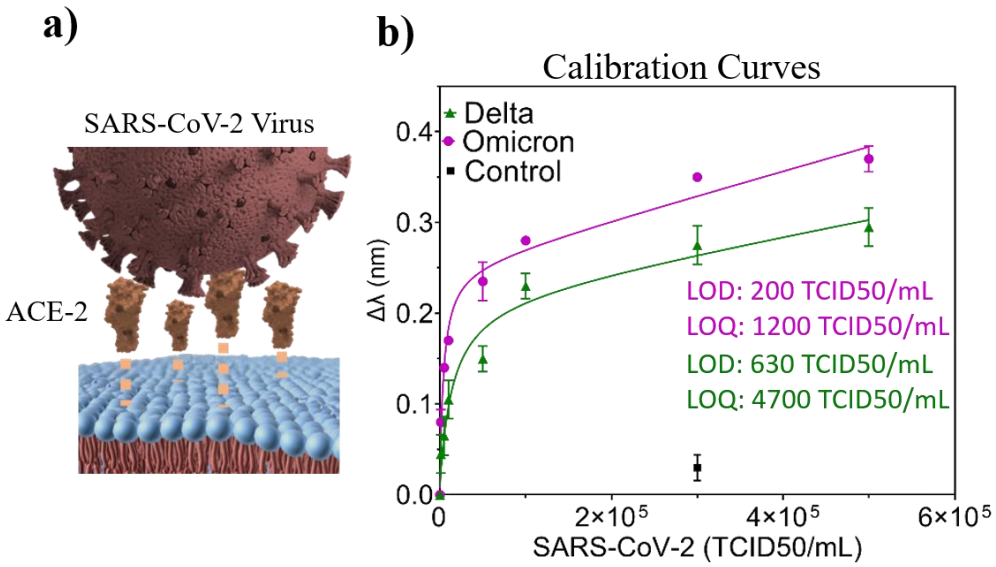

Fig 5. 8. a) Schematic illustration of SARS-CoV-2 virus binding with ACE-2 receptor anchored on biomimetic scaffold. b) Standard calibration curve for the UV-inactivated SARS-CoV-2 virus distinct variants (delta and omicron) achieved with the triplicate measurements of the different virus titters over range between 10^3 TCID50/mL to 5×10^5 TCID50/mL for each specific virus variant.

To our best knowledge, just one study has reported using a plasmonic sensor to detect entire SARS-CoV-2 virus particles, with a detection limit of 370 viral particles per milliliter (vp/mL),[267] which is comparable to our method. However, a key distinction is that their system demonstrated sensitivity using pseudoviruses, while ours was validated with real inactivated viruses, offering a more practical and reliable detection. Additionally, their approach involves post-amplification steps, leading to longer assay times and increased assay complexity. In contrast, our system enables direct detection in under 20 minutes, providing a rapid and more straightforward solution.

In order to test whether our high sensitivity can be attributed to the biomimetic scaffold, we did a direct comparison with conventional SAM. In this comparison, we functionalized SPR biosensor with the ACE-2 receptor onto a conventional SAM (using MHDA 1 mM) and tested its ability to detect various SARS-CoV-2 variants, including the wild type, Gamma, and Delta strains (Figure 5.9). The sensitivity and limit of detection for this conventional method were in the range of 10^3 TCID50/mL**,** but it showed low reproducibility, particularly at higher virus concentrations.

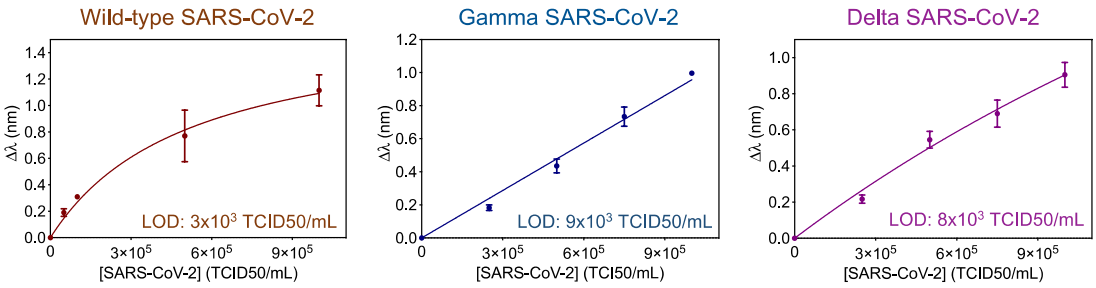

Fig 5. 9. Calibration curves performed for the detection of 3 different variants of SARS-CoV-2 virus obtained with a SPR biosensor functionalized with ACE-2 receptor immobilized on a conventional MHDA SAM.

A 5-fold improvement in detection limit was achieved with our biomimetic SPR sensor with high reproducibility. The superior sensitivity of the SLB-functionalize sensor is largely due to its biomimetic environment, which closely mimics the lipid membrane structure found in living cells. This similarity enhances virus-receptor interactions, allowing for more efficient binding between viral particles and ACE-2 receptors, as well as improved detection capabilities. In contrast to the SAM, SLB offers greater fluidity and structural characteristics that resemble biological membranes. While the SLB sensor shows enhanced sensitivity in this context, it does not imply that SLB is superior to SAM in all scenarios. The key advantage lies in the SLB's ability to provide a more natural platform for virus-receptor interactions, ultimately leading to better detection and sensitivity for viral particles.

5.4. Evaluation of monoclonal antibodies as anti-viral immunotherapy

Once the protocol for the receptor-virus interaction assay was established, we developed a neutralization assay to evaluate the effectiveness of monoclonal antibodies therapy. In this assay, we use a fixed concentration of virus, while varying the titers of the antibodies to determine their ability to inhibit the virus from binding to the ACE-2 receptor. By assessing the reduction in receptor-virus interactions at different antibody concentrations, we can quantitatively evaluate the neutralizing potential of antibody therapy.

To create SPR biosensor-based neutralization assay, we chose two different commercial SARS-CoV-2 neutralizing monoclonal antibodies (NAbs): NAb1, a recombinant IgG directed towards wild-type SARS-CoV-2 Spike protein, and NAb2, a recombinant IgM directed against a recombinant SARS-CoV-2 RBD protein. To assess and validate the reactivity and affinity of both NAbs towards the two SARS-CoV-2 viral types, a preliminary evaluation study was conducted using viral antigens as bioreceptors anchored to the sensor surface (Figure 5.10). Both viral antigens (Omicron-S and Delta-S proteins) were immobilized onto a traditional alkanethiol SAM using EDC/NHS chemistry.

Concentration-dependent binding curves were obtained by flowing varying concentrations of NAb1 and NAb2 over each immobilized viral antigen, ranging from 15 ng/mL to 200 ng/mL (Figure 5.10b and 5.10c). Additionally, we examined a negative control sample (200 ng/mL of SARS-CoV-2 Nucleocapside (N) protein), which showed negligible non-specific binding in both cases. These binding curves show that both neutralizing antibodies have the proper affinity and specificity for the two virus variants.

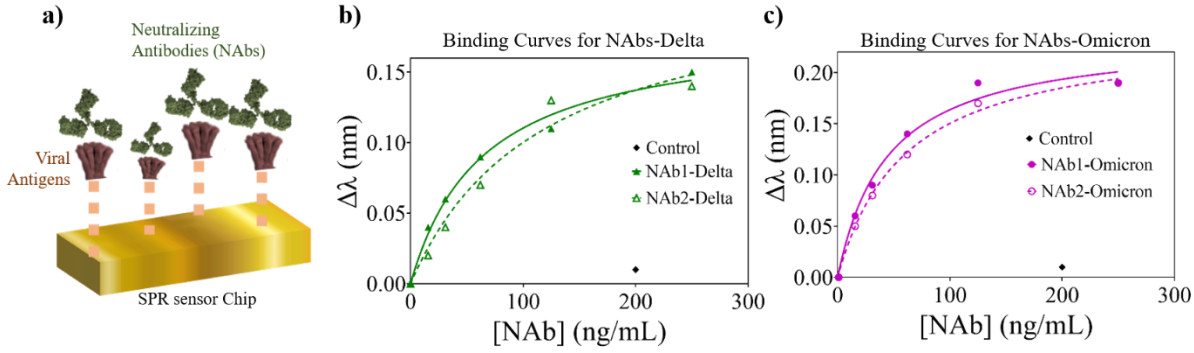

Fig 5. 10. a) Schematic illustrations of binding interactions of neutralizing antibodies with viral antigens (Omicron-S and Delta-S proteins) immobilized via EDC/NHS chemistry on conventional SAM SPR biosensor, b) Standard binding curves for Delta-S protein with NAb1 and NAb2, respectively, and c) Standard binding curves for Omicron-S protein with NAb1 and NAb2, respectively.

Later, we performed competitive immunoassays using the ACE-2 biolayer, where viral antigens were kept at a fixed concentration, and varying concentration of neutralizing antibodies were introduced. This assay was conducted directly on the SLB to assess the blocking ability of the antibodies between the ACE-2 receptor and the viral antigens. We have employed various dilutions of both neutralizing antibodies (NAb1 and NAb2) ranging from 7.8 to 5000 ng/mL, incubated them for 10 minutes with viral S-proteins: Delta and Omicron, respectively, at a constant concentration of 500 ng/mL.

The recorded sensorgrams show an effective neutralizing ability of both NAbs, at increasing NAbs concentration corresponding to the decreasing the sensor signals (Figure 5.11). The SPR sensorgrams obtained for the neutralization of SARS-CoV-2 Delta antigens with NAb1 and NAb2 are represented in Figures 5.11a and 5.11b, respectively. Similarly, the SPR sensorgrams obtained for the neutralization of SARS-CoV-2 Omicron antigens with NAb1 and NAb2 are shown in Figures 5.11c and 5.11d, respectively.

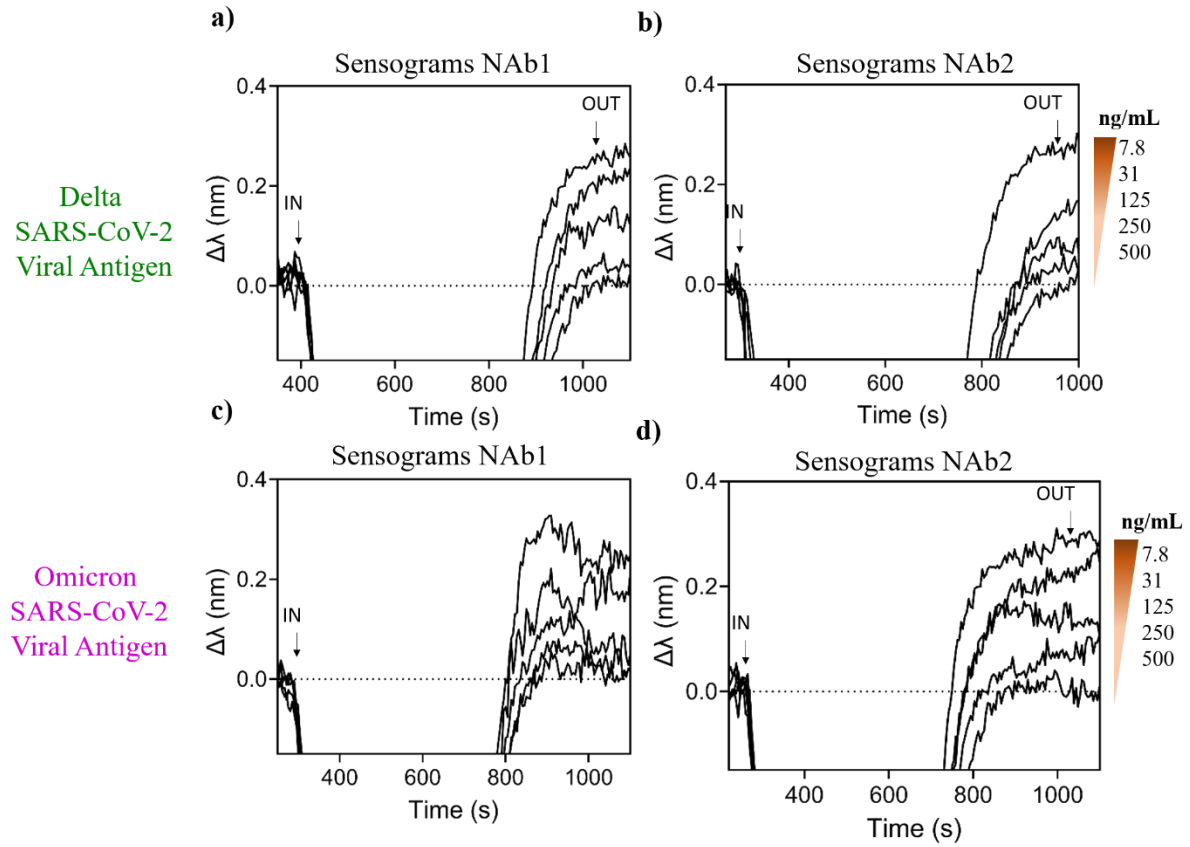

Fig 5. 11. a) Representative SPR sensorgrams obtained for different concentrations of NAb1 with Delta SARS-CoV-2 antigens, b) Representative SPR sensorgrams obtained for different concentrations of NAb2 with Delta SARS-CoV-2 antigens, c) Representative SPR sensorgrams obtained for different concentrations of NAb1 with Omicron SARS-CoV-2 antigens, and d) Representative SPR sensorgrams obtained for different concentrations of NAb2 with Omicron SARS-CoV-2 antigens.

In addition, a blank sample including the viral antigen sample absent of NAbs was incorporated into our analysis. This blank sample acted as a baseline to see how the viral antigens naturally interacted with the sensor surface. Furthermore, a negative control sample was included, comprising of 5000 ng/mL of NAbs in the absence of viral antigens. The fact that the blank and negative control samples produced either a null or minimal signal proved that the effects seen in the experimental samples were exclusively the consequence of the interaction between the antibodies and the viral antigens.

From the sensorgrams, the dose-response inhibition curves were obtained by plotting the normalized biosensor response (percentage inhibition) against the logarithm concentration of NAbs, and data were fitted to a sigmoidal dose-response model (Figure 5.12). As expected, presence of the neutralizing antibodies was able to block interaction between viral antigens and immobilized ACE-2 receptor in every instance, ultimately reducing and obstructing it at concentrations more than 2000 ng/mL.

Comparing the two distinct NAbs revealed some minor variations, as the assays using NAb2 (neutralizing IgM) reduced the signal earlier than those using NAb1 (neutralizing IgG).

These differences were confirmed by determining the half maximum inhibition concentration (IC_{50}) value, which represents concentration required to block 50% of a biological activity. Lower values denote greater potency. The IC_{50} values for both NAb1 and NAb2 were calculated, providing the comparative neutralization efficiency of the antibodies against the Delta and Omicron virus variants. In Delta variant assay, the IC_{50} for NAb1 was obtained at 142 ng/mL, while for NAb2, it was 68 ng/mL (Figure 5.12b). For Omicron variant assay, IC_{50} for NAb1 was calculated at 122 ng/mL, and for NAb2, it was 39 ng/mL, (Figure 5.12c). These results can be described by structural variances between two NAbs. An IgG is a Y-shaped molecule with two antigen-binding sites, while an IgM is a larger, pentameric molecule with up to ten antigen-binding sites. Therefore, it can be assumed that IgMs are more efficient at trapping viral antigens in solution, making them more effective at quickly blocking their interaction with ACE-2 receptors.

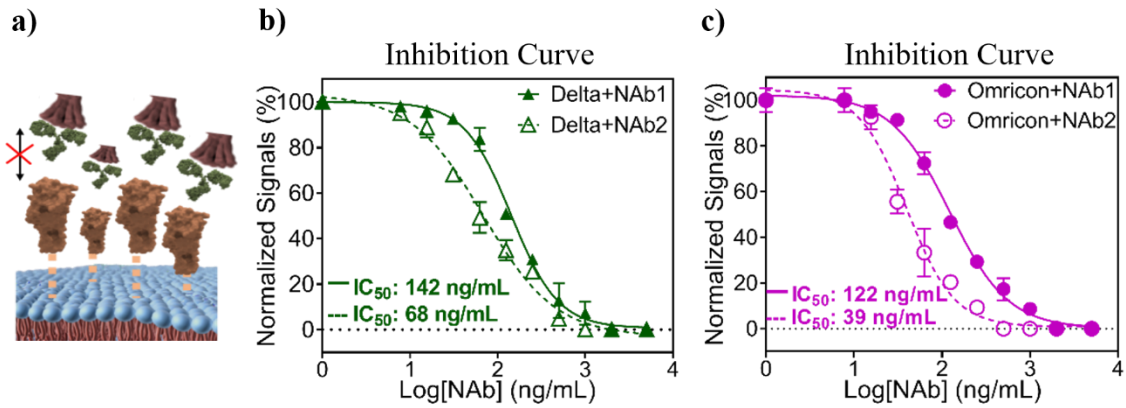

Fig 5. 12. Competitive immunoassay with the SARS-CoV-2 viral antigens: a) Schematic representations of SARS-CoV-2 antigen neutralization assay accomplished with the SARS-CoV-2 viral antigens and neutralizing antibodies over an ACE-2 receptor anchored to SLB-functionalized SPR biosensor, b) Inhibition curves attained for Delta-S protein at a constant concentration (500 ng/mL) incubated with the different concentrations of both neutralizing antibodies, and c) Inhibition curves acquired for Omicron-S protein at a constant concentration (500 ng/mL) incubated with different concentrations of both neutralizing antibodies. All the sensor signals were normalized according to the maximum signal (100%) and the minimum signal (0%) to facilitate comparison.

Finally, we validated our biomimetic plasmonic sensor for evaluating neutralizing monoclonal antibodies against SARS-CoV-2 whole viruses. The viral competitive immunoassays were conducted using an approach identical to the viral antigen assays. A fixed concentration of UV-inactivated SARS-

CoV-2 virus (5×10^4 TCID50/mL) was incubated for 10 minutes with varying concentrations of NAb1 and NAb2, ranging from 7.8 to 5000 ng/mL. Following incubation, the mixture was directly applied to the sensor, which had been functionalized with an artificial cell membrane displaying ACE-2 receptors.

The recorded sensorgrams demonstrate an effective neutralizing ability of both NAbs, at increasing NAbs concentration corresponding to the decreasing the sensor signals (Figure 5.13). The SPR sensorgrams obtained for the neutralization of SARS-CoV-2 Delta virus with NAb1 and NAb2 are represented in Figures 5.13a and 5.13b, respectively. The SPR sensorgrams obtained for the neutralization of SARS-CoV-2 Omicron virus with NAb1 and NAb2 are represented in Figures 5.13c and 5.13d, respectively.

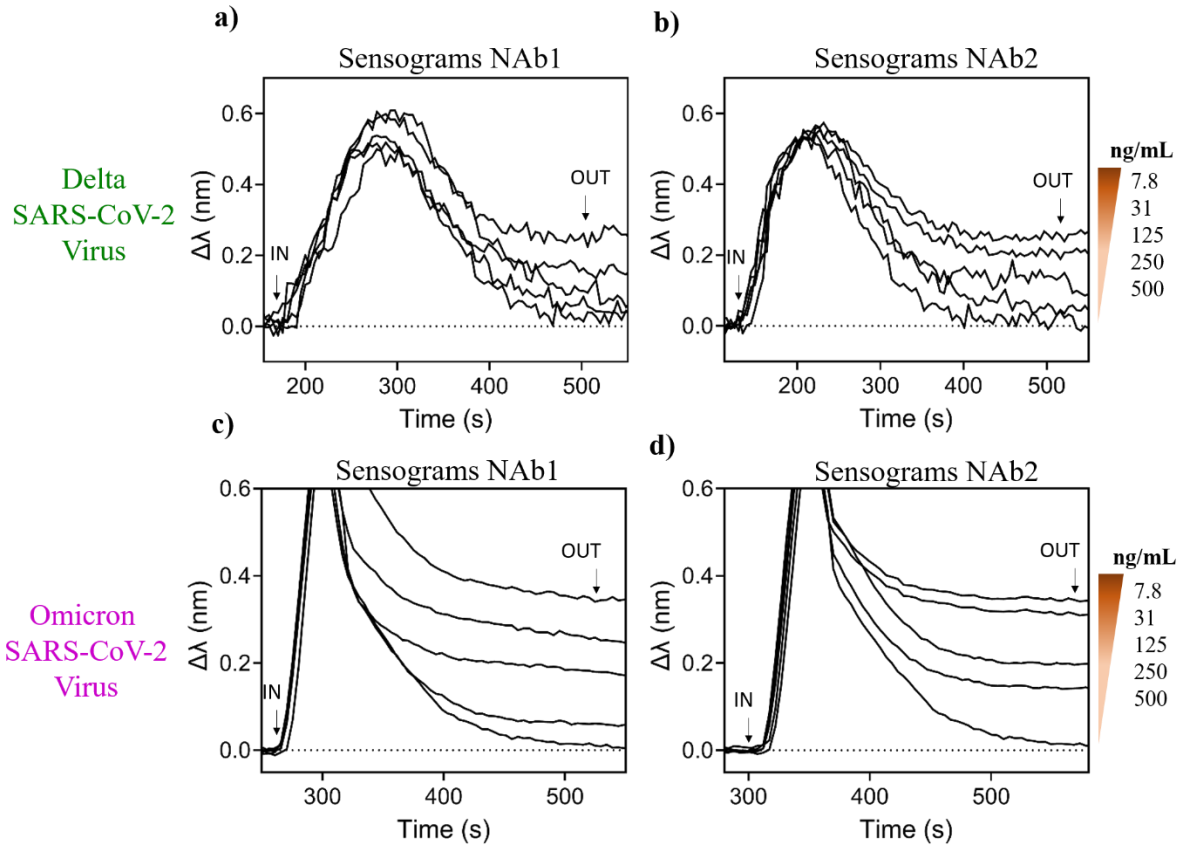

Fig 5. 13. a) Representative SPR sensorgrams obtained for different concentrations of NAb1 with Delta SARS-CoV-2 virus, b) Representative SPR sensorgrams obtained for different concentrations of NAb2 with Delta SARS-CoV-2 virus, c) Representative SPR sensorgrams obtained for different concentrations of NAb1 with Omicron SARS-CoV-2 virus, and d) Representative SPR sensorgrams obtained for different concentrations of NAb2 with Omicron SARS-CoV-2 virus.

From the sensorgrams, the dose-response inhibition curves were generated by plotting the normalized biosensor response against the logarithmic concentration of NAbs. The data was then fitted to a sigmoidal dose-response model, allowing for the calculation of IC_{50} value. The IC_{50} values for both NAb1 and NAb2 were determined for each virus variant (Figure 5.14), providing a comparison of the neutralization efficiency of these antibodies against SARS-CoV-2 viruses.

The IC_{50} values for each assay were calculated as 100 ng/mL for NAb1 and 78 ng/mL for NAb2 for the Delta variant (Figure 5.14b). For the Omicron variant, the IC_{50} values were 44 ng/mL for NAb1 and 22 ng/mL for NAb2 (Figure 5.14c). In this scenario, the differences between the two NAbs are less pronounced than those observed in the neutralization assay using viral antigens in solution. This reveal the importance of performing assays in a biomimetic environment, where both ACE-2 receptors and Spike proteins are integrated into their natural cell membranes. Although NAb2 is an IgM molecule with more available the binding sites, steric hindrance limits its ability to cooperate with a group of antigens, resulting in an inhibition ability similar to that of the IgG antibodies. On the other hand, both antibodies demonstrate a superior ability to neutralize the Omicron variant more effectively than the Delta variant. This is reflected in overall lower IC_{50} values and the achievement of complete inhibition at a lower dose, approximately 250 ng/mL.

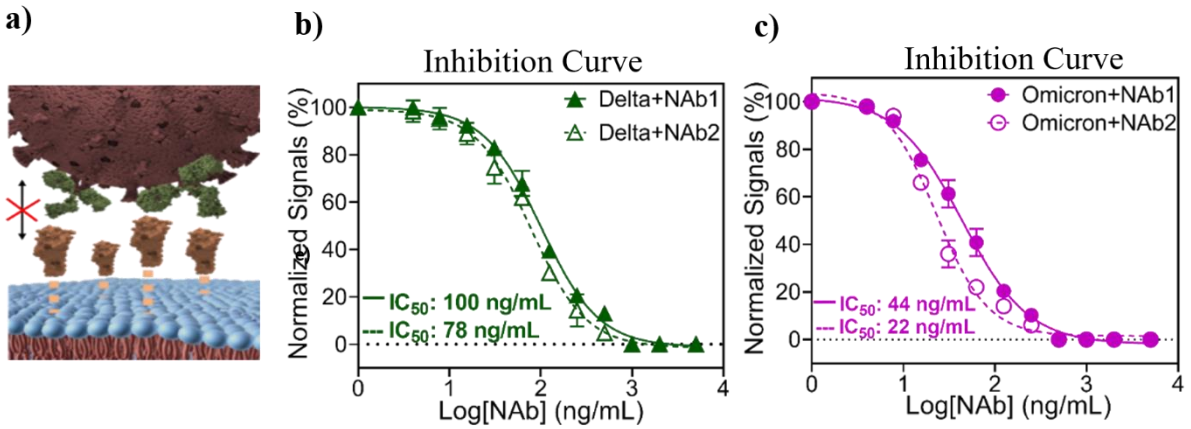

Fig 5.14. Competitive immunoassay with the SARS-CoV-2 virus variants: a) Schematic representations of neutralization assay executed with SARS-CoV-2 viruses and the neutralizing antibodies over the ACE-2 receptor anchored to a SLB-functionalized SPR biosensor, b) Inhibition curves attained for Delta SARS-CoV-2 virus at a constant concentration (5×10^4 TCID50/mL) incubated with the various concentrations of both neutralizing antibodies, and c**)** The inhibition curves obtained for Omicron SARS-CoV-2 viruses at the constant concentration (5×10^4 TCID50/mL) incubated with the different concentrations of both neutralizing antibodies. All the sensor signals were normalized according to the maximum signal (100%) and the minimum signal (0%) to facilitate comparison.

A summary of all bioanalytical parameters determined in this Chapter is provided in Table 5.1.

Table 5. 1. Summary of the main analytical parameters.

SARS-CoV-2 target and variant	**Direct & Label-free Detection**		**Neutralization Assay**	
	LOD	LOQ (ng/mL)	IC_{50} (NAb1)	IC_{50} (NAb2)
Delta S protein	18 ng/mL	49 ng/mL	142 ng/mL	68 ng/mL
Omicron S protein	12 ng/mL	36 ng/mL	122 ng/mL	39 ng/mL
Delta SARS-CoV-2 virus	630 TCID50/mL	4.8×10^3 TCID50/mL	100 ng/mL	78 ng/mL
Omicron SARS-CoV-2 virus	200 TCID50/mL	1.2×10^3 TCID50/mL	44 ng/mL	22 ng/mL

A comparison of this study with those involving approved monoclonal antibody therapies, like casirivimab, bamlanivimab, sotrovimab, and imdevimab, indicates that IC_{50} values determined using our biomimetic sensing designed assay is aligned well with those obtained through standard techniques, like ELISA, typically providing values ranging between 10 and 1000 ng/mL.[268] This alignment confirms accuracy of our analysis. Also, it is very important to highlight that biomimetic SPR sensor provides several key benefits over conventional techniques.

One of the key advantages is the speed and potential for automating the assays, eliminating the need for amplification, washing, or labeling processes. This accelerates the procedure and makes it more efficient. Additionally, the SPR sensor allows for a very similar-to-nature analysis, providing reliable results without complex and time-consuming procedure of mammalian cell culturing. Another notable advantage is the ability to perform the assay using a small volume of virus sample (150 μL) at concentrations similar to those commonly found in patients with mild or moderate symptoms (5×10^4 TCID50/mL). This makes the technique not only efficient but also highly relevant for practical applications.

These characteristics become especially critical when evaluating novel therapeutic candidates, particularly during a global health emergency like the COVID-19 pandemic. The ability to conduct simpler, label-free, faster, and more reliable therapy screening and assessment studies could significantly accelerate the selection and approval of the most promising formulations. This streamlined approach would help reduce production and manufacturing costs, ultimately speeding up the introduction of new therapies into healthcare systems worldwide. Such efficiency is crucial for improving access to effective treatments and ensuring rapid responses to global health challenges.

5.5. Summary and conclusions

We have developed a simple, rapid and user-friendly biomimetic sensing assay designed in order to streamline SARS-CoV-2 neutralization studies and expedite the production and optimization of new COVID-19 immunotherapies based on monoclonal antibodies. Our plasmonic sensor, functionalized with an artificial cell membrane, mimics real virus-cell interactions, allowing for label-free and real-time monitoring of the SARS-CoV-2 S protein binding to the human cell receptor (ACE-2 receptor). This approach eliminates the need for external tags and achieves exceptional sensitivity, with detection limits in the range of 10^2 TCID50/mL for major SARS-CoV-2 variants like Delta and Omicron—surpassing many existing plasmonic biosensors, which typically detect at 10^3–10^4 viruses/mL.

The biomimetic sensor was used to evaluate two distinct monoclonal antibodies as a potential candidate for the early treatment of COVID-19. The neutralization assays, performed with real inactivated SARS-CoV-2 viruses, yielded IC_{50} values comparable to those of approved monoclonal antibody therapies. Unlike conventional techniques that rely on the biomolecular immunoassays or the cell culture methods, our approach offers a precise and reliable assessment of antibody affinity and neutralization capabilities in a label-free, real-time format. This method requires only a small sample volume at realistic viral titers, making it particularly relevant for early treatment applications in non-hospitalized COVID-19 patients with mild to moderate symptoms. The results reveal potential of our biomimetic biosensor technology as an effective stage for evaluating the other types of antibodies or an immunotherapy, whether for emerging SARS-CoV-2 variants or other infectious diseases, autoimmune disorders, or cancers. In the future, we envision these biosensors being implemented as a simple and reliable tool in biomedical and pharmaceutical labs, helping to speed up the development and distribution of new therapies worldwide.

5.6. Experimental section

5.6.1. Chemical and biological reagents

Acetone and ethanol were acquired from Panreac Applichem (Barcelona, Spain). Lipids (POPC, 1-palmitoyl-2-oleoyl-snglycero-3-phosphocholine) and DOPS (1,2-dioleoyl-sn-glycero-3-phospho-L-serine) were delivered by Avanti Polar Lipids (Alabaster, Alabama, USA). Reagents for buffer preparation (10 mM PBS (Phosphate buffer saline, pH 7.4), 50 mM HEPES (N-(2-Hydroxyethyl) piperazine-N-(2-ethanesulfonic acid, pH 7.24), and MES (2-(N-morpholino) ethane sulfonic acid, pH 5.0)) and reagents for carboxylic groups activation (1-ethyl-3(3- dimethylaminopropyl) carbodiimide hydrochloride (EDC) and sulfo-N-hydroxysuccinimide (s-NHS)) were acquired to Sigma-Aldrich (Steinhem, Germany). Angiotensin-converting enzyme 2 (ACE-2), SARS-CoV-2 S proteins, and

neutralizing monoclonal antibody 2 (NAb2) were acquired from GenScript (Leiden, The Netherlands). The neutralizing monoclonal antibody 1 (Nab1) was acquired from Sino Biologicals (Eschborn, Germany). The inactivated SARS-CoV-2 viruses Omicron BA.1 (hCoV-19/Italy/LAZ-INMI-2890/2021, GISAID accession ID EPI_ISL_7716384), and B1.617.2/delta (hCoV-19/Italy/LAZ-INMI-648/2021 GISAID accession ID EPI_ISL_2000624) were delivered by our collaborator Dr. Giulia Matusali from The National Institute of Infectious Diseases Lazzaro Spallanzani (INMI, Rome, Italy). The virus manufacture and inactivation measures have been defined in.[266]

5.6.2. SPR biosensor description

Our proprietary SPR biosensor, designed and assembled in-house, utilizes the Kretschmann configuration in a compact and small device to monitor binding events in real-time through resonance wavelength interrogation at a fixed incidence angle ($\theta = 70°$). The plasmonic sensor chip is positioned between a trapezoidal glass prism, connected via refractive index matching oil (n=1.512), and a custom-made polymeric single-channel flow cell. This flow cell is linked to a fluid delivery system consisting of a syringe pump and a manually operated injection valve with a 150 µL loop for sample injection. The syringe pump ensures a consistent flow rate, which can be adjusted as needed. A collimated TM-polarized broadband light source excites the sensor surface through prism coupling, with the reflected light collected and fiber-coupled to a CCD mini-spectrometer (Jaz Module, Ocean Optics, Orlando, FL, USA). Real-time shifts in the plasmonic resonance peak (λ_{SPR}) are monitored and analyzed using a user-friendly software developed in Python, utilizing polynomial fitting. The plasmonic thin films (1 nm Ti, 49 nm Au) are coated with a 10 nm layer of SiO_2 to create a hydrophilic surface, ideal for efficient lipid bilayer formation. Prior to mounting the plasmonic chip on the SPR sensor, a specific cleaning protocol was followed: the chip was sonicated for 1 minute at room temperature in acetone, ethanol, and Milli-Q water, then dried with an N_2 stream. Finally, the chip surface was made more hydrophilic by placing it in a UV/Ozone Procleaner Plus (Bioforce Nanosciences, Utah, US) for 30 minutes.

5.6.3. Transmission electron microscopy

Transmission electron microscopy (TEM) was performed using a JEM-400 (JEOL USA, Pleasanton, CA) transmission electron microscope, equipped with a Gatan Inc. Orius SC1000 CCD camera (Gatan, Pleasanton, CA). Samples were prepared using an air-dried negative staining method. In brief, 8 µL of the sample mixture was placed on carbon-coated copper grids and incubated at room temperature for 1 minute. Excess sample was carefully removed using filter paper. The samples were then negatively stained by applying 8 µL of 2% uranyl acetate and incubating for 1 minute at room temperature. After staining, the excess stain was drained off as before, and the grids were allowed to air dry.

5.6.4. Data analysis

Data analysis was performed using Origin 8.0 (OriginLab, MA, USA) and GraphPad Prism 8 (GraphPad Software, CA, USA). Detection calibration curves were plotted, showing the mean and standard deviation (mean ± SD) of the biosensor response (Δλ) versus the target concentration. These data were fitted to a two-site specific binding model curve. The limit of detection often referred to as LOD represents the smallest change in the RI that can be reliably detected from background noise level. It can be defined as (Equation 1):

$$LOD = 3\delta/S \qquad (1)$$

Here, δ represent the standard deviation of the background signal in nanometer (nm) over the time in a sensogram and S is the sensitivity of sensor in nm per unit RI (nm/RIU). Additionally, quantification limit (LOQ), defined as minimum concentration which can be reliably detected and quantified. The LOD and LOQ correspond to the concentrations at 3 and 10 times the standard deviation of the sensor signal baseline, respectively.

5.6.5. SARS-CoV-2 virus detection

A biomimetic sensor chip functionalized with ACE-2 was used to optimize and evaluate virus detection assay, which was designed to target the Delta and Omicron versions of SARS-CoV-2. This was done using both viral antigens and whole UV-inactivated SARS-CoV-2 viruses. Calibration curves were generated by measuring the concentrations for viral antigens ranging from 30 ng/mL to 5000 ng/mL including whole viruses ranging from 10^3 TCID50/mL to $5x10^5$ TCID50/mL in a standard buffer (HEPES, 50 mM, pH 7.4) with a flow rate of 20 µL/min. Receptor-analyte connections were disturbed after each sample measurement, and biosensor surface was restored by infusing a 10 mM NaOH solution for two minutes at the same flow rate.

5.6.6. Competitive assay

For the competitive assay, the virus samples which are containing monoclonal antibodies with different concentrations (0 to 5000 ng/mL) were pre-incubated at room temperature for 10 minutes. And then flowed over the functionalized surface of sensor at a flow rate of 20 µL/min, keeping PBS 10Mm pH 7.4 as a running buffer. The inhibition calibration curves were plotted as the mean and standard deviation of the normalized biosensor response percentages. The data were fitted to a dose-response inhibition curve, and the half-maximal inhibitory concentration (IC_{50}) was calculated. Analyte concentrations were tested in triplicate for determining this value, and the signals (mean ± SD) were plotted against the analyte concentration's logarithmic value. With permission from the Autonomous

University of Barcelona (UAB) Biosafety Committee (HR-599-20), all viral detection tests were carried out in the ICN2 BSL2 facilities.

Chapter 6

Application to cancer immunotherapy evaluation

In this chapter, we use the AuNDs sensors from Chapter 2, combined with the artificial cell membrane from Chapter 4, to develop a biomimetic nanoplasmonic biosensor for real-time, label-free assessment of immune checkpoint inhibitors as cancer immunotherapy. It represents a proof-of-concept of the potential of our biosensor technology for more complex immunotherapy evaluation applications.

6. Application to cancer immunotherapy evaluation

6.1. Context and motivation

Immune checkpoint inhibitors (ICIs) are a kind of immunotherapy that works by restoring balance to the tumor immunosuppressive environment, enabling the patient's immune system to combat cancer. These drugs function by targeting certain cell receptors, known as immunological checkpoints, which serve as immune system brakes, stopping the body's ability to fight cancer cells. By interfering with these checkpoints, ICIs enable the immune system to more efficiently identify and eliminate tumor cells. Programmed cell death protein 1 (PD1) receptor, mostly expressed on T cell surfaces, is one of the important immunological checkpoints in cancer therapy. Tumor cells may inhibit the T cell's ability to kill by upregulating the corresponding ligand (PD-L1), but when the PD1/PD-L1 pathway is blocked by ICIs, the T cell's regulatory capacity to kill cancer cells can be restored (Figure 6.1).[269]

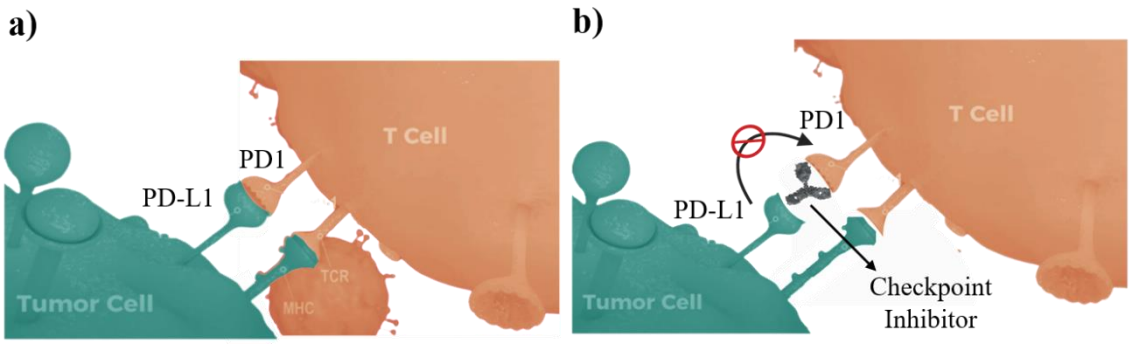

Fig 6. 1. a) Schematic illustration of direction interaction of PD1 receptor with PD-L1 ligand, and b) Illustration of the immune checkpoint inhibitor screening assay for PD1/PD-L1 pathway blocking. The figure is only for illustrative purposes; elements (nanodisks, lipids, proteins, and antibodies) are not to scale.

Currently, the US Food and Drug Administration and the European Medicines Agency have licensed several mAbs that target either PD1 (e.g., nivolumab, pembrolizumab, cemiplimab) or PD-L1 (e.g., atezolizumab, durvalumab, avelumab) for the treatment of various cancers.[270] The significance of ICIs in cancer treatment comes from their capacity to provide long-lasting effects in a wide range of cancer types, such as lymphoma, lung, bladder, and breast cancer, among many others. In contrast to conventional cancer therapies such as chemotherapy, which aim to eradicate cancer cells directly, ICIs may offer persistent advantages by preparing the body's defense to identify and eradicate cancer cells

throughout the body. As a result of this, the overall survival and quality of life for patients with advanced or metastatic cancers have significantly improved. Nonetheless, it is important to note that not all patients react to ICIs, and research is still being done to find out why some people benefit from ICIs more than others in order to create solutions to increase their efficacy.

The development of tumor resistance mechanisms is a major drawback of ICIs treatment. Cancer cells are able to adapt and elude immune monitoring through a variety of strategies, including as the activation of alternative immune checkpoints, modifications to antigen presentation, and the recruitment of immunosuppressive cells. Improving the long-term effectiveness of ICIs requires an understanding and strategy for overcoming these resistance mechanisms. Furthermore, assessing the efficacy of ICIs can be complex. It may require new analytical techniques for rapid screening of different inhibitor candidates and their dose-response curves. These techniques also help study new immune checkpoints and characterize the mechanism of action and the patient's immune response.

Currently used techniques for immune checkpoint inhibitor screening and assessment include SPR biosensing, ELISA, fluorescence-based technologies, nuclear magnetic resonance (NMR) spectroscopy, isothermal titration calorimetry (ITC), microscale thermophoresis (MST), and biolayer interferometry (BLI).[271] However, these techniques often require expensive equipment or labeling, making them laborious and time-consuming. Additionally, they do not account for the mobility or restrictions of ligands when they are expressed on the cell membranes. To address this, cell-based assays can be performed using bioluminescence or fluorescent receptors in cell culture experiments. These assays help evaluate the activation of T cells by targeting specific receptors or monitoring cytokine secretion events.[271] While these techniques are useful for evaluating the fundamental biological roles and impacts of ICIs, the results are frequently of a qualitative nature. Additionally, cell culture studies are laborious and complex, needing expert staff and specialized equipment, and the variety of cell populations or labelling interferences may cause them to be biased.

Based on our previous developments in this Thesis, we propose to employ of a biomimetic nanoplasmonic biosensor for the label-free, real-time, fast assessment and screening of ICIs by combining the key advantages of optical biosensor technologies with cell-based assays in order to produce and accurate and dependable data while reducing the need for laborious culture procedures and potential labelling interferences. We will be using the Au nanodisks (AuNDs) sensors developed in Chapter 2, which rely on the LSPR phenomenon for highly sensitive evanescent-field sensing of biomolecular interactions in a compact, user-friendly device. The nanoplasmonic sensors will be directly functionalized with the artificial cell membrane from Chapter 4, which mimics the molecular mobility of a tumor cell membrane. This membrane will be precisely functionalized with immune

checkpoint ligands, allowing us to study checkpoint receptors and inhibitors without the need for cell culture experiments, enabling efficient and accurate analysis of these interactions.

The chapter begins by studying the PD1/PD-L1 interaction. The biomimetic PD-L1 functionalized membrane will closely mimic the natural tumor cell surface, allowing for real-time monitoring of the PD1 receptor binding events using the nanoplasmonic sensor (Figure 6.2a). This will provide a highly sensitive and specific method to detect PD1/PD-L1 interactions, which are critical in immune response modulation. Next, the biosensor will be used to evaluate the therapeutic efficacy of ICIs (Figure 6.2b). The biomimetic sensor will measure the ability of immune checkpoint inhibitor to inhibit the PD1/PD-L1 interaction by binding to the PD1 receptor. The platform will provide real-time evaluation of this inhibiting bioassay, offering a direct and efficient method for assessing the performance of ICI in cancer immunotherapy.

By simplifying both the direct monitoring of PD1/PD-L1 interactions and the evaluation of ICI, this dual-function biosensor will reduce the complexity and time required for analysis, making it highly adaptable for rapid screening. The biomimetic properties of the artificial membrane will ensure that laboratory results are transferable to clinical settings, contributing to the advancement of cancer immunotherapy research and therapeutic development.

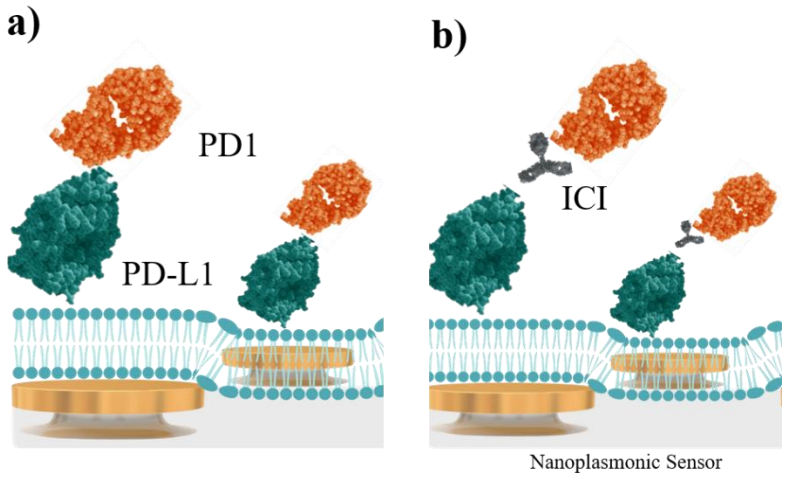

Fig 6. 2. a) Schematic illustration of the biomimetic LSPR sensor approach for monitoring direct interaction of PD1 receptor with PD-L1 ligand, and b) Schematic illustration of the immune checkpoint inhibitor screening assay for PD1/PD-L1 pathway blocking. The figure is only for illustrative purposes; elements (nanodisks, lipids, proteins, and antibodies) are not to scale.

6.2. Formation of PD-L1 functional membranes

Similarly, to our previous application study (Chapter 5), to create an on-chip artificial tumor cell membrane, we employed human recombinant PD-L1 ligand conjugated to an Fc domain to be immobilized on a COOH-functional SLB scaffold. However, prior to the immobilization on the lipid bilayer, we performed a brief protocol optimization and assessment employing AuNDs functionalized with conventional SAM (Figure 6.3). We essentially tested various immobilization parameters including pH level (5 to 8) in different buffers, such as MES 50 mM and PBS 10 mM, different ratios of SAMs (MHDA:MUOH), and concentrations of PD-L1 ranging from 10 to 50 µg/mL.

In terms of buffer and pH, best performance in terms of binding efficiency was obtained with MES buffer at pH 5.5 (Figure 6.3b**)**. In terms of SAM functionality, the COOH-OH 1:10 molar ratio offered the best results, possibly because it provided a balanced surface density that maximized the availability of functional groups for PD-L1 binding without causing steric hindrance (Figure 6.3c). And finally, we found that 50 µg/mL of PD-L1 provided optimal immobilization, yielding the highest signal and fully occupying the available binding sites on the sensor (Figure 6.3d).

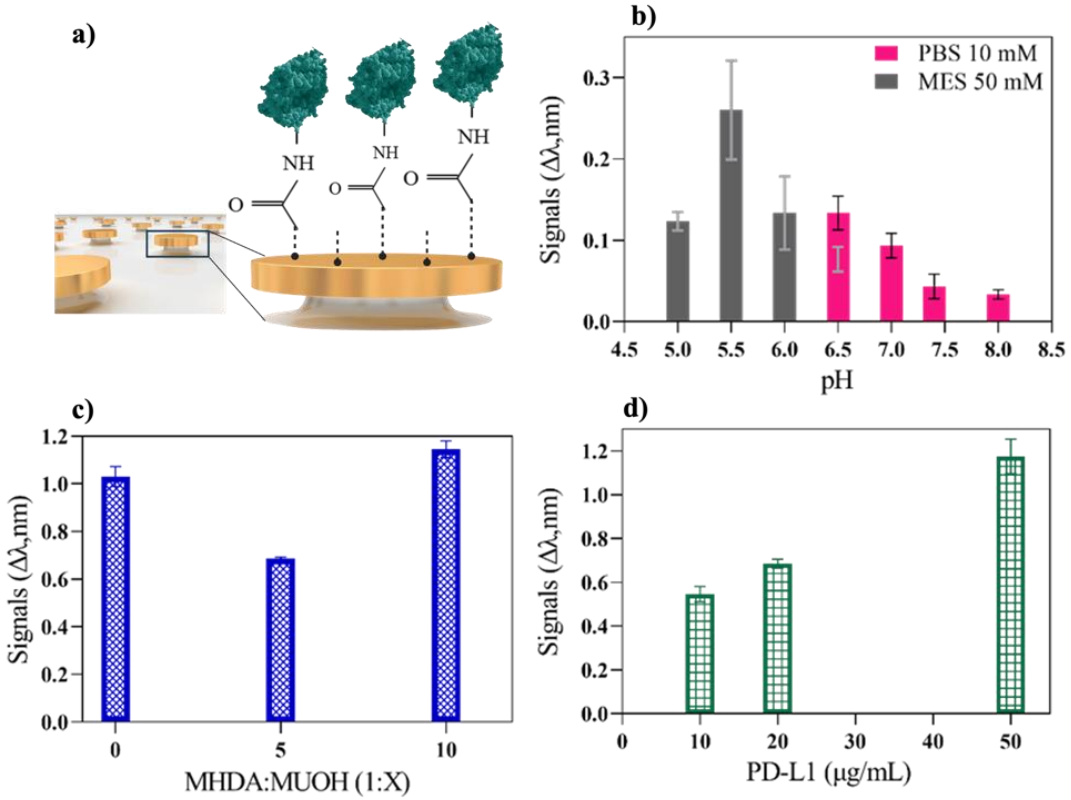

Fig 6. 3. Illustrates the optimization protocol for PD-L1 immobilization through EDC/NHS chemistry utilizing a conventional self-assembled monolayer on gold plasmonic nanostructures. a) Schematic representation of SAM formation on gold plasmonic nanostructures. b) Bar graph depicting various pH

levels across different buffers. c) Illustrating different ratios of MHDA:MUOH. d) Bar graph demonstrating the different concentrations of PD-L1 ligand.

With this optimized immobilization conditions, we addressed the formation and functionalization of a PD-L1 lipid membrane scaffold (Figure 6.4). The COOH-functional SLB (POPC:DOPS 10:1) was formed on the AuNDs sensors without the need of a SiO_2 coating, as previously optimized and demonstrated in Chapter 4. The resulting sensorgram shows the clear increase of the sensor signal, reaching equilibrium at approximately 4 nm shift, and maintaining stability for several minutes, even after introduction of a cleaning solution (NaOH) (Figure 6.4a). Once the SLB layer was stabilized, the PD-L1 molecules were covalently immobilized through EDC/NHS chemistry on the SLB surface. Figure 6.4b shows the obtained sensorgram. The binding of PD-L1 caused a significant signal increase (about 3 nm), which remained stable even after ethanolamine deactivation and a NaOH cleaning step. The consistency and reliability of the entire biofunctionalization process were tested across more than 15 sensor chips, resulting in a 6% variation for the SLB formation and a 12% variation for the PD-L1 immobilization.

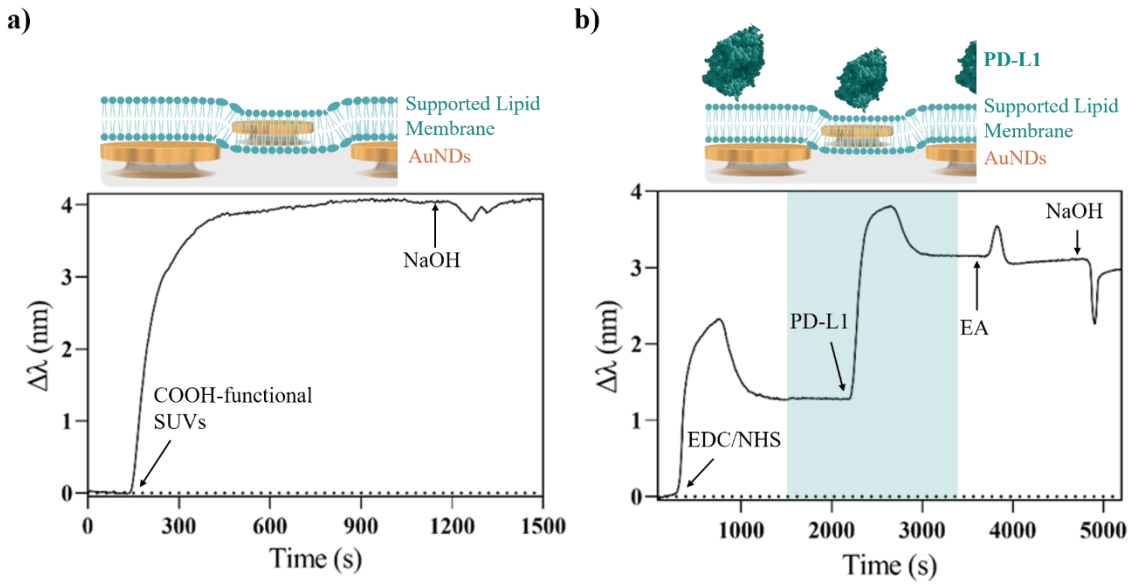

Fig 6. 4. a) The LSPR sensorgram illustrates the formation of a SLB by the disruption of small unilamellar vesicles, followed by a NaOH cleaning step. b) The LSPR sensorgram shows the covalent attachment of PD-L1 molecules onto the SLB using EDC/NHS chemistry. Please note that the figure is for illustration only, and the elements (nanodisks, lipids, proteins, and antibodies) are not shown to scale.

6.3. Highly sensitive analysis and monitoring of PD1 / PD-L1 interactions

To demonstrate the applicability of our biomimetic nanoplasmonic sensor, we first focused on analyzing and monitoring the interactions between PD-L1 and PD1 immune checkpoints. This involved optimizing the assay conditions to ensure maximum recognition efficiency by PD-L1 while reducing the possible non-specific absorption (Figure 6.5).

First, we systematically investigated how different buffer compositions and pH levels influenced the binding kinetics and specificity of PD1/PD-L1 interactions. Given that tumor microenvironments typically exhibit lower pH levels (between 5.5 and 7.0), pH-dependent protein-ligand interactions can be leveraged to alter drug affinity and specificity for a wide range of malignancies.[272] Specifically, we flowed a fixed concentration of PD1 (2 μg/mL) diluted in different buffers with pH levels ranging from 5 to 9 (Figure 6.5a). Additionally, to assess the assay's specificity under each buffer condition, we introduced a high concentration of C-reactive protein (4 μg/mL) as a negative control (Figure 6.5b).

Acetate buffer at pH 5 and borate buffer at pH 6.5 exhibited high affinity but also significantly increased non-specific interactions. In contrast, PBST (PBS with 0.05 % Tween 20, a nonionic surfactant) at pH 6.5 demonstrated high affinity with negligible non-specific interactions. The addition of Tween 20 in PBS helps minimize non-specific binding and protein-protein interactions, making it useful for various biochemical applications. However, the surfactant content of PBST is unsuitable for our biomimetic scaffold, as lipid membranes easily disrupt in presence of detergents and surfactants.[273]

We also examined HEPES buffer across various pH levels, finding that 50 mM HEPES at pH 7.5 exhibited significant affinity (parrot green bar). With these conditions, the negative control showed a negligible sensor signal, reflecting the minimal non-specific interactions with the sensor surface. The results confirmed that the sensor response is essentially due to PD1/PD-L1 interactions at pH 7.5 with HEPES 50 mM buffer.

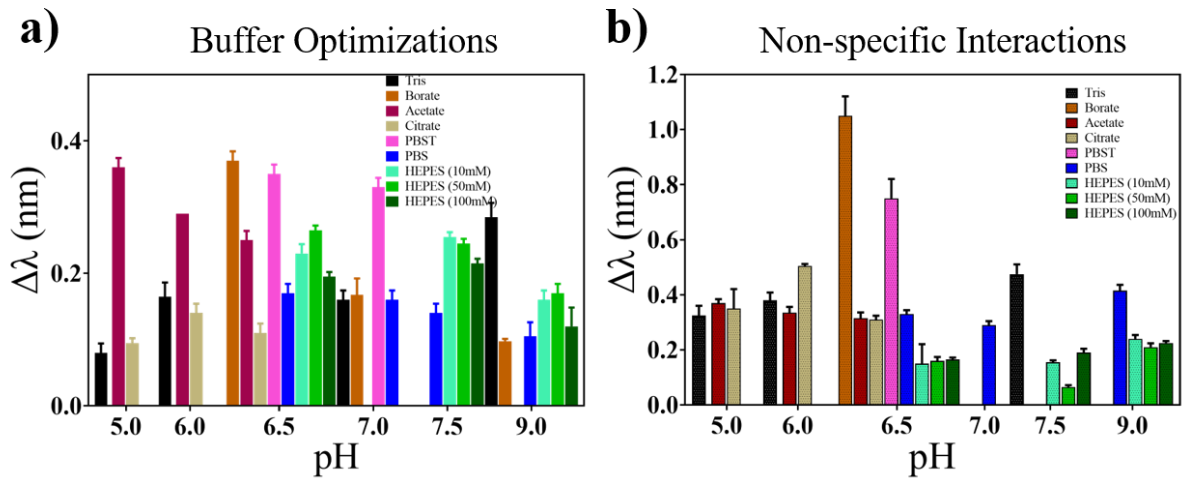

Fig 6. 5. a) Buffer and pH optimization of direct assay conditions for PD1/PD-L1 interactions, and b) Assessment of non-specific interactions in different buffers.

After optimizing the experimental conditions, we proceeded to study the direct interaction between PD1 and PD-L1 using our biomimetic nanoplasmonic sensor. For the generation of a calibration curve, we prepared a series of PD1 samples with concentration ranging from 7.6 to 5000 ng/mL diluted in 50 mM HEPES buffer, and they were flowed over the PD-L1 biomimetic sensor surface, using 10 mM PBS as running buffer. The recorded sensorgrams show an effective binding of PD1 with PD-L1, with increasing sensor signals corresponding to the increasing PD1 concentrations, as expected (Figure 6.6).

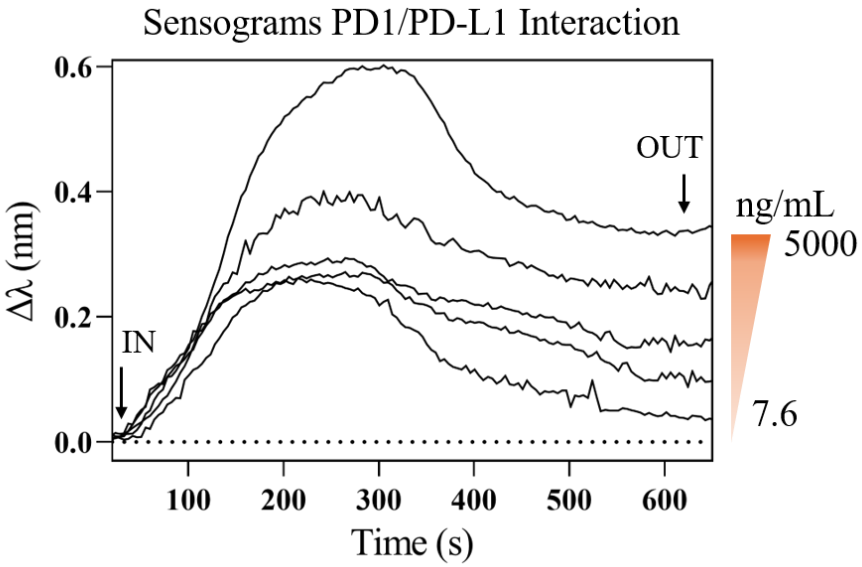

Fig 6. 6. Representative LSPR sensorgrams obtained for different concentrations of PD1 binding to PD-L1. All the measurements were performed in triplicate for each data point.

We obtained the standard calibration curve from these sensograms by plotting the sensor signals (Δλ) against PD1 concentrations, and the curve was fitted to a one-site saturation binding model (Figure 6.7). To assess potential non-specific interactions, we also introduced a negative control sample (CRP), at varying concentrations. The non-specific signals were negligible, confirming that the sensor response was primarily driven by the PD1/PD-L1 interactions. Additionally, this outcome indicated that the lipid membrane effectively covered the entire sensor surface, successfully preventing non-specific adsorption. The detection limit and quantification limit were determined at 6.7 ng/mL (0.2 nM) and 79 ng/mL (2.6 nM), respectively.

These results highlight the exceptional sensitivity of our biosensor, achieving limits of detection that are up to an order of magnitude better than those previously reported with plasmonic sensors for analyzing PD1/PD-L1 interactions, obtaining LODs at 0.77 μM[274] and 1.9 μM.[275] The reason could be attributed to the unique design and biomimetic LSPR surface modification that enhanced the sensitivity compared to conventional SPR sensor, by enabling lateral mobility of the PD-L1. Lastly, it is important to note that the entire binding affinity assay can be completed in under 20 minutes using just a 150 μL sample volume. This process does not require any additional reagents and can be conducted with a compact and user-friendly instrument.

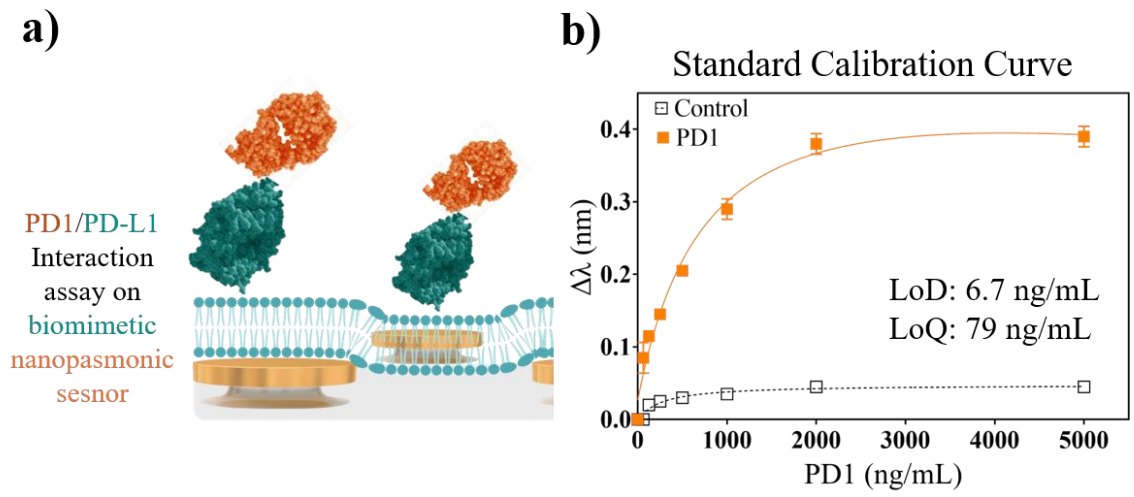

Fig 6. 7. a) Schematic illustration of PD1 binding to PD-L1 ligands anchored to biomimetic nanoplasmonic sensor, b) Standard calibration curve performed for the detection of PD1 receptor, including data for a negative control protein (square) at different concentrations. All the measurements were performed in triplicate for each data point. The figure (a) is only for illustrative purposes; elements (nanodisks, lipids, proteins, and antibodies) are not to scale of PD1 protein.

6.4. Assessment of monoclonal antibody as PD1 checkpoint inhibitor

Finally, our biomimetic nanoplasmonic sensor was utilized to evaluate a PD1 checkpoint inhibitor as potential candidates for cancer immunotherapy. For the competitive assay development, we utilized a commercially available anti-PD1 monoclonal antibody as inhibitor. This mAb is an IgG1 isotype antibody, chosen for its high affinity, specificity, and structural stability. The inhibition assay was conducted by immobilizing PD-L1 on the functional SLB, and incubating for 10 min the PD1 sample at a fixed concentration (2000 ng/mL) with serial dilutions of inhibitory mAbs, ranging from 0 to 6500 ng/mL. The sensograms obtained for the inhibition of PD1 with anti-PD1 mAb are represented in Figure 6.8. In the sensogram, increasing concentrations of anti-PD1 monoclonal antibodies progressively inhibit the interaction between PD1 and PD-L1, as expected.

At lower mAb concentrations, partial inhibition occurs, allowing some PD1/PD-L1 binding, resulting in a smaller signal. As the concentration increases, more PD1 receptors are inhibited by the mAbs, reducing the interaction with PD-L1. This causes the signal to rise initially and then decrease as the inhibition becomes more effective, showing that higher mAb concentrations lead to stronger inhibition of the PD1/PD-L1 interaction. We also tested a negative control sample (6500 ng/mL with no PD1) which resulted in negligible signal, and a blank sample (PD1 with no antibody), showing the highest signal.

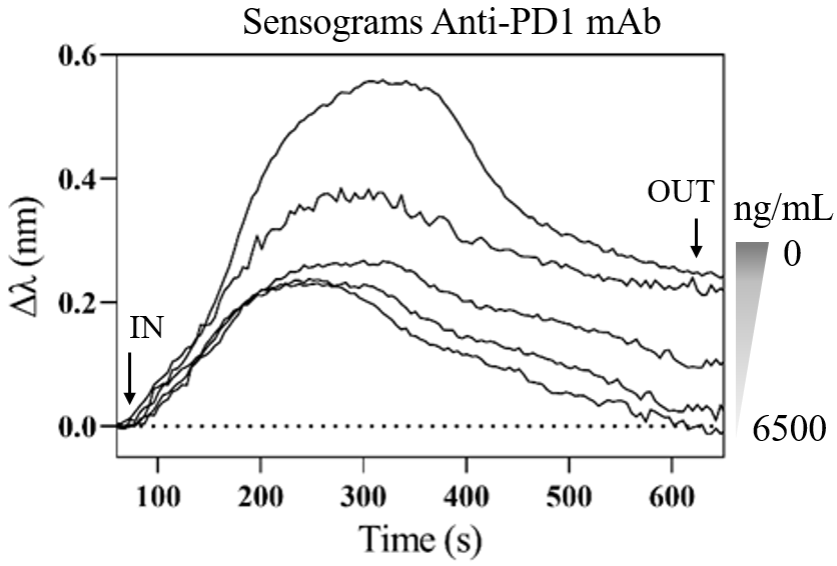

Fig 6. 8. Representative LSPR sensorgrams obtained for different concentrations of anti-PD1 mAb mixed with PD1 receptors, and their binding to PD-L1. All the measurements were performed in triplicate for each data point.

From the sensogram, we extracted the dose-response inhibition curve by plotting the normalized biosensor response against the logarithmic concentration of inhibitory monoclonal antibody. The data were fitted to a sigmoidal dose-response model, allowing for the calculation of IC_{50} value. In Figure 6.9, it can be seen that the presence of mAb binding to PD1 was able to hamper the cell receptors interaction, achieving the complete blocking of PD1/PD-L1 pathway at a mAb concentration of 2000 ng/mL. The determination of the IC_{50} parameter for inhibiting antibody was at 64.76 ng/mL (0.43 nM). These IgG1 antibodies interact with PD1 through their antigen-binding (Fab) regions, which bind with high affinity to PD-1 on immune cells. This binding blocks the interaction with PD-L1, effectively preventing inhibitory signaling and promoting T cell activation, thus enhancing anti-tumor immune responses.[276]

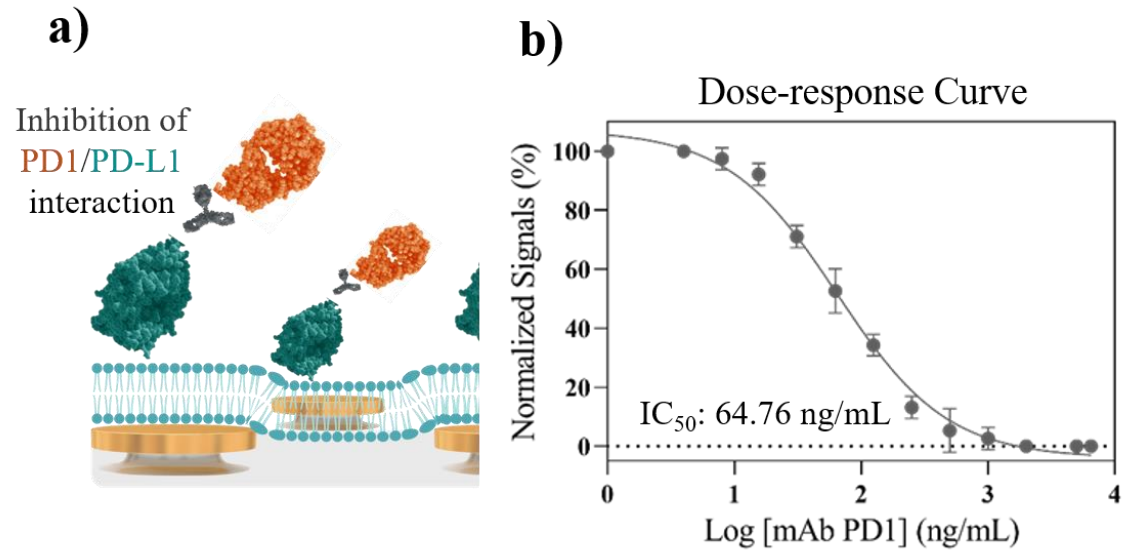

Fig 6. 9. Evaluation of mAb as PD1 checkpoint inhibitor: a) Schematic illustration of the competitive assay performed with an anti-PD1 mAb over the PD-L1-functionalized biosensor, and b) Dose–response inhibition curve obtained for a fixed concentration of PD1 (2000 ng/mL) incubated in a series of dilutions of anti-PD1 mAb. All the measurements were performed in triplicate for each data point. The figure (a) is only for illustrative purposes; elements (nanodisks, lipids, proteins, and antibodies) are not to scale.

A comparison of inhibitory (IC_{50}) values with FDA approved mAb inhibitors, such as pembrolizumab (keyturda), cemiplimab (libtayo) and nivolumab (opdivo), determined through standard techniques, like flow cytometry and ELISA, indicates that the inhibitory value obtained from our biomimetic LSPR sensing assay is in good agreement (Table 6.1). For example, various studies have analyzed and assessed nivolumab, the most widely used PD1 inhibitor drug, determining its IC_{50} at 1.3 nM with fluorescence techniques[277] and at 2.52 nM using an SPR biosensor.[278] On the other hand, novel PD1 immune checkpoint inhibitors like pembrolizumab, camrelizumab, cemiplimab, and murine

monoclonal antibodies have been thoroughly studied using flow cytometry, with IC_{50} values ranging from more than 5 nM to as low as 0.24 nM.[279,280] Here, our findings confirm the validity of our novel biomimetic technique with an IC_{50} of 0.43 nM for an anti-PD1 mAb.

This comparison study emphasizes the unique benefits of the biomimetic LSPR sensing approach for evaluating monoclonal antibodies as checkpoint inhibitors in cancer immunotherapy. Unlike flow cytometry, which can be labour-intensive and less sensitive to subtle protein interactions, our biomimetic LSPR sensor accurately simulates the tumor microenvironment, providing a realistic view of anti-PD1 monoclonal antibody interactions. This innovative method allows for real-time tracking without enzymatic markers, delivering results in under 20 minutes and making it a potential candidate for high-throughput screening with minimal sample requirements.

Table 6. 1. Comparison of PD1 checkpoint inhibitors evaluation results with different analytical techniques.

Technique	**Checkpoint Inhibitor**	**IC_{50} (nM)**	**Reference**
Biomimetic LSPR Sensor	anti-PD1 mAb	0.43	This work
Fluorescence	nivolumab	1.3	[277]
SPR sensor	nivolumab	2.52	[278]
Flow cytometry	camrelizumab	5.6	[279]
Flow cytometry	cemiplimab	2.6	[279]
Flow cytometry	pembrolizumab	0.9	[279]
Flow cytometry	anti-PD1 mAb	0.24	[280]

Additionally, our biosensor is integrated into a point-of-care device, offering quick, label-free examination and improved accuracy through biomimetic environments that mimic individual cell interactions. The high sensitivity of this device reduces reagent and cell sample usage, potentially lowering costs in pre-clinical research and therapy production. Overall, the biomimetic LSPR sensing approach presents great advantages in evaluating cancer immunotherapy checkpoint inhibitors, facilitating faster and more effective drug development.

6.5. Summary and conclusions

We have developed a simple, rapid, and user-friendly biomimetic nanoplasmonic sensing assay to study and assess checkpoint inhibitors in cancer immunotherapy based on anti-PD1 monoclonal antibody. Our low-density short-order nanoplasmonic sensor, functionalized with an artificial cell membrane, mimics tumor microenvironment, enabling for label-free and real-time monitoring of PD1 immune

check point to the human recombinant receptor (PD-L1). This approach eliminates the need for external label and achieves the exceptional sensitivity, with detection limit of 0.2 nM surpassing the existing plasmonic biosensors, which typically detect at 0.77 μ M – 1.9 mM. The nanoplasmonic biomimetic sensor was used to evaluate the inhibiting potency of check point inhibitor as potential candidate for cancer immunotherapy. The inhibition assay, performed with anti-PD1 monoclonal antibody, yielded IC_{50} value comparable to the value determined with conventional analytical techniques for similar therapeutic formulations.

Unlike conventional techniques that rely on the cell culture methods, our approach offers a precise and reliable assessment of antibody binding and inhibiting capabilities in a label-free and real-time format with a minimal amount of sample. The results demonstrate the potential of our biomimetic nanoplasmonic biosensor technology as an effective stage for assessing of different immune check point inhibitors, or possible tumor resistance mechanisms. In the future, we envision our biomimetic sensor technology as a simple and reliable tool that could be used to determine affinity and kinetic parameters of different checkpoint inhibitors or other cell receptor-ligand interactions in cancer research labs, helping to improve the effectiveness of immunotherapies and speed up their validation and use in clinics worldwide.

6.6. Experimental Section

6.6.1. Chemical and biological reagents

Reagents for cleaning the sensor chips acetone, and ethanol were provided by Panreac Applichem (Barcelona, Spain). Lipids (POPC, 1-palmitoyl-2-oleoyl-sn-glycero-3-phosphocholine) and DOPS (1,2-dioleoyl-sn-glycero-3-phospho-L-serine) were acquired from Avanti Polar Lipids (Alabaster, Alabama, USA). All buffer compounds, including 10 mM PBS (phosphate-buffered saline, pH 7.5), 50 mM HEPES (N-(2-hydroxyethyl) piperazine-N'-(2-ethanesulfonic acid), pH 7.5), and MES (2-(N-morpholino) ethane sulfonic acid, pH 5.5), as well as 1-ethyl-3-(3-dimethylaminopropyl) carbodiimide hydrochloride (EDC) and sulfo-N-hydroxysuccinimide (s-NHS), Tris, Acetate, Borate, Phosphate buffer saline with Tween 20 (PBST), 16-mercaptohexadecanoic acid (MHDA) and 11-marcapto-1-undecanol (MUOH) were obtained from Sigma-Aldrich (Steinhem, Germany). Programmed death-ligand 1 (PD-L1), programmed cell death protein 1 (PD1), and neutralizing monoclonal antibody (mAb) were purchased from GenScript (Leiden, The Netherlands).

6.6.2. Data analysis

Data analysis was conducted using GraphPad Prism 8 (GraphPad Software, CA, US) and Origin 8.0 (OriginLab, MA, US). Detection calibration curves were constructed by plotting the mean sensor response ($\Delta\lambda$) along with its standard deviation (mean ± SD) against the target concentration. Dataset fitting was performed using a two-site specific binding model curve. The limits of detection and quantification were determined using concentrations equivalent to three and ten times the standard deviation of the baseline sensor signal, respectively. After normalizing the biosensor response to percentages, inhibition calibration curves were constructed using the mean and standard deviation. An inhibitory dose-response fitting curve was used to fit the data. It is possible to define the half maximal inhibitory concentration (IC_{50}) as the 50% amount of medication needed to inhibit a certain biological process. Analyte concentrations was tested in triplicates to determine this value, and the signals (mean ± SD) were plotted against the analyte concentration's logarithmic value.

6.6.3. Binding affinity analysis

A binding affinity test was conducted to assess the interaction between PD1 and PD-L1 molecules. The optimization of binding affinity analysis between PD1 and PD-L1 was achieved employing a biomimetic PD-L1 functionalized LSPR sensor chip. A calibration curve was created by measuring PD1 concentrations ranging from 7.6 ng/mL to 5000 ng/mL in HEPES buffer (50 mM, pH 7.5) at a flow rate of 20 uL/min. Following each concentration measurement, the interaction between PD1 and PD-L1 was disrupted by flushing with a 10 mM NaOH solution for two minutes at the same flow rate, and the biosurface was regenerated.

6.6.4. Competitive assay

For the competitive assay, the PD1 sample containing monoclonal antibodies at various concentrations ranging from 0 to 6500 ng/mL were pre-incubated for 10 minutes at room temperature, then flowed over the PD-L1 functionalized sensor surface at a flow rate of 20 µL/min, keeping PBS 10 mM pH 7.5 as a running buffer. Inhibition calibration curve was plotted as the mean and standard deviation of the normalized biosensor response percentages. The data was fitted to a dose-response inhibition curve, and the half-maximal inhibitory concentration (IC_{50}) was calculated.

General conclusions and future prospective

This PhD thesis has explored and developed advanced nanophotonic biosensors for the rapid and sensitive detection of biomolecular and cell interactions, focusing on applications in immunotherapy evaluation for infectious diseases and cancer.

Our research focused first on improving the resolution and performance of nanoplasmonic sensors by investigating the effects of different nanostructure dimensions, geometries, and materials (gold and silver). Through computational modelling and experimental validation, we developed and characterized a nanosensor based on short-ordered arrays of gold nanodisks (AuNDs) with improved refractometeric sensing performance compared to previously established designs. The AuNDs sensors were fabricated at large scales with a cost-effective method based on hole-mask colloidal lithography (HCL), and they were integrated in a compact device with user-friendly operation.

In addition, we explored the potential of all-dielectric silicon nanostructures for refractometeric sensing in the visible spectral range. Arrays of silicon nanodisks (SiNDs) were designed and optimized through computational modelling, and a nanofabrication route based on HCL was established for large-scale production. The novel SiNDs sensors could also be operated with the previously developed point-of-care device, showing sharp and sensitive electromagnetic resonances analogous to traditional nanoplasmonic sensors. Although the resolution of the SiNDs sensor did not surpass that of AuNDs sensor, their unique properties in terms of minimum absorption losses, high hydrophilicity, and biocompatibility make them promising candidates for complex sensing applications, such as on-chip cell studies. In this context, next steps will address sensor biofunctionalization and implementation for cell immunotherapy studies, aiming to fully harness the capabilities of this innovative technology.

A significant achievement of this Thesis is the formation of stable lipid membranes directly on nanoplasmonic sensor surfaces. These planar lipid bilayers were functionalized with specific cell receptors and ligands to mimic artificial cell membranes, enabling real-time monitoring of cell-cell interactions with improved efficacy compared to conventional biofunctionalization strategies (i.e., self-assembled monolayers). Our biomimetic nanophotonic sensors were demonstrated for the evaluation of two immunotherapies based on monoclonal antibodies (mAb): an anti-viral treatment for neutralization of SARS-CoV-2 viruses, and an immune checkpoint inhibitor (ICI) for cancer therapy.

For COVID-19 research, our biosensor technology allowed for the rapid screening and comparison of mAb candidates targeting different SARS-CoV-2 variants. We demonstrated direct monitoring of virus-

cell interactions with detection limits in the 10^2 TCID50/mL range, and the virus neutralization assays were performed with a realistic virus titer (10^5 TCID50/mL) and a low sample volume (200 μL). The final dose-response parameters were validated in comparison to other mAb therapies approved by regulatory agencies.

For cancer immunotherapy, our sensors demonstrated high sensitivity and accuracy in the study and assessment of the PD1/PD-L1 immune checkpoint pathway. By creating a tumor-mimicking artificial cell membrane, we could detect and monitor direct PD1/PD-L1 binding interaction with a limit of detection of 6.7 ng/mL, outperforming previously reported plasmonic sensors. Also, we proved the capability of evaluating the efficacy of mAb inhibitors, obtaining dose-response values (IC_{50} = 0.43 nM) consistent with those reported by standard analytical techniques. Future work in this line will address the direct analysis of immune cell interactions, aiming at enhancing the reliability of the pre-clinical evaluation.

Overall, this PhD thesis represents a leap forward to the implementation of new biosensor technologies within the biomedical research area. Both the nanoplasmonic and all-dielectric nanophotonic sensors provide accurate, label-free analysis with point-of-care capabilities, making them particularly valuable for precision diagnosis, drug screening, and personalized therapy evaluation. Additionally, the formation of on-chip artificial cell membranes expands the utility of these biosensors for studying live cell interactions, offering a promising alternative to labor-intensive and time-consuming cell culture methods. We foresee the adoption of these biosensors in pharmaceutical and biomedical laboratories as tools to accelerate the design and validation of advanced biological therapies, reducing production costs, and contributing to the widespread implementation of precision medicine.

Future work will address the integration of artificial cell membranes with SiNDs sensors. The hydrophilicity, biocompatibility, and especially the negligible local heating of dielectric nanostructures makes them ideal platforms for the application to on-chip live cell studies. Upcoming research aim to develop a high-resolution, all-dielectric biosensor for the label-free identification of anti-tumor immune cells as potential targets for cell immunotherapies (i.e., CAR-T cell or tumor-infiltrating lymphocytes (TIL) approaches). To achieve this, the lipid membrane will be functionalized with specific tumor antigens, enabling rapid screening, detection, and isolation of high-affinity tumor-specific T cells. Additionally, by co-immobilizing cooperative ligands and receptors, the system will mimic the real immunological synapse, potentially triggering T cell activation and signaling responses. This biosensor could therefore be used for in-situ monitoring of T cell secretion events in real-time, providing a holistic evaluation of immune cells functionality for therapeutic applications. This innovative platform may offer a valuable alternative or complementary technique to fluorescence-based flow cytometry assays

and ELISA, significantly reducing assay times, cells and reagent consumption, and the overall complexity of in-vitro assessment of patient-derived cells.

On the technology side, the next objectives will focus on developing and integrating our nanophotonic sensors into advanced prototypes with multiplexing capability, automated sample handling, and an improved software interface for use by non-specialized operators. A key step toward the eventual technology transfer of the nanophotonic devices, particularly the novel SiNDs sensors, will be the implementation of a new nanofabrication protocol based on cost-effective and scalable techniques such as nanoimprinting lithography (NIL). This lithography method offers large-scale fabrication of precise nanostructure arrays with high resolution, which will allow for fine-tuning of the optimal sensor geometry while ensuring long-term, reproducible, and affordable production of sensor chips.

Looking ahead, the work presented in this PhD thesis paves the way for research directions that may have a significant impact in different areas, including nanophotonic and material sciences, biochemistry, molecular and cell biology, and medicine. Moreover, the versatility and transformative potential of these biosensors extend beyond biomedical research, with promising applications in clinical diagnostics, environmental monitoring, and telecommunications, among others. This research not only advances current scientific understanding but also opens up exciting possibilities for innovation across multiple disciplines.

Annex

Nanofluidic Scattering Microscopy (NSM) technique for single molecules

Here, we report the work performed during the 3-month international PhD Internship at Chalmers University of Technology (Sweden).

A. Nanofluidic Scattering Microscopy (NSM) technique for single molecules

A.1. Introduction

Understanding chemical and biological processes at the single-molecule level is critical for advancing research in biomedical fields. However, studying small biomolecules at this level has always posed major challenges. Traditional methods often involve steps that modify the biomolecule, such as fluorescent labelling or surface attachment, which can interfere with its natural behaviour. Prof. Christoph Langhammer and colleagues at Chalmers University of Technology (Sweden), have developed a novel technique called Nanofluidic Scattering Microscopy (NSM), that enables label-free, real-time imaging of single biomolecules diffusing inside nanofluidic channels. NSM uses nanochannels into an optically transparent matrix, smaller than the wavelength of light, combined with dark-field microscopy to achieve high-contrast imaging. This method allows not only to detect biomolecules as they move through the channels but also to determine their molecular weight. The technique's sensitivity and accuracy can be demonstrated through various applications, including the detection and analysis of single DNA molecules and proteins with molecular weights as low as tens of kilodaltons (kDa).[281]

The core principle behind NSM lies in the interaction of light with nanoscale objects, where the scattering of light is influenced by the optical properties of both the nanochannel and the biomolecules present (Figure A.1). When a focused laser beam illuminates these nanochannels, both the channel walls and the molecules scatter the incident light. The scattered light is collected by the microscopy system and carries critical information about the physical properties of the molecules, such as their size, shape, and refractive index. This allows to characterize individual molecules and their interactions in real time without the need for fluorescent labels or other molecular markers.

The NSM technique can be explained through the principles of Rayleigh and Mie scattering,[36,38] where the size of the biomolecules determines by the type of scattering and the nature of the collected signal. When light interacts with objects much smaller than the wavelength of light, Rayleigh scattering dominates. Larger objects, such as nanochannel walls, produce Mie scattering. The combination of these scattering mechanisms allows for a comprehensive analysis of the nanochannel environment and the biomolecules within it.

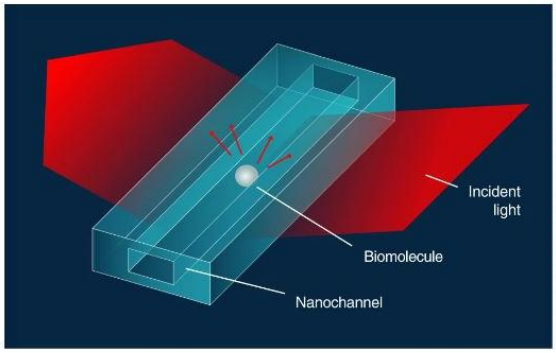

Fig A. 1. Schematic illustration of incident light shining on a nanochannel containing a biomolecule, with scattered light collected using a dark-field setup. This image is adapted from Reference 294.[281]

NSM employs a differential imaging approach to isolate the molecular signal from background noise (Figure A.2). The process begins by measuring the scattered light from an empty nanochannel, which provides a baseline scattering profile. This baseline is necessary because the nanochannel itself contributes to the overall scattering signal, independent of any biomolecules that may be present. Once biomolecules are introduced into the nanochannel, they alter the scattering pattern due to differences in their optical properties, such as refractive index and absorption characteristics.

To accurately detect and characterize these biomolecules, the scattering profile of the empty nanochannel is subtracted from the scattering profile with the biomolecules present. This subtraction process yields a differential scattering image that highlights the presence of the biomolecules while minimizing the influence of the nanochannel structure. This differential imaging technique is a key feature of NSM, allowing for the precise identification of molecular interactions without interference from the surrounding nanochannel.

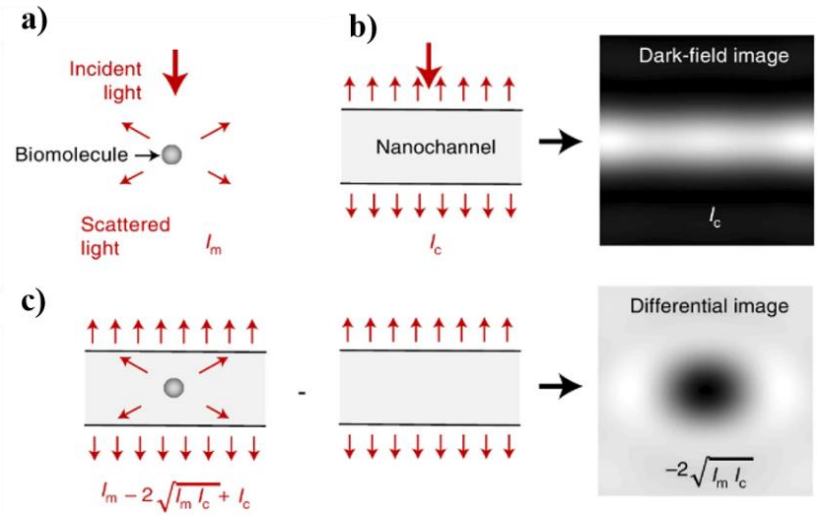

Fig A. 2. Schematic illustrations of: a) Light scattered by a single biomolecule, b) Light scattered by a nanochannel and the corresponding dark-field image, and c) Light scattered by a nanochannel with a single biomolecule, and corresponding differential dark-field image, created by subtracting the image of the empty nanochannel from the image with the biomolecule inside. This image is adapted from reference 294.[281]

A.2. Design of nanofluidic chip

The nanofluidic chips used in NSM experiments are fabricated at the Chalmers´ cleanroom, made of silicon on a glass substrate and with different depths, ranging from 50 nm to 200 nm. The chip design is simple yet effective, resembling the letter "I" in structure, with two inlets for introducing the sample and two outlets for removing the sample. This design ensures efficient fluid flow and interaction within the nanochannels. The nanochannels themselves are meticulously etched into the silicon substrate, creating the environment where molecular interactions take place (Figure A.3). These nanofluidic chips are central to the NSM system, as they provide the platform on which light scattering and molecular interaction studies are conducted.

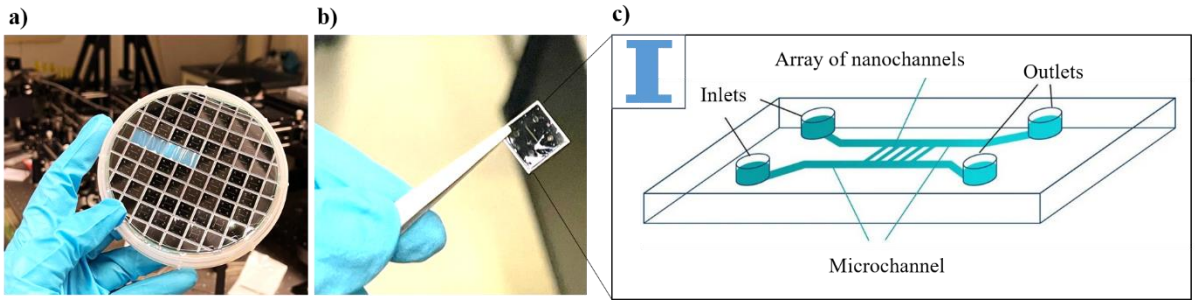

Fig A. 3. a and b) Photographs of fabricated nanofluidic chips, and c) Scamatic illustration of nanofluidic chip, reprinted from reference 294.[281]

A.3. Nanofluidic scattering microscopy operation

The NSM system operates with two laser sources: one for scattering and another for fluorescence, allowing for more sophisticated studies, combining scattering and fluorescence techniques to gather comprehensive data on molecular interactions. A complex optical arrangement, including micromirrors, ensures precise control of the light beams. These micromirrors adjust the focus of the laser in real time, keeping the beam tightly focused on the nanofluidic chip, which is mounted on an objective lens. The interaction of the light with the nanochannels within the chip generates the scattered and reflected light, which is collected and sent to a camera for image capture (Figure A.4a). This high-contrast image displays the nanochannels and microchannels of the nanofluidic chip. The bright lines visible in the center represent fluid flowing or present inside the nanochannels, and the larger structures on the sides are microchannels. The dark-field microscopy technique used here enhances the contrast, making the fluid appear bright against a dark background, which helps in tracking the flow and behaviour of molecules in real-time (Figure A.4b).

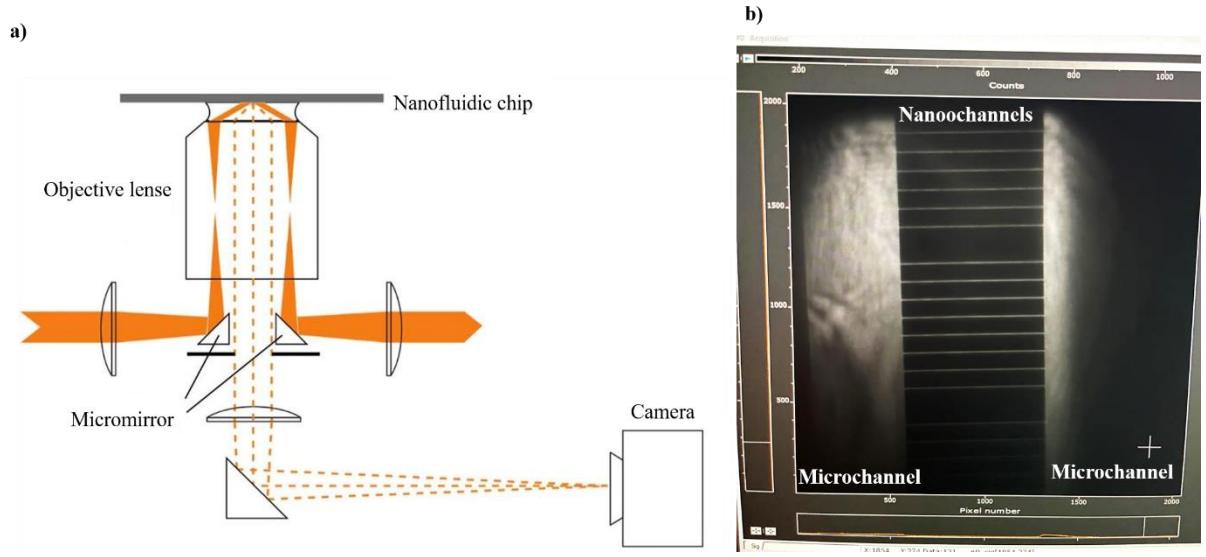

Fig A. 4. a) Schematic representation of NSM configuration, adapted from reference 294,[281] and b) high-contrast image of the nanofluidic chip.

A.4. Challenges in NSM with nanofluidic channels

A.4.1. Surface passivation through small vesicles

One of the key challenges in NSM is the passivation of the nanochannels. Passivation is essential to make the nanowalls of the channels less reactive and to prevent unwanted interactions between the walls

and the biomolecules under study. Initially, passivation was attempted using small lipid vesicles, which will form a supported lipid membrane for uniformly coating the walls (Figure A.5).

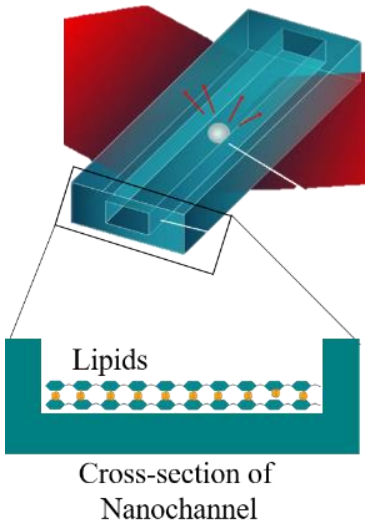

Fig A. 5. Schematic representation of a nanofluidic channel with a cross-sectional view showing lipid bilayers coating the inside surface of the nanochannel.

To evaluate the efficience of lipid membranes, a fluorescent avidin protein was flowed through the nanochannels and monitored in real time (Figure A.6). As can be observed, in the non-passivated condition (Figure A.6 a-c), the nanochannel surface is exposed, allowing avidin to bind freely. Avidin is positively charged at physiological pH, while nanochannel walls are typically negatively charged. This charge difference can lead to electrostatic interactions and accumulation of avidin on the channel walls. The fluorescence image (Figure A.6b) shows a strong signal within the dashed region, indicating substantial avidin attachment to the surface. The corresponding row sum of fluorescence intensities (Figure A.6c) shows high fluorescence peaks, confirming extensive binding across the nanochannel. These results indicate the vulnerability of the non-passivated channel to surface fouling, as avidin can easily interact with and adhere to the unprotected channel surface.

In contrast, the lipids passivated condition (Figure A.6 d-f) demonstrates how lipid coatings can reduce surface fouling. The schematic in Figure A.6d shows a nanochannel coated with a lipid bilayer, designed to block avidin binding. The fluorescence image in Figure A.6e shows minimal fluorescence in the region of interest, indicating that only a small amount of avidin has bound to the surface. The row sum of the fluorescence intensities in Figure A.6f confirms this, showing much lower fluorescence peaks compared to the non-passivated channel. This reduction in fluorescence demonstrates the partial success of lipid passivation in inhibiting avidin binding, but not completely.

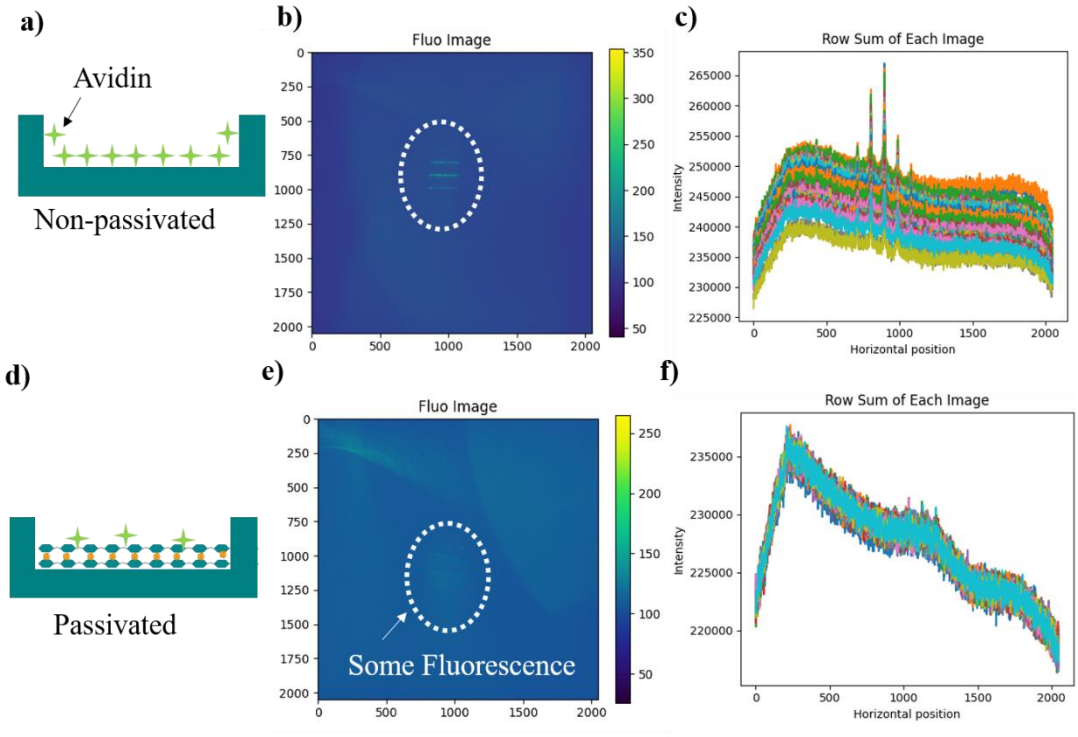

Fig A. 6. a) Schematic illustration of a non-passivated nanochannel, b) Fluorescence image of a non-passivated nanochannel (dashed circle), c) The row sum of each image in the non-passivated condition, d) Schematic representation of a passivated nanochannel, e) Fluorescence image of a passivated nanochannel, and f) The row sum of each image in the passivated condition.

The incomplete coating coating of the nanochannel walls could be attributed to the high fluidity and mobility of the lipid bilayer, which might allow the protein to find empty spaces for binding to the surface. This hypothesis was confirmed by a kymograph (Figure A.7a), which demonstrates the high mobility of lipid vesicles within the nanochannel. The vesicles exhibited uneven flow, sometimes splitting apart, re-joining, or overlapping, leading to incomplete passivation of the nanochannel. This irregular behaviour may a key factor in the ineffective coating process.

Additionally, the three-dimensional intensity versus time graphs (Figure A.7b and c) represent the lipid density distribution over the nanochannel surface. The colour contrast in the 3D plot shows that deeper intensity peaks represent regions where the lipids have strongly adhered to the channel surface, while lighter contrast regions indicate areas where the lipids are simply passing over without attaching. This uneven lipid distribution contributes to the incomplete and inconsistent passivation of the nanochannels.

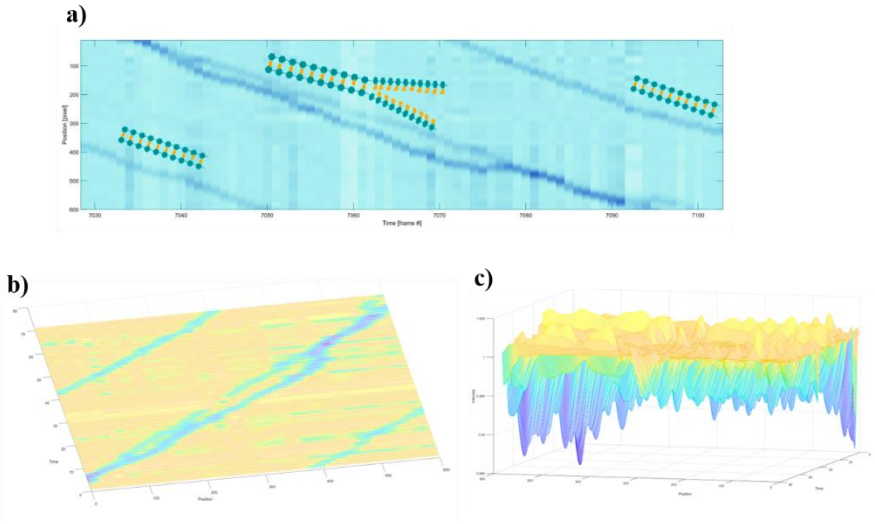

Fig A. 7. a) Kymograph displaying the movement of lipid vesicles within the nanochannel, b and c) Three-dimensional intensity vs. time graphs illustrating the lipid density distribution along the nanochannel surface.

A.4.2. Surface passivation through PEGylated polymer

A different passivation strategy was proposed and assessed based on a hydrophilic polymer coating. PLL-PEG (poly-L-lysine-graft-poly(ethylene glycol)) is a copolymer known for its strong antifouling properties, making it an excellent material for surface passivating in research applications. Its structure consists of a positively charged PLL backbone with PEG side chains.[282] This allows PLL-PEG to attach to negatively charged surfaces through electrostatic interactions while forming a dense, protective polymer brush (Figure A.8).

The antifouling effect comes primarily from the PEG side chains, which create a hydrophilic layer that prevents proteins from sticking to the surface and resists biomolecules (cell and proteins etc.) attachment. This barrier reduces non-specific protein binding and helps maintain the cleanliness of the surface, improving its reliability for experiments.[283] PLL-PEG works on a variety of negatively charged materials, including glass, silicon, metal oxides, and certain polymers.

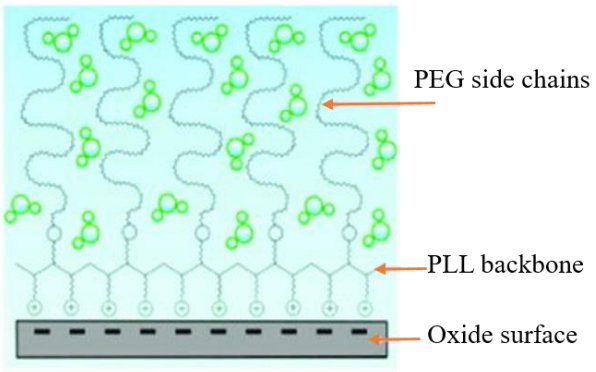

Fig A. 8. Schematic illustration of PLL-g-PEG structure showing adsorption on a negatively charged surface. Reprinted from reference 296.[283]

We conducted a test using PLL-PEG in HEPES buffer at pH 7.4, compared to a non-passivated surface, particularly in preventing avidin binding in nanochannels. Initially, nanochannels were exposed, allowing avidin to bind freely, and observed strong florescent signal (Figure A.9 a-c). Conversely, the passivated condition (Figure A.9 d-f) showcases the effectiveness of PLL-PEG coating in preventing avidin attachment to the nanochannel surface. The fluorescence image in Figure A.9e shows no signal within the circled region, indicating successful blocking of avidin binding. This qualitative observation is corroborated by the quantitative analysis in Figure A.9f, where the row sum of fluorescence intensity remains consistently low and flat across the surface, demonstrating the efficacy of PLL-PEG passivation in preventing avidin binding.

As a result, PLL-PEG effectively prevented nonspecific binding of proteins to the nanochannel walls. This improvement allowed for more accurate studies of molecular interactions within the channels. By creating an antifouling surface, the PLL-PEG coating ensured that the observed molecular behaviour was due to specific interactions rather than unwanted adhesion to the channel surfaces. This contribution was not only successful but also opened the door to future collaborations with the Langhammer lab, as they continue to explore the use of PLL-PEG polymers in their nanofluidic systems for monitoring molecular interactions.

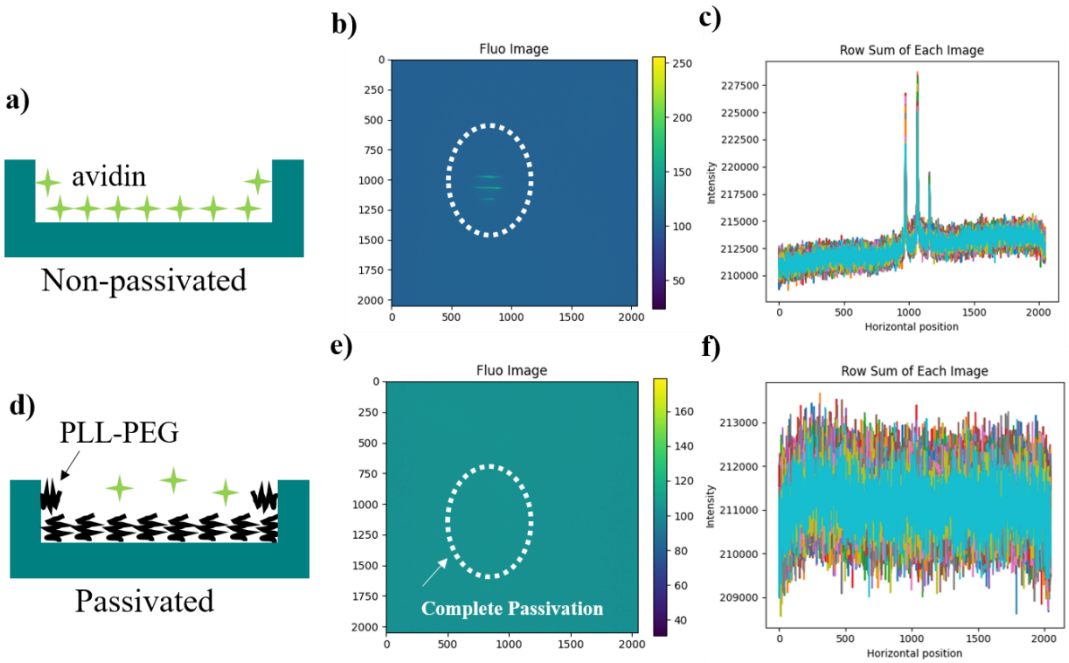

Fig A. 9. Comparison of avidin binding on non-passivated and PLL-PEG passivated nanochannel surfaces. a) Schematic of a non-passivated surface, showing avidin freely binding, b) Fluorescence image of a non-passivated nanochannel (dashed circle), c) Row sum of the fluorescence intensity across the non-passivated surface, d) Schematic representation of a passivated nanochannel surface, e) Fluorescence image of a passivated nanochannel surface, and f) Row sum of the fluorescence intensity across the passivated surface.

A.5. Summary and conclusions

NSM is a powerful technique that allows real-time observation of biomolecules without the need for labelling. However, one of the major challenges has been the unwanted adhesion of biomolecules to the nanochannel walls, which can interfere with data accuracy. Initial attempts to use a lipid bilayer for passivation were met with limited success, as the membrane's high mobility led to incomplete and inconsistent coverage of the nanochannel surfaces. To overcome this, we introduced PLL-PEG polymer as an effective antifouling agent. This polymer creates a stable, hydrophilic barrier on the nanochannel surface, preventing biomolecules from adhering to the walls. Through our experiments, we demonstrated that PLL-PEG passivation completely reduced nonspecific biomolecule binding, including avidin, which commonly adhered to non-passivated surfaces. Fluorescence imaging and intensity analysis confirmed that the passivated nanochannels showed no biomolecule attachment.

In conclusion, we have addressed a key challenge in NSM by improving nanochannel passivation, which is vital for accurate molecular interaction studies. By introducing PLL-PEG polymer as an effective antifouling agent, we successfully prevented unwanted biomolecule adhesion to the

nanochannel walls, significantly improving data accuracy. This advancement enhances the reliability of NSM for future single-molecule biomolecular interaction research.

A.6. Experimental section

A.6.1. Chemicals and reagents

Reagents for cleaning the microfluidic chips, including hydrogen peroxide (H_2O_2) 30% and sulfuric acid (H_2SO_4) 96% were purchased from Sigma-Aldrich (Steinheim, Germany). Lipids (POPC) 1-Palmitoyl-2-oleoyl-glycero-3-phosphocholine and DOPS (1,2-dioleoyl-sn-glycero-3-phospho-L-serine) was purchased from Avanti Polar Lipids (Alabaster, Alabama, USA). Reagents for buffer preparation (10 mM PBS (Phosphate buffer saline, pH 7.4), 50 mM HEPES (N-(2-Hydroxyethyl) piperazine-N-(2-ethanesulfonic acid), pH 7.4) and Avidin, Egg White were purchased from Sigma-Aldrich (Steinhem, Germany). PLL-PEG (poly-L-lysine-graft-poly(ethylene glycol)) was acquired from SuSoS AG (Dubendrof, Switzerland).

A.6.2. NSM experimental setup

The optical setup was based on the microscope platform RM21 (Mad City Labs). A supercontinuum laser (NKT Photonics, SuperK EXTREME EXB-6) generated a broad light beam with wavelengths ranging from 400–2,350 nm. This beam was filtered by the tunable filter (NKT Photonics, SuperK VARIA) to select wavelengths between 450–750 nm. The beam, with 250 mW power, was focused onto the back of a microscope objective (NA = 1.49, Nikon) and directed to the fluidic chip at an angle using a micromirror. Reflected light was filtered by another micromirror, and the scattered light was captured by a CMOS camera (Andor, Zyla) with a magnification of 220×. For experiments with 20 μm long nanochannels, a 1 mm wide beam illuminated a 10 μm area of the fluidic chip, and the camera recorded image 50 frames per second. For 100 μm long nanochannels, the beam was expanded to cover 30 μm, and the camera recorded image at the same frame rate.

A.6.3. Nanofluidic chip preparation

The nanofluidic chips (1 × 1 cm^2) were prepared for mounting on the optical setup by first immersing them overnight in a piranha solution (3:1 mixture of H_2SO_4 and H_2O_2) to clean the surface. After this, the chips were thoroughly rinsed with Milli-Q water and dried using a nitrogen (N_2) stream. To remove any trapped air bubbles, air-gas was flowed through the inlets of the chip for 15 minutes.

A.6.4. Passivation protocol

The passivation study was performed first by introducing the avidin as a reference, prepared a solution of 50 µg/mL in 10 mM PBS buffer pH 7.4. Flowed the sample over the cleaned surface for 30 minutes, removed any excess avidin by rinsing with Milli-Q water for 5 minutes. Next, for lipid vesicle passivation, we prepared a vesicle solution containing POPC:DOPS (1:10) at 1 mg/mL in 10 mM PBS buffer pH 7.4, introduced into the nanochannels and flowed for 30 minutes. After passivation, avidin was reintroduced to assess the surface passivation effect. Lastly, for PLL-PEG polymer passivation, we prepared a solution of 1 mg/mL PLL-PEG polymer in 10 mM HEPES buffer pH 7.4, flowed through the nanochannels to passivate the walls and recorded data to evaluate the effectiveness of the PLL-PEG passivation. Throughout the experiment, air pressure 2500 mbar was employed to flow the sample into the nanochannels.

A.6.5. Data analysis

The images recorded by the camera were processed and analyzed using Python software (Matplotlib).

Publications

Journal Articles

A Novel Biomimetic Nanoplasmonic Sensor for Rapid and Accurate Evaluation of Checkpoint Inhibitor Immunotherapy
R. Batool, M. Soler, R.Singh and L. M. Lechuga
2024 Analytical and Bioanalytical Chemistry (in press)
https://doi.org/10.1007/s00216-024-05398-3

Immune checkpoint inhibitors (ICIs) are promising cancer immunotherapies, but face challenges like tumor heterogeneity, resistance mechanisms, and complex in vitro testing. To overcome these, we developed a novel biomimetic, label-free nanoplasmonic biosensor for rapid and reliable screening of ICIs. The sensor, based on gold nanodisks, forms a functional supported lipid bilayer mimicking an artificial cell membrane for tumor ligand immobilization. It enables real-time, sensitive analysis of immune checkpoint pathways and monoclonal antibody blocking effects in under 20 minutes. Our approach demonstrated accurate PD1/PD-L1 interaction monitoring with a detection limit of 6.7 ng/mL and an IC_{50} of 0.43 nM for anti-PD1 antibodies, comparable to conventional methods. This platform integrates plasmonic technologies for rapid, label-free analysis with the reliability of cell-based assays, and is housed in a compact, user-friendly device suitable for biomedical and pharmaceutical labs.

Biomimetic Nanoplasmonic Sensor for Rapid Evaluation of Neutralizing SARS-CoV-2 Monoclonal Antibodies as Antiviral Therapy
R. Batool, M. Soler, F. Colavita, L. Fabeni, G. Matusali and L. M. Lechuga
2023 Biosensors and Bioelectronics 226, 115137
https://doi.org/10.1016/j.bios.2023.115137

Monoclonal antibody (mAb) therapy shows great potential for early COVID-19 treatment, but current manufacturing and evaluation processes are slow, complex, and costly, limiting accessibility. To address this, we proposed a biomimetic nanoplasmonic biosensor for faster, simpler, and reliable screening of COVID-19 mAb therapies. The sensor mimics an artificial cell membrane, allowing real-time monitoring of virus-cell interactions and antibody blocking effects in under 20 minutes. We achieved detection limits of 10^2 TCID50/mL for SARS-CoV-2 and demonstrated accurate evaluation of neutralizing antibodies against Delta and Omicron variants, with IC50 values in the ng/mL range. This user-friendly technology can accelerate and simplify the development of effective immunotherapies for COVID-19 and other diseases

Conferences

Biomimetic Nanoplasmonic sensor for the evaluation of COVID-19 antiviral immunotherapy
R. Batool, M. Soler, L. M. Lechuga
Photonics Online Meet-Up, on-line 15th November 2024 **Poster presentation**
Translational Research Award

Biomimetic Nanoplasmonic sensor for the evaluation of COVID-19 antiviral immunotherapy
R. Batool, M. Soler, L. M. Lechuga
XXVII Transfrontier Meeting on Sensors and Biosensors, Banyuls-sur-Mer (France) 28th – 29th September 2023 **Oral presentation**

Biomimetic Nanoplasmonic sensor for the evaluation of COVID-19 antiviral immunotherapy
R. Batool, M. Soler, L. M. Lechuga
7th Scientific Meeting of PhD Student, Barcelona (Spain) 7th – 9th June 2023 **Oral presentation**

Biomimetic label-free Plasmonic Sensing Platform for COVID-19 Immunotherapy Analysis
R. Batool, M. Soler, L. M. Lechuga
Present and Future of Nanomedicine: A Meetup between Researchers and Clinicians Workshop, Barcelona (Spain) 26th May 2022 **Poster presentation**

Biomimetic Label-free Plasmonic Sensor for COVID-19 Immunotherapy Evaluation
M. Soler, R. Batool, L. M. Lechuga
XV Conference on Optical Chemical Sensors and Biosensors EUROPT(R)ODE, Warsaw (Poland) 28th November - 1st December 2021 **Poster presentation**

Abbreviations and acronyms

mAbs	Monoclonal antibodies
ICIs	Immune checkpoint inhibitors
PD-1	Programmed cell death 1
CAR-T	Chimeric antigen receptor
ELISA	Enzyme-Linked Immunosorbent Assay
BLI	Biolayer Interferometry
ITC	Isothermal Titration Calorimetry
SPR	Surface Plasmon Resonance
ADCC	Antibody-dependent cell-mediated cytotoxicity
CDC	Complement-dependent cytotoxicity
HPLC	High-performance liquid chromatography
RI	Refractive index
EW	Evanescent wave
TIR	Total internal reflection
LSPR	Localized Surface Plasmon Resonance
Au	Gold
Ag	Silver
Al	Aluminium
Cu	Copper
SPP	Surface plasmon polariton
TM	Transverse magnetic
FWHM	Full width at half maximum
LEDs	Light emitting diodes
CMOS	Metal oxide semiconductor
UV	Ultraviolet
EUV	Extreme ultraviolet
EBL	Electron beam
FIB	Focused ion beam
NIL	Nanoimprint lithography
HCL	Hole-Mask Colloidal Lithography

LOD	Limit of Detection
FOM	Figure of Merit
BIC	Bound states in the continuum
PSA	Prostate-specific antigen
CRP	C-reactive protein
TiO_2	Titanium dioxide
Ge	Germanium
Si	Silicon
NIR	Near-infrared
IR	Infrared
LOC	Lab-on-chip
MIPs	Molecularly imprinted polymers
SAMs	Self-assembled monolayers
SLBs	Supported lipid bilayers
TCR	T-cell receptor
AuNDs	Gold nanodisks
FEM	Finite element method
3D	Three-dimensional
SiO_2	Silicon dioxide
h	Height
d	Diameter
g	Gap
HCl	Hydrochloric acid
PMMA	Polymethyl methacrylate
PDDA	Poly (diallyldimethylammonium chloride
RIE	Reactive ion etching
Ti	Titanium
SEM	Scanning electron microscopy
$\Delta\lambda$	Wavelength displacements
S/N	Signal-to-noise ratio
Δn	Refractive index changes
η_B	Bulk sensitivity

RIU	Refractive index units
CV	Coefficient of variability
H_2O_2	Hydrogen peroxide
H_2SO_4	Sulfuric acid
MHDA	16-mercaptohexadecanoic acid
MUOH	11-marcapto-1-undecanol
RT	Room temperature
SEIRA	Surface-enhanced infrared absorption
SiNDs	Silicon nanodisks
polySi	Polycrystalline Silicon
ICP	Inductively couple plasms
RF	Radio frequency
KI	Potassium iodide
SDS	Sodium dodecyl sulfate
SUV	Small unilamellar vesicles
PC	Phosphatidylcholine
PE	Phosphatidylethanolamine
PS	Phosphatidylserine
PG	Phosphatidylglycerol
POPC	1-palmitoyl-2-oleoyl-snglycero-3-phosphocholine
DOPS	1,2-dioleoyl-sn-glycero-3-phospho-L-serine
EDC	1-ethyl-3-(3-dimethylaminopropyl) carbodiimide
NHS	N-hydroxysuccinimide
PBS	Phosphate buffered saline
HEPES	4-(2-hydroxyethyl)-1-piperazineethanesulfonic acid
MES	2-(N-morpholino) ethanesulfonic acid
BSA	Bovine serum albumin
COVID-19	Coronavirus infectious disease 19
WHO	World Health Organization
SARS-CoV-2	Severe acute respiratory syndrome-related coronavirus
RBD	Receptor binding domain
ACE-2	Angiotensin-converting enzyme 2

EMA	European Medicine Agency
FDA	American Food and Drug Administration
BSL-2	Biosafety laboratories level 2
INMI	National Institute of Infectious Diseases
RNA	Ribonucleic acid
TEM	Transmission electron microscopy
NAbs	Neutralizing monoclonal antibodies
N protein	Nucleocapside protein
IC_{50}	Half maximum inhibition concentration
NHA	Nanohole arrays

List of Figures

Chapter 1: Introduction

Chapter 2: Design, fabrication, and characterization of nanoplasmonic sensors

Chapter 3: Design, Fabrication, and Characterization of All-Dielectric Nanophotonic Sensors

Chapter 5: Application to COVID-19 immunotherapy evaluation

Chapter 6: Application to cancer immunotherapy evaluation

Annex: Nanofluidic Scattering Microscopy (NSM) technique for single molecules

List of Tables

Bibliography

1. Makuku R, Khalili N, Razi S, Keshavarz-Fathi M, Rezaei N. Current and Future Perspectives of PD-1/PDL-1 Blockade in Cancer Immunotherapy. *J Immunol Res*. 2021;2021. doi:10.1155/2021/6661406
2. Wang Q, Shao X, Zhang Y, et al. Role of tumor microenvironment in cancer progression and therapeutic strategy. *Cancer Med*. 2023;12(10):11149-11165. doi:10.1002/cam4.5698
3. Meng L, Wu H, Wu J, et al. Mechanisms of immune checkpoint inhibitors: insights into the regulation of circular RNAS involved in cancer hallmarks. *Cell Death Dis*. 2024;15(1). doi:10.1038/s41419-023-06389-5
4. Das CK, Singh SK. Immune Checkpoint Inhibitors in Cancer Therapy: A Ray of Hope. In: *Biomedical Translational Research*. Springer Nature Singapore; 2022:393-411. doi:10.1007/978-981-16-8845-4_20
5. Ai L, Chen J, Yan H, et al. Research status and outlook of pd-1/pd-l1 inhibitors for cancer therapy. *Drug Des Devel Ther*. 2020;14:3625-3649. doi:10.2147/DDDT.S267433
6. Twomey JD, Zhang B. Cancer Immunotherapy Update: FDA-Approved Checkpoint Inhibitors and Companion Diagnostics. *AAPS J*. 2021;23(2). doi:10.1208/s12248-021-00574-0
7. Uscanga-Palomeque AC, Chávez-Escamilla AK, Alvizo-Báez CA, et al. CAR-T Cell Therapy: From the Shop to Cancer Therapy. *Int J Mol Sci*. 2023;24(21). doi:10.3390/ijms242115688
8. Kelly W, Lotze MT, Atkins MB. History of Cancer Immunotherapy. *Cancer Immunother Princ Pract*. 2018:1-18. doi:10.1891/9781617052736.0001
9. Carlson RD, Flickinger JC, Snook AE. Talkin' toxins: From Coley's to modern cancer immunotherapy. *Toxins*. 2020;12(4):1-23. doi:10.3390/toxins12040241
10. Kumar M, Thangavel C, Becker RC, Sadayappan S. Monoclonal antibody-based immunotherapy and its role in the development of cardiac toxicity. *Cancers*. 2021;13(1):1-12. doi:org/10.3390/cancers13010086
11. Dobosz P, Dzieciątkowski T. The Intriguing History of Cancer Immunotherapy. *Front Immunol*. 2019;10. doi:10.3389/fimmu.2019.02965
12. Davis AA, Patel VG. The role of PD-L1 expression as a predictive biomarker: An analysis of all US food and drug administration (FDA) approvals of immune checkpoint inhibitors. *J Immunother Cancer*. 2019;7(1):1-8. doi:10.1186/s40425-019-0768-9
13. Hnasko R. *ELISA*. Vol 1318. (Hnasko R, ed.). Springer New York; 2015. doi:10.1007/978-1-4939-2742-5
14. Tang C, Verwilligen A, Sadoff J, et al. Absolute quantitation of binding antibodies from clinical samples. *npj Vaccines*. 2024;9(1). doi:10.1038/s41541-023-00793-w

15. Aweda TA, Meares CF. Combination of isothermal titration calorimetry and time-resolved luminescence for high affinity antibody–ligand interaction thermodynamics and kinetics. *Methods*. 2012;56(2):145-153. doi:10.1016/j.ymeth.2011.09.011
16. Schuck P, Zhao H. The Role of Mass Transport Limitation and Surface Heterogeneity in the Biophysical Characterization of Macromolecular Binding Processes by SPR Biosensing. In: Mol NJ, Fischer MJE, eds. *Life Sciences*. Vol 627. Methods in Molecular Biology. Humana Press; 2010:15-54. doi:10.1007/978-1-60761-670-2_2
17. Wang B, Yang C, Jin X, et al. Regulation of antibody-mediated complement-dependent cytotoxicity by modulating the intrinsic affinity and binding valency of IgG for target antigen. *MAbs*. 2020;12(1):1-15. doi:10.1080/19420862.2019.1690959
18. Kalina T, Lundsten K, Engel P. Relevance of Antibody Validation for Flow Cytometry. *Cytom Part A*. 2020;97(2):126-136. doi:10.1002/cyto.a.23895
19. Lu LL, Suscovich TJ, Fortune SM, Alter G. Beyond binding: antibody effector functions in infectious diseases. *Nat Rev Immunol*. 2018;18(1):46-61. doi:10.1038/nri.2017.106
20. Dudok de Wit C. Electrochemical biosensors: recommended definitions and classification. *Biosens Bioelectron*. 2001;16(1-2):31-121. doi:10.1016/s0956-5663(01)00115-4
21. Morton TA, Myszka DG. Kinetic analysis of macromolecular interactions using surface plasmon resonance biosensors. *Methods Enzymol*. 1998;295:268-282. doi:10.1016/S0076-6879(98)95044-3
22. Cooper MA. Label-free screening of bio-molecular interactions. *Anal Bioanal Chem*. 2003;377(5):834-842. doi:10.1007/s00216-003-2111-y
23. Olaru A, Bala C, Jaffrezic-Renault N, Aboul-Enein HY. Surface Plasmon Resonance (SPR) Biosensors in Pharmaceutical Analysis. *Crit Rev Anal Chem*. 2015;45(2):97-105. doi:10.1080/10408347.2014.881250
24. Park JH, Cho YW, Kim TH. Recent Advances in Surface Plasmon Resonance Sensors for Sensitive Optical Detection of Pathogens. *Biosensors*. 2022;12(3). doi:10.3390/bios12030180
25. Chiu NF. The Current Status and Future Promise of SPR Biosensors. *Biosensors*. 2022;12(11):10-13. doi:10.3390/bios12110933
26. González-Guerrero AB, Maldonado J, Herranz S, Lechuga LM. Trends in photonic lab-on-chip interferometric biosensors for point-of-care diagnostics. *Anal Methods*. 2016;8(48):8380-8394. doi:10.1039/c6ay02972h
27. Estevez MC, Alvarez M, Lechuga LM. Integrated optical devices for lab-on-a-chip biosensing applications. *Laser Photonics Rev*. 2012;6(4):463-487. doi:10.1002/lpor.201100025
28. Yu H, Peng Y, Yang Y, Li ZY. Plasmon-enhanced light–matter interactions and applications. *npj Comput Mater*. 2019;5(1):1-14. doi:10.1038/s41524-019-0184-1
29. Homola J. Present and future of surface plasmon resonance biosensors. *Anal Bioanal Chem*. 2003;377(3):528-539. doi:10.1007/s00216-003-2101-0

30. Britto EC, Krishnamoorthi B, Rajasekar R, Nizar SM. Photonic Crystal–Based Nanoscale Multipurpose Biosensor for Detection of Brain Tumours, HIV, and Anaemia with High Sensitivity. *Plasmonics*. 2024;(0123456789). doi:10.1007/s11468-024-02199-3
31. Inan H, Poyraz M, Inci F, et al. Photonic crystals: Emerging biosensors and their promise for point-of-care applications. *Chem Soc Rev*. 2017;46(2):366-388. doi:10.1039/c6cs00206d
32. Leitão C, Pereira SO, Marques C, et al. Cost-Effective Fiber Optic Solutions for Biosensing. *Biosensors*. 2022;12(8). doi:10.3390/bios12080575
33. Butt MA, Shahbaz M, Piramidowicz R. Racetrack Ring Resonator Integrated with Multimode Interferometer Structure Based on Low-Cost Silica–Titania Platform for Refractive Index Sensing Application. *Photonics*. 2023;10(9). doi:10.3390/photonics10090978
34. Soler M, Lechuga LM. Principles, technologies, and applications of plasmonic biosensors. *J Appl Phys*. 2021;129(11). doi:10.1063/5.0042811
35. Wood RW. On a remarkable case of uneven distribution of light in a diffraction grating spectrum. *Proc Phys Soc London*. 1901;18(1):269-275. doi:10.1088/1478-7814/18/1/325
36. Maradudin AA, Simonsen I, Polanco J, Fitzgerald RM. Rayleigh and Wood anomalies in the diffraction of light from a perfectly conducting reflection grating. *J Opt (United Kingdom)*. 2016;18(2). doi:10.1088/2040-8978/18/2/024004
37. Barbillon G. Plasmonics and its applications. *Materials*. 2019;12(9):10-13. doi:10.3390/ma12091502
38. Kreibig U, Zacharias P. Surface plasma resonances in small spherical silver and gold particles. *Zeitschrift für Phys*. 1970;231(2):128-143. doi:10.1007/BF01392504
39. Locarno M, Brinks D. Analytical calculation of plasmonic resonances in metal nanoparticles: A simple guide. *Am J Phys*. 2023;91(7):538-546. doi:10.1119/5.0094967
40. Zhang Y, Min C, Dou X, et al. Plasmonic tweezers: for nanoscale optical trapping and beyond. *Light Sci Appl*. 2021;10(1). doi:10.1038/s41377-021-00474-0
41. Chen J, Badioli M, Alonso-González P, et al. Optical nano-imaging of gate-tunable graphene plasmons. *Nature*. 2012;487(7405):77-81. doi:10.1038/nature11254
42. Albella P, Poyli MA, Schmidt MK, et al. Low-loss electric and magnetic field-enhanced spectroscopy with subwavelength silicon dimers. *J Phys Chem C*. 2013;117(26):13573-13584. doi:10.1021/jp4027018
43. Suárez I, Ferrando A, Marques-Hueso J, et al. Propagation length enhancement of surface plasmon polaritons in gold nano-/micro-waveguides by the interference with photonic modes in the surrounding active dielectrics. *Nanophotonics*. 2017;6(5):1109-1120. doi:10.1515/nanoph-2016-0166
44. Dong J, Wang X, Zhang C, Yang H. Narrow-area average method for measurement of the propagation length of surface plasmon polaritons using nanoslit-grating structures. *Results Phys*. 2023;44(October 2022):106185. doi:10.1016/j.rinp.2022.106185

45. Barnes WL, Dereux A, Ebbesen TW. Surface plasmon subwavelength optics. *Nature*. 2003;424(6950):824-830. doi:10.1038/nature01937
46. Boriskina S V., Cooper TA, Zeng L, et al. Losses in plasmonics: from mitigating energy dissipation to embracing loss-enabled functionalities. *Adv Opt Photonics*. 2017;9(4):775. doi:10.1364/aop.9.000775
47. Hinman SS, McKeating KS, Cheng Q. Surface Plasmon Resonance: Material and Interface Design for Universal Accessibility. *Anal Chem*. 2018;90(1):19-39. doi:10.1021/acs.analchem.7b04251
48. Lopez GA, Estevez MC, Soler M, Lechuga LM. Recent advances in nanoplasmonic biosensors: Applications and lab-on-a-chip integration. *Nanophotonics*. 2017;6(1):123-136. doi:10.1515/nanoph-2016-0101
49. Vinogradov AP, Dorofeenko A V., Pukhov AA, Lisyansky AA. Exciting surface plasmon polaritons in the Kretschmann configuration by a light beam. *Phys Rev B*. 2018;97(23):1-9. doi:10.1103/PhysRevB.97.235407
50. Jana J, Ganguly M, Pal T. Enlightening surface plasmon resonance effect of metal nanoparticles for practical spectroscopic application. *RSC Adv*. 2016;6(89):86174-86211. doi:10.1039/c6ra14173k
51. Wu C-L, Hsueh C-H, Li J-H. Surface plasmons excited by multiple layer grating. *Opt Express*. 2019;27(2):1660. doi:10.1364/oe.27.001660
52. Moreira C, Wang Y, Blair S, Carvalho I, Cruz RS. Aluminum-Based Deep-Ultraviolet Surface Plasmon Resonance Sensor. *Plasmonics*. 2020;15(6):1891-1901. doi:10.1007/s11468-020-01207-6
53. Morsin M, Salleh MM, Umar AA, Sahdan MZ. Gold nanoplates for a localized surface plasmon resonance-based boric acid sensor. *Sensors (Switzerland)*. 2017;17(5):1-9. doi:10.3390/s17050947
54. Earp RL, Dessy RE. Surface plasmon resonance. *Chem Anal*. 1998;148(Mirabella 7):99-164.
55. Kats MA, Yu N, Genevet P, Gaburro Z, Capasso F. Effect of radiation damping on the spectral response of plasmonic components. *Opt Express*. 2011;19(22):21748. doi:10.1364/oe.19.021748
56. Mayer KM, Hafner JH. Localized Surface Plasmon Resonance Sensors. *Chem Rev*. 2011;111(6):3828-3857. doi:10.1021/cr100313v
57. Tokel O, Inci F, Demirci U. Advances in plasmonic technologies for point of care applications. *Chem Rev*. 2014;114(11):5728-5752. doi:10.1021/cr4000623
58. Wu JZ, Ghopry SA, Liu B, Shultz A. Metallic and Non-Metallic Plasmonic Nanostructures for LSPR Sensors. *Micromachines*. 2023;14(7). doi:10.3390/mi14071393
59. LABERKE JA. [Therapy of chronic pulmonary abscess]. *Ther Ggw*. 1951;90(5):183-185. http://www.ncbi.nlm.nih.gov/pubmed/14835545

60. Starowicz Z, Wojnarowska-Nowak R, Ozga P, Sheregii EM. The tuning of the plasmon resonance of the metal nanoparticles in terms of the SERS effect. *Colloid Polym Sci*. 2018;296(6):1029-1037. doi:10.1007/s00396-018-4308-9
61. Sofani M, Putra MH, Djuhana D. The sensitivity calculation of localized surface plasmon resonance (LSPR) Au nanorod by applying a boundary element system simulation. *IOP Conf Ser Mater Sci Eng*. 2020;763(1). doi:10.1088/1757-899X/763/1/012076
62. Estevez MC, Otte MA, Sepulveda B, Lechuga LM. Trends and challenges of refractometric nanoplasmonic biosensors: A review. *Anal Chim Acta*. 2014;806:55-73. doi:10.1016/j.aca.2013.10.048
63. Mazzotta F, Johnson TW, Dahlin AB, Shaver J, Oh SH, Höök F. Influence of the evanescent field decay length on the sensitivity of plasmonic nanodisks and nanoholes. *ACS Photonics*. 2015;2(2):256-262. doi:10.1021/ph500360d
64. Otte MA, Sepúlveda B, Ni W, Juste JP, Liz-Marzán LM, Lechuga LM. Identification of the optimal spectral region for plasmonic and nanoplasmonic sensing. *ACS Nano*. 2010;4(1):349-357. doi:10.1021/nn901024e
65. Robotham AC, Kelly JF. *LC-MS Characterization of Antibody-Based Therapeutics: Recent Highlights and Future Prospects*. Elsevier; 2020. doi:10.1016/B978-0-08-103019-6.00001-1
66. Alhazmi HA, Albratty M. Analytical Techniques for the Characterization and Quantification of Monoclonal Antibodies. *Pharmaceuticals*. 2023;16(2). doi:10.3390/ph16020291
67. Prior S, Hufton SE, Fox B, Dougall T, Rigsby P, Bristow A. International standards for monoclonal antibodies to support pre- and post-marketing product consistency: Evaluation of a candidate international standard for the bioactivities of rituximab. *MAbs*. 2018;10(1):129-142. doi:10.1080/19420862.2017.1386824
68. Sayed FA, Elsayed HA, Al-Dossari M, Eissa MF, Mehaney A, Aly AH. Angular surface plasmon resonance-based sensor with a silver nanocomposite layer for effective water pollution detection. *Sci Rep*. 2023;13(1):1-19. doi:10.1038/s41598-023-48837-4
69. Pires D, Hedrick JL, De Silva A, et al. Nanoscale Three-Dimensional Patterning of Molecular Resists by Scanning Probes. *Science (80-)*. 2010;328(5979):732-735. doi:10.1126/science.1187851
70. Mack C. *Fundamental Principles of Optical Lithography*. Wiley; 2007. doi:10.1002/9780470723876
71. Fu N, Liu Y, Ma X, Chen Z. EUV Lithography: State-of-the-Art Review. *J Microelectron Manuf*. 2019;2(2):1-6. doi:10.33079/jomm.19020202
72. Dahlin AB, Wittenberg NJ, Höök F, Oh S-H. Promises and challenges of nanoplasmonic devices for refractometric biosensing. *Nanophotonics*. 2013;2(2):83-101. doi:10.1515/nanoph-2012-0026
73. Fruncillo S, Su X, Liu H, Wong LS. Lithographic Processes for the Scalable Fabrication of

Micro- And Nanostructures for Biochips and Biosensors. *ACS Sensors*. 2021;6(6). doi:10.1021/acssensors.0c02704

74. Schock M, Bräse S. Reactive & efficient: Organic azides as cross-linkers in material sciences. *Molecules*. 2020;25(4). doi:10.3390/molecules25041009
75. Wang X, Xu J, Quan X, Li Y, Wang Y, Cheng X. Fast fabrication of silicon nanopillar array using electron beam lithography with two-layer exposure method. *Microelectron Eng*. 2020;227(February):111311. doi:10.1016/j.mee.2020.111311
76. Kim CS, Ahn SH, Jang DY. Review: Developments in micro/nanoscale fabrication by focused ion beams. *Vacuum*. 2012;86(8):1014-1035. doi:10.1016/j.vacuum.2011.11.004
77. Gilles S, Meier M, Prömpers M, et al. UV nanoimprint lithography with rigid polymer molds. *Microelectron Eng*. 2009;86(4-6):661-664. doi:10.1016/j.mee.2008.12.051
78. Manfrinato VR, Zhang L, Su D, et al. Resolution limits of electron-beam lithography toward the atomic scale. *Nano Lett*. 2013;13(4):1555-1558. doi:10.1021/nl304715p
79. Łaszcz A, Czerwinski A, Pruszyńska-Karbownik E, Wzorek M, Szmigiel D. Sensitive Metal-Semiconductor Nanothermocouple Fabricated by FIB to Investigate Laser Beams with Nanometer Spatial Resolution. *Sensors*. 2021;22(1):287. doi:10.3390/s22010287
80. Kaye S, Zeng Z, Sanders M, et al. Label-free detection of DNA hybridization with a compact LSPR-based fiber-optic sensor. *Analyst*. 2017;142(11):1974-1981. doi:10.1039/C7AN00249A
81. Horák M, Bukvišová K, Švarc V, Jaskowiec J, Křápek V, Šikola T. Comparative study of plasmonic antennas fabricated by electron beam and focused ion beam lithography. *Sci Rep*. 2018;8(1):1-8. doi:10.1038/s41598-018-28037-1
82. Gamo K. Focused ion beam lithography. *Nucl Instruments Methods Phys Res Sect B Beam Interact with Mater Atoms*. 1992;65(1-4):40-49. doi:10.1016/0168-583X(92)95011-F
83. Li P, Chen S, Dai H, et al. Recent advances in focused ion beam nanofabrication for nanostructures and devices: Fundamentals and applications. *Nanoscale*. 2021;13(3):1529-1565. doi:10.1039/d0nr07539f
84. Unno N, Mäkelä T. Thermal Nanoimprint Lithography—A Review of the Process, Mold Fabrication, and Material. *Nanomaterials*. 2023;13(14). doi:10.3390/nano13142031
85. Barcelo S, Li Z. Nanoimprint lithography for nanodevice fabrication. *Nano Converg*. 2016;3(1):21. doi:10.1186/s40580-016-0081-y
86. Bhattacharjee RR, Dasgupta U. Seed-mediated synthesis of silver nanoparticles: Tunable surface Plasmon and their facile fabrication. *Mater Today Proc*. 2020;43(xxxx):1342-1347. doi:10.1016/j.matpr.2020.09.167
87. Vinnacombe-Willson GA, Conti Y, Stefancu A, Weiss PS, Cortés E, Scarabelli L. Direct Bottom-Up In Situ Growth: A Paradigm Shift for Studies in Wet-Chemical Synthesis of Gold Nanoparticles. *Chem Rev*. 2023;123(13):8488-8529. doi:10.1021/acs.chemrev.2c00914
88. Manoharan H, Kc D, Sai VVR. Controlled In Situ Seed-Mediated Growth of Gold and Silver

Nanoparticles on an Optical Fiber Platform for Plasmonic Sensing Applications. *Plasmonics*. 2020;15(1):51-60. doi:10.1007/s11468-019-01008-6

89. Izak-Nau E, Huk A, Reidy B, et al. Fabrication of plasmonic nanostructures by hole-mask colloidal lithography: Recent development. *Biosens Bioelectron*. 2019;2(1):6-17. doi:10.1016/j.apmt.2018.12.014
90. Stokes K, Clark K, Odetade D, Hardy M, Goldberg Oppenheimer P. Advances in lithographic techniques for precision nanostructure fabrication in biomedical applications. *Discov Nano*. 2023;18(1):153. doi:10.1186/s11671-023-03938-x
91. Colson P, Henrist C, Cloots R. Nanosphere lithography: A powerful method for the controlled manufacturing of nanomaterials. *J Nanomater*. 2013;2013. doi:10.1155/2013/948510
92. Chen J, Lian X, Zhao M, Xie C. Multimode Fano Resonances Sensing Based on a Non-Through MIM Waveguide with a Square Split-Ring Resonance Cavity. *Biosensors*. 2022;12(5):1-14. doi:10.3390/bios12050306
93. She S, Shen S, Wang Z, Tan Q, Xiong J, Zhang W. Fano-resonance-based refractive index sensor with ultra-high sensitivity. *Results Phys*. 2021;25:104327. doi:10.1016/j.rinp.2021.104327
94. Chung T, Wang H, Cai H. Dielectric metasurfaces for next-generation optical biosensing: a comparison with plasmonic sensing. *Nanotechnology*. 2023;34(40). doi:10.1088/1361-6528/ace117
95. Huang SH, Wu PC. Exploring plasmonic gradient metasurfaces for enhanced optical sensing in the visible spectrum. *Nanophotonics*. 2024;13(7):1099-1108. doi:10.1515/nanoph-2023-0809
96. Zheng Z, Rocco D, Ren H, et al. Advances in nonlinear metasurfaces for imaging, quantum, and sensing applications. *Nanophotonics*. 2023;12(23):4255-4281. doi:10.1515/nanoph-2023-0526
97. Lee Y, Kim S-J, Park H, Lee B. Metamaterials and Metasurfaces for Sensor Applications. *Sensors*. 2017;17(8):1726. doi:10.3390/s17081726
98. Qin J, Jiang S, Wang Z, et al. Metasurface Micro/Nano-Optical Sensors: Principles and Applications. *ACS Nano*. 2022;16(8):11598-11618. doi:10.1021/acsnano.2c03310
99. Tabassum S, Nayemuzzaman SK, Kala M, Kumar Mishra A, Mishra SK. Metasurfaces for Sensing Applications: Gas, Bio and Chemical. *Sensors*. 2022;22(18). doi:10.3390/s22186896
100. Qi J, Li C, Xia Y, et al. Research progress of biomolecular detection based on metasurfaces. *Infrared Phys Technol*. 2024;136:105111. doi:10.1016/j.infrared.2023.105111
101. Choi M, Park J, Shin J, et al. Realization of high-performance optical metasurfaces over a large area: a review from a design perspective. *npj Nanophotonics*. 2024;1(1):31. doi:10.1038/s44310-024-00029-2
102. Seong J, Jeon Y, Yang Y, Badloe T, Rho J. Cost-Effective and Environmentally Friendly Mass

Manufacturing of Optical Metasurfaces Towards Practical Applications and Commercialization. *Int J Precis Eng Manuf - Green Technol*. 2024;11(2):685-706. doi:10.1007/s40684-023-00580-x

103. Yang W, Zhou J, Tsai DP, Xiao S. Advanced manufacturing of dielectric meta-devices. *Photonics Insights*. 2024;3(2):R04. doi:10.3788/PI.2024.R04
104. Spackova B, Wrobel P, Bockova M, Homola J. Optical Biosensors Based on Plasmonic Nanostructures. *Proc IEEE*. 2016;104(12):2380-2408. doi:10.1109/JPROC.2016.2624340
105. Mauriz E, Dey P, Lechuga LM. Advances in nanoplasmonic biosensors for clinical applications. *Analyst*. 2019;144(24):7105-7129. doi:10.1039/C9AN00701F
106. Soler M, Huertas CS, Lechuga LM. Label-free plasmonic biosensors for point-of-care diagnostics: a review. *Expert Rev Mol Diagn*. 2019;19(1):71-81. doi:10.1080/14737159.2019.1554435
107. Soler M, Estevez MC, Villar-Vazquez R, Casal JI, Lechuga LM. Label-free nanoplasmonic sensing of tumor-associate autoantibodies for early diagnosis of colorectal cancer. *Anal Chim Acta*. 2016;930:31-38. doi:10.1016/j.aca.2016.04.059
108. Soler M, Mesa-Antunez P, Estevez MC, et al. Highly sensitive dendrimer-based nanoplasmonic biosensor for drug allergy diagnosis. *Biosens Bioelectron*. 2015;66:115-123. doi:10.1016/j.bios.2014.10.081
109. López-Muñoz GA, Estévez MC, Vázquez-García M, et al. Gold/silver/gold trilayer films on nanostructured polycarbonate substrates for direct and label-free nanoplasmonic biosensing. *J Biophotonics*. 2018;11(8). doi:10.1002/jbio.201800043
110. Evlyukhin AB, Reinhardt C, Seidel A, Luk'Yanchuk BS, Chichkov BN. Optical response features of Si-nanoparticle arrays. *Phys Rev B - Condens Matter Mater Phys*. 2010;82(4):1-12. doi:10.1103/PhysRevB.82.045404
111. Evlyukhin AB, Novikov SM, Zywietz U, et al. Demonstration of magnetic dipole resonances of dielectric nanospheres in the visible region. *Nano Lett*. 2012;12(7):3749-3755. doi:10.1021/nl301594s
112. García-Etxarri A, Gómez-Medina R, Froufe-Pérez LS, et al. Strong magnetic response of submicron Silicon particles in the infrared. *Opt Express*. 2011;19(6):4815. doi:10.1364/oe.19.004815
113. Kuznetsov AI, Miroshnichenko AE, Fu YH, Zhang J, Luk'yanchuk B. Magnetic light. *Sci Rep*. 2012;2(1):492. doi:10.1038/srep00492
114. Geffrin JM, García-Cámara B, Gómez-Medina R, et al. Magnetic and electric coherence in forward-and back-scattered electromagnetic waves by a single dielectric subwavelength sphere. *Nat Commun*. 2012;3. doi:10.1038/ncomms2167
115. Decker M, Staude I. Resonant dielectric nanostructures: A low-loss platform for functional nanophotonics. *J Opt*. 2016;18(10):1-31. doi:10.1088/2040-8978/18/10/103001

116. Yavas O, Svedendahl M, Dobosz P, Sanz V, Quidant R. On-a-chip Biosensing Based on All-Dielectric Nanoresonators. *Nano Lett*. 2017;17(7):4421-4426. doi:10.1021/acs.nanolett.7b01518
117. van de Haar MA, van de Groep J, Brenny BJM, Polman A. Controlling magnetic and electric dipole modes in hollow silicon nanocylinders. *Opt Express*. 2016;24(3):2047. doi:10.1364/OE.24.002047
118. Liu W, Kivshar YS. Generalized Kerker effects in nanophotonics and meta-optics. *Opt Express*. 2018;26(10):13085. doi:10.1364/OE.26.013085
119. Kuznetsov AI, Miroshnichenko AE, Brongersma ML, Kivshar YS, Luk'yanchuk B. Optically resonant dielectric nanostructures. *Science (80-)*. 2016;354(6314). doi:10.1126/science.aag2472
120. Wiecha PR, Cuche A, Arbouet A, et al. Strongly Directional Scattering from Dielectric Nanowires. *ACS Photonics*. 2017;4(8):2036-2046. doi:10.1021/acsphotonics.7b00423
121. Kivshar Y, Miroshnichenko A. Meta-Optics with Mie Resonances. *Opt Photonics News*. 2017;28(1):24. doi:10.1364/OPN.28.1.000024
122. Bonatti L, Gil G, Giovannini T, Corni S, Cappelli C. Plasmonic Resonances of Metal Nanoparticles: Atomistic vs. Continuum Approaches. *Front Chem*. 2020;8:1-15. doi:10.3389/fchem.2020.00340
123. Paniagua-Domínguez R, Luk'yanchuk B, Miroshnichenko A, Sánchez-Gil JA. Dielectric nanoresonators and metamaterials. *J Appl Phys*. 2019;126(15). doi:10.1063/1.5129100
124. Ushanov VI, Eremeev S V., Silkin VM, Chaldyshev V V. Unveiling Influence of Dielectric Losses on the Localized Surface Plasmon Resonance in (Al,Ga)As:Sb Metamaterials. *Nanomaterials*. 2024;14(2):1-11. doi:10.3390/nano14020167
125. Cortés E, Wendisch FJ, Sortino L, et al. Optical Metasurfaces for Energy Conversion. *Chem Rev*. 2022;122(19):15082-15176. doi:10.1021/acs.chemrev.2c00078
126. Semouchkina E, Duan R, Semouchkin G, Pandey R. Sensing based on Fano-type resonance response of all-dielectric metamaterials. *Sensors*. 2015;15(4):9344-9359. doi:10.3390/s150409344
127. García-Cámara B, Gómez-Medina R, Sáenz JJ, Sepúlveda B. Sensing with magnetic dipolar resonances in semiconductor nanospheres. *Opt Express*. 2013;21(20):23007. doi:10.1364/oe.21.023007
128. Alexander DTL, Flauraud V, Demming-Janssen F. Near-Field Mapping of Photonic Eigenmodes in Patterned Silicon Nanocavities by Electron Energy-Loss Spectroscopy. *ACS Nano*. 2021;15(10):16501-16514. doi:10.1021/acsnano.1c06065
129. Yan J, Liu P, Lin Z, Yang G. New type high-index dielectric nanosensors based on the scattering intensity shift. *Nanoscale*. 2016;8(11):5996-6007. doi:10.1039/c5nr07871g
130. Paquin F, Rivnay J, Salleo A, Stingelin N, Silva C. Multi-phase semicrystalline

microstructures drive exciton dissociation in neat plastic semiconductors. *J Mater Chem C*. 2015;3:10715-10722. doi:10.1039/b000000x

131. Osaki T, Takeuchi S. Artificial Cell Membrane Systems for Biosensing Applications. *Anal Chem*. 2017;89(1):216-231. doi:10.1021/acs.analchem.6b04744
132. Soler M, Estevez M-C, Alvarez M, Otte M, Sepulveda B, Lechuga L. Direct Detection of Protein Biomarkers in Human Fluids Using Site-Specific Antibody Immobilization Strategies. *Sensors*. 2014;14(2):2239-2258. doi:10.3390/s140202239
133. Huertas CS, Carrascosa LG, Bonnal S, Valcárcel J, Lechuga LM. Quantitative evaluation of alternatively spliced mRNA isoforms by label-free real-time plasmonic sensing. *Biosens Bioelectron*. 2016;78:118-125. doi:10.1016/j.bios.2015.11.023
134. Zhu Z, Feng M, Zuo L, et al. An aptamer based surface plasmon resonance biosensor for the detection of ochratoxin A in wine and peanut oil. *Biosens Bioelectron*. 2015;65:320-326. doi:10.1016/j.bios.2014.10.059
135. Jia Y, Chen S, Wang Q, Li J. Recent progress in biosensor regeneration techniques. *Nanoscale*. 2024;16(6):2834-2846. doi:10.1039/d3nr05456j
136. Gajos K, Petrou P, Budkowski A. Comparison of Physical Adsorption and Covalent Coupling Methods for Surface Density-Dependent Orientation of Antibody on Silicon. *Molecules*. 2022;27(12). doi:10.3390/molecules27123672
137. Morales MA, Halpern JM. Guide to Selecting a Biorecognition Element for Biosensors. *Bioconjug Chem*. 2018;29(10):3231-3239. doi:10.1021/acs.bioconjchem.8b00592
138. Lichtenberg JY, Ling Y, Kim S. Non-Specific Adsorption Reduction Methods in Biosensing. *Sensors*. 2019;19(11):2488. doi:10.3390/s19112488
139. Mohamad NR, Marzuki NHC, Buang NA, Huyop F, Wahab RA. An overview of technologies for immobilization of enzymes and surface analysis techniques for immobilized enzymes. *Biotechnol Biotechnol Equip*. 2015;29(2):205-220. doi:10.1080/13102818.2015.1008192
140. Datta S, Christena LR, Rajaram YRS. Enzyme immobilization: an overview on techniques and support materials. *3 Biotech*. 2013;3(1):1-9. doi:10.1007/s13205-012-0071-7
141. Shen Q, Yang R, Hua X, Ye F, Zhang W, Zhao W. Gelatin-templated biomimetic calcification for β-galactosidase immobilization. *Process Biochem*. 2011;46(8):1565-1571. doi:10.1016/j.procbio.2011.04.010
142. Vericat C, Vela ME, Benitez G, Carro P, Salvarezza RC. Self-assembled monolayers of thiols and dithiols on gold: new challenges for a well-known system. *Chem Soc Rev*. 2010;39(5):1805-1834. doi:10.1039/b907301a
143. Soler M, Lechuga LM. Biochemistry strategies for label-free optical sensor biofunctionalization: advances towards real applicability. *Anal Bioanal Chem*. 2022;414(18):5071-5085. doi:10.1007/s00216-021-03751-4
144. Puumala LS, Grist SM, Morales JM, et al. Biofunctionalization of Multiplexed Silicon

Photonic Biosensors. *Biosensors*. 2023;13(1):1-96. doi:10.3390/bios13010053

145. Trilling AK, Beekwilder J, Zuilhof H. Antibody orientation on biosensor surfaces: A minireview. *Analyst*. 2013;138(6):1619-1627. doi:10.1039/c2an36787d
146. Löfås S, Johnsson B. A novel hydrogel matrix on gold surfaces in surface plasmon resonance sensors for fast and efficient covalent immobilization of ligands. *J Chem Soc Chem Commun*. 1990;(21):1526-1528. doi:10.1039/C39900001526
147. Hucknall A, Rangarajan S, Chilkoti A. In pursuit of zero: Polymer brushes that resist the adsorption of proteins. *Adv Mater*. 2009;21(23):2441-2446. doi:10.1002/adma.200900383
148. Gooding JJ, Ciampi S. The molecular level modification of surfaces: From self-assembled monolayers to complex molecular assemblies. *Chem Soc Rev*. 2011;40(5):2704-2718. doi:10.1039/c0cs00139b
149. Ahmadi Y, Kim KH. Functionalization and customization of polyurethanes for biosensing applications: A state-of-the-art review. *TrAC - Trends Anal Chem*. 2020;126:115881. doi:10.1016/j.trac.2020.115881
150. Ulman A. Formation and Structure of Self-Assembled Monolayers Abraham. *Chem*. 1996;43(96):1533-1554. doi:10.1111/j.1151-2916.1960.tb13612.x
151. Smith CL, Milea JS, Nguyen GH. Immobilization of Nucleic Acids Using Biotin-Strept(avidin) Systems. In: *Topics in Current Chemistry*. Vol 261. ; 2005:63-90. doi:10.1007/128_017
152. Carvalho PM, Makowski M, Domingues MM, Martins IC, Santos NC. Lipid membrane-based therapeutics and diagnostics. *Arch Biochem Biophys*. 2021;704:108858. doi:10.1016/j.abb.2021.108858
153. Siontorou C, Nikoleli G-P, Nikolelis D, Karapetis S. Artificial Lipid Membranes: Past, Present, and Future. *Membranes*. 2017;7(3):38. doi:10.3390/membranes7030038
154. Kurniawan J, Ventrici De Souza JF, Dang AT, Liu GY, Kuhl TL. Preparation and Characterization of Solid-Supported Lipid Bilayers Formed by Langmuir-Blodgett Deposition: A Tutorial. *Langmuir*. 2018;34(51):15622-15639. doi:10.1021/acs.langmuir.8b03504
155. Lee YK, Lee H, Nam JM. Lipid-nanostructure hybrids and their applications in nanobiotechnology. *NPG Asia Mater*. 2013;5(5):1-13. doi:10.1038/am.2013.13
156. Ayscough SE, Clifton LA, Skoda MWA, Titmuss S. Suspended phospholipid bilayers: A new biological membrane mimetic. *J Colloid Interface Sci*. 2023;633:1002-1011. doi:10.1016/j.jcis.2022.11.148
157. Jonsson MP, Jönsson P, Dahlin AB, Höök F. Supported lipid bilayer formation and lipid-membrane-mediated biorecognition reactions studied with a new nanoplasmonic sensor template. *Nano Lett*. 2007;7(11):3462-3468. doi:10.1021/nl072006t
158. Rebaud S, Maniti O, Girard-Egrot AP. Tethered bilayer lipid membranes (tBLMs): Interest and applications for biological membrane investigations. *Biochimie*. 2014;107:135-142.

doi:10.1016/j.biochi.2014.06.021

159. Jackman J, Knoll W, Cho N-J. Biotechnology Applications of Tethered Lipid Bilayer Membranes. *Materials*. 2012;5(12):2637-2657. doi:10.3390/ma5122637
160. Sut TN, Tan SW, Jeon WY, Yoon BK, Cho NJ, Jackman JA. Streamlined Fabrication of Hybrid Lipid Bilayer Membranes on Titanium Oxide Surfaces: A Comparison of One-and Two-Tail SAM Molecules. *Nanomaterials*. 2022;12(7). doi:10.3390/nano12071153
161. Sabirovas T, Valiūnienė A, Valincius G. Hybrid bilayer membranes on metallurgical polished aluminum. *Sci Rep*. 2021;11(1):1-11. doi:10.1038/s41598-021-89150-2
162. Sabirovas T, Valiūnienė A, Gabriunaite I, Valincius G. Mixed hybrid bilayer lipid membranes on mechanically polished titanium surface. *Biochim Biophys Acta - Biomembr*. 2020;1862(6). doi:10.1016/j.bbamem.2020.183232
163. Wong JY, Majewski J, Seitz M, Park CK, Israelachvili JN, Smith GS. Polymer-cushioned bilayers. I. A structural study of various preparation methods using neutron reflectometry. *Biophys J*. 1999;77(3):1445-1457. doi:10.1016/S0006-3495(99)76992-4
164. Dahlin A, Zäch M, Rindzevicius T, Käll M, Sutherland DS, Höök F. Localised surface plasmon resonance sensing of lipid-membrane-mediated biorecognition events. *J Am Chem Soc*. 2005;127(14):5043-5048. doi:10.1021/ja043672o
165. Limaj O, Etezadi D, Wittenberg NJ, et al. Infrared Plasmonic Biosensor for Real-Time and Label-Free Monitoring of Lipid Membranes. *Nano Lett*. 2016;16(2):1502-1508. doi:10.1021/acs.nanolett.5b05316
166. Soler M, Li X, John-Herpin A, Schmidt J, Coukos G, Altug H. Two-Dimensional Label-Free Affinity Analysis of Tumor-Specific CD8 T Cells with a Biomimetic Plasmonic Sensor. *ACS Sensors*. 2018;3(11):2286-2295. doi:10.1021/acssensors.8b00523
167. Yoon BK, Park H, Zhdanov VP, Jackman JA, Cho NJ. Real-time nanoplasmonic sensing of three-dimensional morphological changes in a supported lipid bilayer and antimicrobial testing applications. *Biosens Bioelectron*. 2021;174:112768. doi:10.1016/j.bios.2020.112768
168. Peláez EC, Estevez M-C, Portela A, Salvador J-P, Marco M-P, Lechuga LM. Nanoplasmonic biosensor device for the monitoring of acenocoumarol therapeutic drug in plasma. *Biosens Bioelectron*. 2018;119:149-155. doi:10.1016/j.bios.2018.08.011
169. Unser S, Bruzas I, He J, Sagle L. Localized surface plasmon resonance biosensing: Current challenges and approaches. *Sensors*. 2015;15(7):15684-15716. doi:10.3390/s150715684
170. Scholl JA, Koh AL, Dionne JA. Quantum plasmon resonances of individual metallic nanoparticles. *Nature*. 2012;483(7390):421-427. doi:10.1038/nature10904
171. Manjavacas A, García de Abajo FJ. Tunable plasmons in atomically thin gold nanodisks. *Nat Commun*. 2014;5(1):3548. doi:10.1038/ncomms4548
172. Zheng X, Peng Y, Cui X, Zheng W. Modulation of the shape and localized surface plasmon resonance of silver nanoparticles via halide ion etching and photochemical regrowth. *Mater*

Lett. 2016;173:88-90. doi:10.1016/j.matlet.2016.02.120

173. Lee YM, Kim SE, Park JE. Strong coupling in plasmonic metal nanoparticles. *Nano Converg*. 2023;10(1). doi:10.1186/s40580-023-00383-5
174. Farooq S, Wali F, Zezell DM, de Araujo RE, Rativa D. Optimizing and Quantifying Gold Nanospheres Based on LSPR Label-Free Biosensor for Dengue Diagnosis. *Polymers*. 2022;14(8):1592. doi:10.3390/polym14081592
175. Mendoza Herrera LJ, Arboleda DM, Schinca DC, Scaffardi LB. Determination of plasma frequency, damping constant, and size distribution from the complex dielectric function of noble metal nanoparticles. *J Appl Phys*. 2014;116(23). doi:10.1063/1.4904349
176. Loiseau A, Asila V, Boitel-Aullen G, Lam M, Salmain M, Boujday S. Silver-based plasmonic nanoparticles for and their use in biosensing. *Biosensors*. 2019;9(2). doi:10.3390/bios9020078
177. Boisselier E, Astruc D. Gold nanoparticles in nanomedicine: preparations, imaging, diagnostics, therapies and toxicity. *Chem Soc Rev*. 2009;38(6):1759-1782. doi:10.1039/b806051g
178. Tong L, Wei H, Zhang S, Xu H. Recent Advances in Plasmonic Sensors. *Sensors*. 2014;14(5):7959-7973. doi:10.3390/s140507959
179. Auguié B, Barnes WL. Collective resonances in gold nanoparticle arrays. *Phys Rev Lett*. 2008;101(14). doi:10.1103/PhysRevLett.101.143902
180. Bradley Z, Cunningham D, Bhalla N. Refractive Index-Modulated LSPR Sensing in 20–120 nm Gold and Silver Nanoparticles: A Simulation Study. *ECS Sensors Plus*. 2023;2(4):043402. doi:10.1149/2754-2726/ad08d8
181. Gish DA, Nsiah F, Mcdermott MT, Brett MJ. Evaluation of silver nanostructures fabricated using glancing angle deposition as localized surface plasmon resonance biosensors. *Tech Proc*. 2007;2(11):461-464.
182. Hostetler JL, Smith AN, Czajkowsky DM, Norris PM. Measurement of the electron-phonon coupling factor dependence on film thickness and grain size in Au, Cr, and Al. *Appl Opt*. 1999;38(16):3614. doi:10.1364/ao.38.003614
183. Tebbe M, Kuttner C, Mayer M, et al. Silver-Overgrowth-Induced Changes in Intrinsic Optical Properties of Gold Nanorods: From Noninvasive Monitoring of Growth Kinetics to Tailoring Internal Mirror Charges. *J Phys Chem C*. 2015;119(17):9513-9523. doi:10.1021/acs.jpcc.5b03155
184. Iyer VK, Asimow RM. The electrical resistivity of gold-silver alloys. *J Less Common Met*. 1967;13(1):18-23. doi:10.1016/0022-5088(67)90043-4
185. Kolwas K, Derkachova A. Impact of the interband transitions in gold and silver on the dynamics of propagating and localized surface plasmons. *Nanomaterials*. 2020;10(7):1-27. doi:10.3390/nano10071411
186. Malitson IH. Interspecimen Comparison of the Refractive Index of Fused Silica. *J Opt Soc*

Am. 1965;55(10):1205. doi:10.1364/JOSA.55.001205

187. Oh S-H, Altug H. Performance metrics and enabling technologies for nanoplasmonic biosensors. *Nat Commun*. 2018;9(1):5263. doi:10.1038/s41467-018-06419-3
188. Bommali RK, Mahapatra DP, Gupta H, et al. Angle dependent localized surface plasmon resonance from near surface implanted silver nanoparticles in SiO2 thin film. *J Appl Phys*. 2018;124(6):1-11. doi:10.1063/1.5043386
189. Oheim M, Salomon A, Weissman A, Brunstein M, Becherer U. Calibrating Evanescent-Wave Penetration Depths for Biological TIRF Microscopy. *Biophys J*. 2019;117(5):795-809. doi:10.1016/j.bpj.2019.07.048
190. Fredriksson H, Alaverdyan Y, Dmitriev A, et al. Hole-mask colloidal lithography. *Adv Mater*. 2007;19(23):4297-4302. doi:10.1002/adma.200700680
191. Mayer M, Schnepf MJ, König TAF, Fery A. Colloidal Self-Assembly Concepts for Plasmonic Metasurfaces. *Adv Opt Mater*. 2019;7(1). doi:10.1002/adom.201800564
192. Peláez EC, Estevez MC, Portela A, Salvador JP, Marco MP, Lechuga LM. Nanoplasmonic biosensor device for the monitoring of acenocoumarol therapeutic drug in plasma. *Biosens Bioelectron*. 2018;119:149-155. doi:10.1016/j.bios.2018.08.011
193. Izak-Nau E, Huk A, Reidy B, et al. Impact of storage conditions and storage time on silver nanoparticles' physicochemical properties and implications for their biological effects. *RSC Adv*. 2015;5(102):84172-84185. doi:10.1039/c5ra10187e
194. Keast VJ. Atmospheric Corrosion of Silver and Silver Nanoparticles. *Corros Mater Degrad*. 2022;3(2):221-234. doi:10.3390/cmd3020013
195. Barbillon G. Latest Advances in Metasurfaces for SERS and SEIRA Sensors as Well as Photocatalysis. *Int J Mol Sci*. 2022;23(18). doi:10.3390/ijms231810592
196. Tseng ML, Jahani Y, Leitis A, Altug H. Dielectric Metasurfaces Enabling Advanced Optical Biosensors. *ACS Photonics*. 2021;8(1):47-60. doi:10.1021/acsphotonics.0c01030
197. Kharratian S, Conteduca D, Procacci B, Shaw DJ, Hunt NT, Krauss TF. Metasurface-enhanced mid-infrared spectroscopy in the liquid phase. *Chem Sci*. 2022;114:12858-12864. doi:10.1039/d2sc03927c
198. Yavas O, Svedendahl M, Quidant R. Unravelling the Role of Electric and Magnetic Dipoles in Biosensing with Si Nanoresonators. *ACS Nano*. 2019;13(4):4582-4588. doi:10.1021/acsnano.9b00572
199. Evlyukhin AB, Eriksen RL, Cheng W, et al. Optical spectroscopy of single Si nanocylinders with magnetic and electric resonances. *Sci Rep*. 2014;4:1-7. doi:10.1038/srep04126
200. Evlyukhin AB, Reinhardt C, Chichkov BN. Multipole light scattering by nonspherical nanoparticles in the discrete dipole approximation. *Phys Rev B - Condens Matter Mater Phys*. 2011;84(23):1-8. doi:10.1103/PhysRevB.84.235429
201. Chen HT, Taylor AJ, Yu N. A review of metasurfaces: Physics and applications. *Reports Prog*

Phys. 2016;79(7). doi:10.1088/0034-4885/79/7/076401

202. Miroshnichenko AE, Evlyukhin AB, Yu YF, et al. Nonradiating anapole modes in dielectric nanoparticles. *Nat Commun*. 2015;6:1-8. doi:10.1038/ncomms9069
203. Todisco F, Malureanu R, Wolff C, et al. Magnetic and electric Mie-exciton polaritons in silicon nanodisks. *Nanophotonics*. 2020;9(4):803-814. doi:10.1515/nanoph-2019-0444
204. Sansa M, Sage E, Bullard EC, et al. Frequency fluctuations in silicon nanoresonators. *Nat Nanotechnol*. 2016;11(6):552-558. doi:10.1038/nnano.2016.19
205. Länk NO, Verre R, Johansson P, Käll M. Large-Scale Silicon Nanophotonic Metasurfaces with Polarization Independent Near-Perfect Absorption. *Nano Lett*. 2017;17(5):3054-3060. doi:10.1021/acs.nanolett.7b00416
206. Koirala I, Shrestha VR, Park CS, Gao S, Lee SS, Choi DY. All dielectric transmissive structural multicolor pixel incorporating a resonant grating in hydrogenated amorphous silicon. *Sci Rep*. 2017;7(1):1-7. doi:10.1038/s41598-017-14093-6
207. Abd-Elkader AES, ELDamarawy E, Hameed MFO, Obayya SSA. Ultra-compact SOS-based bi-metallic TM-pass polarizer. *Opt Quantum Electron*. 2022;54(4):1-15. doi:10.1007/s11082-022-03636-5
208. Díaz-Escobar E, Barreda ÁI, Griol A, Martínez A. Experimental observation of higher-order anapoles in individual silicon disks under in-plane illumination. *Appl Phys Lett*. 2022;121(20). doi:10.1063/5.0108438
209. van Loon T, Liang M, Delplace T, et al. Refractive index sensing using quasi-bound states in the continuum in silicon metasurfaces. *Opt Express*. 2024;32(8):14289. doi:10.1364/oe.514787
210. Watanabe K, Iwanaga M. Nanogap enhancement of the refractometric sensitivity at quasi-bound states in the continuum in all-dielectric metasurfaces. *Nanophotonics*. 2023;12(1):99-109. doi:10.1515/nanoph-2022-0565
211. Wang Z, Sun J, Li J, et al. Customizing 2.5D Out-of-Plane Architectures for Robust Plasmonic Bound-States-in-the-Continuum Metasurfaces. *Adv Sci*. 2023;10(7):1-11. doi:10.1002/advs.202206236
212. Alves ID, Lecomte S. Study of G-Protein Coupled Receptor Signaling in Membrane Environment by Plasmon Waveguide Resonance. *Acc Chem Res*. 2019;52(4):1059-1067. doi:10.1021/acs.accounts.9b00007
213. Hodnik V, Anderluh G. Surface Plasmon Resonance for Measuring Interactions of Proteins with Lipid Membranes. In: Kleinschmidt JH, ed. Vol 974. Methods in Molecular Biology. Humana Press; 2013:23-36. doi:10.1007/978-1-62703-275-9_2
214. Mozsolits H, Wirth HJ, Werkmeister J, Aguilar MI. Analysis of antimicrobial peptide interactions with hybrid bilayer membrane systems using surface plasmon resonance. *Biochim Biophys Acta - Biomembr*. 2001;1512(1):64-76. doi:10.1016/S0005-2736(01)00303-0
215. Hardy GJ, Nayak R, Zauscher S. Model cell membranes: Techniques to form complex

biomimetic supported lipid bilayers via vesicle fusion. *Curr Opin Colloid Interface Sci*. 2013;18(5):448-458. doi:10.1016/j.cocis.2013.06.004

216. Kilic A, Kok FN. Biomimetic lipid bilayers on solid surfaces: Models for biological interactions. *Surf Innov*. 2016;4(3):141-157. doi:10.1680/jsuin.16.00008
217. Neupane S, De Smet Y, Renner FU, Losada-Pérez P. Quartz Crystal Microbalance With Dissipation Monitoring: A Versatile Tool to Monitor Phase Transitions in Biomimetic Membranes. *Front Mater*. 2018;5:1-8. doi:10.3389/fmats.2018.00046
218. Richter RP, Brisson AR. Following the formation of supported lipid bilayers on Mica: A study combining AFM, QCM-D, and ellipsometry. *Biophys J*. 2005;88(5):3422-3433. doi:10.1529/biophysj.104.053728
219. Richter RP, Bérat R, Brisson AR. Formation of solid-supported lipid bilayers: An integrated view. *Langmuir*. 2006;22(8):3497-3505. doi:10.1021/la052687c
220. Tero R. Substrate Effects on the Formation Process, Structure and Physicochemical Properties of Supported Lipid Bilayers. *Materials*. 2012;5(12):2658-2680. doi:10.3390/ma5122658
221. Lind TK, Cárdenas M. Understanding the formation of supported lipid bilayers via vesicle fusion—A case that exemplifies the need for the complementary method approach (Review). *Biointerphases*. 2016;11(2). doi:10.1116/1.4944830
222. Sezgin E, Schwille P. Fluorescence Techniques to Study Lipid Dynamics. *Cold Spring Harb Perspect Biol*. 2011;3(11):a009803-a009803. doi:10.1101/cshperspect.a009803
223. Urban AS, Fedoruk M, Horton MR, Rädler JO, Stefani FD, Feldmann J. Controlled nanometric phase transitions of phospholipid membranes by plasmonic heating of single gold nanoparticles. *Nano Lett*. 2009;9(8):2903-2908. doi:10.1021/nl901201h
224. Lind TK, Skoda MWA, Cárdenas M. Formation and Characterization of Supported Lipid Bilayers Composed of Phosphatidylethanolamine and Phosphatidylglycerol by Vesicle Fusion, a Simple but Relevant Model for Bacterial Membranes. *ACS Omega*. 2019;4(6):10687-10694. doi:10.1021/acsomega.9b01075
225. Lyu D, Zhang L, Zhang Y. Effects of cholesterol on bilayers with various degrees of unsaturation of their phospholipid tails under mechanical stress. *RSC Adv*. 2020;10(19):11088-11094. doi:10.1039/d0ra00624f
226. Duan R, Sun X, Liu J, Gong T, Zhang Z. Mixed micelles loaded with silybin-polyene phosphatidylcholine complex improve drug solubility. *Acta Pharmacol Sin*. 2011;32(1):108-115. doi:10.1038/aps.2010.192
227. Xia Z, Woods A, Quirk A, Burgess IJ, Lau BLT. Interactions between polystyrene nanoparticles and supported lipid bilayers: impact of charge and hydrophobicity modification by specific anions. *Environ Sci Nano*. 2019;6(6):1829-1837. doi:10.1039/C9EN00055K
228. González-Henríquez CM, Villegas-Opazo VA, Sagredo-Oyarce DH, Sarabia-Vallejos MA, Terraza CA. Thermal response analysis of phospholipid bilayers using ellipsometric

techniques. *Biosensors*. 2017;7(3):1-17. doi:10.3390/bios7030034

229. Richter RP, Brisson AR. Following the formation of supported lipid bilayers on Mica: A study combining AFM, QCM-D, and ellipsometry. *Biophys J*. 2005;88(5):3422-3433. doi:10.1529/biophysj.104.053728
230. Reimhult E, Kasemo B, Höök F. Rupture pathway of phosphatidylcholine liposomes on silicon dioxide. *Int J Mol Sci*. 2009;10(4):1683-1696. doi:10.3390/ijms10041683
231. Jackman JA, Špačková B, Linardy E, et al. Nanoplasmonic ruler to measure lipid vesicle deformation. *Chem Commun*. 2016;52(1):76-79. doi:10.1039/c5cc06861d
232. Parkkila P, Elderdfi M, Bunker A, Viitala T. Biophysical Characterization of Supported Lipid Bilayers Using Parallel Dual-Wavelength Surface Plasmon Resonance and Quartz Crystal Microbalance Measurements. *Langmuir*. 2018;34(27):8081-8091. doi:10.1021/acs.langmuir.8b01259
233. de Mol NJ, Fischer MJE. *Surface Plasmon Resonance*. Vol 627. (Mol NJ, Fischer MJE, eds.). Humana Press; 2010. doi:10.1007/978-1-60761-670-2
234. Hardy GJ, Nayak R, Zauscher S. Model cell membranes: Techniques to form complex biomimetic supported lipid bilayers via vesicle fusion. *Curr Opin Colloid Interface Sci*. 2013;18(5):448-458. doi:10.1016/j.cocis.2013.06.004
235. Tsai T-C, Liu C-W, Wu Y-C, Ondevilla NAP, Osawa M, Chang H-C. In situ study of EDC/NHS immobilization on gold surface based on attenuated total reflection surface-enhanced infrared absorption spectroscopy (ATR-SEIRAS). *Colloids Surfaces B Biointerfaces*. 2019;175:300-305. doi:10.1016/j.colsurfb.2018.12.009
236. Shu W, Laue ED, Seshia AA. Investigation of biotin-streptavidin binding interactions using microcantilever sensors. *Biosens Bioelectron*. 2007;22(9-10):2003-2009. doi:10.1016/j.bios.2006.08.047
237. Li L, Wang S, Xiao Y, Wang Y. Recent Advances in Immobilization Strategies for Biomolecules in Sensors Using Organic Field-Effect Transistors. *Trans Tianjin Univ*. 2020;26(6):424-440. doi:10.1007/s12209-020-00234-y
238. Mohamad NR, Marzuki NHC, Buang NA, Huyop F, Wahab RA. An overview of technologies for immobilization of enzymes and surface analysis techniques for immobilized enzymes. *Biotechnol Biotechnol Equip*. 2015;29(2):205-220. doi:10.1080/13102818.2015.1008192
239. Giarola JF, Santos J, Estevez MC, Ventura S, Pallarès I, Lechuga LM. An α-helical peptide-based plasmonic biosensor for highly specific detection of α-synuclein toxic oligomers. *Anal Chim Acta*. 2024;1304. doi:10.1016/j.aca.2024.342559
240. Peláez EC, Estevez MC, Portela A, Salvador JP, Marco MP, Lechuga LM. Nanoplasmonic biosensor device for the monitoring of acenocoumarol therapeutic drug in plasma. *Biosens Bioelectron*. 2018;119:149-155. doi:10.1016/j.bios.2018.08.011
241. Ferhan AR, Jackman JA, Malekian B, et al. Nanoplasmonic Sensing Architectures for

Decoding Membrane Curvature-Dependent Biomacromolecular Interactions. *Anal Chem*. 2018;90(12):7458-7466. doi:10.1021/acs.analchem.8b00974

242. Ferhan A, Ma G, Jackman J, Sut T, Park J, Cho N-J. Probing the Interaction of Dielectric Nanoparticles with Supported Lipid Membrane Coatings on Nanoplasmonic Arrays. *Sensors*. 2017;17(7):1484. doi:10.3390/s17071484
243. Mohan B, Vinod N. COVID-19: An Insight into SARS-CoV2 Pandemic Originated at Wuhan City in Hubei Province of China. *J Infect Dis Epidemiol*. 2020;6(4). doi:10.23937/2474-3658/1510146
244. Hadi AG, Kadhom M, Hairunisa N, Yousif E, Mohammed SA. A review on COVID-19: Origin, spread, symptoms, treatment, and prevention. *Biointerface Res Appl Chem*. 2020;10(6):7234-7242. doi:10.33263/BRIAC106.72347242
245. Sheervalilou R, Shirvaliloo M, Dadashzadeh N, et al. COVID-19 under spotlight: A close look at the origin, transmission, diagnosis, and treatment of the 2019-nCoV disease. *J Cell Physiol*. 2020;235(12):8873-8924. doi:10.1002/jcp.29735
246. Sen-Crowe B, McKenney M, Boneva D, Elkbuli A. A state overview of COVID19 spread, interventions and preparedness. *Am J Emerg Med*. 2020;38(7):1520-1523. doi:10.1016/j.ajem.2020.04.020
247. Kevadiya BD, Machhi J, Herskovitz J, et al. Diagnostics for SARS-CoV-2 infections. *Nat Mater*. 2021;20(5):593-605. doi:10.1038/s41563-020-00906-z
248. Ludwig S, Zarbock A. Coronaviruses and SARS-CoV-2: A Brief Overview. *Anesth Analg*. 2020;131(1):93-96. doi:10.1213/ANE.0000000000004845
249. Wang H, Li X, Li T, et al. The genetic sequence, origin, and diagnosis of SARS-CoV-2. *Eur J Clin Microbiol Infect Dis*. 2020;39(9):1629-1635. doi:10.1007/s10096-020-03899-4
250. Dinnes J, Deeks JJ, Berhane S, et al. Rapid, point-of-care antigen and molecular-based tests for diagnosis of SARS-CoV-2 infection. *Cochrane Database Syst Rev*. 2021;2021(3). doi:10.1002/14651858.CD013705.pub2
251. Singh KRB, Rathee S, Nagpure G, Singh J, Singh RP. Smart and emerging nanomaterials-based biosensor for SARS-CoV-2 detection. *Mater Lett*. 2022;307:131092. doi:10.1016/J.MATLET.2021.131092
252. Thapa S, Singh KRB, Verma R, Singh J, Singh RP. State-of-the-Art Smart and Intelligent Nanobiosensors for SARS-CoV-2 Diagnosis. *Biosens 2022, Vol 12, Page 637*. 2022;12(8):637. doi:10.3390/BIOS12080637
253. Creech CB, Walker SC, Samuels RJ. SARS-CoV-2 Vaccines. 2021;325(13):1318-1320.
254. Jackson CB, Farzan M, Chen B, Choe H. Mechanisms of SARS-CoV-2 entry into cells. *Nat Rev Mol Cell Biol*. 2022;23(1):3-20. doi:10.1038/s41580-021-00418-x
255. Wouters OJ, Shadlen KC, Salcher-Konrad M, et al. Challenges in ensuring global access to COVID-19 vaccines: production, affordability, allocation, and deployment. *Lancet*.

2021;397:1023-1034. doi:10.1016/S0140-6736(21)00306-8

256. AminJafari A, Ghasemi S. The possible of immunotherapy for COVID-19: A systematic review. *Int Immunopharmacol*. 2020;83(March):106455. doi:10.1016/j.intimp.2020.106455
257. Pashaei M, Rezaei N. Immunotherapy for SARS-CoV-2: potential opportunities. *Expert Opin Biol Ther*. 2020;20(10):1111-1116. doi:10.1080/14712598.2020.1807933
258. Li L, Zhang W, Hu Y, et al. Effect of Convalescent Plasma Therapy on Time to Clinical Improvement in Patients with Severe and Life-threatening COVID-19: A Randomized Clinical Trial. *JAMA - J Am Med Assoc*. 2020;324(5):460-470. doi:10.1001/jama.2020.10044
259. Plaze M, Attali D, Prot M, et al. Inhibition of the replication of SARS-CoV-2 in human cells by the FDA-approved drug chlorpromazine. *Int J Antimicrob Agents*. 2021;57(3):106274. doi:10.1016/j.ijantimicag.2020.106274
260. Drożdżal S, Rosik J, Lechowicz K, et al. FDA approved drugs with pharmacotherapeutic potential for SARS-CoV-2 (COVID-19) therapy. *Drug Resist Updat*. 2020;53:100719. doi:10.1016/j.drup.2020.100719
261. Lim SP. Targeting SARS-CoV-2 and host cell receptor interactions. *Antiviral Res*. 2023;210:105514. doi:10.1016/j.antiviral.2022.105514
262. Sparrow E, Friede M, Sheikh M, Torvaldsen S. Therapeutic antibodies for infectious diseases. *Bull World Health Organ*. 2017;95(3):235-237. doi:10.2471/BLT.16.178061
263. Payne S. Methods to Study Viruses. In: *Viruses*. Vol 21. Elsevier; 2017:37-52. doi:10.1016/B978-0-12-803109-4.00004-0
264. Coutu J, Ricard P, Djaïleb A, et al. Large-scale validation of a plasmonic sensor for SARS-CoV-2 pseudo-neutralization with a cohort of food and retail workers. *Sensors and Diagnostics*. 2024;3(5):850-862. doi:10.1039/d3sd00333g
265. Sars-cov- B, Ricard P, Lavallée E, et al. Cross-reactivity of antibodies from non-hospitalized COVID-19 positive individuals against the native and. :1-22. doi:doi.org/10.21203/rs.3.rs-646031/v1
266. Ruiz-Vega G, Soler M, Carmen Estevez M, et al. Rapid and direct quantification of the SARS-CoV-2 virus with an ultrasensitive nanobody-based photonic nanosensor. *Sensors & Diagnostics*. 2022;1:983-993. doi:10.1039/d2sd00082b
267. Huang L, Ding L, Zhou J, et al. One-step rapid quantification of SARS-CoV-2 virus particles via low-cost nanoplasmonic sensors in generic microplate reader and point-of-care device. *Biosens Bioelectron*. 2021;171:112685. doi:10.1016/J.BIOS.2020.112685
268. Hwang YC, Lu RM, Su SC, et al. Monoclonal antibodies for COVID-19 therapy and SARS-CoV-2 detection. *J Biomed Sci*. 2022;29(1):1-50. doi:10.1186/s12929-021-00784-w
269. Buchbinder EI, Desai N. PD-1PD-L1 immune checkpoint Potential target for cancertherapy.pdf. *Am J Clin Oncol*. 2016;39(1):98-106. https://www.ncbi.nlm.nih.gov/pmc/articles/PMC4892769/

270. Pan C, Liu H, Robins E, et al. Next-generation immuno-oncology agents: current momentum shifts in cancer immunotherapy. *J Hematol Oncol*. 2020;13(1):29. doi:10.1186/s13045-020-00862-w

271. Liu C, Seeram NP, Ma H. Small molecule inhibitors against PD-1/PD-L1 immune checkpoints and current methodologies for their development: a review. *Cancer Cell Int*. 2021;21(1):1-17. doi:10.1186/s12935-021-01946-4

272. Klyukin K, Alexandrov V. Kinetics of pH-dependent interactions between PD-1 and PD-L1 immune checkpoint proteins from molecular dynamics. *Proteins Struct Funct Bioinforma*. 2020;88(9):1162-1168. doi:10.1002/prot.25885

273. Nazari M, Kurdi M, Heerklotz H. Classifying surfactants with respect to their effect on lipid membrane order. *Biophys J*. 2012;102(3):498-506. doi:10.1016/j.bpj.2011.12.029

274. Magnez R, Thiroux B, Taront S, Segaoula Z, Quesnel B, Thuru X. PD-1/PD-L1 binding studies using microscale thermophoresis. *Sci Rep*. 2017;7(1):17623. doi:10.1038/s41598-017-17963-1

275. Butte MJ, Keir ME, Phamduy TB, Sharpe AH, Freeman GJ. Programmed Death-1 Ligand 1 Interacts Specifically with the B7-1 Costimulatory Molecule to Inhibit T Cell Responses. *Immunity*. 2007;27(1):111-122. doi:10.1016/j.immuni.2007.05.016

276. Lee HT, Lee SH, Heo YS. Molecular interactions of antibody drugs targeting PD-1, PD-L1, and CTLA-4 in immuno-oncology. *Molecules*. 2019;24(6):1-16. doi:10.3390/molecules24061190

277. Wang M, Wang J, Wang R, et al. Identification of a monoclonal antibody that targets PD-1 in a manner requiring PD-1 Asn58 glycosylation. *Commun Biol*. 2019;2(1). doi:10.1038/s42003-019-0642-9

278. Wang C, Thudium KB, Han M, et al. In vitro characterization of the anti-PD-1 antibody nivolumab, BMS-936558, and in vivo toxicology in non-human primates. *Cancer Immunol Res*. 2014;2(9):846-856. doi:10.1158/2326-6066.CIR-14-0040

279. Chu CW, Čaval T, Alisson-Silva F, et al. Variable PD-1 glycosylation modulates the activity of immune checkpoint inhibitors. *Life Sci Alliance*. 2024;7(3):3. doi:10.26508/lsa.202302368

280. Bu MT, Yuan L, Klee AN, Freeman GJ. A Comparison of Murine PD-1 and PD-L1 Monoclonal Antibodies. *Monoclon Antib Immunodiagn Immunother*. 2022;41(4):202-209. doi:10.1089/mab.2021.0068

281. Špačková B, Klein Moberg H, Fritzsche J, et al. Label-free nanofluidic scattering microscopy of size and mass of single diffusing molecules and nanoparticles. *Nat Methods*. 2022;19(6):751-758. doi:10.1038/s41592-022-01491-6

282. Egea AMC, Trévisiol E, Vieu C. Direct patterning of probe proteins on an antifouling PLL-g-dextran coating for reducing the background signal of fluorescent immunoassays. *Biointerphases*. 2013;8(1). doi:10.1186/1559-4106-8-37

283. Daniels CR, Reznik C, Kilmer R, et al. Permeability of anti-fouling PEGylated surfaces probed by fluorescence correlation spectroscopy. *Colloids Surfaces B Biointerfaces*. 2011;88(1):31-38. doi:10.1016/j.colsurfb.2011.05.044